

**Platinum-free Electrocatalysts Based  
on Graphene and Carbon Nanohorn  
for Polymer Electrolyte Membrane  
Fuel Cell Cathode**

**Thesis Submitted to AcSIR  
For the Award of the Degree of**

**DOCTOR OF PHILOSOPHY  
In Chemical Sciences**



By

**Mr. Sreekuttan M. Unni  
Registration Number: 10CC11J26003**

**Under the guidance of  
Dr. Sreekumar Kurungot**

**CSIR-National Chemical Laboratory, Pune-411008,  
India**



## Certificate

This is to certify that the work incorporated in this Ph.D. thesis entitled '**Platinum-free Electrocatalysts Based on Graphene and Carbon Nanohorn for Polymer Electrolyte Membrane Fuel Cell Cathode**' submitted by **Mr. Sreekuttan M. Unni** to Academy of Scientific and Innovative Research (AcSIR) in fulfilment of the requirements for the award of the Degree of Doctor of Philosophy, embodies original research work under my guidance. I further certify that this work has not been submitted to any other University or Institution in part or full for the award of any degree or diploma. Research material obtained from other sources has been duly acknowledged in the thesis. Any text, illustration, table etc., used in the thesis from other sources, have been duly cited and acknowledged.

Mr. Sreekuttan M. Unni  
(Student)

Dr. Sreekumar Kurungot  
(Supervisor)

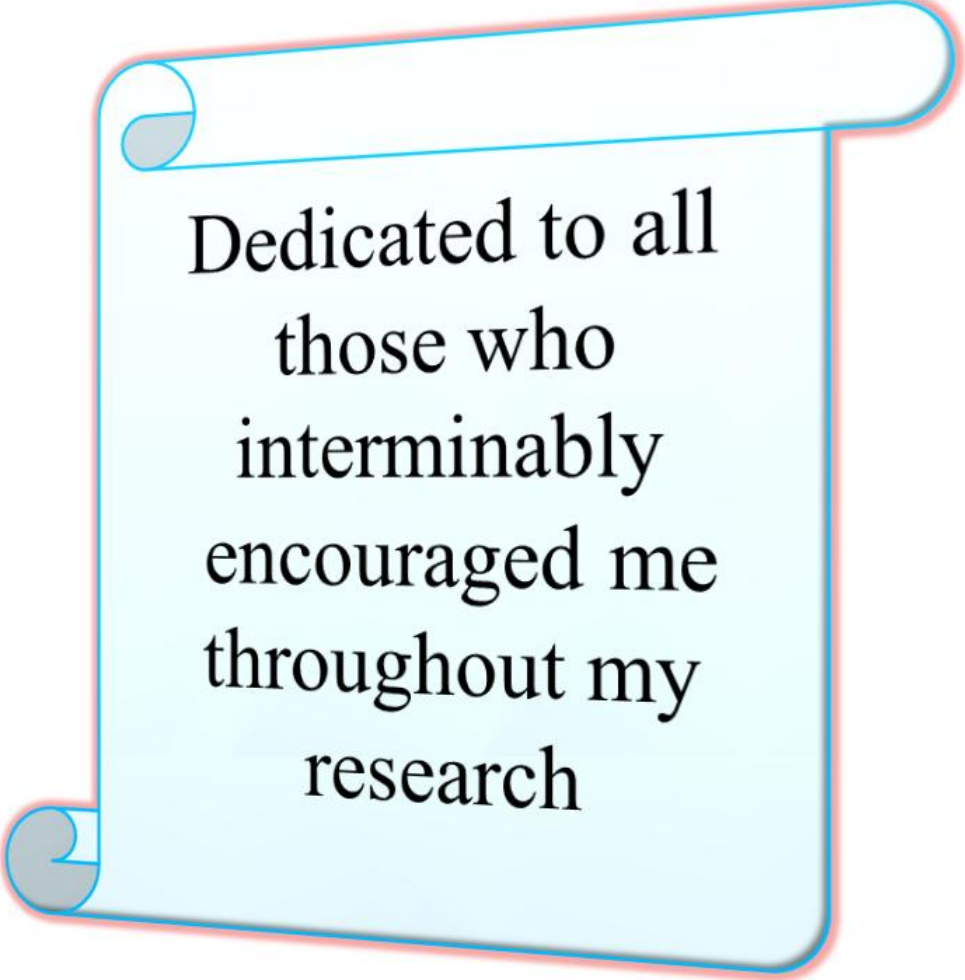


## Declaration

I, hereby declare that all the experiments in this thesis entitled ‘**Platinum-free Electrocatalysts Based on Graphene and Carbon Nanohorn for Polymer Electrolyte Membrane Fuel Cell Cathode**’ submitted for the degree of Doctor of Philosophy in Chemical Sciences, to the Academy of Scientific and Innovative Research (AcSIR) have been carried out by me at the Physical and Materials Chemistry Division, CSIR-National Chemical Laboratory, Pune-411008, India, under the supervision of Dr. Sreekumar Kurungot. The work is original and has not been submitted in part or full by me, for any degree or diploma to any other university or institutions.

Mr. Sreekuttan M. Unni  
Physical and Materials Chemistry Division  
CSIR-National Chemical Laboratory  
Pune-411008, India





Dedicated to all  
those who  
interminably  
encouraged me  
throughout my  
research





## Acknowledgment

*With the help of God Almighty, I am going to achieve the highest degree in my life “Doctor of Philosophy”. His helping hands reached me in the form of my teachers, my friends, my colleagues and other forms to fulfil my dream. At this moment, I would like to thank each and everyone who directly or indirectly helped me to achieve this goal.*

*First of all, I would like to thank my research guide Dr. Sreekumar Kurungot for his effort to mould me as an independent researcher. He provides the freedom to think, freedom to design a work, freedom to execute the work and showed me how to shape a research work into an attractive research article and technologies. He is the person who showed me the way of writing a manuscript, reports, research proposal, etc. His extensive correction of manuscripts is memorable. By assigning research interns under my supervision, he taught me how to guide a student. During my seven years of association with him, I learned enormously and I am confident to stand on my own foot as an independent researcher in the next phase of my career.*

*This is the time to acknowledge Dr. K. Vijayamohan Pillai, Director, CSIR-NCL and CSIR-CECRI, with whom I worked nearly for three years. He is the person who showed me the wonderful world of nanomaterials and electrochemistry. His friendly nature and helping hands always inspired me a lot. The most attractive character of Dr. Vijayamohan is his positive attitude towards experimental results. When we go for a discussion, I never heard a word “This is a useless result” even though, it was a worst one!!!!. I cannot forget his morning classes on electrochemistry. I am lucky because I was the last person who attended his class before he left CSIR-NCL in 2012 as the director of CSIR-CECRI. His excellent teaching and presentation skills also inspired me and I indeed tried to adopt most his qualities in my career.*

*I would like to thank Professor Nicolas Alonso-Vante, Universite de Poitiers, France. I am very fortunate to associate with him for six months during my tenure as a Raman-Charpak Fellow. I learned a lot of practical electrochemistry lessons from him. This helped me to improve my practical skills. He was very much interested in scientific discussions at anytime. Evening coffee time was always devoted to fruitful discussions. His approaches towards students and the importance he has given to weekly reports have taught me lessons, which will surely be going to play very important roles in my future career. He showed me how to write a manuscript, while starting an experiment by practising the habit of a series of weekly reports. My labmates Roberto, Manuel, Jesus, Wong, Yun and Mirabbos made my stay in France a memorable one. A special thanks to Dr. Aurelien Habrioux for his effective scientific discussions.*

*I would like to thank Dr. Sourav Pal, former Director of CSIR-NCL, with whom I associated few weeks in his theory group during the initial days of my master’s project. His teaching skills are par excellent and attractive. He taught the brain-storming subject; ‘Quantum Mechanics’ like a wonderful story. I also thank Dr. Anil Kumar, Chair of Physical and Materials Chemistry Division, for providing me the infrastructure to work at his division.*

*I would like to thank Dr. Ashish Lele for his helping hand during my stay in NCL. Also, his excellent leadership for the development of the fuel cell system through effective group activities inspired me a lot. At this moment, I would also like to acknowledge the kind helps obtained from Dr. Ulhas Kharul and Dr. Neelima Bulakh.*

*I would like to thank Dr. Ogale for his timely help and effective collaboration. His classes on spectroscopy are marvellous. Even though he taught me the spectroscopy few years back, I still remember everything without polishing the topic. His friendly nature as well as helping hand to everyone irrespective of the position has inspired me a lot. I also thank his students Dr. Dattakumar, Dr. Rohan and Dr. Prasad for the effective collaborations. I also thank Ms. Dhanya for helping me to carry out SEM analysis of my samples.*

*I would like to thank my doctoral advisory committee members, Dr. Guruswamy, Dr. Ulhas Kharul and Dr. B. L. V Prasad for their fruitful suggestions on every stage of my research.*

*I would like to thank the funding agencies like Department of Science and Technology (DST)- India, Council of Scientific and Industrial Research (CSIR)-India, University Grand Commission (UGC)-India, Indo-French Centre for the Promotion of Advanced Research (IFCPAR)-India, Universite de Poitiers-France and CSIR-National Chemical Laboratory (CSIR-NCL)-India.*

*I would like to thank the publishing houses like Royal Society of Chemistry (RSC), American Chemical Society (ACS), Wiley International, Elsevier, Taylor and Francis for publishing my research works and also for giving permission for reproducing the data during the preparation of my thesis.*

*I would like to thank Dr. K. R. Patil and his students Babasaheb and Sagar Patil for their assistance to get the XPS analysis in less time, which is one of the inevitable characterization methodologies in my research activities. I also, thank Dr. Rahul Banerjee and his students Dr. Pradip Patchfule and Sharath for the BET surface area analysis.*

*Thanks to Mr. Golap, Mr. Kiran, Dr. Naren, Mr. Pandiraj, Mr. Anuj, Ms. Sravani and Mr. Ketan for doing TEM/SEM analyses of my samples.*

*I would like to thank Mr. Dipakji, Mr. Punekar and Mr. Akbar for their assistance related to some of the official works.*

*I would like to thank the former student academic office Chairmen Dr. P. A. Joy, Dr. C. G. Suresh and the current Chairman Dr. Sasidhar, AcSIR Coordinator Dr. Chetan Gadgil and other staff in SAO for their timely help in processing the documents related to my coursework and PhD.*

*I would like to thank Dr. Sujith Ghosh (IISER, Pune) and his student Dr. Sanjog, Dr. Presanjith Ghosh (IISER, Pune) and his student Mr. Nandha, Dr. Nandini Devi and her students Jijil and Leena, Dr. C. S. Gopinath, Dr. C. P. Vinod, Dr. B. L. V. Prasad, Dr. M. V. Badiger, Dr. Suresh Bhatt, Dr. Manjusha, Dr. Ajith Kumar, Dr. Mayadevi, Dr. Rajmohanan and Dr. Santosh for effective collaborations and timely help. I cannot forget the help and encouragement of Mr. Santhosh, INCO, in each stage of my career.*

*I would like to thank my former teachers of the School of Chemical Sciences, M. G. University Campus, Dr. A. S. Padmanabhan, Dr. M. Padmanabhan Dr. Madhavan Pillai, Dr. Pius, Dr. Radhakrishnan, Dr. Sabu Thomas, Dr. Ibnu Saud, Dr. Sureash Mathew, Dr. C. V. Ashokan, Dr. Anil Kumar, Dr. Beena and Dr. Devaki for the encouragement and appreciation during each stage of my study and research. I acknowledge the help and encouragement from my former teachers of SNM College Maliankara, Prof. C. K. Ranjan, Dr. Cibi, Dr. Sulekha, Dr. Beena, Dr. Bhuvaneshwary, Dr. Sleema, Prof. Chitra, Prof. Madhusudhanan, Prof. Manoranjan, Dr. Joshi, Prof. Usha, Prof. Honey (Chemistry Department), Prof. Kairali, Prof. Chandrika, Prof. Vijayalekshmi, Prof. Geetha, Prof. Usha (Physics Department), Prof. Jalajamani, Prof. Soya (Hindi Department). I also thank help from Asokettan (SNM College).*

*My special thanks to my seniors Dr. Sneha, Dr. Mahima, Dr. Balchandra, Dr. Meera, Dr. Kannan, Dr. Bhaskar, Dr. Sanjay, Dr. Pravin, Dr. Dhanraj Rathode, Dr. Dhanraj Shinde, Mr. Joyashish and Dr. Beena for mentoring and caring during my initial days in NCL.*

*My special thanks to my juniors Dr. Palaniselvam, Dr. Vishal, Dr. Bihag, Harshitha, Siddhu, Rajith, Santhosh, Pandiraj, Kashyap, Roby, Ayasha, Vidyanand, Pranav, Maya, Sarath, Mrs. Ruhi, Ajinkya, Pritish, Sachin, Harshal, Anita, Smita and Aniket for creating cherishful moments in the lab.*

*I wish to acknowledge the extensive help from Neetha, Siddhu and Rajith during my research in CSIR-NCL.*

*I would like to thank Savariraj, Sai Krishna, Nisha, Sarath, Pranav, Neeraj, Hasna, Sampreeth, Smita and Shilpa, the projects interns who worked with me for their master program. Their interesting works and contributions to my research activities are highly appreciated.*

*I would like to thank my former colleagues Hussain, Nilesh, Vinisha, Bipinlal, Abizer, Ranjith, Manjoor, Hari, Ajinkya, Lal Busher, Manila, Manju, Sajna, Aswani and Nishant.*

*I thank my G-30 members Rahul, Mufzir, Dr. Hari, Dr. Sadiq, Dr. Remy, Reji, Jijil, Bipinlal, Rajesh, Rajith, Girish, Anumon, Arun Torris and Dr. Vijayadas for providing an enjoyable environment for many years. I also thank my kids in G-1, Sarath, Sanoop, Pranav, Rajith and Shibin for creating a friendly atmosphere and nice food. Special thanks to my new roommates of SA-50, Prabhakar, Pranjal and Gopikrishna.*

*I would like to thank my Malayali, Tamil, Telugu, Marathi and north Indian friends for their support during my stay in NCL. I am also thankful to Dr. Harikrishanan, Dr. Shijo, Dr. Arjith, Dr. Thanay, Dr. Bindu, Dr. Nisha, Prajitha, Dr. Deepa, Rajashree, Dr. Subdeep, Mr. Suresha, Dr. Thushara, Naresh, Dr. Jima, Dr. Aany for their friendship.*

*Even though we have several friend circles, I have to mention that the care, love and support provided by my friends Jijil, Rakesh (Palu) and Vinayak (Mr. Kale) are memorable. I hope it will continue longer. It is needless to use the word thanks to my sister Leena for her care, love and support during my stay in NCL. She was with me at every up and down in my life in NCL. I am very thankful to NCL that I have got a best friend and sister from NCL.*

*More importantly, I would like to thank (I know it is nothing, if I mention the word 'thank') my elder brother 'Ankuttan' for his care, love, support, criticism and fruitful scientific discussions during my stay in NCL. I thank God for providing me such a wonderful person as my close friend when I was alone. His scientific suggestions and criticisms always polished my knowledge, writing skill, character, presentation skill and personality. I also thank Minu Arun for her delicious food. Arun and Minu, you both make my last days in NCL more cherish and memorable.*

*Finally, words are not enough to express my feelings for my parents who struggled and suffered a lot for me and my education. Without their support, I will not grow into this position. I don't know, what I should write for them. But I know their life is for me. I am very thankful to my sister Sreedevi and my brother-in-law Murali for their support throughout my education and growth. My sister encouraged me at each stage of my education. Even though I didn't stay enough time with my 'Abi', his love and affection is memorable.*

*Though, many have not been mentioned by name, I didn't forget their support throughout.*

**Sreekuttan M. Unni**



## **List of Abbreviations**

<b><u>Abbreviations</u></b>	<b><u>Expansions</u></b>
AEMFC	Anion Exchange Membrane Fuel cell
AEM	Anion Exchange Membrane
ADT	Accelerated Durability Test
CNF	Carbon Nanofiber
CNT	Carbon Nanotube
CA	Chronoamperometry
CE	Counter Electrode
CNG	Nitrogen doped graphene wrapped Carbon nitride
CN <sub>x</sub>	Carbon Nitride
CNH	Carbon Nanohorn
CO	Carbon Monoxide
COF	Covalent Organic Framework
CQD	Carbon Quantum Dots
CV	Cyclic Voltammetry
CVD	Chemical vapour deposition
DOE	Department of Energy
DMFC	Direct Methanol Fuel Cell
DFT	Density Functional Theory
EDAX	Energy Dispersive X-ray Analysis
ESCA	Electron Microscopy for Chemical Analysis

ESCA	Electrochemical Surface Area
FCNH	Functionalized carbon Nanohorn
FeNCNH	Iron and Nitrogen Co-doped Carbon Nanohorn
FeGNT	Iron encapsulated Graphene Nanotube
FeNCNT	Iron Encapsulated Nitrogen Doped Nanotube
FeNC	Iron and Nitrogen Co-doped Carbon
FeCNO	Oyster type morphology from CNH and iron
GO	Graphene Oxide
GC	Glassy Carbon
GEPPY	Pyrrrole Reduced Graphene Oxide
HOR	Hydrogen Oxidation reaction
HR-TEM	High Resolution Transmission Electron Microscopy
K-L	Koutecky-Levich
LSV	Linear Sweep Voltammetry
MEA	Membrane Electrolyte Assembly
MCFC	Molten Carbonate Fuel Cell
MOF	Metal Organic Framework
MOR	Methanol Oxidation Reaction
MMT	Montmillorite
NGE	Nitrogen Doped Graphene
NCNT	Nitrogen doped Carbon Nanotube
NCNH	Nitrogen Doped Carbon Nanohorn
ORR	Oxygen Reduction Reaction
PAFC	Phosphoric Acid Fuel Cell
PBI	Polybenzimidazole

PEEK	Polyether ether Ketone
PEM	Polymer Electrolyte Membrane
PEMFC	Proton Exchange Membrane Fuel Cell
PGM	Platinum Group Metal
RGO	Reduced Graphene Oxide
RHE	Reference Hydrogen Electrode
RDE	Rotating Disc Electrode
RDS	Rate Determining Step
RRDE	Rotating Ring Disc Electrode
SEM	Scanning Electron Microscopy
SWCNH	Single Wall Carbon Naohorn
SOFC	Solid Oxide Fuel Cell
slpm	Standard Litter Per Minute
TEM	Transmission Electron Microscopy
TPB	Triple Phase Boundary
WE	Working Electrode
XRD	X-ray Diffraction
XPS	X-ray Photoelectron Spectroscopy
1D	One Dimensional
2D	Two Dimensional
3D	Three Dimensional
$\mu$ LFFC	Micro Laminar Flow Fuel Cell





## Table of Contents

<b>Abstract</b> .....	<b>1</b>
<b>Chapter 1: Introduction: Electrocatalysts for oxygen reduction reaction in polymer electrolyte membrane fuel cells</b> .....	<b>7</b>
1.1. Fuel cell and its classification.....	8
1.2 Polymer electrolyte membrane fuel cell.....	10
1.2.1 Proton exchange membrane fuel cell (PEMFC).....	11
1.2.2 Anion exchange membrane fuel cells.....	14
1.3. Electrocatalysts for PEM fuel cells.....	15
1.3.1 Hydrogen/fuel oxidation reaction.....	15
1.3.2. Oxygen reduction reaction.....	16
1.3.2.1 Pt based electrocatalysts for ORR.....	20
1.3.2.1.1 Shape controlled Pt nanocrystals.....	20
1.3.2.1.2 Pt alloy catalysts.....	22
1.3.2.1.3 Pt core-shell nanostructures for ORR.....	25
1.3.2.1.4 Support modified Pt catalysts.....	27
1.3.2.2 Pt-free metal electrocatalysts for ORR.....	29
1.3.2.2.1 Noble metal other than Pt.....	29
1.3.2.2.2 Transition metal oxide for ORR.....	29
1.3.2.2.3 Perovskites and Brownmillerites for ORR.....	30
1.3.2.2.4 Metal chalcogenides for ORR.....	31
1.3.2.2.5 Metal nitrides, oxynitrides and carbides for ORR.....	32
1.3.2.2.6 M-N-C electrocatalysts for ORR.....	33
1.3.2.2.6.1 Mechanism of ORR on Fe-N-C.....	37
1.3.2.2.7 Metal encapsulated nanotubes for ORR.....	38
1.3.2.2.8 Fe-P-C based catalysts for ORR.....	39

1.3.2.3 Metal-free electrocatalysts for ORR.....	39
1.3.2.3.1 Doping of carbon morphologies using single heteroatom for ORR.....	41
1.3.2.3.1.1 Nitrogen doping .....	41
1.3.2.3.1.2 Boron doping.....	44
1.3.2.3.1.3 Sulphur doping.....	44
1.3.2.3.1.4 Phosphorous doping .....	45
1.3.2.3.1.5 Dopants other than ‘N, S, B, P’ .....	46
1.3.2.3.2 Co-doping of carbon morphologies using two heteroatoms for ORR.....	46
1.3.2.3.2.1 Boron and nitrogen co-doping .....	46
1.3.2.3.2.2 Sulphur and nitrogen co-doping .....	47
1.3.2.3.2.3 Phosphorous and nitrogen co-doping .....	47
1.3.2.3.3 Co-doping of carbon morphologies using three heteroatoms for ORR .....	48
1.3.2.3.4 ORR mechanism on the N-doped carbon materials (CNT and graphene)....	49
1.4 Scope and objectives of the present thesis .....	54
1.5 References .....	56

**Chapter 2: Nitrogen doped graphene based electrocatalysts for oxygen reduction reaction..... 71**

2.1 Introduction.....	72
<b>Part A: Nitrogen doped graphene from pyrrole mediated reduced graphene oxide for ORR.....</b>	<b>74</b>
2A.1 Experimental .....	74
2A.1.1 Preparation of pyrrole reduced graphene oxide .....	74
2A.1.2 Preparation of NGE.....	75
2A.1.3 Structural characterization.....	75
2A.1.4 Electrochemical studies .....	75
2A.2 Results and discussion.....	76
2A.2.1 TEM analysis .....	76

2A.2.2 FT-IR analysis .....	77
2A.2.3 TGA analysis .....	78
2A.2.4 Raman analysis.....	79
2A.2.5 XRD analysis.....	80
2A.2.6 Surface area analysis.....	81
2A.2.7 XPS analysis.....	82
2A.2.8 Electrochemical analysis .....	85
<b>Part B: Layer-separated distribution of nitrogen doped graphene by its wrapping on carbon nitride tetrapods for enhanced ORR.....</b>	
2B.1 Experimental.....	92
2B.1.1 Graphene oxide (GO) synthesis.....	92
2B.1.2 Preparation of CN <sub>x</sub> wrapped nitrogen doped graphene (CNG).....	92
2B.1.3 Preparation of nitrogen doped graphene (Bulk NG) .....	92
2B.1.4 Materials characterization.....	93
2B.1.5 Electrochemical Measurements.....	94
2B.2 Results and discussion.....	95
2B.2. 1 SEM and TEM analysis .....	95
2B.2.2 Raman and XRD analyses .....	99
2B.2.3 Surface area analysis .....	100
2B.2.4 XPS analysis .....	101
2B.2.5 Electrochemical studies.....	105
2.2 Conclusion.....	111
2.3 Reference.....	112
<b>Chapter 3: Nitrogen doped carbon nanohorn and its metal chalcogenide composite as ORR electrocatalysts.....</b>	
3.1 Introduction.....	118

<b>Part A. Nitrogen doped carbon nanohorn as an efficient oxygen reduction electrocatalyst</b> .....	119
3A.1 Experimental .....	119
3A.1.1 Materials .....	119
3A.1.2 Functionalization and nitrogen doping of SWCNH .....	119
3A.1.3 Materials characterization .....	120
3A.1.4 Electrochemical measurements .....	121
3A.1.5 Anion exchange membrane fuel cell test .....	122
3A.1.5.1 Membrane pretreatment .....	122
3A.1.5.2 Electrode preparation .....	122
3A.1.5.3 MEA fabrication .....	122
3A.1.5.4 Test Station Details .....	122
3A.2 Results and discussion .....	123
3A.2.1 TEM and EDAX analysis .....	123
3A.2.2 Raman analysis .....	125
3A.2.3 Surface area analysis .....	126
3A.2.4 Four-probe electrical conductivity measurement .....	127
3A.2.5 XPS analysis .....	128
3A.2.6 Electrochemical analysis .....	130
<b>Part B: CoSe<sub>2</sub> supported nitrogen-doped carbon nanohorn for ORR</b> .....	139
3B.1 Experimental section .....	140
3B.1.1 Materials .....	140
3B.1.2 Synthesis of nitrogen doped nanohorn (NCNH) .....	140
3B.1.3 Synthesis of 40 wt.% CoSe <sub>2</sub> supported nitrogen doped nanohorn (CoSe <sub>2</sub> /NCNH) .....	140
3B.1.4 Electrochemical characterization .....	141
3B.1.5 Air breathing micro laminar flow fuel cell .....	142
3B.1.5.1 Electrodes fabrication .....	142

---

3B.2 Results and discussion.....	144
3B.2.1 XRD analysis .....	144
3B.2.2 Raman analysis .....	145
3B.2.3 TEM analysis .....	146
3B.2.4 Surface area analysis .....	147
3B.2.5 XPS analysis .....	148
3B.2.6 Electrochemical analysis.....	149
3.2 Conclusion.....	155
3.3 Reference.....	157
<b>Chapter 4: Nitrogen and iron co-doped carbon nanohorn for ORR .....</b>	<b>161</b>
4.1 Introduction.....	162
<b>Part A. Surface-modified single wall carbon nanohorn as an effective electrocatalyst for platinum-free fuel cell cathodes .....</b>	<b>164</b>
4A.1 Experimental.....	164
4A.1.1 Functionalization of SWCNH .....	164
4A.1.2 Synthesis of FeNCNH .....	164
4A.1.3 Synthesis of FeNC.....	165
4A.1.4 Synthesis of Fe complex on SWCNH.....	165
4A.1.5 Physical characterizations.....	165
4A.1.6 Electrochemical Characterization .....	166
4A.1.7 Anion exchange membrane fuel cell test.....	166
4A.2 Results and Discussion .....	168
4A.2.1 TEM and SEM analysis .....	168
4A.2.2 Raman and XRD analysis.....	169
4A.2.3 Surface area analysis.....	170
4A.2.4 XPS analysis.....	171
4A.2.5 Electrochemical studies .....	174

<b>Part B: Carbon Nanohorn-derived Graphene Nanotube System as a Platinum-free Fuel Cell Cathode</b> .....	182
4B.1 Experimental section.....	182
4B.1.1 Materials.....	182
4B.1.2 Functionalization of SWCNH (FCNH) .....	182
4B.1.3 Preparation of graphene nanotube from single wall carbon nanohorn (FeGNT) .....	183
4B.1.4 Preparation of nanotube from melamine powder (FeNCNT) .....	183
4B.1.5 Preparation of nano oyster type morphology from CNH and iron (FeCNO)..	183
4B.1.6 Preparation of nitrogen doped nanohorn (NCNH).....	184
4B.1.7 Material characterization.....	184
4B.1.8 Electrochemical measurements .....	184
4B.1.9 Single cell analysis.....	185
4B.2 Results and discussion .....	186
4B.2.1 XRD and Raman analysis.....	187
4B.2.2 FE-SEM and Elemental mapping.....	188
4B.2.3 HR-TEM analysis.....	189
4B.2.4 Surface area analysis.....	194
4B.2.5 XPS analysis.....	195
4B.2.6 Electrochemical studies .....	197
4.2 Conclusion.....	203
4.3 References .....	204
<b>Chapter 5: Summary and Conclusion</b> .....	<b>209</b>
5.1 Summary.....	210
5.2 Future prospects .....	216
<b>List of Publications</b> .....	<b>217</b>
<b>Erratum</b> .....	<b>223</b>

## Abstract

Total population of the world has crossed 7.325 billion in the year 2014 and this has been increasing in a rapid pace. Apparently, energy demands are also increasing in an alarming rate. Currently, the fossil fuels are still the major sources for fulfilling the global energy requirements. However, the greenhouse gases produced during the combustion of the fossil fuels create enormous environmental hazards and impact to the living systems in the planet. To ensure a safe and healthy life in the future, it is the time to replace the conventional energy systems with the greener and renewable energy sources and technologies. Even though, many renewable resources and related devices are being explored to extract energy, at present, none of them can replace the fossil fuel based devices in terms of efficiency.

Recent development in the hydrogen economy is a *horizon of hope* for the development of the green energy electrochemical devices known as fuel cells. The fuel cell consumes hydrogen gas and produces electricity, heat and water. Since the by-product of a fuel cell is water, it can be considered as a green energy device. Similarly, since moving parts are absent in a fuel cell, it is quite silent and, hence, it delivers high efficiency. The maximum practical efficiency of the fuel cell lies in between 35-60% depending on the operating conditions. This efficiency is quite high as compared with the current devices that work with the fossil fuels. Among the varieties of fuel cells currently available, polymer membrane electrolyte (PEM) fuel cells are the most attractive due to their simple structure as well as portable and low temperature operations.

Since PEM fuel cell is working in a temperature below 200 °C, the electrode reactions require much costlier catalysts to catalyze the respective reactions, *i.e.* hydrogen oxidation and oxygen reduction. Since the cathode reaction (oxygen reduction reaction (ORR)) is quite sluggish at low temperature, it requires Pt or Pt based catalysts to deliver high output from the fuel cell. This forces the industry to use Pt on the fuel cell electrodes and ultimately leads to high cost of the cells. The high cost of the Pt electrocatalyst is mainly due to the scarcity of this noble metal in earth. This is the main issue which hampers the commercialization of the fuel cells, especially the PEM fuel cells. This issue

can be solved by using alternative electrocatalysts to Pt which should be of low cost and wide abundance in earth.

Since, the overall efficiencies of the fuel cell strongly depend on the cathode catalysts, these materials can be considered as the ‘*heart*’ of the fuel cells. Therefore, the selection of the alternative electrocatalysts to Pt should meet high ORR activity and stability. In this scenario, carbon based catalysts have been recently emerged as alternatives to Pt. However, generally, the ORR activities of these catalysts lag behind the activity of the Pt catalysts. In order to boost the activity of the carbon based electrocatalysts and ensure their performance in a wide range of pH of the electrolytes, it is necessary to modify or improve the nature and number density of the active reaction centres on such materials. This can be achieved only through a careful effort to simultaneously tune the morphology, surface area, reactive edges, electrical conductivity and preferred heteroatom coordinations in the carbon catalysts.

Hence, it is realized that a concerted effort is needed by the judicious selection of the carbon morphologies and methodologies to create large number of the potential active sites which can facilitate ORR under a wide range of experimental conditions. Maintenance of the number density and preferred coordination of the active sites can be strongly influenced by the carbon morphology and the process adopted for creating the sites. A systematic study in this direction has been carried out by targeting these goals by tuning the physicochemical properties of the carbon morphologies by selecting graphene and carbon nanohorn as the preferred substrate candidates. The present thesis compiles the outputs achieved in this effort of developing a group of potential non-precious metal based ORR electrocatalysts by narrowing down the overpotential and increasing the current density for oxygen reduction.

Chapter-wise abstracts are given below:

Chapter 1: This chapter starts with a short description about the fuel cell, and its classifications, followed by a detailed description on polymer electrolyte membrane (PEM) fuel cells and their classifications, mainly, proton exchange membrane fuel cells (PEMFCs) and anion exchange membrane fuel cells (AEMFCs). In continuation, this chapter elaborates the importance of electrocatalysis for oxygen reduction reaction (ORR) followed by a brief literature review of the different electrocatalysts reported so far for



ORR. All the electrocatalysts are categorized in three major classes respectively, Pt group metal, non-Pt group metal and non-metal electrocatalysts. The objectives and scope of this thesis are highlighted at the end of the chapter.

Chapter 2: This chapter deals with two viable strategies by which graphene can be converted into potential oxygen reduction electrocatalysts through nitrogen doping. Two different approaches are adopted with an aim to enhance the number density of the active sites for facilitating oxygen reduction reaction (ORR) in nitrogen doped graphene (NGE). The first half of the chapter describes the synthesis of NGE through pyrrole mediated reduction of graphene oxide (GO) followed by annealing in an inert atmosphere. This method produces NGE with a surface area of  $528 \text{ m}^2 \text{ g}^{-1}$ . This material shows significantly improved positive onset potential for oxygen reduction, which is found to be even higher than that of the commercial Pt/C. XPS analysis reveals the presence of higher percentage of pyrrolic coordination which in turn is responsible for the enhanced activity of the system towards ORR in alkaline medium. NGE also displays excellent electrochemical stability and fuel tolerance. The second half of the chapter deals with a strategy by which simultaneous nitrogen doping and wrapping of the nitrogen doped graphene sheets on carbon nitride tetrapods could be achieved. This is accomplished by dip-coating of GO on melamine foam followed by annealing at high temperature, which helps to produce three dimensional (3D) NGE wrapped carbon nitride tetrapods (CNG). This morphology assists the systems to attain efficient reactant distribution with more accessible surface and active sites. This material shows promising ORR activity in acidic condition with an overpotential of 100 mV compared to Pt/C. Moreover, the prepared CNG samples display excellent electrochemical stability and methanol tolerance.

Chapter 3: This chapter focuses on the development of nitrogen doped carbon nanohorn (NCNH) and its metal chalcogenide composite for achieving improved ORR activity in alkaline medium. Nitrogen doping in single walled carbon nanohorn (SWCNH) was carried out by the high temperature annealing of SWCNH and urea mixture in an inert atmosphere. Surface area and electrical conductivity of SWCNH could be easily modulated during the nitrogen doping. More positive half-wave potential ( $E_{1/2}$ ) of NCNH indicates that the active reaction centre density has been improved drastically by modifying the physical properties. Moreover, NCNH shows excellent electrochemical stability and fuel tolerance for ORR. Furthermore,  $\text{CoSe}_2$  nanoparticles were dispersed on the surface of

NCNH to study the substrate effect of a non-precious catalyst towards ORR. Experimental results show that the nitrogen atoms in NCNH improve the ORR activity of CoSe<sub>2</sub> and help to display more positive E<sub>1/2</sub> by the system, which is even better than that displayed by the current *state-of-the-art* Pt/C catalysts. This further proved that the substrate also has a very critical role in a system in modulating the reaction centre density. CoSe<sub>2</sub> supported NCNH (CoSe<sub>2</sub>/NCNH) shows excellent tolerance towards methanol and the system provides high power density (15 mW cm<sup>-2</sup>) in micro-laminar flow fuel cells.

Chapter 4: This chapter elaborates on the synthesis of nitrogen and iron co-doped carbon nanohorns and their ORR activity. Here, influence of the relative loading of nitrogen and iron precursor on the morphology of the resultant co-doped carbon nanohorn is studied along with its effect in the ORR activity accomplished by the modification of the active reaction centre density. Nitrogen and iron co-doped nanostructures were synthesised by thermal annealing of the materials in an inert atmosphere. At lower loading of the nitrogen and iron precursor, morphology of nanohorn (FeNCNH) remains intact after the annealing. This material shows excellent ORR activity and electrochemical stability in alkaline medium and outperforms the commercial Pt/C catalyst. However, the ORR performance of FeNCNH is relatively poor in acidic conditions. When the iron and nitrogen precursor loadings are higher, the morphology of carbon nanohorn transforms to graphene nanotube with the iron oxide nanoparticles encapsulated at the tip (FeGNT). These materials perform well towards ORR in both alkaline and acidic conditions. An overpotential of 100 mV was observed for ORR in the case of FeGNT, as compared to Pt/C in acidic condition and it also outperforms Pt/C in alkaline medium. Moreover, the electrochemical stability of FeGNT is far better in comparison with Pt/C. Single cell performance of FeGNT as the cathode catalyst provides a maximum power density of 200 mW cm<sup>-2</sup> using Nafion<sup>®</sup> 212 as a proton conducting membrane.

Chapter 5: This chapter provides an overall summary and conclusion of the research activities as explained in the previous chapters targeting on the development of efficient non-precious metal based electrocatalysts for ORR. The chapter highlights the approaches adopted and implemented for improving the ORR performance of the non-precious electrocatalysts by modifying the active reaction cite density by inducing changes in the physicochemical properties of graphene and carbon nanohorn. The proper selection of the carbon morphologies along with the attainment of high surface area with micro or

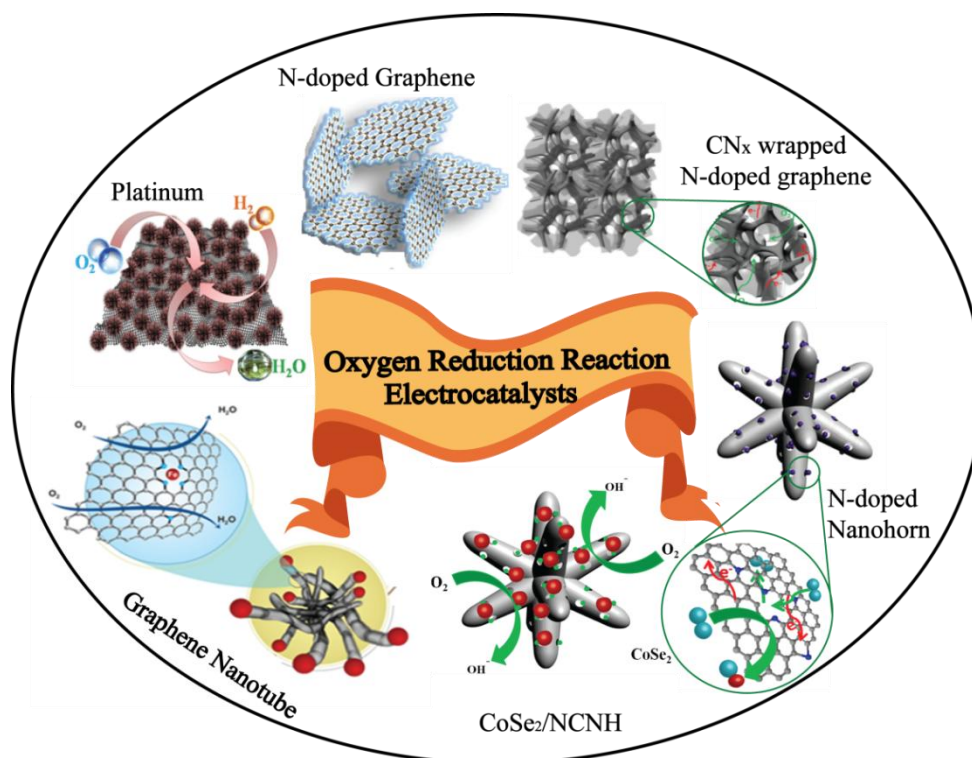
mesopores, good electrical conductivity and preferred coordination of the heteroatoms etc are found to be strongly influencing the activity of a non-precious electrocatalyst. The different approaches used for modifying these properties are concisely summarized in this chapter. This chapter also highlights the future prospects of the materials described in the thesis for other inevitable energy sectors like batteries, solar cells, water splitting etc. Moreover, this chapter also provides a glimpse about the current global scenario of the non-precious fuel cell catalyst research and the position of India in the world map among other countries involved in the development of the non-precious electrocatalysts.



# Chapter 1

## *Introduction: Electrocatalysts for oxygen reduction reaction in polymer electrolyte membrane fuel cells*

This chapter starts with a short description about fuel cell, and its classifications, followed by a detailed description on polymer electrolyte membrane (PEM) fuel cells and their classifications, mainly, proton exchange membrane fuel cells (PEMFCs) and anion exchange membrane fuel cells (AEMFCs). In continuation, this chapter elaborates the importance of electrocatalysis for oxygen reduction reaction (ORR) followed by a brief literature review of the different electrocatalysts reported so far for ORR. All electrocatalysts are categorized in three major classes respectively, Pt group metal, non-Pt group metal and non-metal electrocatalysts. The objectives and scope of this thesis are highlighted at the end of the chapter.



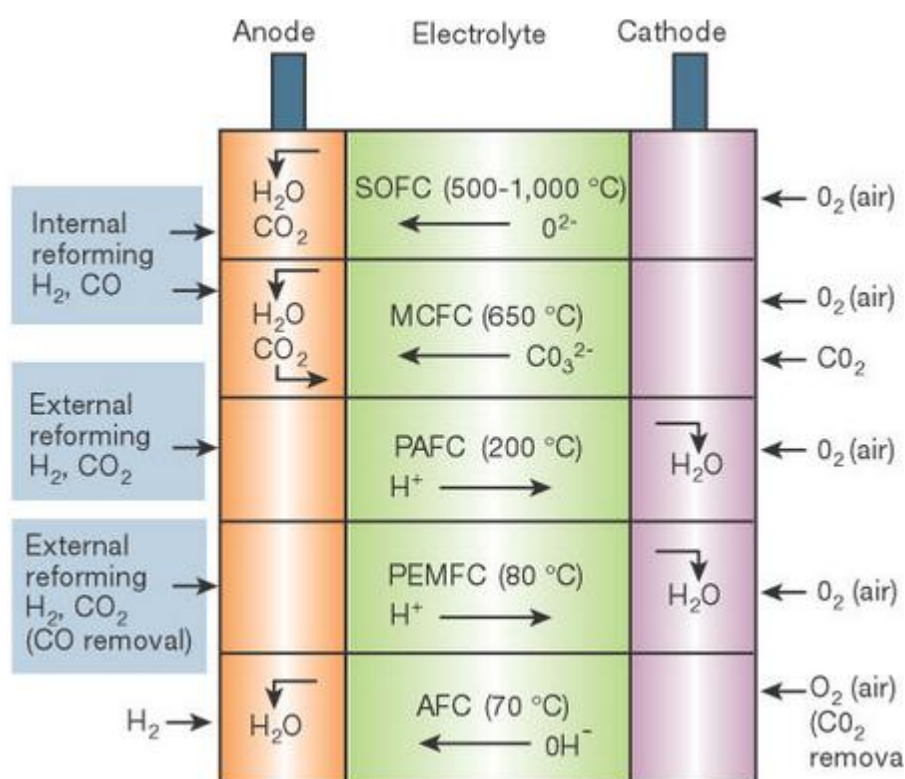
“*Water-powered vehicle*” is a fascinating dream of man-kind in the context of the current *world* squeezed by energy crisis. Attempts to realize the dream of “*water as fuel*” started long ago and are still continuing. However, many questions arise in connection with this concept, such as, whether water could be used as a fuel? Whether water could burn and produce energy? Is it thermodynamically feasible? However, scientists all over the world who try to employ water as fuel do not bother about these questions and believe that these will squash the technologies or innovations. In 1919, chemistry Nobel Laureate Francis Aston said “Energy from a glass of water can drive the *Queen Mary* across the Atlantic and back at full speed”.<sup>[1]</sup> Prof. Aston was talking about “the energy from one glass of water” mainly pointing to the energy liberated during the fusion of hydrogen derived from one glass of water. However, such a fusion reaction is quite difficult in water and would be hard to realize. Apart from the fusion reaction of hydrogen, there are some interesting curiosities related to the “*water as fuel*” concept to provide the society with a cheap and clean source of energy. Such efforts often lead to failures and end up with the fates similar to Ramar Pillai’s herbal-mediated conversion of water to petrol, Stanley Mayer’s “water-powered car”, John Kanzius’s “burning water” etc.<sup>[2]</sup> It would be interesting to know how water produces energy to drive a car as in Mayer’s water-powered car. Mayer’s car involves an electrolyser for splitting water to its constituent elements. These movements throw light to a new direction to use “*water as fuel*” for automobiles by integrating two devices, one for hydrogen production and the other for conversion. With modern technologies, water splitting can be achieved by energy efficient techniques such as photochemical, photo-electrochemical and electrochemical methods, but the question is “which device converts the produced hydrogen (green fuel) to energy?” The answer is very clear: “fuel cell”!

### 1.1 Fuel cell and its classification

‘Fuel cell’ is an electrochemical device that converts chemical energy stored in fuels to electrical energy. Usually, green gas (hydrogen) and other small organic molecules (methanol, ethanol, formic acid etc.) are used as fuels. By-products of the fuel cell reaction are water and heat. This electrochemical device was invented by Sir William Grove in 1839.<sup>[3]</sup> However, practical fuel cell came to the scene a century later (1937) through Francis T. Bacon.<sup>[4]</sup> Theoretically, a fuel cell has a cell voltage of 1.23 V and an efficiency of 90% at the higher heating value of hydrogen and practically it comes close to 60%.<sup>[5]</sup>

**Table 1.1** Classification of fuel cells based on the electrolyte used:

Fuel Cell	Electrolyte	Efficiency (%) (Lower hydrogen heating value)
Solid Oxide Fuel Cell (SOFC)	Metal oxide, perovskites etc. (Ytria stabilized zirconia)	60
Molten Carbonate Fuel Cell (MCFC)	Metal carbonates	50
Phosphoric Acid Fuel Cell (PAFC)	Phosphoric acid or phosphoric acid doped polymer membranes	40
Alkaline Fuel Cell (AFC)	Potassium hydroxide solution	60
Polymer Electrolyte Membrane (PEM) Fuel Cells	Polymer membrane capable of conducting protons or hydroxides	30-60

**Figure 1.1:** Fuel cell classification (Reused with permission from Ref [6a], copyright, Nature publishing group-2001).

The basic structure of a fuel cell consists of two electrodes and electrolyte (separator) for conduction of ions. The electrode at which the fuel is consumed is the anode and the electrode at which the oxidant is reduced is the cathode. Depending on the electrolyte used, the fuel cells are known by different names.<sup>[5-6]</sup> The nature of the

electrolyte even decides the operating temperature and efficiency. The Table 1.1 and Figure 1.1 give information about the different types of fuel cells.

Based on the present advancements, a fuel cell has been regarded as a promising energy conversion device for future applications. It has higher efficiency compared to combustion engines with zero emission of greenhouse gases. Fuel cell converts chemical energy to electrical energy in a single step. It should be noted that, the same process occurs *via* several steps in a normal combustion engine.<sup>[5]</sup> Since it has no moving parts, the lifetime of the fuel cell is quite high. It is easy to control the size of the fuel cells according to the intended application. Higher power can be generated by integrating many cells in a series. Global fuel cell demand in the year 2011 was worth US \$ 355.3 million and it will increase up to US \$ 910 million in 2018.<sup>[7]</sup> According to the ‘*Transparency Market Research*’ report, Asia-pacific and North America are top in demand for the fuel cell and Europe will be the future market place.<sup>[7]</sup> Many companies are involved in fuel cell manufacturing all over the world, Fuel Cell Energy, Ballard, Clearedge, Toshiba, Panasonic, Plug Power Inc. and Hydrogenics Corporation, to name a few.<sup>[8]</sup>

Among different fuel cells, polymer electrolyte membrane (PEM) fuel cells are more desirable for portable applications because of their compact design, low temperature operability, high power output, fast start-up and simplicity.

## 1.2 Polymer electrolyte membrane fuel cell

Polymer electrolyte membrane (PEM) fuel cells, also known as membrane fuel cells, employ a polymer electrolyte in the form of a thin ion permeable sheet (resistant towards gases). Depending on the nature of the membrane and its chemical functionalities, it conducts protons and hydroxides; and hence these systems are further classified as (i) Proton exchange membrane fuel cells (PEMFCs) and (ii) Anion exchange membrane fuel cells (AEMFCs). These fuel cells normally work at low temperature, *i.e.* below 100 °C and require expensive catalysts for the respective electrode reactions. Moreover, PEM fuel cells require membrane humidification for efficient ion transport.

Even though, there is a huge market interest for PEM fuel cells and the overwhelming profit that they bring out, their wide commercialization is still hampered by the components used in it. The major problem lies in the electrocatalyst for the respective electrode reactions. High cost and scarcity of Pt or platinum group metal (PGM)-based



catalysts result in more than 50% of the total cost of the fuel cells (Figure 1.2).<sup>[9]</sup> Department of energy (DOE) target for the PGM catalyst loading in a fuel cell for the year 2015 is 0.25 mg/cm<sup>2</sup> and this is projected to be further reduced by half in 2017.<sup>[10]</sup> Another bottleneck in PEM fuel cell is its membrane. Nafion<sup>®</sup>; a product of DuPont, is an expensive proton conducting membrane and it requires humidity for efficient proton conduction.<sup>[11]</sup> In case of the hydroxy ion conducting membrane fuel cell, the membrane developments are still in infancy and none of them is reported to be as efficient as Nafion<sup>®</sup>.<sup>[12]</sup> Bipolar plate, the current collector in a PEM fuel cell, which is made up of graphite, is also a matter of concern.<sup>[13]</sup> Since temperature of the PEM fuel cell operation is higher than 80 °C with applied pressure, breakage of the plate will create a serious issue by degrading its performance. Overall, in order to put forward the PEM fuel cell as the fuel cell of choice, one should take care of all the material as well as engineering aspects to get high performing and durable fuel cells.

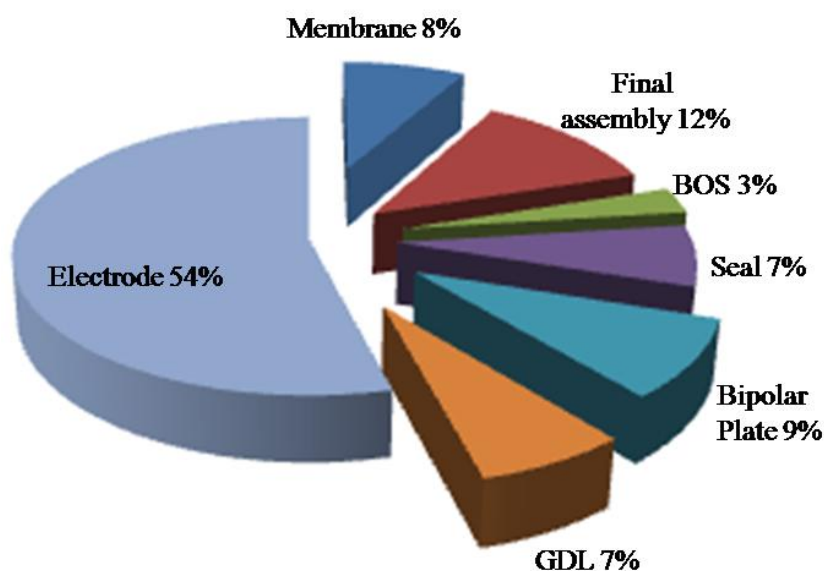
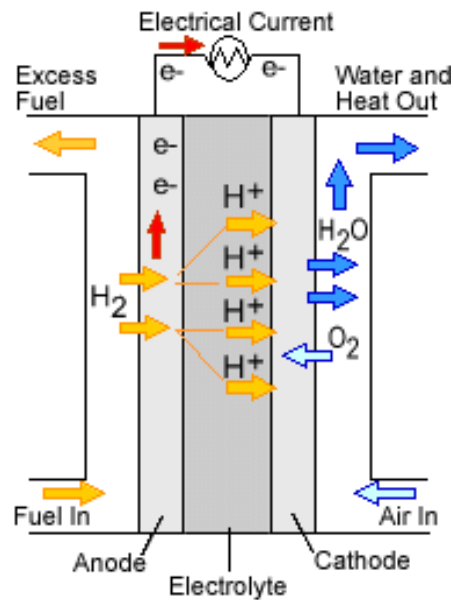


*Figure 1.2: PEM fuel cell cost in terms of its individual components.*

### 1.2.1 Proton exchange membrane fuel cell (PEMFC)

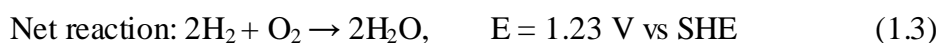
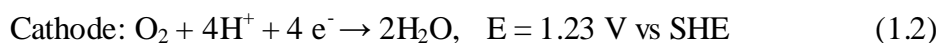
Proton exchange membrane fuel cell (PEMFC) (Figure 1.3) consists of a proton conducting membrane placed in between the cathode and the anode. Fuel (mainly, hydrogen) gets oxidized on the anode and produces hydrogen ions (protons) and electrons. Electrons are transferred to the external circuit and are reached the cathode compartment and this energy is generated.<sup>[14]</sup> The protons produced move through the proton conducting

membrane and reach the cathode compartment where the oxygen gets reduced in presence of the electron and proton to form water. Since the chemical reaction is exothermic, along with water, heat is also produced.<sup>[15]</sup> Usually, Nafion<sup>®</sup> membranes with different thickness are used as the proton conducting membrane. Apart from Nafion<sup>®</sup>, poly ether ether ketone (PEEK), sulphonated PEEK, Nafion-sulphonated carbon nanotube composite membrane, Nafion-SiO<sub>2</sub>/ZrO<sub>2</sub> composite membrane, etc. are also being used as efficient proton conducting membranes in PEMFC.<sup>[16]</sup> In order to attain efficient ion transport through the membrane, humidification of the polymer membrane is necessary. Proton conduction in a perfluoro-sulphonic acid membrane (Nafion) is mainly through the sulphonic acid functionality.<sup>[16e]</sup> Water can assist the efficient transport of proton through the sulphonic acid groups in the membrane by *Grotthuss* or *hopping* mechanism. Since the by-product of the fuel cell reaction is water, it will also assist in the humidification of the membrane. This may be the prime reason why this type of fuel cell operates below 100 °C.



**Figure 1.3:** Schematic diagram of a PEMFC (Courtesy Wikipedia.com).

Electrode reactions of a PEMFC are as follows<sup>[17]</sup>:



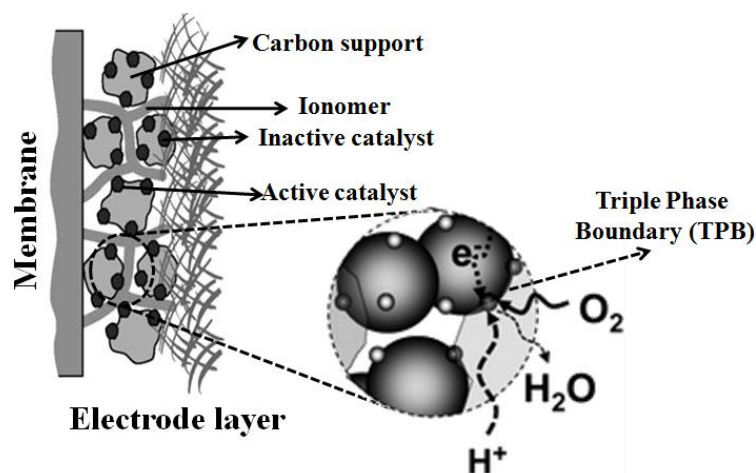


**Figure 1.4:** Schematic diagram of a PEMFC electrode layer and the triple phase boundary (Courtesy Wikipedia.com). Reprinted with the permission from Ref [18] Copyright © 2013, Royal Society of Chemistry.

Since PEMFC is working at low temperature ( $< 100\text{ }^{\circ}\text{C}$ ), expensive electrocatalysts are required for the respective electrode reactions, mainly, hydrogen oxidation reaction (HOR) and oxygen reduction reaction (ORR). Usually Pt and platinum group metals (PGMs) are used as the electrocatalysts for these electrode reactions.<sup>[19]</sup> Since Pt is used as the electrocatalyst, high purity hydrogen (hydrogen with less than 10 ppm CO) is required as the fuel.<sup>[20]</sup> Presence of carbon monoxide (CO) in the feed gas, that has strong affinity for chemisorption onto the Pt based metal, will reduce the electrode reaction rates by blocking the active reaction centers. Moreover, overall efficiency of a PEMFC depends on the cathode reaction where kinetically sluggish ORR takes place.<sup>[21]</sup> In order to boost the reduction of dioxygen molecules at lower temperature, efficient PGM based electrocatalysts are necessary. PGM based electrocatalysts in nanometer size supported on different conductive carbon substrates are used in both anode and cathode. These electrodes contain sufficient amount of proton conducting ionomer for efficient ion transport throughout the electrode. Hence, the effective formation of triple phase boundary (TPB), where the reactant gases, electrocatalyst and electrolyte create an efficient electrode electrolyte interface, is an important criterion for successful PEMFC operation<sup>[18]</sup> (see Figure 1.4).

## 1.2.2 Anion exchange membrane fuel cells

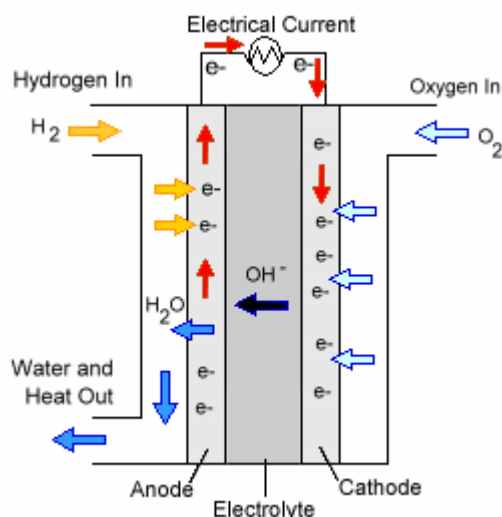


**Figure 1.5:** Schematic diagram of an AEMFC (Courtesy: Wikipedia.com).

Anion exchange membrane fuel cells (AEMFCs) (Figure 1.5) are another class of PEM fuel cells in which hydroxyl ion conducting membrane is used as the electrolyte (Fumion membrane, Tokuyama membranes, polysulphone based membrane, poly ether-imide polymers etc.).<sup>[12]</sup> Unlike AFC, AEMFC uses solid polymer membrane capable of  $\text{OH}^-$  ion conduction. All the anion exchange membranes (AEMs) contain quaternary ammonium groups to conduct the hydroxyl ions. The electrode reactions in an AEMFC are quite different from PEMFC (Equations 4 -6).<sup>[22]</sup> At the cathode, oxygen molecules are reduced to hydroxyl ions in presence of water and electrons. Hydroxyl ions produced pass through the AEM and facilitate the oxidation of hydrogen molecule at the anode and produce water. Electrons ejected are used for useful work that reach again at the cathode and assist the reduction of  $\text{O}_2$  to  $\text{OH}^-$  in presence of water. Since water is a pre-requisite part of the cathode reaction, feed gas should be humidified during the electrode reactions. Since  $\text{OH}^-$  is moving from the cathode to anode, methanol like fuel can be a suitable fuel for AEMFC because issues related to methanol crossover may not occur during the fuel cell operation. More importantly, compared to PEMFC, the electrode reactions are kinetically fast in alkaline medium; thus the PGM electrocatalysts can be replaced by suitable alternatives. However, the size of hydrated  $\text{OH}^-$  ion is comparatively higher than  $\text{H}_3\text{O}^+$  ions; hence, the ion conductivity of AEM is two-fold lower than that of PEM.<sup>[23]</sup> The electrode reactions in AEMFC are given below<sup>[23]</sup>:



### 1.3 Electrocatalysts for PEM fuel cells

According to Swedish scientist J. J. Berzilius “catalytic power means that substances are able to awake affinities that are asleep at a temperature by their mere presence”.<sup>[24]</sup> Catalyst is a substance, which alters the rate of a chemical reaction, without undergoing a chemical change. The catalysts which alter the electrode reactions can be termed as electrocatalysts.<sup>[25]</sup> In PEMFC/AEMFC, both hydrogen/fuel oxidation (anode reaction) and oxygen reduction (cathode reaction) occur only in presence of the electrocatalyst, mainly platinum supported on carbon (Pt/C). The fuel cell performance strongly depends on the electrode reactions, which in turn reflects the importance of a perfect electrocatalyst for efficient fuel cell reactions. Hence, the electrocatalyst may be considered as the “heart” of fuel cells.

#### 1.3.1 Hydrogen/fuel oxidation reaction

In particular, since PEMFC/AEMFC works at low temperature, the precious-electrocatalysts are inevitable for the electrode reactions. Commonly, Pt-based catalysts are used as efficient electrocatalysts in PEM fuel cells. Hydrogen oxidation on the Pt-based electrode is comparatively faster and experiencing less overpotential (<50 mV).<sup>[26]</sup> If the fuel changes from H<sub>2</sub> to methanol (or any other aliphatic alcohol or acid), the current *state-of-the-art* Pt catalyst shows rather poor stability or activity with time.<sup>[20]</sup> By-product adsorption on the Pt catalysts during such oxidation-reduction reactions reduces the available active centres. This issue could be solved by using alloy nanoparticles of Pt. It is interesting to observe that most of the hydrogen oxidation reaction (HOR) and direct alcohol oxidation reaction require expensive catalysts based on Pt and its alloy or core-shell type electrocatalysts. Recently, some efforts were taken to replace the Pt catalyst due to its cost and unavailability. However, performance of such electrocatalysts lags far behind the Pt catalysts. Metal oxides, mainly mixed oxides of cobalt, oxides of tin etc. show alcohol oxidation activity in the range of non-Pt catalysts.<sup>[27]</sup> Even though there is no perfect alternative for the Pt catalysts, there are reports that Cr<sub>2</sub>O<sub>3</sub> doped Ni, alloys of Mo, W and Co, RuO<sub>2</sub> etc. show comparable hydrogen oxidation activities.<sup>[28]</sup>

### 1.3.2 Oxygen reduction reaction

In a PEM fuel cell, the cathode reaction (ORR) is one of the major electrode reactions, which strongly influences the overall fuel cell performance. ORR has relatively sluggish kinetics and is influenced by many factors, such as the nature of the catalyst, pH, temperature etc. It experiences much higher overpotential ( $>200$  mV) on PGM catalyst for both PEMFC and AEMFC.<sup>[29]</sup> In a typical ORR process, the electron transfer between the catalyst and adsorbed dioxygen molecule reduces the bond order of the oxygen molecule and increases the elongation of O-O bond which in turn leads to the product depending on the pH of the medium. Depending on the nature of electron transfer between the catalyst and adsorbed oxygen molecule, ORR occurs *via* two different pathways. In other words, reduction of dioxygen mainly follows 4e<sup>-</sup> and 2e<sup>-</sup> pathways. These two different pathways depend on the catalytic centre and nature of the adsorption of oxygen molecule. Even though the nature of chemisorption of the oxygen molecule on the surface of the catalyst is not clear yet, there are few models that describe the plausible adsorption (Figure 1.6).<sup>[30]</sup>

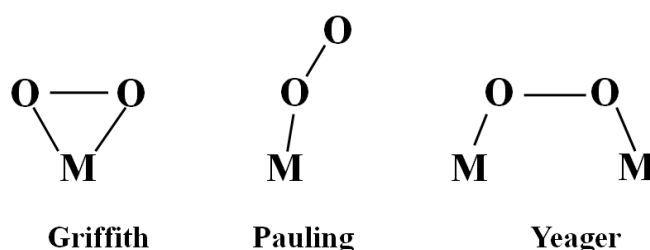


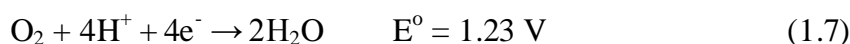
**Figure 1.6:** Different modes of adsorption of oxygen molecule on the catalyst surface.

Griffith model explains the interaction of dioxygen molecule on a single atom of the catalyst.<sup>[31]</sup> Here, the bond is formed between the  $\sigma$  orbital of oxygen and the empty  $d_z^2$  orbital of the metal atoms and a back  $\sigma$  bond is formed between the  $\pi^*$  orbital of oxygen and the partially filled  $d_{xy}$  or  $d_{xz}$  orbital of the metal. This model probably follows a four electron pathway. An end on mode of adsorption oxygen molecule was observed in the *Pauling model*, where the  $\sigma$  bond formation is occurred in between the  $\sigma$  orbital of oxygen and the  $d_z^2$  orbital of the metal.<sup>[32]</sup> Yeager proposed a bridged mode of adsorption between the oxygen molecule and two atoms of the catalyst. This particular mode will lead either to 2e<sup>-</sup> or 4e<sup>-</sup> pathway.<sup>[33]</sup> In acidic medium, the oxygen molecule is reduced to water molecule through a 4e<sup>-</sup> pathway (direct pathways). However, peroxide will be the major product if the reduction follows a 2e<sup>-</sup> pathway. Under alkaline conditions, hydroxy compound is the major product of the 4e<sup>-</sup> pathway and the 2e<sup>-</sup> pathway leads to the

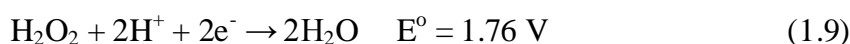
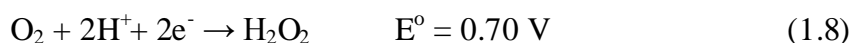
peroxide. For a PEM fuel cell, the direct pathway is more preferable because, the 2e- reduction mode always produces reactive intermediates and will lead to the degradation of the fuel cell components such as the membrane, bipolar plate and catalyst substrate. Moreover, it will also reduce the cell potentials as given below:

***In acidic medium***

4e<sup>-</sup> pathway:



2e<sup>-</sup> pathway:

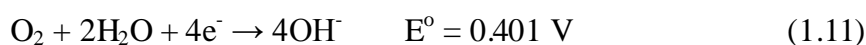


Disproportionation between the peroxide molecules also produces water and oxygen as follows:

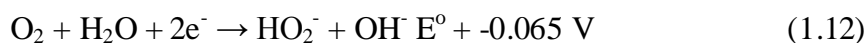


***In alkaline medium***

4e<sup>-</sup> pathway:



2e<sup>-</sup> pathway:



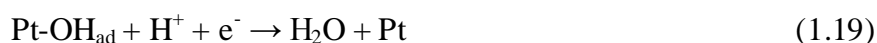
Disproportionation between OH<sub>2</sub><sup>-</sup> species also produces OH<sup>-</sup> and oxygen as follows:



The 4e- and 2e- pathways for ORR usually follow either associative or dissociative mechanism on transition metals (mainly Pt).<sup>[29, 34]</sup>

Associative mechanism deals with the adsorption of oxygen molecule on the electrocatalyst during the reduction process followed by electron/proton transfer leading to

the formation of OOH. This further splits to O and OH. Hence, this mechanism explains the indirect ( $2e^-$ ) pathway and the final product in this case may be peroxide or OH radicals.



In a dissociative mechanism, splitting of oxygen molecules occurs on the catalytic surface and protonation provides OH. This further reacts to form  $\text{H}_2\text{O}$ . This mechanism gives an idea about the direct ( $4e^-$ ) pathway for the ORR.



ORR is kinetically more complex and a proper mechanism is still not clear. Among the transition metals, Au and Hg usually show poor ORR with the  $2e^-$  pathway.<sup>[35]</sup> However, other PGM catalysts such as Pt, Pd, etc. reduce oxygen molecule through the  $4e^-$  pathway. Using these possible ORR pathways, there are several theoretical approaches to dig out the rate determining step (RDS) of ORR. According to Anderson *et al.*, the first electron transfer has high activation energy and proton transfer occurs as the RDS.<sup>[36]</sup> This first electron transfer step was supported by many researchers using different techniques.<sup>[37]</sup> From the calculation of Goddard, in spite of being gas or liquid, the highest energy barrier is experienced for hydration of the adsorbed oxygen molecule. According to his calculations, by providing hydrophobic conditions in the water formation step, it is easy to reduce the barrier for hydration of the adsorbed oxygen, which improves the ORR process.<sup>[38]</sup>

More clear and widely accepted model was introduced by Nørskov *et al.*<sup>[29, 39]</sup> According to their calculations, the reaction intermediate adsorption on the surface of the



catalyst plays a crucial role for ORR. Using free energy calculations of all the intermediates with respect to electrode potential, they propose the origin of overpotential for ORR. Further, using DFT calculations, they also calculated the bond energy of oxygen and hydroxyl group on different metals and plotted the activity against the bond energy (Figure 1.7). From their calculation, RDS strongly depends on the mode of interaction between the adsorbed intermediates. If adsorption of oxygen is too strong, removal of the intermediate species is the RDS. If adsorption of oxygen is very weak, the electron transfer and protonation will be the RDS. This model suggests the development of better electrocatalysts by lowering the binding energy of the adsorption of oxygen (preferably 0.2 eV lower than the binding energy of Pt). Further, the micro kinetic model developed by Nørskov *et al.* by calculating the activity on a catalyst by varying the OH binding energy indicates that the optimum activity for the reduction of oxygen to water through the 4e-pathway is 0.2 eV weaker binding of OH than the binding of OH on Pt(111) and for 2e-pathways it will be 0.3 eV.<sup>[39c]</sup>

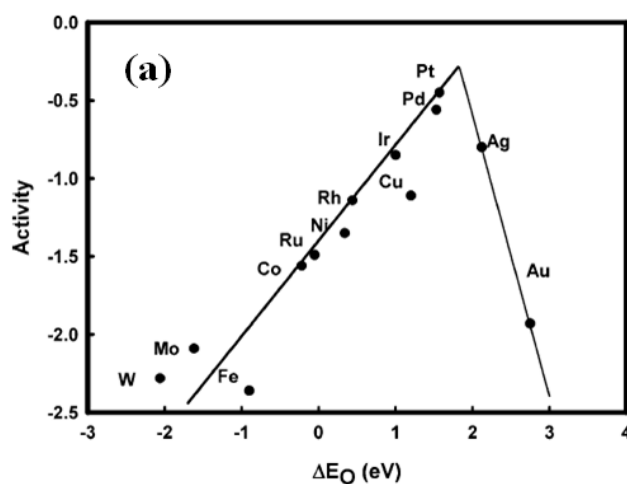


**Figure 1.7:** (a) Thermodynamic Volcano plot (oxygen reduction activity versus oxygen binding energy). Reprinted with the permission from Ref. [29] Copyright© 2004 and 2012, American Chemical Society.

Nørskov *et al.* also introduced a linear relation between the oxygen-metal bond interaction and the  $d$  band centre ( $d$  state relative to Fermi level) of the metal.<sup>[29]</sup> The difference in the oxygen-metal binding with respect to the different transition metals strongly depends on the coupling between the  $2p$  state of oxygen and the  $d$  state of the metal. This suggests that the up shift of the  $d$  band centre of the metal relative to the Fermi level results in a stronger bond and the down shift helps to reduce the weaker interaction. This linear relationship

between the oxygen-metal bond interaction and the  $d$  band centre will help the development of an efficient electrocatalyst for ORR. In case of the Pt based catalysts, the down shift in the  $d$  band centre relative to the Fermi level can be achieved by making alloy nanoparticles or by tuning the surface metals.<sup>[40]</sup>

### 1.3.2.1 Pt based electrocatalysts for ORR

Even though a large share of research in the area of electrocatalysts for ORR deals with replacing the current *state-of-the-art* Pt catalysts from the fuel cell cathode, none of these alternatives performs better than or equal to the Pt catalysts in a fuel cell. Even though Pt is expensive and scarce, fuel cell market mainly depends on this electrocatalyst and the research activities embark to develop new Pt based catalysts by modifying its surface electronic structure, surface composition, morphology etc. Modification of these basic properties of Pt catalyst leads to improved activity and better stability. The main approaches for modifying the surface structure properties of the Pt catalyst are listed below:

1. Modifying the shape of Pt nanocrystals
2. Combination of Pt with other metals (alloys, core-shell etc.)
3. Dispersion of Pt catalyst in modified support

#### 1.3.2.1.1 Shape controlled Pt nanocrystals

It is well known that the ORR activity of the Pt catalyst varies with the crystal planes. In perchloric acid, the activity is in the order Pt (110) > Pt (111) > Pt (100).<sup>[41]</sup> However, in sulphuric acid, the activity of Pt {100}c facet is higher than that of Pt {111}.<sup>[42]</sup> It may be attributed to the strong adsorption of bisulphate anion on the Pt {111} facet which reduces the ORR activity. This bisulphate adsorption on Pt {111} is three times higher than that of the Pt {100} facet. This observation highlights the importance of the morphological characteristics in the development of the Pt based catalysts. El-Sayed *et al.* and Sun *et al.*<sup>[43]</sup> showed that {111} bound tetrahedral and nonocube of Pt respectively are more active towards ORR. Even at higher concentration of sulphuric acid (1.5 M), Pt nonocube with {100} facet shows excellent performance, in which specific activity is two times higher than that of the commercial Pt/C. Apart from the low indexed planes, researchers have tried to synthesize high indexed planes for improved ORR activity. High indexed facets show remarkably higher activity than the low indexed facets. Studies by

Feliu *et al.* and Xia *et al.*, on high indexed Pt nanostructures are the best examples in this category.<sup>[44]</sup> The concave nanoparticles prepared by Xia *et al.* have {510}, {720} and {830} facets, which show enhanced ORR activity compared to the corresponding cubic Pt and commercial Pt/C.<sup>[44c]</sup> Even though, high indexed facets have high intrinsic activity towards ORR, it lacks good stability under the fuel cell operating conditions. Under these conditions, the morphology of high indexed facets of Pt catalyst changes leading to the reduction in the electrochemical surface area (ECSA) for efficient ORR. Different possible morphologies of Pt nanostructures are listed in Figure 1.8.<sup>[45]</sup>

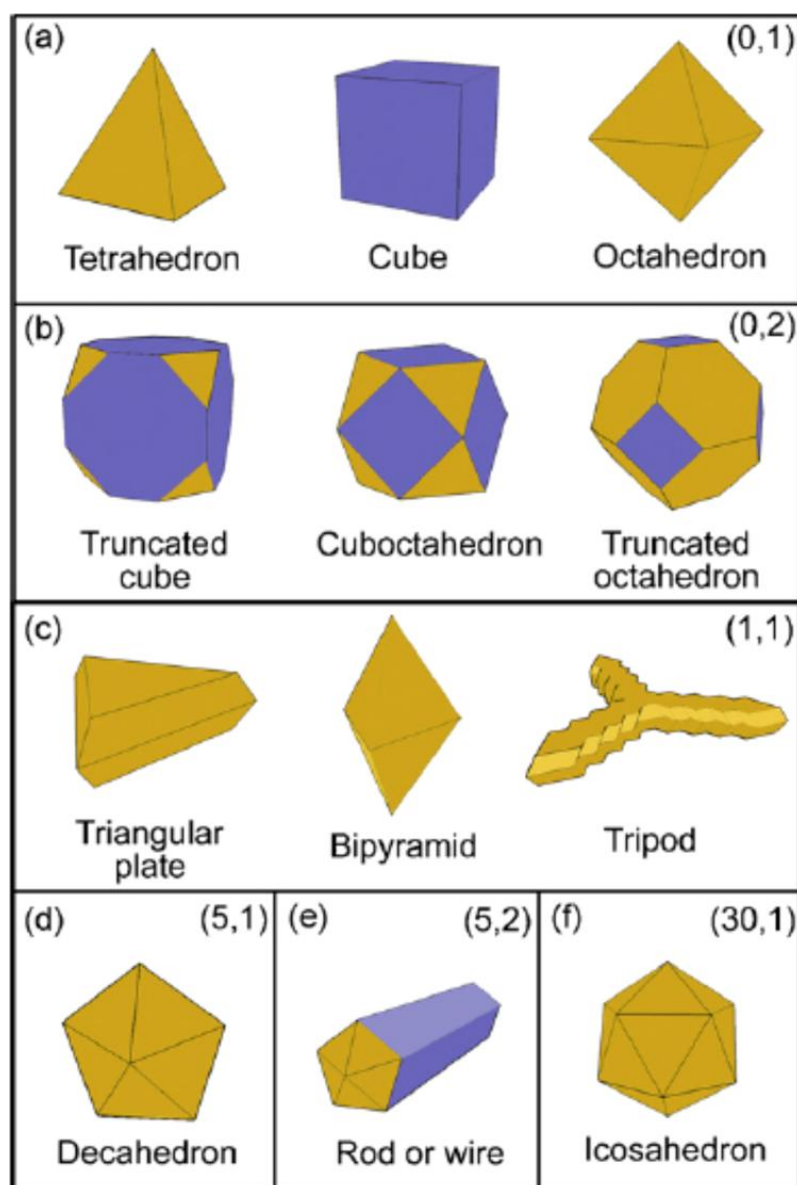


**Figure 1.8:** High indexed and low indexed facets of Pt with different morphologies. Reprinted with the permission from Ref [45]. Copyright © 2008 Elsevier Ltd.

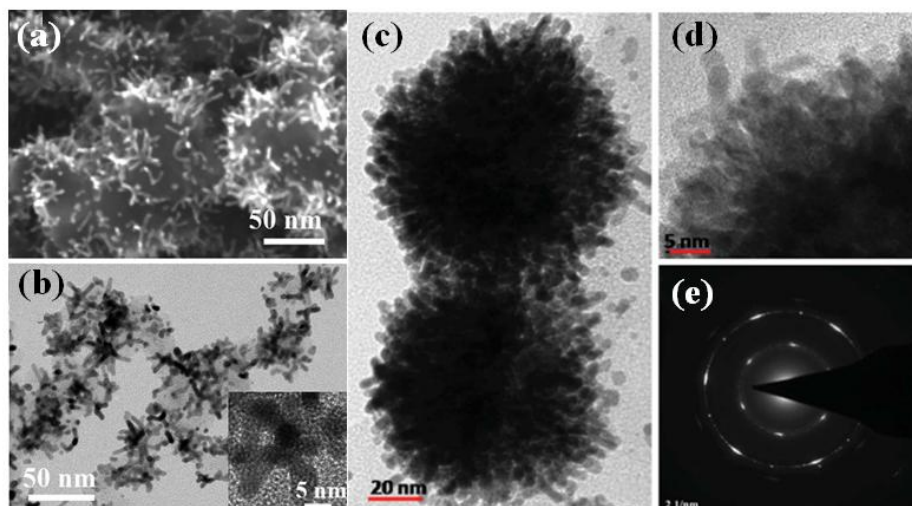


**Figure 1.9:** (a and b) Multi-armed Pt nanostar supported on carbon. Reprinted with permission from Ref [46]. Copyright © 2011 WILEY-VCH Verlag GmbH & Co. KGaA, Weinheim and (c-e) Pt nanourchin supported on graphene. Reprinted with permission from Ref [47] Copyright © 2013 The Royal Society of Chemistry.

Pt based catalysts in the zero dimension always create issues in fuel cells, such as agglomeration of Pt due to catalyst migration or support corrosion. This reduces the overall performance due to the reduction in ECSA. In order to avoid such issues in electrocatalysts, researchers have developed different anisotropic structures of Pt, such as Pt wire, Pt tube, Pt dendrites, Pt urchin etc. (Figure 1.9).<sup>[46-48]</sup> These hetero-structures have high surface area with more reactive edges, corners etc., that provide high performance with better stability under the fuel cell operating conditions, as compared to the Pt nanoparticles supported on carbon. Wang *et al.* reported 3D inter-connected Pt morphologies that show 2.2 times higher specific activity than Pt/C.<sup>[49]</sup> Also, it is more stable under acidic conditions compared to the commercial Pt/C. Zhang *et al.* reviewed the systematic approaches available for the development of the anisotropic Pt nanostructures.<sup>[50]</sup>

### 1.3.2.1.2 Pt alloy catalysts

As explained in the previous sections, electrocatalytic activity for oxygen reduction strongly depends on the surface properties of the catalyst. However, the Pt atoms inside the nanoparticle have no role in the overall ORR process. In order to reduce the Pt content, researchers usually follow two approaches - synthesis of Pt based alloy catalysts and core-shell type catalysts (features of the core-shell nanoparticles are detailed in the following

section). Alloy nanoparticles show improved ORR activity compared to the monometallic catalysts due to the modification in the surface electronic structure of Pt induced by other transition metals.<sup>[51]</sup> There are several reports on the Pt based alloy catalysts.<sup>[50, 52]</sup> DFT studies on the alloy nanoparticles indicated that short range ligand effect (electronic charge transfer effect) and long range geometric effect (lattice strain) are the main reasons behind the modified chemisorption of the adsorbed oxygen molecules on the alloy nanoparticles. This indicates that the change in the *d*-band centre of Pt modifies the bond strength of the adsorbate, which alters the chemisorption of the intermediate during ORR. Stemenkovik *et al.* studied the activity performance of Pt alloyed with different 3*d* transition metals and showed the changes in the *d*-band centre modification with respect to the transition metal loading.<sup>[39a]</sup> They also obtained a volcano type behavior on the ORR activity with respect to the change in the *d*-band centre. Their studies showed that alloying with Fe, Co and Ni

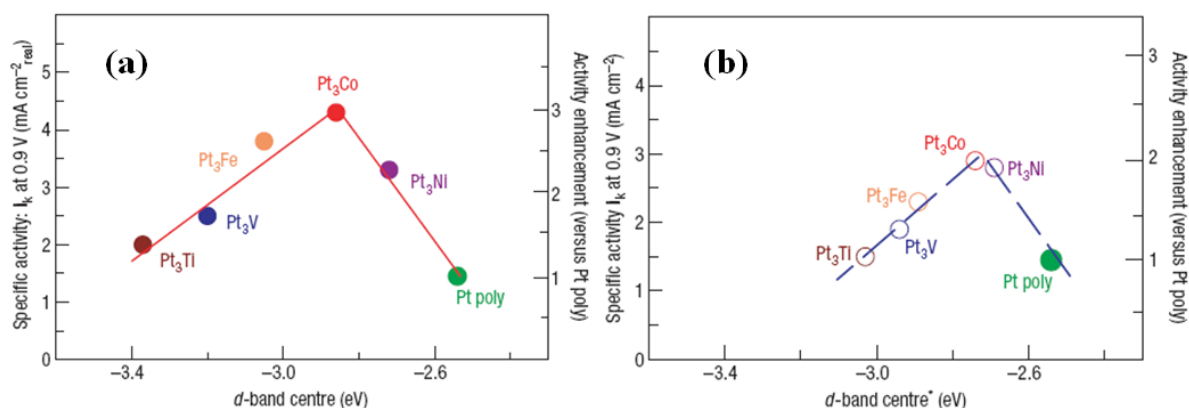


**Figure 1.10:** Relationship between the specific activity (measured in 0.1 M HClO<sub>4</sub> at 333 K) and *d*-band centre of (a) Pt-skin and (b) Pt-skeleton. Reprinted with permission from Ref [53] Copyright © 2007, Rights Managed by Nature Publishing Group.

makes the catalyst more active for ORR. They also proved that balancing the surface coverage of the blocking species and adsorption energy of the intermediate species governs the catalytic activity of an electrocatalyst. In the context of the work by Stemenkovik on engineered catalytic synthesis, they synthesized Pt<sub>3</sub>Co, Pt<sub>3</sub>Fe and Pt<sub>3</sub>Ni with the same size and composition. These systems also showed the volcano type behavior, where Pt<sub>3</sub>Co shows ~ 2-3 times higher specific activity compared to Pt/C (Figure 1.10).<sup>[53]</sup> Apart from the Stemenkovik's pioneering work, there has been some other approaches for the development of the Pt alloy catalysts. Chen *et al.* prepared Pt-W catalyst with improved activity and stability.<sup>[54]</sup> Sun *et al.* introduced a generalized synthetic protocol for preparing

monodisperse Pt-M (M is Fe, Co, Ni, Zn and Cu) catalyst through a co-reduction approach at 300 °C with oleilamine.<sup>[55]</sup>

Pt based alloy nanoparticles show improved intrinsic ORR activity, however, their stability under acidic conditions is a major hurdle and the activity decreases on prolonged use. This is mainly due to the leaching of non-noble metal from the alloy nanoparticles. This dissolution creates porosity in the nanostructure. However, some of the synthetic approaches deliberately create nanopores on the alloy nanoparticles to improve the activity by creating more surface area and active reaction centres. This also assists in the efficient transport of oxygen molecules and results in improved ORR activity. Recently, Chen *et al.* prepared a 3-D nanoframe of Pt<sub>3</sub>Ni by interior leaching of PtNi<sub>3</sub> polyhedra in solution (Figure 1.11).<sup>[56]</sup>

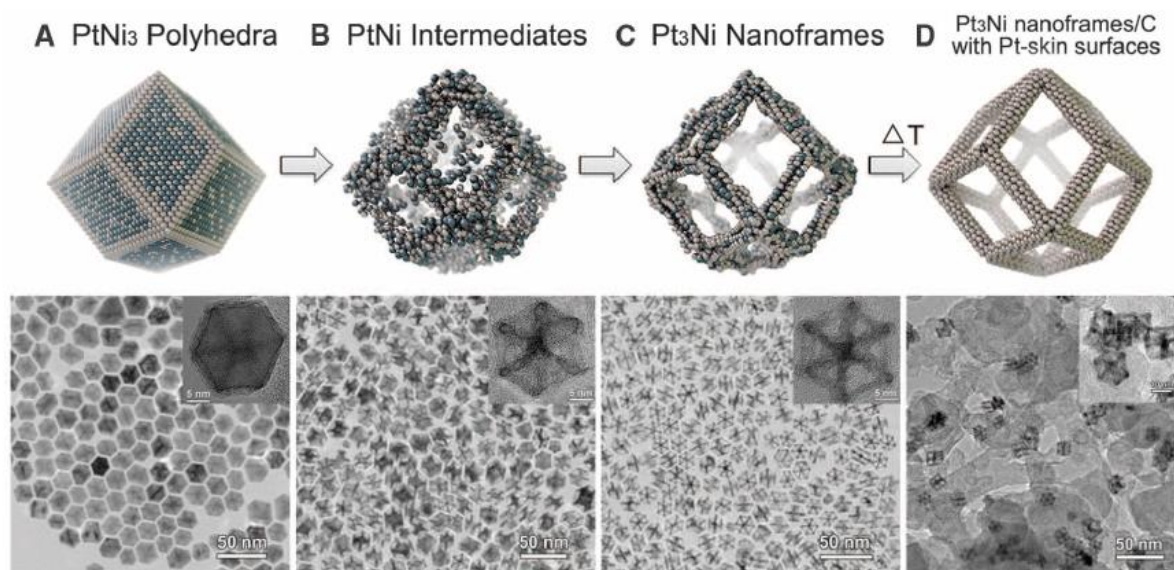


**Figure 1.11:** Different stages in the preparation of Pt<sub>3</sub>Ni nanoframes. Reprinted with permission from Ref [56] Copyright © 2014, American Association for the Advancement of Science.

The nanoframe catalyst shows improved mass activity as well as specific activity 36 and 22 times higher than Pt/C, respectively. Moreover, this nanoframe shows excellent stability under acidic conditions without any deformation of its morphology. De-alloying of nanoparticles creates more porosity and makes the buried non-functional noble metals more accessible to the reactant molecule and modifies the physicochemical properties of the Pt catalysts. Apart from creating nanoporosity in the catalyst, introduction of high

indexed facets also improves the activity of the alloy catalysts. As mentioned in the previous section, the improved activities of such catalysts are mainly due to the changes in electronic structure by lattice strain. Icosahedral nanocrystals of Pt-M (M = Au, Ni) and concave-nanocubic morphologies of Pt-Ni alloys are some examples for the high indexed facet alloy nanoparticles.<sup>[57]</sup> Other than the zero dimensional nanostructure, there have been reports of PtNi and Pt-Fe nanowires showing improved ORR activity compared to the corresponding nanoparticles.<sup>[58]</sup>

Alloy catalysts with active facets also improve the activity towards ORR as explained in the previous section. For example, single crystal Pt<sub>3</sub>Ni{111} shows 10 fold higher activity compared to Pt{111} and 90 fold higher activity compared to Pt/C. This is the most active catalyst reported to date.<sup>[59]</sup> However, the activity drastically decreases when one moves from the single crystals to the nanoparticles. Theoretical studies on Pt<sub>3</sub>Ni nanooctahedra with {111} facet suggest that the structure is stable and similar surface segregation may be observed as in extended Pt<sub>3</sub>Ni.<sup>[59-60]</sup> Following this study, Pt<sub>3</sub>Ni truncated octahedra prepared by Yang *et al.* shows higher ORR activity compared to Pt/C, but less compared to single crystalline Pt<sub>3</sub>Ni.<sup>[61]</sup> This reduction in the activity is mainly due to the adsorption of the surfactant molecules, which are used for the synthesis of the nanoparticles to obtain a particular morphology. There are several other approaches to remove this chemically adsorbed surfactant using potential cycling, plasma treatment, calcination etc. Since these techniques are not feasible under commercial implications, Peng *et al.* recently introduced a scalable, surfactant-free Pt-Ni octahedral nanoparticle for ORR.<sup>[62]</sup> This catalyst shows improved ORR activity compared to Pt/C.

### 1.3.2.1.3 Pt core-shell nanostructures for ORR

Leaching of non-Pt materials from the alloy nanoparticles always leads to the reduction in the ORR activity. This can be solved by introducing a thin layer of noble metal (here Pt) covering on the non-noble metal core. This will improve the activity as well as the durability of the catalysts. Normally, the inner core of the catalyst is not significant for the reaction whereas the noble metal shell and non-noble metal core are always of commercial interest. There are many core-shell type catalysts such as Cu@Pt, AuCu@Pt, Pd@Pt, Ni@Pt, etc. that can be synthesized through different approaches as shown in Figure 1.12.<sup>[63]</sup> Adzic and co-workers were the first to introduce such core-shell type nanostructures based on Pd@Pt/C using the under-potential deposition technique.<sup>[64]</sup>

Leaching/de-alloying of the Pt alloy nanoparticles creates more surface roughness and leads to Pt-skeleton nanostructure. Pt with unsaturated coordination also shows high activity if the Pt shell thickness is very small, and was introduced by Toda *et al.* Another approach to create a clean monolayer of the Pt shell is the heat treatment of the mother Pt alloy nanostructures.<sup>[65]</sup> This Pt skin formation *via* heat treatment provides higher activity than the Pt skeleton nanostructures.<sup>[66]</sup> As reported by Durst *et al.*, through simple acid treatment, the Pt skin can be changed to Pt skeleton and its reversibility is illustrated in Figure 1.13.<sup>[67]</sup>

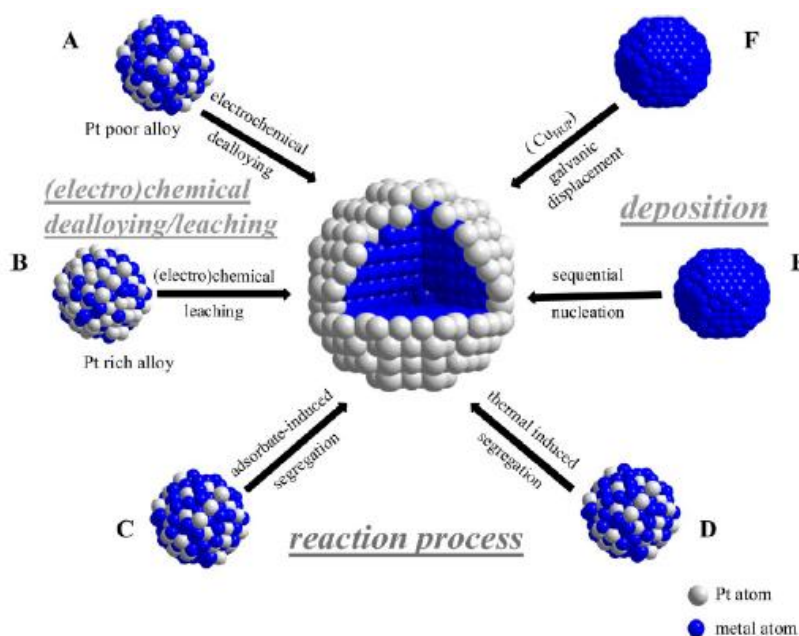


**Figure 1.12:** Different approaches for the synthesis of core-shell nanoparticles. With permission from the Ref [63c] Copyright © 2013, American Chemical Society.

The improved ORR activity of the core-shell catalyst is mainly due to the modification of the electronic structure of the shell by the core atoms and the resulting geometric properties. These properties will tune the chemisorption capabilities and minimize the energy barrier for efficient ORR. High Pt utilization, high ORR activity and durability, better efficiencies etc., can be achieved by creating a thin shell of Pt over a non-noble metal core. However, the synthesis of the core-shell nanoparticle with very thin layer of the Pt shell with proper composition and dispersion on the support material is a challenging task.



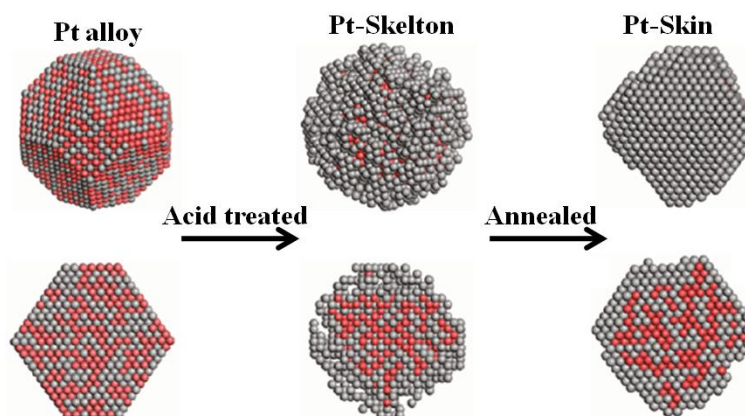


**Figure 1.13:** Illustrations for the formation of the Pt-skeleton and Pt-skin nanostructures. Reproduced with the permission from Ref [66b] Copyright © 2011, American Chemical Society.

#### 1.3.2.1.4 Support modified Pt catalysts

Commercial Pt electrocatalysts are usually supported on highly conducting carbon substrates. Even though, these catalysts perform well for ORR, the corrosion of the carbon support at high potentials is a major issue in fuel cell development. Similarly, weak interactions between the carbon support and the Pt catalysts result in the migration of Pt nanoparticles and lead to Pt agglomeration in long term usage and reduction in the activity due to the reduction in ECSA.<sup>[68]</sup> In order to overcome such issues, varieties of carbon supports are introduced as active substrates for

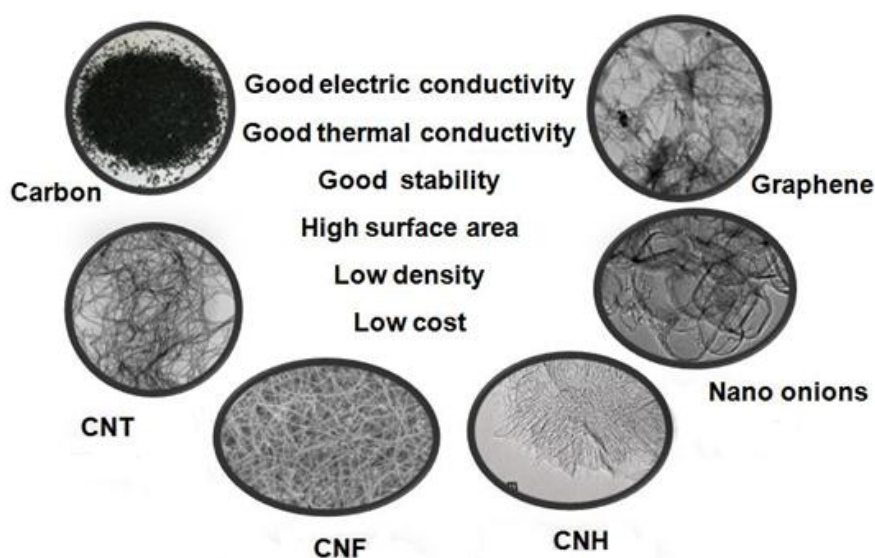


**Figure 1.14:** Different carbon morphologies used for supporting Pt nanoparticles.

Pt nanoparticles.<sup>[69]</sup> Nowadays, graphene, carbon nanotubes, carbon nanohorns, carbon nanofibers, etc. are being used as efficient support materials (Figure 1.14).<sup>[70]</sup> Highly graphitized carbon in these substrates prevents the oxidation, and effective  $\pi$ -conjugation in the carbon matrix interacts strongly with Pt nanoparticles and prevents the migration. The interaction of the  $\pi$  electrons of the substrate and Pt induces influence on the electronic structure of the Pt nanoparticles and thus improves the ECSA with enhancement in ORR.<sup>[71]</sup> Robust carbon supports such as colloidal imprinted carbon, ordered hierarchical nanostructure carbon, graphitic mesoporous carbon, etc. are some of the recent developments in the supporting materials research.<sup>[72]</sup>

Other than carbonaceous materials, metal oxides are also being used as catalyst supports for Pt. The corrosion of carbon substrate can be completely overcome by replacing it with metal oxides.  $\text{WO}_x$ , TiC,  $\text{TiO}_2$ ,  $\text{TaB}_2$  etc. were used as effective supports for the Pt nanoparticles.<sup>[73]</sup> Other than corrosion, the interaction between the metal oxide support and Pt nanoparticles modifies the electronic structure of the surface Pt which in turn improves the ORR activity. Moreover, the metal oxide supported Pt shows improved electrochemical stability during high potential cycling. Recently, Hwang *et al.* used  $\text{Ti}_{0.7}\text{Mo}_{0.3}\text{O}_2$  as the catalyst support for Pt (Figure 1.15).<sup>[74]</sup> The electronic transfer between the non-carbon support and Pt modifies the  $d$ -band centre and yields better activity and stability. The major issues associated with the non-carbon substrate are related to electrical conductivity and poor surface area. Recently, Wei *et al.* used high conducting  $\text{Ti}_3\text{AlC}_2$  as catalyst support for Pt and the resulting catalyst showed better ORR activity and durability.<sup>[75]</sup>

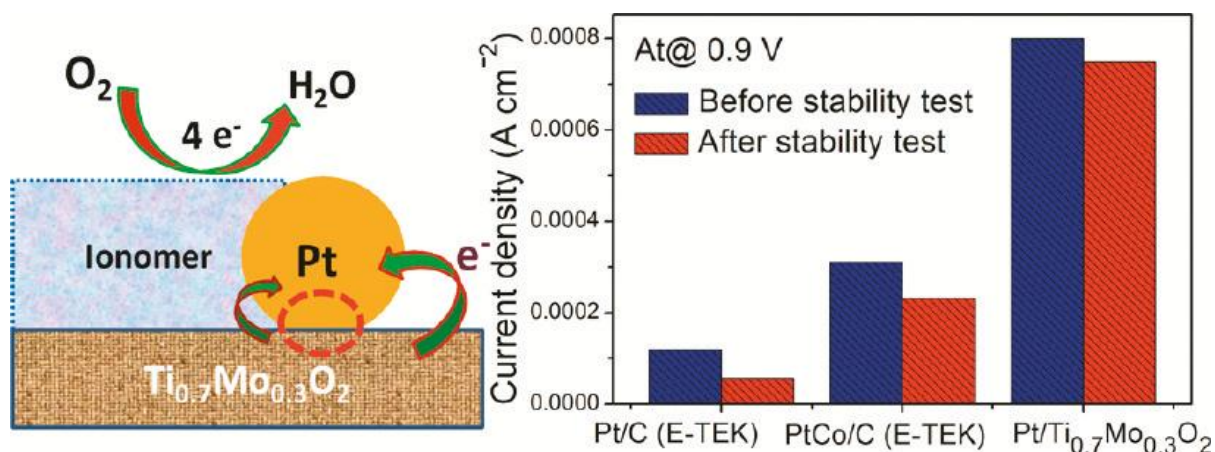


**Figure 1.15:** Stability of  $\text{Pt}/\text{Ti}_{0.7}\text{Mo}_{0.3}\text{O}_2$  compared to  $\text{Pt}/\text{C}$  in  $0.5\text{ M H}_2\text{SO}_4$ . Reprinted with permission from Ref [74] Copyright © 2011, American Chemical Society.

### 1.3.2.2 Pt-free metal electrocatalysts for ORR

The previous sections elaborated the different approaches carried out for reducing the amount of Pt from the fuel cell cathode using alloy and core-shell alternatives. However, researchers are trying to find out different cost-effective materials, free of Pt. These materials include low cost noble metals, metal oxides, perovskites, brownmillerites, chalcogenides, nitrides and carbides, and metal nitrogen coordinated carbon (M-N-C) catalysts. The present section provides a brief review about the developments of materials listed above for applications in the fuel cell cathode.

#### 1.3.2.2.1 Noble metal other than Pt.

Many noble metals such as Ru, Pd, Ag, Ir, etc. have been introduced as alternatives to Pt in the fuel cell cathode.<sup>[76]</sup> Pd is more attractive due to better ORR activity characteristics compared to other non-Pt noble metal catalysts. Even though, Pd is just below Pt in the Volcano plot (Figure 1.7), the ORR activity of Pd is very less compared to the Pt based systems. Several approaches tried at improving the activity of the Pd electrocatalysts by modifying the surface electronic structure with other low cost metals such as Cu, Co, Mo, etc. in the form of core-shell or alloys<sup>[77]</sup> or shape controlled synthesis of the Pd nanoparticles. Since single crystal studies showed that Pd (100) is more active for ORR (which is just opposite in case of Pt), Shao *et al.* prepared Pd cubes, which shows ORR activity higher than the octahedral Pd with facet {111}.<sup>[77-78]</sup> Similar to Pt, tremendous efforts were put into tune the surface electronic structure of Pd by modifying the catalyst support.  $W_{18}O_{49}$ , exfoliated montmorillonite, etc. were used as the supports for Pd, and showed improved activity compared to the Pd supported on carbon.<sup>[79]</sup>

#### 1.3.2.2.2 Transition metal oxide for ORR

Transition metal oxides based on Co, Mn, and Fe show ORR activity in alkaline medium.  $MnO_2$ ,  $Mn_3O_4$ ,  $MnOOH$ , etc. are some of the Mn based oxides that show excellent ORR activity in alkaline medium with high stability and fuel tolerance compared to Pt/C.<sup>[80]</sup> However, the use of these oxides in real application is still a puzzle due to low electrical conductivity. Recently, carbon supported  $MnO_2$  nanowire showed excellent ORR activity due to the presence of more defective sites and effective adsorption of  $O_2$  molecules.<sup>[80b]</sup> Apart from the manganese oxides, cobalt oxides were also used for ORR.<sup>[81]</sup> In this line, Dai *et al.* reported the synthesis of  $Co_3O_4$  supported on graphene and CNT for ORR activity.<sup>[82]</sup> Recently, Feng *et al.* used a simple hydrothermal method for the

preparation of  $\text{Fe}_3\text{O}_4$  nanoparticles on three dimensional nitrogen doped graphene for ORR.<sup>[83]</sup> Apart from metal oxides ( $\text{MO}_x$ ), mixed valance metal oxides with spinel structure were also prepared and used for fuel cells. Dai *et al.* synthesized  $\text{MnCo}_2\text{O}_4$  supported on nitrogen doped graphene for ORR.<sup>[82]</sup>  $\text{Co}_3\text{O}_4$  was also mixed with other 3d elements such as Ni and Cu in order to improve the ORR activity.<sup>[84]</sup> Metal incorporated magnetite ( $\text{M}_x\text{Fe}_{3-x}\text{O}_4$ ) was reported to have efficient ORR activity by Sun *et al.* Different transition metals such as Mn, Co, Cu, etc. were inserted into  $\text{Fe}_3\text{O}_4$  for improving the activity.<sup>[85]</sup> There are reports on the other metal oxides such as  $\text{TiO}_2$ ,  $\text{NbO}_2$ ,  $\text{Ta}_2\text{O}_5$ , etc. for ORR as well as catalyst supports.<sup>[86]</sup>

### 1.3.2.2.3 Perovskites and Brownmillerites for ORR

Perovskites ( $\text{ABO}_3$ ) and brownmillerites ( $\text{A}_2\text{B}_2\text{O}_5$ ) are usually used as electrolytes for solid oxide fuel cells. Very recently, researchers have started using these oxides in PEM fuel cells as the cathode catalysts.<sup>[87]</sup> Moreover, it is also helpful for the oxygen evolution (OER) in alkaline conditions.<sup>[88]</sup> Shao-Horn *et al.* have extensively studied the application of perovskites as potential ORR and OER materials.<sup>[89]</sup> They suggested that any perovskite with  $e_g$  filling (*i.e.*  $\sigma^*$  orbital filling) equal to 1 shows excellent ORR activity (Figure 1.16). This suggests that the covalency between the  $3d$  orbital of the B site transition metal and the  $2p$  orbital of oxygen plays an important role for the reduction of the oxygen molecules. Moreover, incorporation of transition metals such as Fe and Co on the B site also induces ORR activity in perovskites. Co reduces the oxygen molecules preferably through a  $4e^-$  pathway and Fe through a  $2e^-$  pathway. Another class of metal oxides, brownmillerites, were also investigated for ORR in alkaline medium. Jijil *et al.* reported the ORR activity of brownmillerites for the first time using tetrahedral distorted  $\text{Ba}_2\text{InCeO}_{5+\delta}$ .<sup>[90]</sup> The oxygen vacancy and doping of cerium impart higher activity to the material towards ORR. Further, the work was extended to study the effect of cerium doping in  $\text{Ba}_2\text{InCeO}_{5+\delta}$  to modify the electrocatalytic activity by creating oxygen vacancies in the material.<sup>[91]</sup>

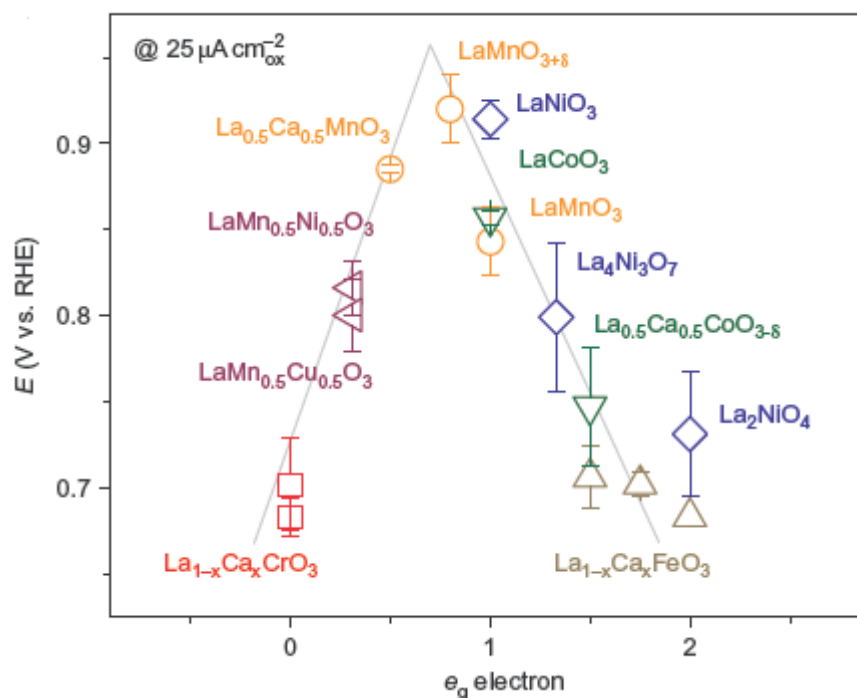


**Figure 1.16:** Potentials at  $25 \text{ mA cm}^{-2}$  as a function of the  $e_g$  orbitals in the perovskite-based oxides. Reprinted with permission from Ref [89] Copyright © 2011, Nature Publishing Group.

#### 1.3.2.2.4 Metal chalcogenides for ORR

Metal chalcogenides are yet another class of non-Pt electrocatalysts used in ORR. Compared to the metal oxides, these catalysts can be a suitable alternative for Pt under acidic conditions. Many attempts are reported using the metal chalcogenides as electrocatalysts and catalyst supports.<sup>[92]</sup> Alonso-Vante *et al.* extensively investigated many noble and/or non-noble metal chalcogenides and their electrochemical and spectroscopic characteristics.<sup>[93]</sup> Many research works are published on  $\text{CoSe}_2$  as the catalyst for ORR. Dai *et al.* prepared  $\text{Co}_x\text{S}_{(1-x)}$  supported on nitrogen doped graphene for ORR under acidic conditions.<sup>[94]</sup> Wu *et al.* synthesised  $\text{Co}_x\text{S}_{(1-x)}$  supported on nitrogen doped carbon and showed excellent activity in alkaline medium that is higher than the current *state-of-the-art* Pt/C catalysts.<sup>[95]</sup> Theoretical studies showed that CoS reduces oxygen molecules as Pt/C via a 4e- pathway.<sup>[96]</sup>

## 1.3.2.2.5 Metal nitrides, oxynitrides and carbides for ORR

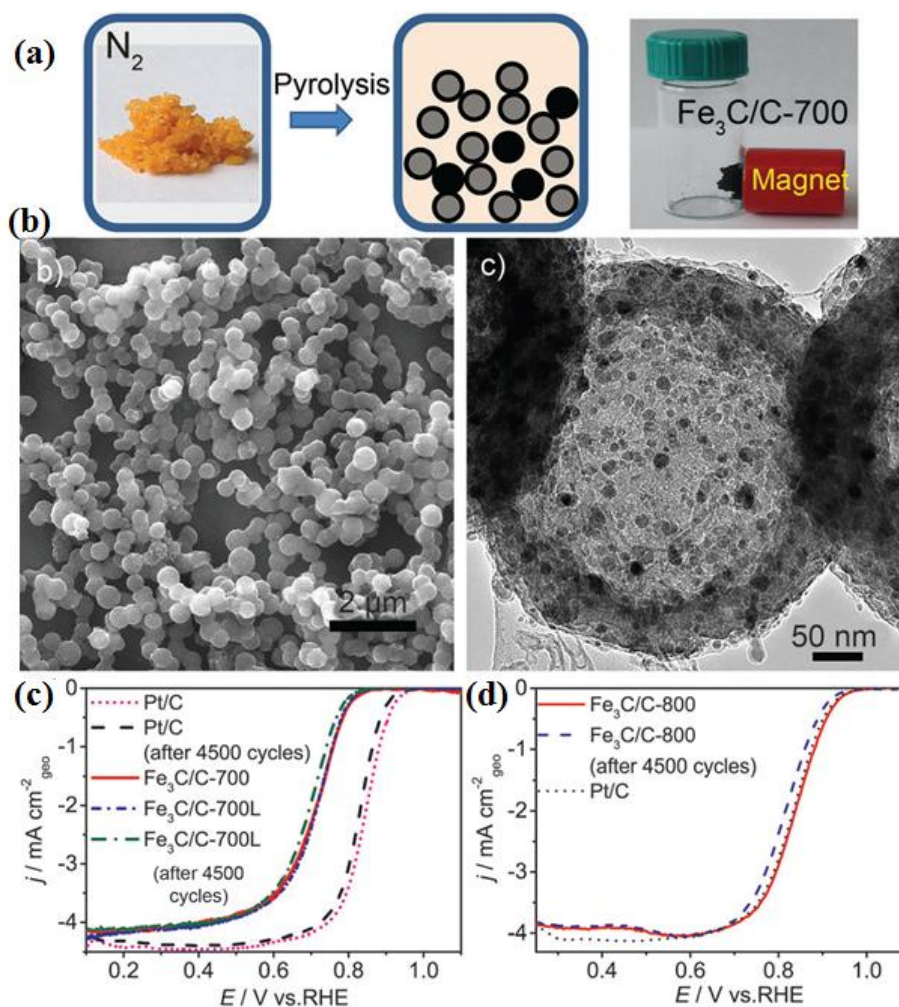


**Figure 1.17:** (a) Scheme for the synthesis of hollow  $Fe_3C/C$  spheres. (b) SEM and TEM images of hollow spheres. (c) Durability analysis of  $Fe_3C$  in 0.1 M  $HClO_4$  in comparison with Pt/C. (d) Durability analysis of  $Fe_3C/C$  under alkaline conditions. Reprinted with the permission from Ref [97] Copyright ©2014 WILEY-VCH Verlag GmbH & Co. KGaA, Weinheim.

Transition metal nitrides, oxynitrides and carbide are recently used as ORR catalysts. Many catalysts based on molybdenum nitride, cobalt molybdenum nitride, cobalt nitride, cobalt carbonitride, etc. have been synthesised and performance towards ORR.<sup>[98]</sup> Since the formation of metal nitrides changes the  $d$  band structure of the metal, it assists in fast electron transfer to the adsorbed oxygen molecule. Apart from the metal nitrides, transition metal oxynitrides were also studied for the ORR activity.  $ZrO_xN_y$ ,  $TaO_xN_y$ ,  $Co_xMo_{1-x}O_yN_2$ , etc. are some of the examples for the metal oxynitrides used in ORR.<sup>[99]</sup> More importantly,

these metal nitrides and oxynitrides perform well towards ORR under acidic conditions. Due to the excellent electron transfer between metal nitrides and adsorbate, these materials are even used as efficient catalyst supports. Other than the metal nitrides, metal carbides are good ORR catalysts as well as better catalyst supports. Park *et al.* have reported tungsten carbide based ORR catalyst and evaluated its ORR activity under acidic conditions.<sup>[100]</sup> Very recently, Li *et al.* reported a high pressure solvo-thermal process to prepare hollow iron carbide supported on carbon for ORR (Figure 1.17).<sup>[97]</sup> Surprisingly, thus prepared catalyst showed excellent ORR activity under acidic conditions with minimum overpotential compared to the Pt/C catalyst. Also, Fe<sub>3</sub>C/C showed excellent electrochemical durability and fuel tolerance under acidic conditions. Chen *et al.* have synthesised core shell Fe/Fe<sub>3</sub>C@C boxes/NRGO hybrid for oxygen reduction in 0.1 M KOH. They used Fe based MOF and GO for the preparation of the core-shell nanoparticles.<sup>[101]</sup> Wen *et al.* reported a core-shell structure of Fe/Fe<sub>3</sub>C for ORR in alkaline medium.<sup>[102]</sup>

#### 1.3.2.2.6 M-N-C electrocatalysts for ORR

Recently, M-N-C catalyst development has attracted more attention and has become one of the fast growing research fields around the world. The most significant advantage of these catalysts is their high ORR activity compared to the other non-precious catalysts in acidic environment with improved stability. Apart from the metal oxides, chalcogenides, perovskites, etc., the M-N-C catalyst is a good candidate to replace Pt from the fuel cell cathode. M-N-C represents metal (Fe or Co) coordinated with nitrogen atoms present/doped in carbon morphologies. Almost all carbon allotropes (carbon, graphene, CNT, CNH, etc.) are used for the preparation of the M-N-C catalysts. Even though, Jasinski *et al.* reported on the ORR activity of cobalt phthalocyanines as early as 1964, there has been no advances in the metal complex based materials for ORR.<sup>[103]</sup> However, the break-through in the synthesis of the M-N-C catalysts was reported by Yeager *et al.* by simple thermal annealing of the respective precursors.<sup>[104]</sup> At present, there are many routes to synthesize the M-N-C catalysts, *viz.*, (i) direct annealing of the mixture of the nitrogen precursor, the metal precursor and the carbon source, (ii) annealing of a mixture of the metal salt and a compound that contains both carbon and nitrogen and (iii) annealing of metal coordinated nitrogen containing macromolecules. Usually, annealing of a mixture containing the metal salt, the nitrogen precursor and carbon is used for the preparation of

the M-N-C catalysts. Fe and Co are widely used for the M-N-C preparation due to the efficient oxygen binding properties of these elements. Large number of nitrogen sources are being employed for the M-N-C catalyst preparation. Ammonia, urea, melamine, dicyanamide, sodium azide, polypyrrole, polyaniline, poly benzimidazole, etc. are commonly used as the nitrogen precursors. The M-N-C based catalyst development is a fast growing arena of research and many literature reviews based on such catalysts have been published recently.<sup>[105]</sup> The following section discusses only few of the break-through research activities in the M-N-C catalyst development.

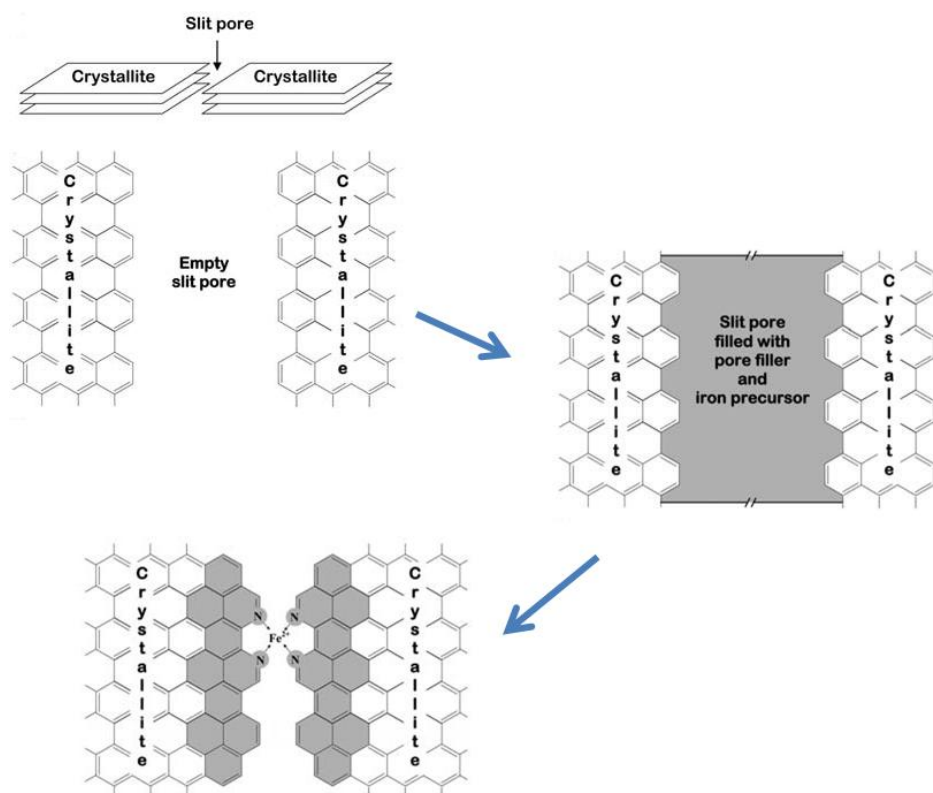


**Figure 1.18:** Representation of pore-filling and catalytically active reaction centre formation on carbon black. Reprinted with the permission from ref [106] Copyright © 2009, American Association for the Advancement of Science.

Among Fe and Co based catalysts, Fe is the most studied one due to its improved ORR activity compared to the Co based M-N-C catalysts. ORR activity of the Fe-N-C catalyst strongly depends on the (i) disordered carbon, (ii) micropores, (iii) iron coordination and (iv) nitrogen content. Dodelet *et al.* reported facile synthesis of an Fe-N-C catalyst by annealing carbon, phenanthroline and iron acetate under an inert atmosphere.<sup>[106]</sup> In order to create defective carbon and proper metal-nitrogen coordination, the micropores on the



carbon black were filled using iron and nitrogen precursors by ball milling before high temperature annealing (Figure 1.18). Thus prepared catalyst showed higher ORR activity under acidic conditions and single cell analysis provided a volumetric activity of  $99 \text{ A cm}^{-3}$  at 0.80 V.

Dodelet *et al.* extended the work to another system where zeolitic imidasolate framework (ZIF) was used as the carbon source and carrier for the iron salt and phenanthroline.<sup>[107]</sup> The selection of the ZIF based metal organic framework for this study was mainly based on the high surface area and high density of micropores. The iron salt and phenanthroline were impregnated to the ZIF, followed by high temperature annealing under inert atmosphere. The catalyst thus prepared showed remarkably high ORR activity and yielded a volumetric power density of  $230 \text{ A cm}^{-2}$  at 0.80  $V_{\text{IR-free}}$ . This, in fact, is the highest reported power density based on the non-Pt based catalysts. A maximum power density of  $910 \text{ mW cm}^{-2}$  was obtained for a single cell study with the ZIF derived catalyst as the cathode. This power density is comparable to the Pt based catalysts.

In 2011, Zelenay *et al.* introduced a new concept for the synthesis of the M-N-C catalysts by high temperature annealing of a mixture containing polyaniline, carbon and Fe and Co salt (Figure 1.19 a).<sup>[108]</sup> This catalyst showed improved ORR activity (only 60 mV overpotential compared to the Pt/C catalyst at the half wave potential) under acidic conditions with a maximum power density of  $550 \text{ mW cm}^{-2}$  in a single cell analysis (Figure 1.19 b & c). It was observed that the Co-N-C catalyst showed poor activity in comparison with Fe-N-C. However, mixing of both Fe and Co improved the activity of the M-N-C catalysts compared to the control. The study was further extended to improve the ORR activity of the catalysts. A power density of  $\sim 1000 \text{ mW cm}^{-2}$  for the FeCo-N-C catalyst as the cathode in PEMFC with an active area of  $5 \text{ cm}^2$  was achieved very recently.<sup>[109]</sup>

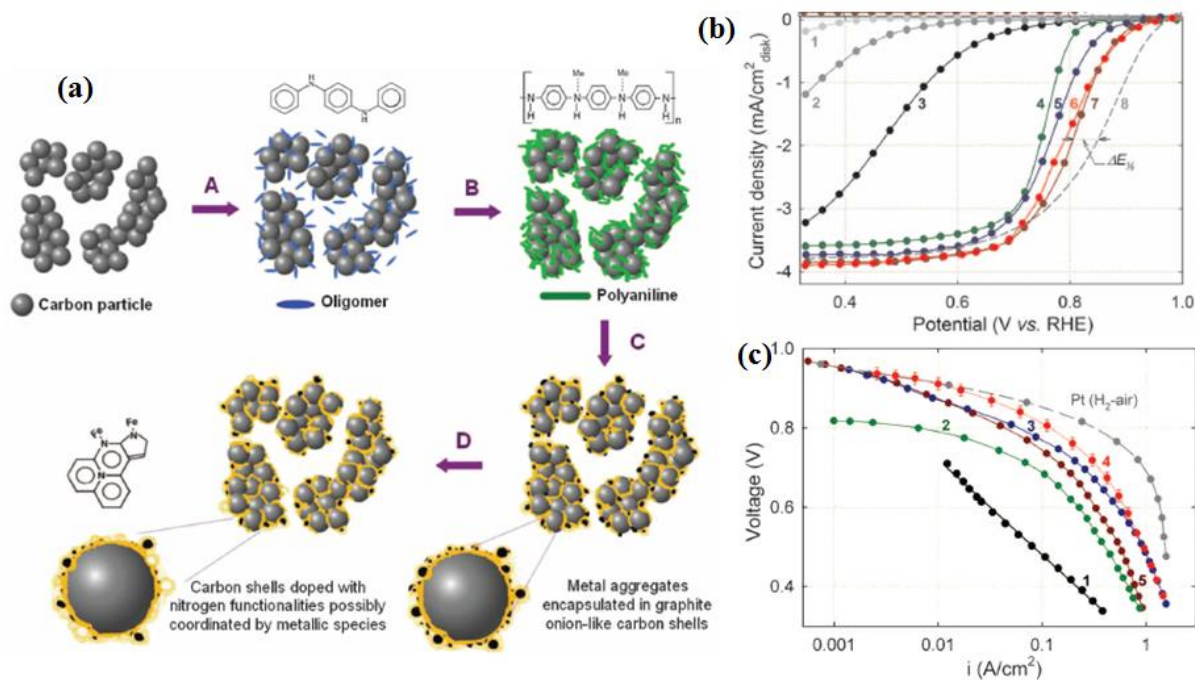


**Figure 1.19:** (a) Synthetic procedure of an FeCo-N-C catalyst and (b) Linear sweep voltammogram (LSV) of FeCo-N-C in 0.5 M H<sub>2</sub>SO<sub>4</sub> in comparison with Pt/C. Here, 1 represents pure carbon black; 2: annealed carbon black; 3: annealed PANI-C; 4: annealed Co-N-C; 5 & 6: FeCo-N-C (annealed at different temperatures); 7: Fe-N-C; and 8: Pt/C. (c) Single cell polarization with a catalyst loading of 4 mg cm<sup>-2</sup> 1: PANI-C; 2: Co-N-C; 3 & 4: FeCo-N-C at different annealing temperatures. Reprinted with permission from Ref [108] Copyright © 2011, American Association for the Advancement of Science.

Even though, there are handful reports on the development of the M-N-C catalysts, the exact active reaction centre in the M-N-C based catalyst is still not established. However, the active reaction centres strongly depend on the metal centre, preferred nitrogen coordination and annealing temperature.<sup>[106]</sup> Dodelet *et al.* reported that in case of the Fe-N-C catalyst, both Fe-N<sub>4</sub>-C (N<sub>4</sub> means four nitrogen coordinated) and Fe-N<sub>2</sub>-C (N<sub>2</sub> means two nitrogen coordinated) are the active reaction centres.<sup>[110]</sup> Theoretical studies showed that the Fe-N<sub>2</sub>-C active centres are more efficient to reduce dioxygen molecule than Fe-N<sub>4</sub>-C. Also, it was concluded that among the different possible reactive centres, the Fe-N<sub>2+2</sub>-C sites are more active compared to the rest of the coordinations.<sup>[111]</sup> Co also exhibits the similar type of coordination. However, the Co-N<sub>2</sub>-C active centre is less common compared to Co-N<sub>4</sub>-C. Recent studies showed that the ORR activity of the Co-N-C catalysts is similar to the nitrogen doped carbon and suggested that Co is just assisting the nitrogen doping during the high temperature annealing.<sup>[108]</sup> However, many reports

strongly corroborate the Fe-N<sub>x</sub>-C active centre, with Fe acting as an effective reaction centre for ORR.<sup>[35]</sup> In case of the Fe and Co alloy systems, the improved activity is ascribed to the synergistic effect of the metal atoms. From DFT calculations, Sun *et al.* confirmed that the ORR activity decreases in the order FeCo-N-C > Fe-N-C > Co-N-C.<sup>[112]</sup> Even though, Co is not directly participating in the ORR process, it assists in lowering the HOMO and LUMO gap in the catalyst. In order to develop an efficient catalyst for ORR, it is thus necessary to improve the density of the active reaction centres. Along with the selection of the metal and nitrogen sources, high specific surface area with well-defined micro/meso porous structures is necessary for the improvement in the ORR activity. This indicates that proper selection of the carbon morphologies with high surface area and good electrical conductivities is a pre-requisite for a non-precious metal/non-metal electrocatalyst.

#### 1.3.2.2.6.1 Mechanism of ORR on Fe-N-C

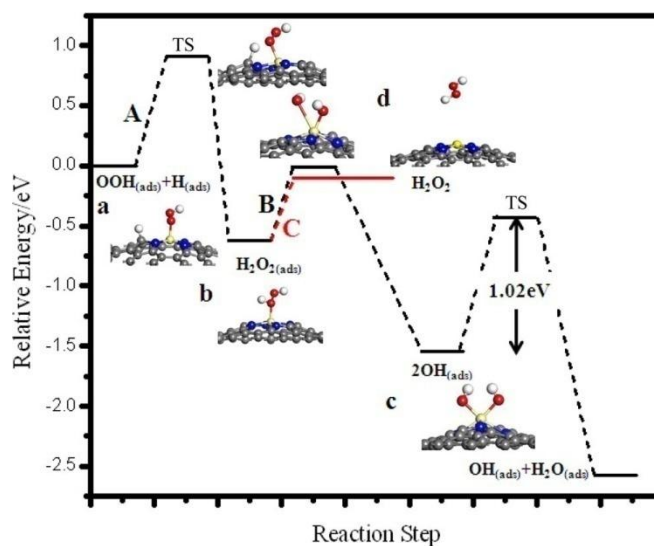


**Figure 1.20:** Relative energies vs different reaction steps for ORR on the Fe-N-C catalysts. (TS = transition state). Reprinted with the permission from Ref [113] Copyright© 2015 Electrochemical Society.

Very recently Zhang *et al.* used DFT calculations for investigating the kinetic and thermodynamic behaviour of ORR on the pyrrolic nitrogen coordinated iron embedded graphene.<sup>[113]</sup> It was found that the oxygen molecule always chemisorbed onto the iron moieties and the dissociation barrier for the adsorbed oxygen molecules is very high irrespective of the mode of adsorption of oxygen (Figure 1.20). ORR on the Fe-N<sub>4</sub>-C active

sites follows a 4e<sup>-</sup> pathway, with OH<sub>(ad)</sub> to H<sub>2</sub>O<sub>(ad)</sub> being the rate determining step. According to this theory, the reduction mechanism of oxygen molecules on Fe-N-C would be as given below:



Even though many reports emphasise that Fe-N<sub>x</sub> is the active reaction centre, Mukerjee *et al.* have recently reported that the high temperature annealed F-N-C catalyst has no direct Fe-N<sub>x</sub> bond as suggested earlier.<sup>[114]</sup> Using *in-situ* experimental techniques for simulating the actual fuel cell condition, it was proved that most of the iron is forming Fe/Fe<sub>x</sub>C nanoparticles and it will remain as a subsurface to the nitrogen doped carbon. The synergistic effect of Fe/Fe<sub>x</sub>C on the nitrogen doped carbon plays an important role for the improved ORR activity of the catalyst in a 4e<sup>-</sup> pathway with negligible formation of (< 5%) hydrogen peroxide. *In-situ* x-ray absorption spectroscopy (XAS) and <sup>57</sup>Fe Mössbauer spectroscopy indicated that there was no direct Fe-N<sub>x</sub> bond. Therefore, ORR in this case mainly occurs at the nitrogen doped carbon surface. In case of the high temperature annealed samples, the main role of iron is the graphitization of nitrogen doped carbon and there is no direct involvement of iron in ORR. Moreover, the authors also explained the improved stability of this electrocatalyst during ORR under acidic conditions. During high potential cycling, carbon corrosion occurs and these iron nanoparticles would dissolve in solution. Trace amounts of dissolved iron may coordinate with the nitrogen atoms doped on the surface of the carbon, which eventually act as new active reaction centres.

### 1.3.2.2.7 Metal encapsulated nanotubes for ORR

Metal encapsulated nitrogen doped carbon nanotubes is the latest development in the non-precious metal catalyst family. In 2012, Dai *et al.* used a simple method for the exfoliation of MWCNT - acid treatment followed by nitrogen doping using ammonia at high temperature.<sup>[115]</sup> Such graphene-carbon nanotube morphology showed excellent catalytic activity in acidic and alkaline mediums. According to the authors, the active reaction centre is mainly formed on the thin layer of the nitrogen doped graphene on iron

nanoparticles as suggested by Mukerjee *et al.*. Later, Zelenay *et al.* came up with the iron encapsulated nanotube and carbon composite by simple thermal annealing of a mixture of dicyanamide, iron acetate and carbon.<sup>[116]</sup> The ‘bamboo’ like nitrogen doped carbon nanotube was formed and showed excellent ORR activity in both acidic and alkaline mediums. Bao and co-workers have reported a series of iron encapsulated nanotubes prepared either by CVD or *via* the method reported by Zelenay *et al.* for ORR.<sup>[117]</sup> MOF template assisted graphene/graphene nanotubes were also studied for efficient ORR in acidic, alkaline and non-aqueous conditions by annealing dicyanamide, the iron salt and the MOF.<sup>[118]</sup> Very recently, Guo *et al.* have synthesised bamboo like nanotube-iron carbide nanoparticles for ORR under alkaline and acidic conditions by simple annealing of melamine and iron nitrate.<sup>[119]</sup> Using DFT calculations, Bao *et al.* explained the improved ORR activity of the metal encapsulated carbon nanotubes. The encapsulated metal reduces the work function on the surrounding carbon.<sup>[117b]</sup> If CNT is doped with nitrogen, the work function decreases further due to an increase in the density of state near the Fermi level. Moreover, the thickness of the carbon layer around the encapsulated metal/metal oxide also plays an important role for tuning the properties of the surface nitrogen doped carbon layer. The influence of the encapsulated metal/metal oxide decreases with increase in the carbon layer covering.

#### 1.3.2.2.8 Fe-P-C based catalysts for ORR

Singh *et al.* have reported Fe-P-C type non-precious metal catalyst for ORR. The catalyst was prepared by annealing the polymeric form of phytic acid and iron chloride at high temperature under inert atmosphere.<sup>[120]</sup> The catalyst thus prepared showed improved ORR activity in acidic medium. In an extension to this work, graphene was used as a conducting medium to further improve the activity of the Fe-P-C reaction centres.<sup>[121]</sup> Even though, Fe-P-C is a new class of non-precious metal catalysts, the activity is low compared to the Fe-N-C based catalysts.

#### 1.3.2.3 Metal-free electrocatalysts for ORR

From the previous sections, it is clear that both Pt and non-noble metal catalysts are useful in ORR. However, there are some disadvantage associated with these catalysts - mainly poor electrochemical stability and fuel tolerance. Thus, metal-free catalysts for ORR are always important for the development of cost effective fuel cells. The



modulates the electronic properties as well as the charge distribution in the carbon matrix. These improved electronic properties would reflect in the chemical nature of the material and ultimately would lead to the applicability of these materials in different applications including ORR.

### 1.3.2.3.1 Doping of carbon morphologies using single heteroatom for ORR

#### 1.3.2.3.1.1 Nitrogen doping

Handful reports are available on the nitrogen doped carbon morphologies for ORR. Small size and high electronegativity of the N-based doping agents improve the electronic structure of carbon with minimum lattice deformations. More importantly, the doping of nitrogen into the carbon matrix is comparatively easy through *in-situ* or post treatment methods. The nitrogen doped carbon morphologies, mainly, CNT, CNF, graphene, CNH, fullerenes, etc. obtained *via* different routes such as arc discharge, laser ablation, CVD, annealing of the mixture of carbon and nitrogen precursor at high temperature in inert atmosphere, are used as the ORR catalysts. The most commonly employed method for the preparation of N-doped CNT (NCNT) is CVD. Usually, methane and ammonia mixture, acetonitrile, etc. are used for the preparation of NCNT *via* the CVD method.<sup>[125]</sup> In the post treatment methods, NCNT can be prepared by annealing the mixture of functionalized CNT and nitrogen precursor at high temperature. Usually, melamine, urea, NH<sub>3</sub>, etc. are used as the nitrogen sources for the synthesis of NCNT.<sup>[123]</sup> The first report on the application of NCNT as a catalyst for ORR was by Dai *et al.* using CVD grown vertically aligned NCNT (VA-NCNT).<sup>[126]</sup> This material showed excellent activity and stability towards ORR in alkaline medium. Very recently, the same material was used under acidic conditions as an effective fuel tolerant cathode for PEMFC.<sup>[127]</sup> Even though the synthesis of NCNT and N-doped fullerenes is known long before, the synthesis of N-doped graphene (NGE) was reported very recently by Dai *et al.*<sup>[128]</sup> Also, there are reports of gram-scale synthesis of NGE *via* solvothermal procedures using tetrachloromethane and lithium nitride.<sup>[129]</sup> Highly porous NGE was also prepared using a silica templated method by annealing the mixture of silica/graphene composite with the nitrogen precursor followed by leaching out of silica.<sup>[130]</sup> Many reports are also available on ball milling techniques for the preparation of edge functionalized/N-doped graphite for ORR.<sup>[131]</sup> Apart from this, *in-situ* synthesis, post modifications *via* thermal treatment etc. also resulted in NGE and the ORR activity of the resulting NGE was found to be appreciable. The first report on the

NGE in this category was by Geng *et al.* and was prepared by annealing graphene oxide (GO) in presence of  $\text{NH}_3$  gas.<sup>[132]</sup> Recently, Dai *et al.* have synthesized N-doped graphitic quantum dots supported on graphene sheets for ORR.<sup>[133]</sup>

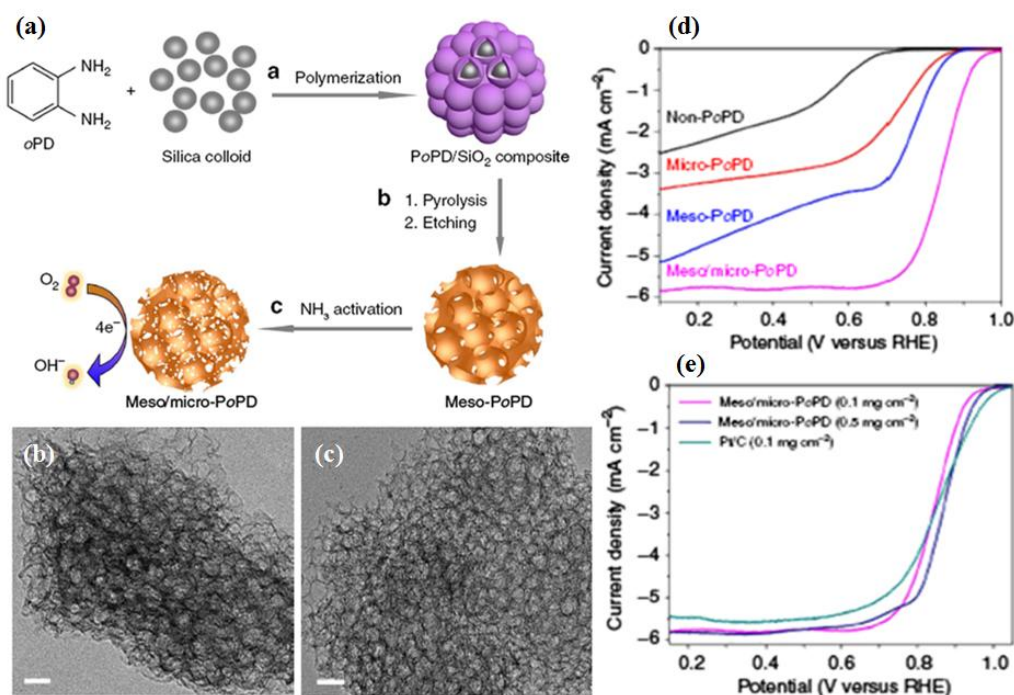


**Figure 1.22:** (a) Schematic representation of the synthesis of meso/micro porous nitrogen doped carbon (micro/meso-PoPD) electrocatalyst, (b-c) TEM image of meso-PoPD and (d-e) LSVs of PoPD in 0.1 M KOH at 1600 rpm and  $10 \text{ mV s}^{-1}$  scan rate. Reprinted with permission from [134] Copyright © 2014, Nature Publishing Group.

N-doped 3D carbon materials were also prepared by using hard and soft template methods. Recently Mullen *et al.* developed highly porous 3D carbon using silica template and showed extraordinary activity in ORR (Figure 1.22).<sup>[134]</sup> The activity was higher compared to the commercial Pt/C in alkaline medium and the overpotential was lower for ORR in acidic environment. This is the best performance ever reported for the non-metal based electrocatalysts. Hydrothermal methods were also adopted for the preparation of 3D graphene. Qu *et al.*<sup>[135]</sup> reported ultra-lightweight 3D graphene for efficient ORR activity in alkaline medium. Other nitrogen doped carbon materials based on graphitic carbon nitride ( $\text{g-C}_3\text{N}_4$ ) were also investigated for ORR.<sup>[136]</sup>  $\text{g-C}_3\text{N}_4$  synthesis usually employs melamine as a starting material and highly porous silica as a template to obtain a 3D morphology. Qiao *et al.* recently proved that an electron conducting medium is necessary for delivering efficient ORR activity by  $\text{g-C}_3\text{N}_4$ .<sup>[137]</sup> Yet another class of nitrogen doped



carbon used for ORR is derived from biomass.<sup>[138]</sup> The synthesis of such materials requires high temperature annealing for a longer time under an inert atmosphere for efficient graphitization. Another family of highly porous 3D nitrogen doped carbon was prepared by annealing metal organic frameworks (MOFs) or covalent organic frameworks (COFs) at high temperature.<sup>[139]</sup> These materials possess high surface area and excellent ORR activity. Apart from the 3D frameworks, polymer derived nitrogen doped carbon is also studied for its ORR activity. High temperature annealed polypyrrole, polyaniline, etc. are also tested for ORR.<sup>[140]</sup> To improve the electrical conductivity, graphitic carbon was also mixed with these polymers for efficient ORR.

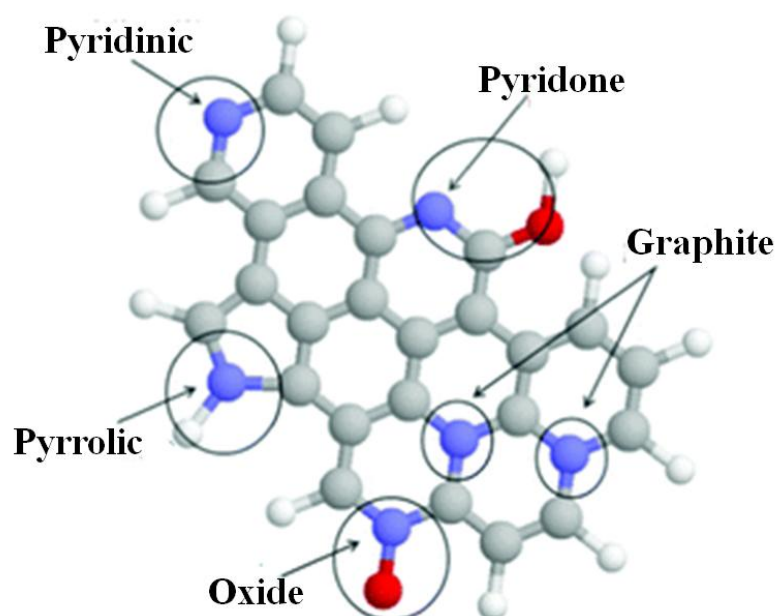


Figure 1.23: Different nitrogen coordinations in the carbon matrix (Blue- Nitrogen, Red- Oxygen, Gray- Carbon). Reprinted with the permission from [141] Copyright 2012, Royal Society of Chemistry.

Nitrogen atoms in carbon nanostructures are distributed randomly. Using scanning tunneling microscopy, Deng *et al.* have proved the perturbation of the electronic structure of graphene by nitrogen doping.<sup>[129]</sup> N-doping modulates the physicochemical properties of carbon morphologies. High surface area, high electrical conductivity and high concentration of the active centres improve the defective sites and better electrochemical properties are also achieved by introducing nitrogen into the carbon nanostructures. Mainly, the nitrogen atoms in the carbon morphologies exist in three different bonding

configurations. They are pyridinic, pyrrolic and graphitic coordinations (Figure 1.23). Preferred nitrogen coordination is inevitable for the ORR and the mechanism of ORR on N-doped carbon nanostructure is explained in detail in the following sections.

### 1.3.2.3.1.2 Boron doping

Boron, a less electronegative atom ( $\chi = 2$ ) compared to carbon ( $\chi = 2.5$ ), is also widely being used as a dopant for different carbon morphologies. As similar to the N-doping, boron doping also changes the electronic structure of the carbon morphologies due to charge inequalities. The first report on the boron doping on CNT was published in 1997 via an arc discharge method.<sup>[142]</sup> Many other techniques such as template assisted synthesis, CVD techniques, laser vaporization, substitution reaction, high temperature annealing of carbon with different boron containing precursors (boric acid, oxide of boron, etc.) have been employed to synthesis the B-doped carbon. Yang *et al.* reported a controlled synthesis of B-doped CNT by adjusting the amount of triphenylborane while keeping the benzene concentration constant using ferrocene as the catalyst.<sup>[143]</sup> Cyclic voltammetry indicated that both onset potential as well as half-wave potential are improved with increasing the atom percentage of boron in CNTs. Excellent ORR activity is also observed for B-doped graphene. Recent report by Sheng *et al.* on B-doped graphene also showed improved ORR activity, comparable to that of Pt/C in an alkaline medium.<sup>[144]</sup> Wang *et al.* also reported the synthesis of B-doped graphene by annealing graphene oxide (GO) with  $\text{BF}_3$  at higher temperature.<sup>[145]</sup> Boron doping improves the physicochemical properties of the carbon, as the electron deficient boron withdraws  $p$  electrons from the conjugated carbon and acts as an active centre for the oxygen reduction reaction. The electron withdrawing effect of boron makes its  $2p_z$  orbital filled with a fraction of lone pair of electrons and creates protruding lobes in the highest occupied molecular orbital (HOMO). This protruding lobe of boron will overlap with the electron deficient lowest unoccupied molecular orbital (LUMO) of oxygen resulting in a Pauling type adsorption and reduce the dioxygen molecule.

### 1.3.2.3.1.3 Sulphur doping

Compared to nitrogen and boron, sulphur doping is comparatively less investigated on carbon morphologies. The first report on the synthesis of sulphur doped carbon was published in 2011. In 2012, Yang *et al.* reported the improved ORR activity of the sulphur

doped graphene (SGE) prepared by high temperature annealing of graphene oxide and benzyl disulphide.<sup>[146]</sup> Even though there are theoretical predictions that S-doping in the carbon matrix is comparatively more difficult than the N- and B-doping, Yang *et al.* suggested that the material has excellent ORR activity, comparable to Pt/C. Moreover, this research also introduced a new discussion on the ORR mechanism. Before S-doping, researchers believed that electronegativity changes between heteroatoms (N and B) and carbon atoms induce changes in the charge density on the carbon, thereby facilitating the ORR process. In case of the S-doping, the electronegativity of both sulphur ( $\chi = 2.58$ ) and carbon ( $\chi = 2.55$ ) are similar and, hence, introduced a new concept called “spin density” for explaining the ORR activity. Following Yang, Mullen *et al.* synthesized highly porous SGE by thermal annealing of the GO/silica mixture under the flow of H<sub>2</sub>S gas.<sup>[147]</sup> The resulting SGE showed improved ORR activity and stability compared to Pt/C. Beak *et al.* adopted the ball milling technique to prepare S-doped graphite.<sup>[148]</sup> Simple ball milling approach using sulphur and graphite created edge selective doping of graphite. SGE was also prepared by annealing of exfoliated graphene under CS<sub>2</sub> flow and showed better activity towards the dioxygen reduction.<sup>[149]</sup> Thermal exfoliation of GO in presence of sulphur was also performed to synthesize the S-doped graphene sheets.<sup>[122e]</sup> Recently, sulphur containing polymers (polythiophene, polyethylenedioxythiophene etc.) are used as precursors for the synthesis of the S-doped carbon for ORR.<sup>[150]</sup> Even though, sulphur doping on graphene provides better ORR activity, the atom percentage of the doped sulphur in graphene is relatively low (< 2%). Moreover, the doped sulphur can easily escape from the carbon matrix at higher temperature.

#### 1.3.2.3.1.4 Phosphorous doping

Phosphorous doped carbon nano-morphologies are rare compared to the N, S, B doped carbon nanostructures. Only a few reports are available on P-doped carbon for ORR. Liu *et al.* reported the use of P-doped graphite in ORR for the first time.<sup>[151]</sup> Simple pyrolysis was employed for the synthesis of the P-doped graphite using a mixture of toluene and triphenylphosphine. Yang *et al.* also investigated P-doped carbon nanosphere and P-doped carbon nanotubes for achieving ORR activity.<sup>[152]</sup> The mechanism of ORR on the P-doped nanocarbons is almost similar to that of the B-doped carbon. Since the electronegativity of phosphorous ( $\chi = 2.19$ ) is comparatively smaller than that of carbon

(2.55), P-doping modifies the electronic charge density around the carbon atoms and improves the ORR activity.

#### 1.3.2.3.1.5 Dopants other than ‘N, S, B, P’

Other than the above mentioned dopants, some other elements such as halogens (F, Cl, Br, I) and Se were also used for doping carbon and studied for ORR. Beak *et al.* synthesized edge functionalized graphite with halogen (Cl, Br and I) for ORR in alkaline medium. The activity towards ORR was in the order  $\text{Cl} < \text{Br} < \text{I}$ .<sup>[153]</sup> Recently, Shen *et al.* came up with the reports of F-doped graphene using arc discharge method for use in ORR.<sup>[154]</sup> Sun *et al.* have also synthesised the F-doped carbon by annealing carbon black with  $\text{NH}_4\text{F}$  for investigating the ORR activities. This F-doped carbon was found to be outperformed Pt/C for ORR under alkaline conditions.<sup>[155]</sup> I-doped graphene was prepared by Yao *et al.* via simple thermal annealing of GO and  $\text{I}_2$ . I-doped graphene showed improved ORR activity compared to pure graphene. Se-doped graphene was also developed by the same group and was synthesized by simple thermal annealing.<sup>[156]</sup> Beak *et al.* have very recently developed antimony doped graphene platelets for ORR. Simple ball milling of graphite and Sb produced Sb-doped platelets and showed better ORR activity compared to pure graphite.<sup>[157]</sup>

#### 1.3.2.3.2 Co-doping of carbon morphologies using two heteroatoms for ORR

##### 3.2.3.2.1 Boron and nitrogen co-doping

Since single atom doping improves the electrochemical ORR by changing the charge density due to the electronegativity differences, dual doping might further improve the electrocatalytic activity of the carbon nanostructures. In this regard, the prime choice was on B, N-co-doped vertically aligned carbon nanotubes (VA-BCN). Dai *et al.* prepared VA-BCN by CVD using melamine diborate as the precursor for both boron and nitrogen.<sup>[158]</sup> VA-BCN nanotubes prepared by Dai *et al.* showed considerably improved ORR activity of the nanotubes over the N- or B-doped nanotubes. More interestingly, this study suggested that N-doping is more efficient for ORR than B-doping. There are reports for the preparation of boron and nitrogen co-doped (BCN) nanotubes much before Dai reported their VA-BCN. The report by Zhang *et al.* is one among them. Bamboo-shaped tubes of BCN were prepared by the pyrolysis of the respective precursors.<sup>[159]</sup> Wang *et al.* also synthesized BCN graphene by high temperature annealing of a mixture of GO, boric

acid and ammonia.<sup>[160]</sup> Hence, the prepared BCN graphene showed ORR activity superior to Pt/C. Controlled doping of B and N atoms into the graphene sheets indicated that the reaction centres are more stable than Pt/C. Ozaki *et al.* prepared BCN by carbonizing boron trifluoride, melamine and the furfural alcohol based polymer for efficient ORR.<sup>[161]</sup> However, this catalyst did not show the activity comparable to that of Pt/C. Reduction in the activity was mainly due to the direct interaction of boron and nitrogen. Mutual electron sharing between boron and nitrogen does not create changes in the charge density and this results into reduced ORR activity. If both nitrogen and boron are separated from each other, the charge density changes and improves the ORR activity. This synergetic effect of co-doping was also reported independently by Zhang *et al.* and Hu *et al.*<sup>[162]</sup>

#### 1.3.2.3.2 Sulphur and nitrogen co-doping

Compared to co-doping of N and B, the reports on S, N-co-doping (SCN) is rather scarce. The first approach in this regard was reported by Qaio *et al.*, via a simple thermal treatment of a mixture of GO, melamine and benzyl disulphide.<sup>[163]</sup> ORR activity of SCN graphene is higher than that of the respective S-doped and N-doped graphene. DFT calculations predicted the higher ORR activity of the SCN-graphene. From the DFT calculations, it was found that higher charge density as well as spin density induced by both sulphur and nitrogen is responsible for the improved ORR activity. In another report by Guan *et al.*, SCN-graphene was prepared by CVD using benzene, pyrimidine and thiophene as carbon, nitrogen and sulphur source respectively.<sup>[164]</sup> SCN-carbon nanosphere prepared by Wohlgemuth *et al.* and SCN-carbon form prepared by Huang *et al.* are some of the recent developments in the S,N-co-doped systems for ORR.<sup>[165]</sup>

#### 1.3.2.3.3 Phosphorous and nitrogen co-doping

P and N co-doped (PCN) carbon nanostructure was first introduced by Woo *et al.* and was prepared via a simple pyrolysis of a mixture of dicyanamide, phosphoric acid and metal salt.<sup>[166]</sup> Metal impurity was completely removed from the pyrolysed sample by acid treatment using aquaregia. The PCN-carbon nanostructure showed improved ORR activity in comparison to the N- doped carbon materials. The improved ORR activity is attributed to the asymmetric

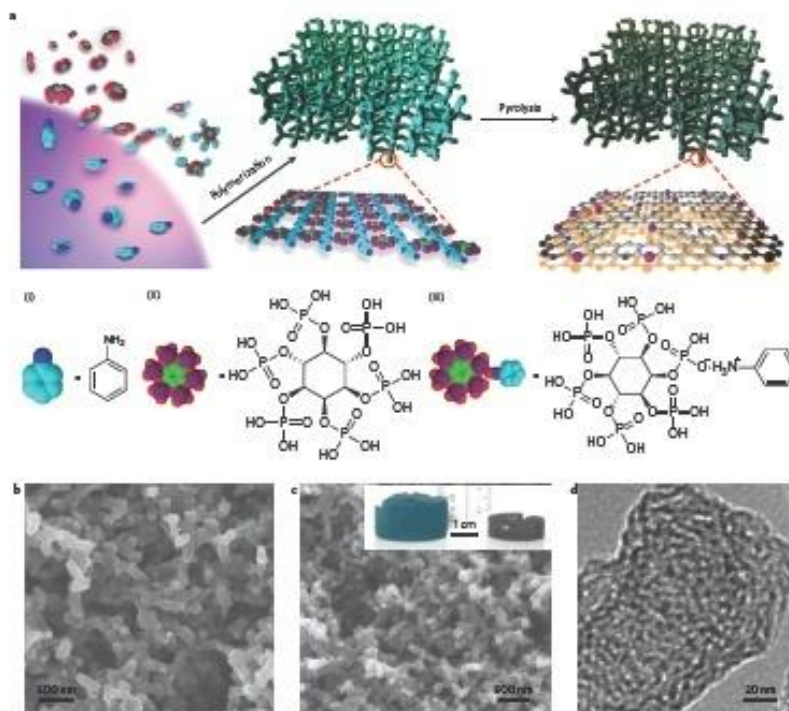


**Figure 1.24:** Schematic representation of the nitrogen and phosphorous doped carbon and its SEM and TEM images. Reprinted with the permission from [167] Copyright © 2015, Rights Managed by Nature Publishing Group.

spin density on the PCN-carbon nanostructure by co-doped P and N. In an extension to this work, Woo *et al.* further confirmed that along with the degree of P-doping, morphology of the PCN-carbon nanostructure also played a crucial role in determining the improved ORR activity.<sup>[168]</sup> Excellent ORR activity was also observed for the PCN-graphene prepared by annealing GO, dicyanamide and phosphoric acid. Dai *et al.* used CVD for the preparation of vertically aligned PCN-nanotubes using pyridine and triphenylphosphine as the carbon, nitrogen and phosphorous source. The obtained nanotubes reduced oxygen molecule *via* a 4e<sup>-</sup> pathway and the ORR activity was comparable to Pt/C in alkaline medium. Very recently, the same group synthesized a PCN-carbon based catalyst by simple pyrolysis of phytic acid and poly aniline in an inert atmosphere.<sup>[167]</sup> This catalyst showed excellent ORR activity under alkaline conditions (Figure 1.24).

### 1.3.2.3.3 Co-doping of carbon morphologies using three heteroatoms for ORR

In order to achieve higher activity of carbon materials as ORR catalysts, ternary doped carbon nanostructures have been developed. The first report in this regard was by Woo *et al.*, where high temperature annealing of a mixture of dicyanamide, boric acid and

phosphoric acid as the nitrogen, boron and phosphorous sources respectively was employed to synthesize P,N,B-doped carbon nanostructures.<sup>[166]</sup> This ternary doped carbon material showed improved mass activity compared to its binary- and mono- atom doped counter parts for ORR. Later, the same group reported ternary doped carbon nanostructures, using controlled S,P,N-doped carbon and studied the ORR activity under acidic conditions.<sup>[169]</sup> Very recently, Kang *et al.* synthesized P,B,N-doped carbon using a simple one pot protocol. In a typical synthesis, urea, phosphoric acid and boric acid were used as the nitrogen, phosphorous and boron sources respectively. The mixture of the precursors was annealed at temperature in the range of 450 – 600 °C and the resulting catalysts exhibited improved ORR activity compared to the corresponding binary- and mono- atom doped carbons.<sup>[170]</sup> Apart from the P,B,N-ternary doped systems, there are reports on S,P,N-doped carbon for ORR. Dai *et al* prepared S,P,N-ternary doped carbon *via* the thermal annealing of MOFs containing the respective elements.<sup>[171]</sup> Even though all these reports showed improved ORR activity compared to the control samples, the activity of the ternary doped carbon is far away from the commercial Pt/C catalyst.

#### 1.3.2.3.4 ORR mechanism on the N-doped carbon materials (CNT and graphene)

N-doped carbon nanostructures (mainly CNT and graphene) show enhanced ORR activities under both alkaline and acidic conditions. However, the active reaction centre and oxygen reduction mechanism promoted by the N-doped carbon nanostructures are still debatable. Quite a few theoretical studies in connection with the experimental approaches investigated the nature of the active reaction centre on the N-doped carbons. This section of the chapter provides a brief review on the reported theoretical and experimental approaches aimed at the elucidation of the mechanism of ORR by the N-doped carbons.

Of course, doping of nitrogen into a carbon matrix changes the electronic structure of the pure carbon, which will alter its physicochemical properties. The improved ORR activity of the N-doped carbon is believed to depend on the effect of the lone pair electrons of the N atom on the conjugated  $\pi$  electrons of the carbon. This shows the importance of the nitrogen content in the carbon matrix in determining the catalytic activity. Studies by Wiggins-Camacho *et al.* showed that there exists a strong relation between the nitrogen content and the physiochemical properties (conductivity, density of state near the Fermi level, work function, ORR activity etc.) of the carbon.<sup>[172]</sup> These theoretical observations were later supported by many reports by controlling the nitrogen content in the carbon.

Nitrogen in the N-doped carbon exists in many forms mainly, the pyridinic, pyrrolic, and graphitic coordinations. There are a lot of reports on these nitrogen coordinations and different opinions prevail on its influence on the electrocatalytic activity. However, any concrete evidence for the exact role of these coordinations and the catalytic centre in the N-doped carbon is not yet found. Among the three possible nitrogen coordinations, most of the reports suggested the enhanced ORR activity by pyridinic nitrogen coordination. Wiggins-Camacho *et al.* reported that the pyridinic nitrogen based catalytic sites are responsible for the dis-proportionation reaction of peroxides during ORR.<sup>[173]</sup> Recently, Yasuda *et al.* selectively prepared pyridinic (90 %) and graphitic (80%) nitrogen coordinated graphene to understand the role of these species in ORR.<sup>[174]</sup> It was found that the pyridinic coordination provides better ORR activity compared to the graphitic coordination and the pyridinic nitrogen reduces dioxygen molecules in a combined reduction pathway. Ruoff *et al.* synthesized nitrogen doped graphene using different nitrogen precursors for elucidating the role of the nitrogen coordinations for ORR.<sup>[175]</sup> This study suggested that the pyridinic nitrogen improved the onset potential (thermodynamic feasibility) and graphitic nitrogen is responsible for the reduction current.

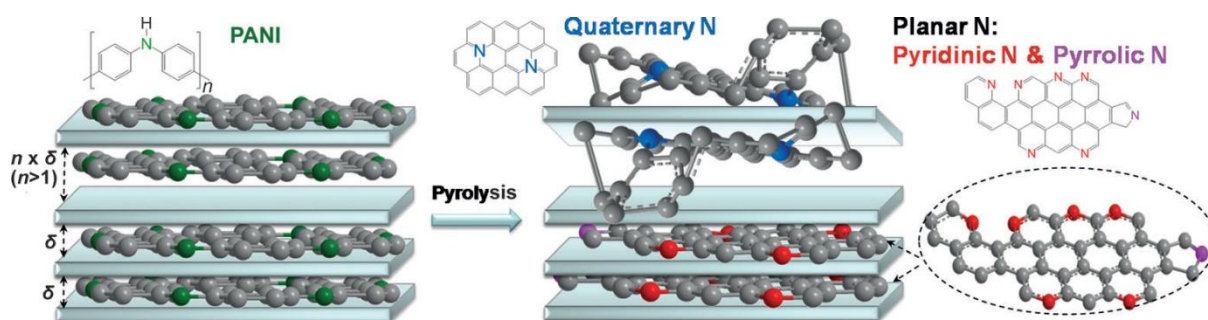


**Figure 1.25:** Schematic illustration of the synthesis of planar nitrogen doped graphene with high atom percentage of the pyridinic and pyrrolic nitrogens using a template assisted method. Reprinted with the permission from [176] Copyright © 2013 WILEY-VCH Verlag GmbH & Co. KGaA, Weinheim.

In order to get more insight into the active reaction centres, Ding *et al.* selectively synthesized the pyridinic and pyrrolic nitrogen doped graphene and graphitic nitrogen doped graphene using montmorillonite (MMT) as a template (Figure 1.25).<sup>[176]</sup> The concept behind this study was that the pyridinic and pyrrolic nitrogen doped carbon have planar structures and the graphitic one has a 3D structure due to the difference in the torsional angle of the C-N bond. In the planar case, the torsional angle is  $0^\circ$  and in the 3D



case, it is 60°. This indicated that the 3D structure of the graphitic nitrogen disturbs the  $\pi$ - $\pi$  conjugation of the carbon matrix and reduces the conductivity and reactivity. Polyaniline was used as the carbon and nitrogen sources and the aniline was polymerized in hard templated MMT. A 90.27% planar N-coordination was achieved using the smallest interspaced nonreactor based on MMT. From the electrocatalytic activity, the planar nitrogen showed excellent activity under acidic conditions with 60 mV higher overpotential compared to Pt/C. The results from Ding *et al.* suggest that the planar pyridinic and pyrrolic nitrogens are responsible for the ORR activity.

Since most of the synthetic approaches towards the N-doped carbon require high temperature annealing, the stability of the N-coordination varies with the annealing temperature. The graphitic coordination of the nitrogen is more stable at higher temperature (>1000 °C). Both the pyridinic and pyrrolic nitrogens get converted to the graphitic nitrogen at higher temperature, and at lower temperature, the pyridinic coordination may be transformed to pyrrolic and *vice-versa*. However, most of the reports on the N-doped carbons claim that the pyridinic nitrogen is the most efficient for ORR. Even though experimental proofs claim that the pyridinic nitrogen is responsible for the ORR activity, the nature of the active reaction centre, the distribution of nitrogen atoms, the kinetics of ORR, etc. are still not clear.

The higher electronegativity of the nitrogen atoms compared to carbon creates a higher positive charge density on carbon. This positive charge on carbon will decrease *via* a redox cycling process in the carbon matrix and it gets re-oxidized to the preferred oxidation state while adsorbing oxygen onto it. The Yeager type adsorption of oxygen molecule is promoted by the nitrogen atoms on the carbon matrix for weakening of the O-O bond for improved dioxygen reduction. Using the DFT calculations, Yang *et al.* suggested the ORR mechanism of the N-doped CNTs.<sup>[177]</sup> The energy barrier for the dioxygen adsorption is dramatically decreased due to the nitrogen doping. This study indicated that the nitrogen atoms withdraw electron from the neighboring carbon and create a positive charge density as explained before. Both pyridinic and graphitic nitrogen may withdraw electrons from the adjacent carbon. However, the number of the *p* electrons in both cases is different and occupancy of electron in a  $\pi^*$  orbital will vary accordingly. Since the graphitic nitrogen has two *p* electrons compared to the pyridinic nitrogen, the graphitic one should be the reaction centre. However, most of the experimental results are

contradicting this suggestion. Moreover, the defect created by nitrogen doping would reduce the band gap where the Fermi level would be up-shifted and show improved ORR activity by lowering the work function.

Yang *et al.* further studied the energy barrier for the oxygen dissociation on the N-doped graphene with respect to the type of nitrogen coordination.<sup>[177b]</sup> For pure graphene sheets, the energy barrier is 2.71 eV and is decreased by the incorporation of one graphitic nitrogen (1.87 eV). If three graphitic nitrogens are doped onto the graphene sheet with preferred arrangements, the overall energy barrier is reduced to 0.19 eV. Instead of graphitic coordination, incorporation of one pyridinic nitrogen reduces the energy barrier to 2.34 eV, which is still lower than that of the pristine graphene, but higher than that of the graphitic nitrogen coordination. If both the graphitic nitrogen and Stone-Wales defects are incorporated in the graphene sheets, the energy barrier would reduce to less than 0.2 eV. From these calculations, incorporation of more nitrogen can reduce the energy barrier effectively for better O<sub>2</sub> dissociation. Moreover, the nitrogen doping in the edges of the carbon nanostructures improves the first electron transfer to precede ORR in a 4e-pathway.

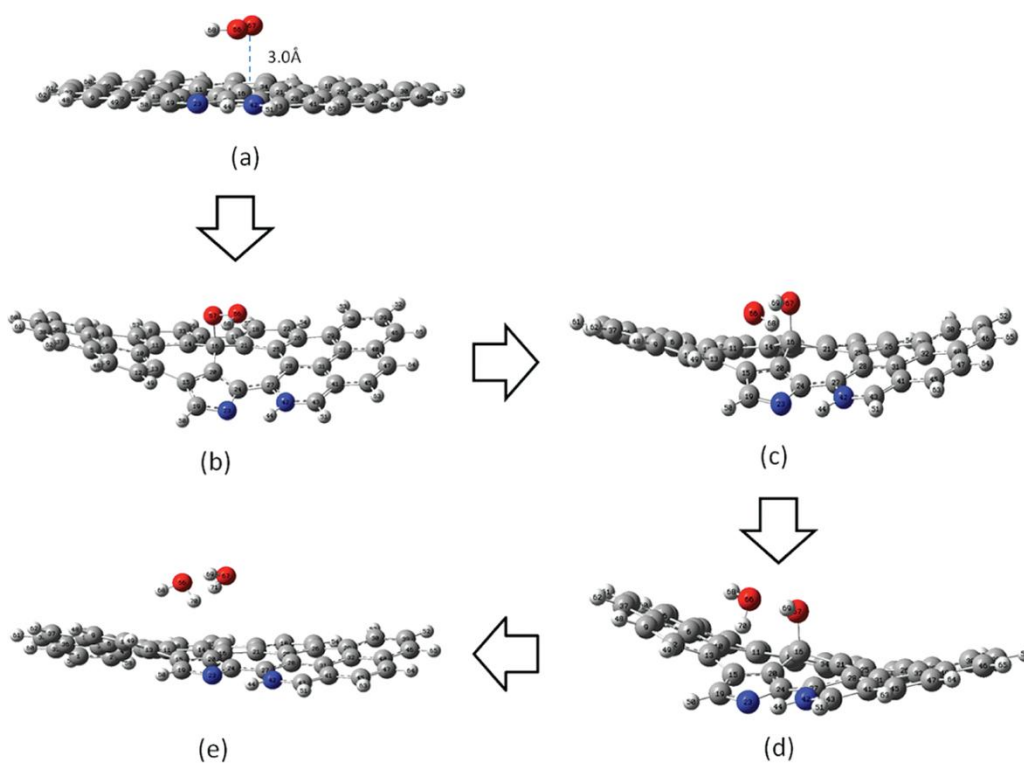


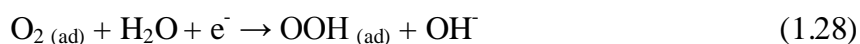
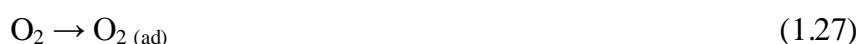
**Figure 1.26:** Mechanism of ORR on the nitrogen doped graphene having Stone-Wales defects. (a) Initial position of OOH from nitrogen-doped graphene, (b) adsorption of OOH

on the graphene, (c) dissociation of the O-O bond, (d) formation of one water molecule, and (e) formation of the second water molecule (Gray-carbon, blue-nitrogen, red-oxygen, and white-hydrogen). Reprinted with the permission from [178] Copyright 2011, American Chemical Society.

Zhang *et al.* have studied the electrocatalytic activity of the N-doped graphene under acidic conditions.<sup>[178]</sup> The high positive charge density and/or high positive spin density are suggested to be responsible for the efficient ORR. The electrocatalytic active centres should have either high spin density or charge density to reduce oxygen efficiently. Later, the same group correlated the ORR activity of the N-doped graphene with both microstructures of the materials and nitrogen dopant in cluster and Stone-Wale defects. The adopted combination of the structure for the calculation is shown in Figure 1.26. These calculations proposed two possible pathways for the first electron transfer: i)  $\text{OOH}^+$  adsorption and ii) direct  $\text{O}_2$  adsorption. Simulations showed that there is no energy barrier for the adsorption of both  $\text{OOH}^+$  and  $\text{OOH}$  onto the carbon near the hetero atoms. Adsorption of oxygen molecules onto the surface of graphene leads to distortions in the plane of graphene resulting in a “saddle shaped” surface where the adsorbed oxygen resides above the plane. Introducing one hydrogen atom at this stage would break the O-O bond and the dissociated OH would be removed from the surface. Further addition of two more hydrogen atoms would form two water molecules and depart from the surface of the graphene sheets. So, the third and fourth electron transfers are responsible for the generation of water during ORR. From the theoretical studies of Zhang *et al.*, both the nitrogen dopants and Stone-Wales defects are closely related to the active reaction site.

Bao and co-workers came up with two possible mechanisms for ORR on the N-doped graphene sheets as seen in case of the Pt based catalysts - the associative mechanism and the dissociative mechanism.<sup>[179]</sup>

#### Associative mechanism





Dissociative mechanism



The dissociative mechanism is energetically less favorable compared to the associative mechanism.

#### 1.4 Scope and objectives of the present thesis

Low cost alternatives to the current *state-of-the-art* Pt/C can be developed by tuning the physicochemical properties of the non-precious electrocatalysts. Improvement in the active reaction site density is essential to redefine the performance characteristics of many non-precious metal based electrocatalysts. The above brief review on the current status of the non-precious metal based electrocatalysts helps to develop new innovative ideas to design efficient cost-effective electrocatalysts for ORR. Most of these reports are mainly focused on the improvement in the active reaction site density for bringing in efficient ORR activity. The main factors, which tune the physicochemical properties of the carbon morphologies to improve the active reaction site density are summarized below:

1. Suitable carbon morphologies with more edge sites
2. Suitable carbon morphologies with high electrical conductivity
3. Suitable carbon morphologies with good graphitization
4. Suitable carbon morphologies with high surface area and porosity
5. The preferred heteroatom coordinations

Hence, it is realized that a concerted effort is needed by the judicious selection of the carbon morphologies and methodologies to create large number of the potential active sites which can facilitate ORR under a wide range of experimental conditions. Maintenance of the number density and preferred coordination of the active sites can be strongly influenced by the carbon morphology and the process adopted for creating the sites. A systematic study in this direction has been carried out by targeting these goals by tuning the physicochemical properties of the carbon morphologies by selecting graphene and

carbon nanohorn as the preferred substrate candidates. The present thesis compiles the developments achieved in this effort of developing a group of potential non-precious metal based ORR electrocatalysts by narrowing down the overpotential and increasing the current density for oxygen reduction. The specific objectives of this thesis are listed below:

1. Investigations on nitrogen doped graphene:
  - a) Synthesis of nitrogen doped graphene (NGE) by high temperature annealing of pyrrole mediated reduced graphene oxide and its ORR performance.
  - b) 3D arrangement of NGE using simple one step synthesis procedure *via* the annealing of GO dip coated melamine and its effect in the electrocatalytic activity towards ORR.
2. Investigations on nitrogen doped carbon nanohorn:
  - a) Synthesis of nitrogen doped nanohorn (NCNH) using simple thermal treatment of a mixture of single walled carbon nanohorn and urea. To study the effect of nitrogen doping on the surface area and electrical conductivity to tune the active reaction centre density for efficient ORR.
  - b) Study the effect of modified NCNH substrate on the electrochemical properties of CoSe<sub>2</sub> non-precious metal catalytic centre.
  - c) Single cell performance evaluation of the prepared cathode catalysts.
3. Investigations on nitrogen and iron co-doped carbon nanohorns
  - a) Synthesis of iron and nitrogen co-doped carbon nanohorn for ORR. To study the effect of iron loading and heat treatment temperature on ORR.
  - b) Synthesis of iron oxide encapsulated graphene nanotubes by thermal annealing of CNH, melamine and iron salt. To study the role of melamine and iron loading to convert the nanohorn morphology to graphene nanotube and its ORR evaluation in both acidic and alkaline mediums.
  - c) Single cell performance evaluation of the prepared cathode catalysts.

## 1.5 References

- [1] A. J. G. Hey, P. Walters, *Einstein's Mirror*, Cambridge University Press, **1997**.
- [2] a)<http://waterpoweredcar.com/stanmeyer.html>; b)<http://skepdic.com/herbfuel.html>;  
c)P. Ball, *Nature* **2007**, doi:10.1038/news070910-13;  
d)[http://peswiki.com/index.php/Directory:John\\_Kanzius\\_Produces\\_Hydrogen\\_from\\_Salt\\_Water\\_Using\\_Radio\\_Waves](http://peswiki.com/index.php/Directory:John_Kanzius_Produces_Hydrogen_from_Salt_Water_Using_Radio_Waves).
- [3] [https://en.wikipedia.org/wiki/William\\_Robert\\_Grove](https://en.wikipedia.org/wiki/William_Robert_Grove).
- [4] [http://ethw.org/Bacon%27s\\_Fuel\\_Cell](http://ethw.org/Bacon%27s_Fuel_Cell).
- [5] R. P. O'Hayre, *Fuel cell fundamentals*, John Wiley & Sons, **2006**.
- [6] a)B. C. H. Steele, A. Heinzel, *Nature* **2001**, *414*, 345-352; b)A. Hamnett, in *Handbook of Fuel Cells*, John Wiley & Sons, Ltd, **2010**.
- [7] <http://www.transparencymarketresearch.com/fuel-cell-market.html>.
- [8] M. Fuel Cells Market (PEMFC, PAFC, SOFC, DMFC & Others) - Global Industry Analysis, Size, Share, Trends, Growth And Forecast 2012 - 2018, 114pages, September 2014.
- [9] I. I. Olsen, *Outlook on fuel cell market and technologies* **2013**.
- [10] [http://www.hydrogen.energy.gov/pdfs/progress14/v\\_a\\_5\\_garzon\\_2014.pdf](http://www.hydrogen.energy.gov/pdfs/progress14/v_a_5_garzon_2014.pdf).
- [11] Y. Shao, G. Yin, Z. Wang, Y. Gao, *J. Power sources* **2007**, *167*, 235-242.
- [12] J. R. Varcoe, P. Atanassov, D. R. Dekel, A. M. Herring, M. A. Hickner, P. A. Kohl, A. R. Kucernak, W. E. Mustain, K. Nijmeijer, K. Scott, T. Xu, L. Zhuang, *Energy Environ. Sci.* **2014**, *7*, 3135-3191.
- [13] F. M. B. Marques, *Frontiers in Energy Research* **2013**, *1*.
- [14] S. J. Peighambaroust, S. Rowshanzamir, M. Amjadi, *International Journal of Hydrogen Energy* **2010**, *35*, 9349-9384.
- [15] F. Barbir, in *PEM Fuel Cells* (Ed.: F. Barbir), Academic Press, Burlington, **2005**, pp. 1-16.
- [16] a)J. S. Wainright, M. H. Litt, R. F. Savinell, in *Handbook of Fuel Cells*, John Wiley & Sons, Ltd, **2010**; b)K. D. Kreuer, in *Handbook of Fuel Cells*, John Wiley & Sons, Ltd, **2010**; c)M. Nakao, M. Yoshitake, in *Handbook of Fuel Cells*, John Wiley & Sons, Ltd, **2010**; d)D. J. Jones, J. Rozière, in *Handbook of Fuel Cells*, John Wiley & Sons, Ltd, **2010**; e)M. Doyle, G. Rajendran, in *Handbook of Fuel Cells*, John Wiley & Sons, Ltd, **2010**.

- [17] C. Sánchez, E. Leiva, in *Handbook of Fuel Cells*, John Wiley & Sons, Ltd, **2010**.
- [18] M. Uchida, Y.-C. Park, K. Kakinuma, H. Yano, D. A. Tryk, T. Kamino, H. Uchida, M. Watanabe, *Phys. Chem. Chem. Phys.* **2013**, *15*, 11236-11247.
- [19] R. R. Adzic, F. H. B. Lima, in *Handbook of Fuel Cells*, John Wiley & Sons, Ltd, **2010**.
- [20] M. Watanabe, in *Handbook of Fuel Cells*, John Wiley & Sons, Ltd, **2010**.
- [21] M. Gattrell, B. MacDougall, in *Handbook of Fuel Cells*, John Wiley & Sons, Ltd, **2010**.
- [22] G. Merle, M. Wessling, K. Nijmeijer, *Journal of Membrane Science* **2011**, *377*, 1-35.
- [23] C. G. Arges, V. Ramani, P. N. Pintauro, *The Electrochemical Society Interface Summer* **2010**, *19*, 31-35.
- [24] V. Ponec, G. C. Bond, *Catalysis by Metals and Alloys*, Elsevier Science, **1995**.
- [25] W. Vielstich, in *Handbook of Fuel Cells*, John Wiley & Sons, Ltd, **2010**.
- [26] a)W. Sheng, Z. Zhuang, M. Gao, J. Zheng, J. G. Chen, Y. Yan, *Nat Commun* **2015**, *6*; b)M. W. Breiter, in *Handbook of Fuel Cells*, John Wiley & Sons, Ltd, **2010**.
- [27] a)N. A. M. Barakat, M. Motlak, B.-S. Kim, A. G. El-Deen, S. S. Al-Deyab, A. M. Hamza, *Journal of Molecular Catalysis A: Chemical* **2014**, *394*, 177-187; b)N. A. M. Barakat, M. A. Abdelkareem, A. Yousef, S. S. Al-Deyab, M. El-Newehy, H. Y. Kim, *International Journal of Hydrogen Energy* **2013**, *38*, 3387-3394; c)P. Manivasakan, P. Ramasamy, J. Kim, *Nanoscale* **2014**, *6*, 9665-9672.
- [28] a)W. Sheng, A. P. Bivens, M. Myint, Z. Zhuang, R. V. Forest, Q. Fang, J. G. Chen, Y. Yan, *Energy Environ. Sci.* **2014**, *7*, 1719-1724; b)S. Lu, J. Pan, A. Huang, L. Zhuang, J. Lu, *Proceedings of the National Academy of Sciences* **2008**; c)E. Borja-Arco, O. Jiménez-Sandoval, L. Magallón-Cacho, P. J. Sebastian, *J. Power sources* **2014**, *246*, 438-442; d)H.-Y. Park, I.-S. Park, B. Choi, K.-S. Lee, T.-Y. Jeon, Y.-E. Sung, S. J. Yoo, *Phys. Chem. Chem. Phys.* **2013**, *15*, 2125-2130; e)J. Ohyama, T. Sato, Y. Yamamoto, S. Arai, A. Satsuma, *J. Am. Chem. Soc.* **2013**, *135*, 8016-8021; f)J. Ohyama, T. Sato, A. Satsuma, *J. Power sources* **2013**, *225*, 311-315; g)M. Shao, *J. Power sources* **2011**, *196*, 2433-2444; h)O. Chanick, H. Kwan Soo, L. SangGap, P. Chung-hyun, Y. Insuk, *Journal of Physics: Condensed Matter* **2006**, *18*, 3335.

- [29] J. K. Nørskov, J. Rossmeisl, A. Logadottir, L. Lindqvist, J. R. Kitchin, T. Bligaard, H. Jónsson, *J. Phys. Chem. B* **2004**, *108*, 17886-17892.
- [30] a) Z. Shi, J. Zhang, Z.-S. Liu, H. Wang, D. P. Wilkinson, *Electrochim. Acta* **2006**, *51*, 1905-1916; b) J. Zhang, *PEM Fuel Cell Electrocatalysts and Catalyst Layers: Fundamentals and Applications*, Springer London, **2008**.
- [31] a) W. E. Mustain, J. Prakash, *J. Electrochem. Soc.* **2007**, *154*, A668-A676; b) P. B. Balbuena, V. R. Subramanian, *Theory and Experiment in Electrocatalysis*, Springer New York, **2010**.
- [32] C. F. Zinola, *Electrocatalysis: Computational, Experimental, and Industrial Aspects*, CRC Press, **2010**.
- [33] R. A. Sidik, A. B. Anderson, *Journal of Electroanalytical Chemistry* **2002**, *528*, 69-76.
- [34] a) V. P. Zhdanov, B. Kasemo, *Electrochem. Commun.* **2006**, *8*, 1132-1136; b) T. Li, P. B. Balbuena, *Chemical Physics Letters* **2003**, *367*, 439-447.
- [35] Y. Nie, L. Li, Z. Wei, *Chem. Soc. Rev.* **2015**, *44*, 2168-2201.
- [36] T. Zhang, A. B. Anderson, *Electrochim. Acta* **2007**, *53*, 982-989.
- [37] a) C. Hartnig, M. T. M. Koper, *Journal of Electroanalytical Chemistry* **2002**, *532*, 165-170; b) T. Toda, H. Igarashi, H. Uchida, M. Watanabe, *J. Electrochem. Soc.* **1999**, *146*, 3750-3756.
- [38] Y. Sha, T. H. Yu, B. V. Merinov, P. Shirvanian, W. A. Goddard, *The Journal of Physical Chemistry Letters* **2011**, *2*, 572-576.
- [39] a) V. Stamenkovic, B. S. Mun, K. J. J. Mayrhofer, P. N. Ross, N. M. Markovic, J. Rossmeisl, J. Greeley, J. K. Nørskov, *Angew. Chem. Int. Ed.* **2006**, *45*, 2897-2901; b) V. Tripković, E. Skúlason, S. Siahrostami, J. K. Nørskov, J. Rossmeisl, *Electrochim. Acta* **2010**, *55*, 7975-7981; c) V. Viswanathan, H. A. Hansen, J. Rossmeisl, J. K. Nørskov, *The Journal of Physical Chemistry Letters* **2012**, *3*, 2948-2951.
- [40] J. Greeley, J. K. Nørskov, *J. Phys. Chem. C* **2009**, *113*, 4932-4939.
- [41] N. M. Marković, R. R. Adžić, B. D. Cahan, E. B. Yeager, *Journal of Electroanalytical Chemistry* **1994**, *377*, 249-259.
- [42] P. Zelenay, M. Gamboa-Aldeco, G. Horányi, A. Wieckowski, *Journal of Electroanalytical Chemistry* **1993**, *357*, 307-326.



- [43] a)C. Wang, H. Daimon, Y. Lee, J. Kim, S. Sun, *J. Am. Chem. Soc.* **2007**, *129*, 6974-6975; b)R. Narayanan, M. A. El-Sayed, *J. Phys. Chem. B* **2005**, *109*, 12663-12676.
- [44] a)M. D. Maciá, J. M. Campiña, E. Herrero, J. M. Feliu, *Journal of Electroanalytical Chemistry* **2004**, *564*, 141-150; b)A. Kuzume, E. Herrero, J. M. Feliu, *Journal of Electroanalytical Chemistry* **2007**, *599*, 333-343; c)T. Yu, D. Y. Kim, H. Zhang, Y. Xia, *Angew. Chem. Int. Ed.* **2011**, *50*, 2773-2777.
- [45] Z. Peng, H. Yang, *Nano Today* **2009**, *4*, 143-164.
- [46] S. Sun, G. Zhang, D. Geng, Y. Chen, R. Li, M. Cai, X. Sun, *Angew. Chem. Int. Ed.* **2011**, *50*, 422-426.
- [47] S. M. Unni, V. K. Pillai, S. Kurungot, *RSC Adv.* **2013**, *3*, 6913-6921.
- [48] A. Chen, P. Holt-Hindle, *Chem. Rev.* **2010**, *110*, 3767-3804.
- [49] B. Y. Xia, W. T. Ng, H. B. Wu, X. Wang, X. W. Lou, *Angew. Chem. Int. Ed.* **2012**, *51*, 7213-7216.
- [50] Y. Bing, H. Liu, L. Zhang, D. Ghosh, J. Zhang, *Chem. Soc. Rev.* **2010**, *39*, 2184-2202.
- [51] W. Yu, M. D. Porosoff, J. G. Chen, *Chem. Rev.* **2012**, *112*, 5780-5817.
- [52] a)J. Wu, A. Gross, H. Yang, *Nano Lett.* **2011**, *11*, 798-802; b)J. Zhang, J. Fang, *J. Am. Chem. Soc.* **2009**, *131*, 18543-18547; c)D. Xu, Z. Liu, H. Yang, Q. Liu, J. Zhang, J. Fang, S. Zou, K. Sun, *Angew. Chem. Int. Ed.* **2009**, *48*, 4217-4221; d)J. Chen, B. Wiley, J. McLellan, Y. Xiong, Z.-Y. Li, Y. Xia, *Nano Lett.* **2005**, *5*, 2058-2062; e)Z. Peng, H. Yang, *J. Am. Chem. Soc.* **2009**, *131*, 7542-7543; f)L. Wang, Y. Nemoto, Y. Yamauchi, *J. Am. Chem. Soc.* **2011**, *133*, 9674-9677; g)X. Teng, M. Feygenson, Q. Wang, J. He, W. Du, A. I. Frenkel, W. Han, M. Aronson, *Nano Lett.* **2009**, *9*, 3177-3184; h)K. A. Kuttiyiel, K. Sasaki, D. Su, L. Wu, Y. Zhu, R. R. Adzic, *Nat Commun* **2014**, *5*; i)H. You, S. Yang, B. Ding, H. Yang, *Chem. Soc. Rev.* **2013**, *42*, 2880-2904; j)Y. Xu, B. Zhang, *Chem. Soc. Rev.* **2014**, *43*, 2439-2450; k)H.-l. Liu, F. Nosheen, X. Wang, *Chem. Soc. Rev.* **2015**, *44*, 3056-3078; l)Y.-J. Wang, N. Zhao, B. Fang, H. Li, X. T. Bi, H. Wang, *Chem. Rev.* **2015**, *115*, 3433-3467.
- [53] V. R. Stamenkovic, B. S. Mun, M. Arenz, K. J. J. Mayrhofer, C. A. Lucas, G. Wang, P. N. Ross, N. M. Markovic, *Nat Mater* **2007**, *6*, 241-247.

- [54] Y. Dai, L. Ou, W. Liang, F. Yang, Y. Liu, S. Chen, *J. Phy. Chem. C* **2011**, *115*, 2162-2168.
- [55] Y. Yu, W. Yang, X. Sun, W. Zhu, X. Z. Li, D. J. Sellmyer, S. Sun, *Nano Lett.* **2014**, *14*, 2778-2782.
- [56] C. Chen, Y. Kang, Z. Huo, Z. Zhu, W. Huang, H. L. Xin, J. D. Snyder, D. Li, J. A. Herron, M. Mavrikakis, M. Chi, K. L. More, Y. Li, N. M. Markovic, G. A. Somorjai, P. Yang, V. R. Stamenkovic, *Science* **2014**, *343*, 1339-1343.
- [57] J. Wu, L. Qi, H. You, A. Gross, J. Li, H. Yang, *J. Am. Chem. Soc.* **2012**, *134*, 11880-11883.
- [58] a)J.-L. Shui, J.-W. Zhang, J. C. M. Li, *J. Mater. Chem.* **2011**, *21*, 6225-6229; b)S. M. Alia, B. A. Larsen, S. Pylypenko, D. A. Cullen, D. R. Diercks, K. C. Neyerlin, S. S. Kocha, B. S. Pivovar, *ACS Catal.* **2014**, *4*, 1114-1119; c)J.-l. Shui, C. Chen, J. C. M. Li, *Adv. Function. Mater.* **2011**, *21*, 3357-3362.
- [59] V. R. Stamenkovic, B. Fowler, B. S. Mun, G. Wang, P. N. Ross, C. A. Lucas, N. M. Marković, *Science* **2007**, *315*, 493-497.
- [60] B. Fowler, C. A. Lucas, A. Omer, G. Wang, V. R. Stamenković, N. M. Marković, *Electrochimi. Acta* **2008**, *53*, 6076-6080.
- [61] J. Wu, J. Zhang, Z. Peng, S. Yang, F. T. Wagner, H. Yang, *J. Am. Chem. Soc.* **2010**, *132*, 4984-4985.
- [62] C. Zhang, S. Y. Hwang, A. Trout, Z. Peng, *J. Am. Chem. Soc.* **2014**, *136*, 7805-7808.
- [63] a)R. Ferrando, J. Jellinek, R. L. Johnston, *Chem. Rev.* **2008**, *108*, 845-910; b)R. Ghosh Chaudhuri, S. Paria, *Chem. Rev.* **2012**, *112*, 2373-2433; c)M. Oezaslan, F. Hasché, P. Strasser, *The Journal of Physical Chemistry Letters* **2013**, *4*, 3273-3291; d)V. M. Dhavale, S. M. Unni, H. N. Kagalwala, V. K. Pillai, S. Kurungot, *Chem. Commun.* **2011**, *47*, 3951-3953; e)S. J. Hwang, S. J. Yoo, J. Shin, Y.-H. Cho, J. H. Jang, E. Cho, Y.-E. Sung, S. W. Nam, T.-H. Lim, S.-C. Lee, S.-K. Kim, *Sci. Rep.* **2013**, *3*.
- [64] a)K. Sasaki, H. Naohara, Y. Cai, Y. M. Choi, P. Liu, M. B. Vukmirovic, J. X. Wang, R. R. Adzic, *Angew. Chem. Int. Ed.* **2010**, *49*, 8602-8607; b)K. Sasaki, H. Naohara, Y. Choi, Y. Cai, W.-F. Chen, P. Liu, R. R. Adzic, *Nat Commun* **2012**, *3*, 1115.
- [65] T. Toda, H. Igarashi, M. Watanabe, *J. Electrochem. Soc.* **1998**, *145*, 4185-4188.

- [66] a)V. R. Stamenkovic, B. S. Mun, K. J. J. Mayrhofer, P. N. Ross, N. M. Markovic, *J. Am. Chem. Soc.* **2006**, *128*, 8813-8819; b)C. Wang, M. Chi, D. Li, D. Strmcnik, D. van der Vliet, G. Wang, V. Komanicky, K.-C. Chang, A. P. Paulikas, D. Tripkovic, J. Pearson, K. L. More, N. M. Markovic, V. R. Stamenkovic, *J. Am. Chem. Soc.* **2011**, *133*, 14396-14403.
- [67] J. Durst, M. Lopez-Haro, L. Dubau, M. Chatenet, Y. Soldo-Olivier, L. Guétaz, P. Bayle-Guillemaud, F. Maillard, *The Journal of Physical Chemistry Letters* **2014**, *5*, 434-439.
- [68] J. C. Meier, C. Galeano, I. Katsounaros, A. A. Topalov, A. Kostka, F. Schüth, K. J. J. Mayrhofer, *ACS Catal.* **2012**, *2*, 832-843.
- [69] Z. Yang, J. Ren, Z. Zhang, X. Chen, G. Guan, L. Qiu, Y. Zhang, H. Peng, *Chem. Rev.* **2015**, *115*, 5159-5223.
- [70] a)B. K. Balan, S. M. Unni, S. Kurungot, *J. Phy. Chem. C* **2009**, *113*, 17572-17578; b)N. Sano, S.-i. Ukita, *Materials Chemistry and Physics* **2006**, *99*, 447-450; c)R. Yuge, T. Ichihashi, Y. Shimakawa, Y. Kubo, M. Yudasaka, S. Iijima, *Adv. Mater.* **2004**, *16*, 1420-1423; d)T. Onoe, S. Iwamoto, M. Inoue, *Catalysis Communications* **2007**, *8*, 701-706; e)Y. Li, Y. Li, E. Zhu, T. McLouth, C.-Y. Chiu, X. Huang, Y. Huang, *J. Am. Chem. Soc.* **2012**, *134*, 12326-12329.
- [71] X. Yu, S. Ye, *J. Power sources* **2007**, *172*, 145-154.
- [72] a)B. Fang, J. H. Kim, M. Kim, J.-S. Yu, *Chem. Mater.* **2009**, *21*, 789-796; b)D. Banham, F. Feng, T. Furstenhaupt, S. Ye, V. Birss, *J. Mater. Chem.* **2012**, *22*, 7164-7171; c)G. Gupta, D. A. Slanac, P. Kumar, J. D. Wiggins-Camacho, J. Kim, R. Ryoo, K. J. Stevenson, K. P. Johnston, *J. Phy. Chem. C* **2010**, *114*, 10796-10805.
- [73] a)Y. Liu, W. E. Mustain, *ACS Catal.* **2011**, *1*, 212-220; b)Y.-J. Wang, D. P. Wilkinson, J. Zhang, *Chem. Rev.* **2011**, *111*, 7625-7651; c)C.-P. Lo, V. Ramani, *ACS Appl. Mater. Inter.* **2012**, *4*, 6109-6116; d)Z. Cui, R. G. Burns, F. J. DiSalvo, *Chem. Mater.* **2013**, *25*, 3782-3784; e)Y. Liu, W. E. Mustain, *J. Am. Chem. Soc.* **2013**, *135*, 530-533; f)A. Kumar, V. Ramani, *ACS Catal.* **2014**, *4*, 1516-1525.
- [74] V. T. T. Ho, C.-J. Pan, J. Rick, W.-N. Su, B.-J. Hwang, *J. Am. Chem. Soc.* **2011**, *133*, 11716-11724.
- [75] X. Xie, Y. Xue, L. Li, S. Chen, Y. Nie, W. Ding, Z. Wei, *Nanoscale* **2014**, *6*, 11035-11040.

- [76] a) K. Jukk, N. Alexeyeva, P. Ritslaid, J. Kozlova, V. Sammelselg, K. Tammeveski, *Electrocatalysis* **2013**, *4*, 42-48; b) J. Qiao, R. Lin, B. Li, J. Ma, J. Liu, *Electrochim. Acta* **2010**, *55*, 8490-8497; c) V. I. Zaikovskii, K. S. Nagabhushana, V. V. Kriventsov, K. N. Loponov, S. V. Cherepanova, R. I. Kvon, H. Bönemann, D. I. Kochubey, E. R. Savinova, *J. Phys. Chem. B* **2006**, *110*, 6881-6890; d) R. Zhou, S. Z. Qiao, *Chem. Mater.* **2014**, *26*, 5868-5873.
- [77] M. H. Shao, T. Huang, P. Liu, J. Zhang, K. Sasaki, M. B. Vukmirovic, R. R. Adzic, *Langmuir* **2006**, *22*, 10409-10415.
- [78] a) Y. Suo, L. Zhuang, J. Lu, *Angew. Chem. Int. Ed.* **2007**, *46*, 2862-2864; b) L. Xiao, L. Zhuang, Y. Liu, J. Lu, H. D. Abruña, *J. Am. Chem. Soc.* **2009**, *131*, 602-608; c) M. Shao, T. Yu, J. H. Odell, M. Jin, Y. Xia, *Chem. Commun.* **2011**, *47*, 6566-6568.
- [79] a) Y. Lu, Y. Jiang, X. Gao, X. Wang, W. Chen, *J. Am. Chem. Soc.* **2014**, *136*, 11687-11697; b) W. Ding, M. R. Xia, Z. D. Wei, S. G. Chen, J. S. Hu, L. J. Wan, X. Q. Qi, X. H. Hu, L. Li, *Chem. Commun.* **2014**, *50*, 6660-6663.
- [80] a) F. Cheng, T. Zhang, Y. Zhang, J. Du, X. Han, J. Chen, *Angew. Chem. Int. Ed.* **2013**, *52*, 2474-2477; b) J.-S. Lee, G. S. Park, H. I. Lee, S. T. Kim, R. Cao, M. Liu, J. Cho, *Nano Lett.* **2011**, *11*, 5362-5366; c) L. Mao, D. Zhang, T. Sotomura, K. Nakatsu, N. Koshihara, T. Ohsaka, *Electrochim. Acta* **2003**, *48*, 1015-1021; d) R. S. Devan, R. A. Patil, J.-H. Lin, Y.-R. Ma, *Adv. Function. Mater.* **2012**, *22*, 3326-3370; e) F. Cheng, Y. Su, J. Liang, Z. Tao, J. Chen, *Chem. Mater.* **2010**, *22*, 898-905.
- [81] a) Y. Li, M. Gong, Y. Liang, J. Feng, J.-E. Kim, H. Wang, G. Hong, B. Zhang, H. Dai, *Nat Commun* **2013**, *4*, 1805; b) J. Xiao, Q. Kuang, S. Yang, F. Xiao, S. Wang, L. Guo, *Sci. Rep.* **2013**, *3*; c) T. Maiyalagan, K. A. Jarvis, S. Therese, P. J. Ferreira, A. Manthiram, *Nat Commun* **2014**, *5*.
- [82] Y. Liang, H. Wang, P. Diao, W. Chang, G. Hong, Y. Li, M. Gong, L. Xie, J. Zhou, J. Wang, T. Z. Regier, F. Wei, H. Dai, *J. Am. Chem. Soc.* **2012**, *134*, 15849-15857.
- [83] Z.-S. Wu, S. Yang, Y. Sun, K. Parvez, X. Feng, K. Müllen, *J. Am. Chem. Soc.* **2012**, *134*, 9082-9085.
- [84] M. De Koninck, B. Marsan, *Electrochim. Acta* **2008**, *53*, 7012-7021.
- [85] H. Zhu, S. Zhang, Y.-X. Huang, L. Wu, S. Sun, *Nano Lett.* **2013**, *13*, 2947-2951.

- [86] a)K. Sasaki, L. Zhang, R. R. Adzic, *Phys. Chem. Chem. Phys.* **2008**, *10*, 159-167; b)G. Wu, M. A. Nelson, N. H. Mack, S. Ma, P. Sekhar, F. H. Garzon, P. Zelenay, *Chem. Commun.* **2010**, *46*, 7489-7491.
- [87] R. F. Savinell, *Nat Chem* **2011**, *3*, 501-502.
- [88] A. Grimaud, K. J. May, C. E. Carlton, Y.-L. Lee, M. Risch, W. T. Hong, J. Zhou, Y. Shao-Horn, *Nat Commun* **2013**, *4*.
- [89] J. Suntivich, H. A. Gasteiger, N. Yabuuchi, H. Nakanishi, J. B. Goodenough, Y. Shao-Horn, *Nat Chem* **2011**, *3*, 546-550.
- [90] C. P. Jijil, S. M. Unni, K. Sreekumar, R. N. Devi, *Chem. Mater.* **2012**, *24*, 2823-2828.
- [91] C. P. Jijil, S. N. Bhange, S. Kurungot, R. N. Devi, *ACS Appl. Mater. Inter.* **2015**, *7*, 3041-3049.
- [92] a)M.-R. Gao, Y.-F. Xu, J. Jiang, S.-H. Yu, *Chem. Soc. Rev.* **2013**, *42*, 2986-3017; b)M.-R. Gao, X. Cao, Q. Gao, Y.-F. Xu, Y.-R. Zheng, J. Jiang, S.-H. Yu, *ACS Nano* **2014**, *8*, 3970-3978; c)M.-R. Gao, Q. Gao, J. Jiang, C.-H. Cui, W.-T. Yao, S.-H. Yu, *Angew. Chem. Int. Ed.* **2011**, *50*, 4905-4908; d)M.-R. Gao, J. Jiang, S.-H. Yu, *Small* **2012**, *8*, 12-12; e)M.-R. Gao, J.-X. Liang, Y.-R. Zheng, Y.-F. Xu, J. Jiang, Q. Gao, J. Li, S.-H. Yu, *Nat Commun* **2015**, *6*; f)M.-R. Gao, Z.-Y. Lin, T.-T. Zhuang, J. Jiang, Y.-F. Xu, Y.-R. Zheng, S.-H. Yu, *J. Mater. Chem.* **2012**, *22*, 13662-13668.
- [93] a)Y. Feng, N. Alonso-Vante, *Electrochimi. Acta* **2012**, *72*, 129-133; b)Y. Feng, A. Gago, L. Timperman, N. Alonso-Vante, *Electrochimi. Acta* **2011**, *56*, 1009-1022; c)Y. Feng, T. He, N. Alonso-Vante, *Electrochimi. Acta* **2009**, *54*, 5252-5256; d)Y. J. Feng, T. He, N. Alonso-Vante, *Fuel Cells* **2010**, *10*, 77-83; e)A. S. Gago, Y. Gochi-Ponce, Y.-J. Feng, J. P. Esquivel, N. Sabaté, J. Santander, N. Alonso-Vante, *ChemSusChem* **2012**, *5*, 1488-1494.
- [94] a)H. Wang, Y. Liang, Y. Li, H. Dai, *Angew. Chem. Int. Ed.* **2011**, *50*, 10969-10972; b)P. Ganesan, M. Prabu, J. Sanetuntikul, S. Shanmugam, *ACS Catal.* **2015**, *5*, 3625-3637.
- [95] G. Wu, H. T. Chung, M. Nelson, K. Artyushkova, K. L. More, C. M. Johnston, P. Zelenay, *ECS Transactions* **2011**, *41*, 1709-1717.
- [96] R. A. Sidik, A. B. Anderson, *J. Phys. Chem. B* **2006**, *110*, 936-941.

- [97] Y. Hu, J. O. Jensen, W. Zhang, L. N. Cleemann, W. Xing, N. J. Bjerrum, Q. Li, *Angew. Chem. Int. Ed.* **2014**, *53*, 3675-3679.
- [98] a)X. Zhong, L. Liu, Y. Jiang, X. Wang, L. Wang, G. Zhuang, X. Li, D. Mei, J.-g. Wang, D. S. Su, *ChemCatChem* **2015**, *7*, 1826-1832; b)B. Cao, J. C. Neufeind, R. R. Adzic, P. G. Khalifah, *Inorganic Chemistry* **2015**, *54*, 2128-2136; c)B. Cao, G. M. Veith, J. C. Neufeind, R. R. Adzic, P. G. Khalifah, *J. Am. Chem. Soc.* **2013**, *135*, 19186-19192; d)Y. Wu, Q. Shi, Y. Li, Z. Lai, H. Yu, H. Wang, F. Peng, *J. Mater. Chem. A* **2015**, *3*, 1142-1151.
- [99] a)S. Doi, A. Ishihara, S. Mitsushima, N. Kamiya, K.-i. Ota, *J. Electrochem. Soc.* **2007**, *154*, B362-B369; b)B. Cao, G. M. Veith, R. E. Diaz, J. Liu, E. A. Stach, R. R. Adzic, P. G. Khalifah, *Angew. Chem. Int. Ed.* **2013**, *52*, 10753-10757; c)A. Ishihara, K. Lee, S. Doi, S. Mitsushima, N. Kamiya, M. Hara, K. Domen, K. Fukuda, K.-i. Ota, *Electrochemical and Solid-State Letters* **2005**, *8*, A201-A203.
- [100] A. R. Ko, Y.-W. Lee, J.-S. Moon, S.-B. Han, G. Cao, K.-W. Park, *Applied Catalysis A: General* **2014**, *477*, 102-108.
- [101] Y. Hou, T. Huang, Z. Wen, S. Mao, S. Cui, J. Chen, *Adv. Energy Mater.* **2014**, *4*, DOI:10.1002/aenm.201400337.
- [102] Z. Wen, S. Ci, F. Zhang, X. Feng, S. Cui, S. Mao, S. Luo, Z. He, J. Chen, *Adv. Mater.* **2012**, *24*, 1399-1404.
- [103] R. Jasinski, *Nature* **1964**, *201*, 1212-1213.
- [104] E. Yeager, *Electrochim. Acta* **1984**, *29*, 1527-1537.
- [105] a)A. Morozan, B. Josselme, S. Palacin, *Energy Environ. Sci.* **2011**, *4*, 1238-1254; b)Z. Chen, D. Higgins, A. Yu, L. Zhang, J. Zhang, *Energy Environ. Sci.* **2011**, *4*, 3167-3192; c)F. Jaouen, E. Proietti, M. Lefevre, R. Chenitz, J.-P. Dodelet, G. Wu, H. T. Chung, C. M. Johnston, P. Zelenay, *Energy Environ. Sci.* **2011**, *4*, 114-130; d)D.-W. Wang, D. Su, *Energy Environ. Sci.* **2014**, *7*, 576-591.
- [106] M. Lefèvre, E. Proietti, F. Jaouen, J.-P. Dodelet, *Science* **2009**, *324*, 71-74.
- [107] E. Proietti, F. Jaouen, M. Lefèvre, N. Larouche, J. Tian, J. Herranz, J.-P. Dodelet, *Nat Commun* **2011**, *2*, 416.
- [108] G. Wu, K. L. More, C. M. Johnston, P. Zelenay, *Science* **2011**, *332*, 443-447.
- [109] [http://www.hydrogen.energy.gov/pdfs/progress14/v\\_a\\_11\\_zelenay\\_2014.pdf](http://www.hydrogen.energy.gov/pdfs/progress14/v_a_11_zelenay_2014.pdf).
- [110] F. Jaouen, S. Marcotte, J.-P. Dodelet, G. Lindbergh, *J. Phys. Chem. B* **2003**, *107*, 1376-1386.

- [111] a)U. I. Kramm, J. Herranz, N. Larouche, T. M. Arruda, M. Lefevre, F. Jaouen, P. Bogdanoff, S. Fiechter, I. Abs-Wurmbach, S. Mukerjee, J.-P. Dodelet, *Phys. Chem. Chem. Phys.* **2012**, *14*, 11673-11688; b)U. I. Kramm, I. Abs-Wurmbach, I. Herrmann-Geppert, J. Radnik, S. Fiechter, P. Bogdanoff, *J. Electrochem. Soc.* **2011**, *158*, B69-B78.
- [112] X. Chen, S. Sun, X. Wang, F. Li, D. Xia, *J. Phy. Chem. C* **2012**, *116*, 22737-22742.
- [113] J. Zhang, Z. Wang, Z. Zhu, Q. Wang, *J. Electrochem. Soc.* **2015**, *162*, F796-F801.
- [114] K. Strickland, E. Miner, Q. Jia, U. Tylus, N. Ramaswamy, W. Liang, M.-T. Sougrati, F. Jaouen, S. Mukerjee, *Nat Commun* **2015**, *6*.
- [115] Y. Li, W. Zhou, H. Wang, L. Xie, Y. Liang, F. Wei, J.-C. Idrobo, S. J. Pennycook, H. Dai, *Nat Nano* **2012**, *7*, 394-400.
- [116] H. T. Chung, J. H. Won, P. Zelenay, *Nat Commun* **2013**, *4*, 1922.
- [117] a)J. Deng, P. Ren, D. Deng, X. Bao, *Angew. Chem. Int. Ed.* **2015**, DOI: 10.1002/anie.201409524; b)D. Deng, L. Yu, X. Chen, G. Wang, L. Jin, X. Pan, J. Deng, G. Sun, X. Bao, *Angew. Chem. Int. Ed.* **2013**, *52*, 371-375; c)X. Zheng, J. Deng, N. Wang, D. Deng, W.-H. Zhang, X. Bao, C. Li, *Angew. Chem. Int. Ed.* **2014**, *53*, 7023-7027.
- [118] Q. Li, P. Xu, W. Gao, S. Ma, G. Zhang, R. Cao, J. Cho, H.-L. Wang, G. Wu, *Adv. Mater.* **2014**, *26*, 1378-1386.
- [119] W. Yang, X. Liu, X. Yue, J. Jia, S. Guo, *J. Am. Chem. Soc.* **2015**.
- [120] K. P. Singh, E. J. Bae, J.-S. Yu, *J. Am. Chem. Soc.* **2015**, *137*, 3165-3168.
- [121] F. Razmjooei, K. P. Singh, E. J. Bae, J.-S. Yu, *J. Mater. Chem. A* **2015**, *3*, 11031-11039.
- [122] a)X.-K. Kong, C.-L. Chen, Q.-W. Chen, *Chem. Soc. Rev.* **2014**, *43*, 2841-2857; b)T.-Y. Ma, L. Liu, Z.-Y. Yuan, *Chem. Soc. Rev.* **2013**, *42*, 3977-4003; c)X. Wang, G. Sun, P. Routh, D.-H. Kim, W. Huang, P. Chen, *Chem. Soc. Rev.* **2014**, *43*, 7067-7098; d)Y. Yan, J. Miao, Z. Yang, F.-X. Xiao, H. B. Yang, B. Liu, Y. Yang, *Chem. Soc. Rev.* **2015**, *44*, 3295-3346; e)J. P. Paraknowitsch, A. Thomas, *Energy Environ. Sci.* **2013**, *6*, 2839-2855; f)K. N. Wood, R. O'Hayre, S. Pylypenko, *Energy Environ. Sci.* **2014**, *7*, 1212-1249; g)N. Daems, X. Sheng, I. F. J. Vankelecom, P. P. Pescarmona, *J. Mater. Chem. A* **2014**, *2*, 4085-4110.
- [123] L. Dai, Y. Xue, L. Qu, H.-J. Choi, J.-B. Baek, *Chem. Rev.* **2015**, *115*, 4823-4892.

- [124] in *Nanostructured Carbon Materials for Catalysis*, The Royal Society of Chemistry, **2015**, pp. 268-311.
- [125] J. Campos-Delgado, I. O. Maciel, D. A. Cullen, D. J. Smith, A. Jorio, M. A. Pimenta, H. Terrones, M. Terrones, *ACS Nano* **2010**, *4*, 1696-1702.
- [126] K. Gong, F. Du, Z. Xia, M. Durstock, L. Dai, *Science* **2009**, *323*, 760-764.
- [127] J. Shui, M. Wang, F. Du, L. Dai, *N-doped carbon nanomaterials are durable catalysts for oxygen reduction reaction in acidic fuel cells, Vol. 1*, **2015**.
- [128] L. Qu, Y. Liu, J.-B. Baek, L. Dai, *ACS Nano* **2010**, *4*, 1321-1326.
- [129] D. Deng, X. Pan, L. Yu, Y. Cui, Y. Jiang, J. Qi, W.-X. Li, Q. Fu, X. Ma, Q. Xue, G. Sun, X. Bao, *Chem. Mater.* **2011**, *23*, 1188-1193.
- [130] D. Mhamane, A. Suryawanshi, S. M. Unni, C. Rode, S. Kurungot, S. Ogale, *Small* **2013**, *9*, 2801-2809.
- [131] a)D. W. Chang, H.-J. Choi, J.-B. Baek, *J. Mater. Chem. A* **2015**, *3*, 7659-7665; b)I.-Y. Jeon, H.-J. Choi, M. J. Ju, I. T. Choi, K. Lim, J. Ko, H. K. Kim, J. C. Kim, J.-J. Lee, D. Shin, S.-M. Jung, J.-M. Seo, M.-J. Kim, N. Park, L. Dai, J.-B. Baek, *Sci. Rep.* **2013**, *3*; c)I.-Y. Jeon, H.-J. Choi, S.-M. Jung, J.-M. Seo, M.-J. Kim, L. Dai, J.-B. Baek, *J. Am. Chem. Soc.* **2013**, *135*, 1386-1393.
- [132] Z.-H. Sheng, L. Shao, J.-J. Chen, W.-J. Bao, F.-B. Wang, X.-H. Xia, *ACS Nano* **2011**, *5*, 4350-4358.
- [133] Y. Li, Y. Zhao, H. Cheng, Y. Hu, G. Shi, L. Dai, L. Qu, *J. Am. Chem. Soc.* **2012**, *134*, 15-18.
- [134] H.-W. Liang, X. Zhuang, S. Brüller, X. Feng, K. Müllen, *Nat Commun* **2014**, *5*.
- [135] Y. Zhao, C. Hu, Y. Hu, H. Cheng, G. Shi, L. Qu, *Angew. Chem. Int. Ed.* **2012**, *51*, 11371-11375.
- [136] Y. Zheng, J. Liu, J. Liang, M. Jaroniec, S. Z. Qiao, *Energy Environ. Sci.* **2012**, *5*, 6717-6731.
- [137] Y. Zheng, Y. Jiao, J. Chen, J. Liu, J. Liang, A. Du, W. Zhang, Z. Zhu, S. C. Smith, M. Jaroniec, G. Q. Lu, S. Z. Qiao, *J. Am. Chem. Soc.* **2011**, *133*, 20116-20119.
- [138] X. Liu, Y. Zhou, W. Zhou, L. Li, S. Huang, S. Chen, *Nanoscale* **2015**, *7*, 6136-6142.
- [139] a)S. Pandiaraj, H. B. Aiyappa, R. Banerjee, S. Kurungot, *Chem. Commun.* **2014**, *50*, 3363-3366; b)Z. Xiang, D. Wang, Y. Xue, L. Dai, J.-F. Chen, D. Cao, *Sci. Rep.* **2015**, *5*.



- [140] a)R. Silva, D. Voiry, M. Chhowalla, T. Asefa, *J. Am. Chem. Soc.* **2013**, *135*, 7823-7826; b)A. Filer, H.-J. Choi, J.-M. Seo, J.-B. Baek, *Phys. Chem. Chem. Phys.* **2014**, *16*, 11150-11161.
- [141] J. B. Xu, T. S. Zhao, *RSC Adv.* **2013**, *3*, 16-24.
- [142] P. Redlich, J. Loeffler, P. M. Ajayan, J. Bill, F. Aldinger, M. Rühle, *Chemical Physics Letters* **1996**, *260*, 465-470.
- [143] W. K. Hsu, S. Firth, P. Redlich, M. Terrones, H. Terrones, Y. Q. Zhu, N. Grobert, A. Schilder, R. J. H. Clark, H. W. Kroto, D. R. M. Walton, *J. Mater. Chem.* **2000**, *10*, 1425-1429.
- [144] Z.-H. Sheng, H.-L. Gao, W.-J. Bao, F.-B. Wang, X.-H. Xia, *J. Mater. Chem.* **2012**, *22*, 390-395.
- [145] L. Wang, Z. Sofer, P. Šimek, I. Tomandl, M. Pumera, *J. Phy. Chem. C* **2013**, *117*, 23251-23257.
- [146] Z. Yang, Z. Yao, G. Li, G. Fang, H. Nie, Z. Liu, X. Zhou, X. a. Chen, S. Huang, *ACS Nano* **2012**, *6*, 205-211.
- [147] S. Yang, L. Zhi, K. Tang, X. Feng, J. Maier, K. Müllen, *Adv. Function. Mater.* **2012**, *22*, 3634-3640.
- [148] J. Xu, J. Shui, J. Wang, M. Wang, H.-K. Liu, S. X. Dou, I.-Y. Jeon, J.-M. Seo, J.-B. Baek, L. Dai, *ACS Nano* **2014**, *8*, 10920-10930.
- [149] H. L. Poh, P. Šimek, Z. Sofer, M. Pumera, *ACS Nano* **2013**, *7*, 5262-5272.
- [150] W. Kiciński, M. Szala, M. Bystrzejewski, *Carbon* **2014**, *68*, 1-32.
- [151] Z.-W. Liu, F. Peng, H.-J. Wang, H. Yu, W.-X. Zheng, J. Yang, *Angew. Chem. Int. Ed.* **2011**, *50*, 3257-3261.
- [152] a)J. Wu, C. Jin, Z. Yang, J. Tian, R. Yang, *Carbon* **2015**, *82*, 562-571; b)D. G. Larrude, M. E. H. Maia da Costa, F. H. Monteiro, A. L. Pinto, F. L. Freire, *Journal of Applied Physics* **2012**, *111*, 064315.
- [153] I.-Y. Jeon, H.-J. Choi, M. Choi, J.-M. Seo, S.-M. Jung, M.-J. Kim, S. Zhang, L. Zhang, Z. Xia, L. Dai, N. Park, J.-B. Baek, *Sci. Rep.* **2013**, *3*.
- [154] B. Shen, J. Chen, X. Yan, Q. Xue, *RSC Adv.* **2012**, *2*, 6761-6764.
- [155] X. Sun, Y. Zhang, P. Song, J. Pan, L. Zhuang, W. Xu, W. Xing, *ACS Catal.* **2013**, *3*, 1726-1729.
- [156] Z. Yao, H. Nie, Z. Yang, X. Zhou, Z. Liu, S. Huang, *Chem. Commun.* **2012**, *48*, 1027-1029.

- [157] I.-Y. Jeon, M. Choi, H.-J. Choi, S.-M. Jung, M.-J. Kim, J.-M. Seo, S.-Y. Bae, S. Yoo, G. Kim, H. Y. Jeong, N. Park, J.-B. Baek, *Nat Commun* **2015**, *6*.
- [158] S. Wang, E. Iyyamperumal, A. Roy, Y. Xue, D. Yu, L. Dai, *Angew. Chem. Int. Ed.* **2011**, *50*, 11756-11760.
- [159] H. R. Zhang, E. J. Liang, P. Ding, Z. L. Du, X. Y. Guo, *Acta Phys. Sin.-Ch. Ed.* **2002**, *51*.
- [160] S. Wang, L. Zhang, Z. Xia, A. Roy, D. W. Chang, J.-B. Baek, L. Dai, *Angew. Chem. Int. Ed.* **2012**, *51*, 4209-4212.
- [161] J.-i. Ozaki, T. Anahara, N. Kimura, A. Oya, *Carbon* **2006**, *44*, 3358-3361.
- [162] L. Yang, S. Jiang, Y. Zhao, L. Zhu, S. Chen, X. Wang, Q. Wu, J. Ma, Y. Ma, Z. Hu, *Angew. Chem. Int. Ed.* **2011**, *50*, 7132-7135.
- [163] J. Liang, Y. Jiao, M. Jaroniec, S. Z. Qiao, *Angew. Chem. Int. Ed.* **2012**, *51*, 11496-11500.
- [164] J. Xu, G. Dong, C. Jin, M. Huang, L. Guan, *ChemSusChem* **2013**, *6*, 493-499.
- [165] a) S.-A. Wohlgemuth, R. J. White, M.-G. Willinger, M.-M. Titirici, M. Antonietti, *Green Chemistry* **2012**, *14*, 1515-1523; b) Z. Liu, H. Nie, Z. Yang, J. Zhang, Z. Jin, Y. Lu, Z. Xiao, S. Huang, *Nanoscale* **2013**, *5*, 3283-3288.
- [166] C. H. Choi, S. H. Park, S. I. Woo, *ACS Nano* **2012**, *6*, 7084-7091.
- [167] J. Zhang, Z. Zhao, Z. Xia, L. Dai, *Nat Nano* **2015**, *10*, 444-452.
- [168] C. H. Choi, S. H. Park, S. I. Woo, *J. Mater. Chem.* **2012**, *22*, 12107-12115.
- [169] C. H. Choi, M. W. Chung, S. H. Park, S. I. Woo, *Phys. Chem. Chem. Phys.* **2013**, *15*, 1802-1805.
- [170] S. Zhao, J. Liu, C. Li, W. Ji, M. Yang, H. Huang, Y. Liu, Z. Kang, *ACS Appl. Mater. Inter.* **2014**, *6*, 22297-22304.
- [171] J.-S. Li, S.-L. Li, Y.-J. Tang, K. Li, L. Zhou, N. Kong, Y.-Q. Lan, J.-C. Bao, Z.-H. Dai, *Sci. Rep.* **2014**, *4*.
- [172] J. D. Wiggins-Camacho, K. J. Stevenson, *J. Phy. Chem. C* **2009**, *113*, 19082-19090.
- [173] J. D. Wiggins-Camacho, K. J. Stevenson, *J. Phy. Chem. C* **2011**, *115*, 20002-20010.
- [174] S. Yasuda, L. Yu, J. Kim, K. Murakoshi, *Chem. Commun.* **2013**, *49*, 9627-9629.
- [175] L. Lai, J. R. Potts, D. Zhan, L. Wang, C. K. Poh, C. Tang, H. Gong, Z. Shen, J. Lin, R. S. Ruoff, *Energy Environ. Sci.* **2012**, *5*, 7936-7942.

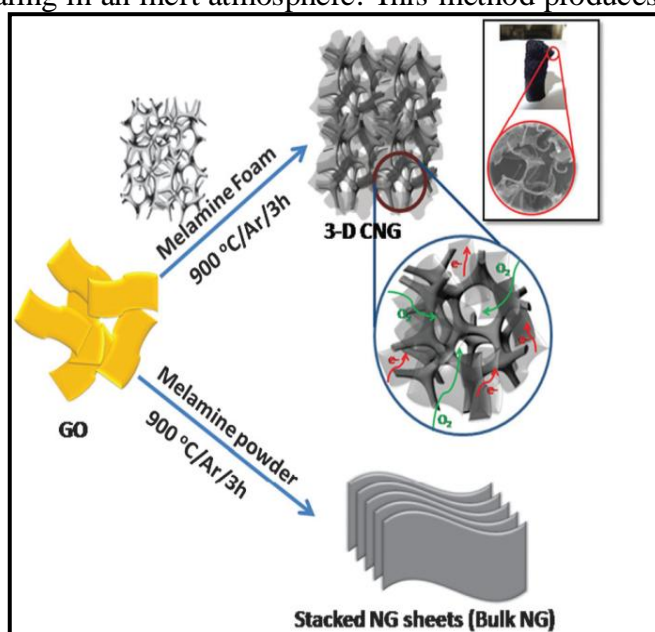
- [176] W. Ding, Z. Wei, S. Chen, X. Qi, T. Yang, J. Hu, D. Wang, L.-J. Wan, S. F. Alvi, L. Li, *Angew. Chem. Int. Ed.* **2013**, *52*, 11755-11759.
- [177] a) Q. Yang, C. B. Wang, S. Zhang, D. M. Zhang, Q. Shen, L. M. Zhang, *Surface and Coatings Technology* **2010**, *204*, 1863-1867; b) S. Ni, Z. Li, J. Yang, *Nanoscale* **2012**, *4*, 1184-1189.
- [178] L. Zhang, Z. Xia, *J. Phy. Chem. C* **2011**, *115*, 11170-11176.
- [179] L. Yu, X. Pan, X. Cao, P. Hu, X. Bao, *J. Catal.* **2011**, *282*, 183-190.



## Chapter 2

### *Nitrogen doped graphene based electrocatalysts for oxygen reduction reaction\**

This chapter deals with two viable strategies by which graphene can be converted into potential oxygen reduction electrocatalysts through nitrogen doping. Two different approaches are adopted with an aim to enhance the number density of the active sites for facilitating oxygen reduction reaction (ORR) in nitrogen doped graphene (NNG). The first half of the chapter describes the synthesis of NNG through pyrrole mediated reduction of graphene oxide (GO) followed by annealing in an inert atmosphere. This method produces NNG with a surface area of  $528 \text{ m}^2 \text{ g}^{-1}$ . This material shows significantly improved positive onset potential for oxygen reduction, which is found to be even higher than that of the commercial Pt/C. XPS analysis reveals the presence of higher percentage of pyrrolic coordination which in turn is responsible for the enhanced activity of the system towards ORR in alkaline medium. NNG also displays excellent electrochemical stability and fuel tolerance. The second half of the chapter deals with a strategy by which simultaneous nitrogen doping and wrapping of the nitrogen doped graphene sheets on carbon nitride tetrapods could be achieved. This is accomplished by dip-coating of GO on melamine foam followed by annealing at high temperature, which helps to produce three dimensional (3D) NNG wrapped carbon nitride tetrapods (CNG). This morphology assists the systems to attain efficient reactant distribution with more accessible surface and active sites. This material shows promising ORR activity in acidic condition with an overpotential of 100 mV compared to Pt/C. Moreover, the prepared CNG samples display excellent electrochemical stability and methanol tolerance.



\*Contents of this chapter were published in the following journals:

S M Unni *et al.*, J. Mater. Chem., 2012, 22, 23506-23513

S M Unni *et al.*, Chem. Commun., 2014, 50, 13769 – 13772

## 2.1 Introduction

In the quest for developing non-metal electrocatalysts for low temperature polymer electrolyte membrane fuel cells (PEMFCs), graphene and its derivatives are envisioned as promising candidates for replacing platinum and non-platinum metal catalysts from the cathode. In terms of electrochemical stability and conductivity, graphene fulfils the requirements that are essential for electrodes in PEMFCs.<sup>[1]</sup> However, its physico-chemical properties are strongly affected and influenced by its mode of preparation. Graphene oxide (GO) reduction is widely adopted to prepare graphene not only because the process is simple but it also provides benefits from efficient interactions between the surface and the reacting moieties.<sup>[2]</sup> However, in most cases, the extent of reduction of GO can be partial. As a result of this, the reduced graphene oxide (RGO) lacks the required electrical conductivity which is essential for most energy devices including PEMFCs.<sup>[3]</sup> Among the different methods available to improve the conductivity of graphene, heteroatom doping is considered as an important strategy because it tunes the electronic charge density of carbon in the graphene matrix.<sup>[4]</sup> Also, many reports are recently available on the doping of nitrogen, phosphorus, boron, iodine, sulphur etc. into the graphene matrix as a viable strategy to enhance the electrocatalytic activity of the material towards oxygen reduction reaction (ORR).<sup>[4b, 4c]</sup> In view of the unaffordable cost of Pt, there exists tremendous curiosity in exploring the potential applications of such materials as cathodes for PEMFCs.

Recently, there has been a significant emphasis on developing nitrogen-doped graphene (NGE).<sup>[4a]</sup> Nitrogen, owing to its higher electronegativity, is expected to change the electron density of carbon. This in turn can broaden the commercial prospects of graphene as a candidate for applications involving PEMFCs, solar cells, supercapacitors and sensors.<sup>[4a]</sup> Many reports are available on different routes to prepare NGE. Chemical vapour deposition (CVD),<sup>[5]</sup> arc discharge,<sup>[6]</sup> nitrogen plasma treatment,<sup>[7]</sup> heat treatment of GO in presence of some nitrogen containing molecules,<sup>[8]</sup> wet chemical synthesis<sup>[9]</sup> etc. are some of the common methods for preparing NGE. However, most of these methods give NGE with much less surface area and content of the doped nitrogen. Different synthesis routes also affect atom percentage of different types of nitrogen coordinations such as pyridinic, pyrrolic and graphitic in the graphene framework which are responsible for creating different functionalities on graphene.<sup>[10]</sup> It is well known that pyridinic, pyrrolic and graphitic nitrogen contents in the graphene sheet enhance the ORR activity of

the system.<sup>[11]</sup> However, recent studies reveal that the pyrrolic and pyridinic forms are reported to be the preferred co-ordinations of nitrogen due to their comparatively higher influence in reducing the overpotential for oxygen reduction.<sup>[12]</sup> On the other hand, it has been identified that the pyridinic coordination of nitrogen alone cannot induce effective ORR activity because graphene with pyridinic nitrogen follows a two electron transfer mechanism rather than the preferred four electron transfer for the reaction.<sup>[13]</sup> Also, the stability of the pyridinic nitrogen in the nitrogen-doped graphene is relatively lower at higher temperatures.<sup>[14]</sup> Apart from the preferred coordination of nitrogen atoms in NGE, the arrangement of graphene sheets in a three dimensional manner also plays a crucial role for the proper accessing of the reactant species to the active reaction centre. Usually, chemically synthesised NGE sheets form a stacked configuration and reduce efficient mass transport of reactant gasses. This may cause the reduction in ORR activity even though more active reaction centre present on it. Therefore, it is important to develop appropriate synthetic methodologies for NGE with high surface area, more reactant accessible path and maximum active reaction centre density by modifying/controlling the preferred nitrogen coordinations for effective dioxygen chemisorption and its binding.

First half (*Part A*) of the chapter discloses NGE preparation through a mutually assisted redox reaction between GO and pyrrole followed by thermal treatment under an inert atmosphere. NGE obtained after the heat treatment of the reduced graphene oxide using pyrrole has displayed a matching oxygen reduction onset potential to that of the commercial 40 wt. % Pt/C. The redox reaction between GO and pyrrole also helps to attain almost complete reduction of GO to graphene (GEPPy) without the intervention of any additional reducing agent. Also, oligomeric form of pyrrole prevents the restacking of graphene sheets and helps to attain high surface area.

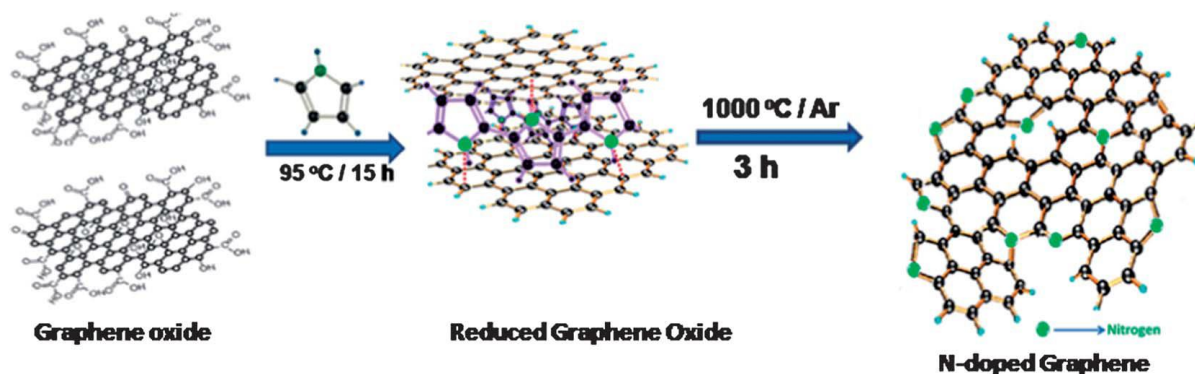
Second half (*Part B*) of the chapter discloses the synthesis of 3-dimensionally (3D) interconnected carbon nitride (CN<sub>x</sub>) tetrapods wrapped with NGE (CNG) through a one-step process, which shows significant ORR activity in acidic/alkaline medium. Dip-coating of melamine foam (MF) with graphene oxide (GO) followed by high temperature annealing in an inert atmosphere converts the melamine foam to a 3D CN<sub>x</sub> framework and GO to graphene respectively, in a well-separated and wrapped state along the tetrapod arms. The nitrogen moieties liberated from MF are trapped by the graphene sheets, which subsequently are doped into the graphene matrix, thereby creating more active sites for oxygen adsorption and its reduction.

## Part A: Nitrogen doped graphene from pyrrole mediated reduced graphene oxide for ORR\*

### 2A.1 Experimental

#### 2A.1.1 Preparation of pyrrole reduced graphene oxide

Graphene oxide (GO) was synthesised using an improved oxidation process.<sup>[15]</sup> In a typical synthesis, 3 g of graphite was mixed well with the required amount of  $\text{KMnO}_4$ . This was then added slowly into a 9:1 mixture of con.  $\text{H}_2\text{SO}_4$  and con.  $\text{H}_3\text{PO}_4$ . Stirring was continued overnight while the temperature was maintained at  $55^\circ\text{C}$ . The resultant solution was poured into ice cooled water containing 3%  $\text{H}_2\text{O}_2$ . A yellow precipitate was formed and this was sequentially washed well with deionised water, 30%  $\text{HCl}$ , ethanol and ether. The precipitate collected after the washing process was allowed to dry at room temperature and the GO obtained in this process was used as such for further studies. The reduced graphene oxide possessing a thin layer of the oxidized products of pyrrole (hereinafter called GEPPy) was prepared from GO by using pyrrole as the reducing agent.



*Scheme 2A.1: Synthesis of nitrogen-doped graphene (NGE).*

In a typical synthesis,<sup>[16]</sup> 100 mg of GO was well dispersed in 100 ml of deionised water (DI water) followed by the addition of 2 ml of the pyrrole monomer (Aldrich). The resulting solution was refluxed for 15 h at  $95^\circ\text{C}$  (Scheme 1). After completion of the reaction, the resulting black solution was filtered using 0.45 mm pore sized PTFE filter paper and the wet cake was washed successively with ethanol, water and dimethyl acetamide to remove unreacted pyrrole monomer and oligomers. The black powder obtained after the filtration was dried in a vacuum oven for 3 h at  $100^\circ\text{C}$ . GEPPy obtained at this stage was used for preparing various NGE samples.

\* Reproduced with permission from Royal Society of Chemistry, Copy right 2012(J. Mater. Chem. 2012, 22, 23506-23513)



### 2A.1.2 Preparation of NGE

NGE was prepared by simple heat treatment of the reduced graphene oxide, which has oxidized products of pyrrole anchored on the surface, in an argon atmosphere at different heating temperatures such as 700, 800, 900 and 1000 °C. The corresponding NGE samples are designated respectively as NGE-700, NGE-800, NGE-900 and NGE-1000. NGE-1000 has been used as the representative material for most of the basic property characterizations. Since the oxygen reduction activity is strongly a function of the heat treatment temperature, the electrochemical ORR activities of the different heat treated catalysts were individually evaluated.

### 2A.1.3 Structural characterization

PANalytical X'pert Pro instrument was used for recording the X-ray diffraction (XRD) patterns of the prepared catalysts. All data were collected with a scan rate of 0.5° per min using Cu Ka (1.5418 Å) radiation. A High Resolution Transmission Electron Microscope (HR-TEM) FEI model TECNAI G2 F30 instrument operated at an accelerating voltage of 300 kV (Cs = 0.6 mm, resolution 1.7 Å) was used for analysing the structure and morphology of the catalysts. TEM samples were prepared by suspending the prepared catalysts in ethanol and then placing a drop of the suspension on a 200 mesh copper grid coated with carbon film (ICON Analytical). This was subsequently dried under vacuum for overnight and then loaded in the electron microscope chamber. X-ray photoelectron spectroscopy (XPS) was done on a VG Microtech Multilab ESCA 3000 spectrometer that was equipped with an Mg Ka X-ray source ( $h\nu = 1253.6$  eV). Raman analyses of all samples were performed on an HR 800 Raman spectrometer (Jobin Yvon, Horiba, France) using 632.8 nm green laser (NRS 1500 W). The Fourier transform IR spectra were taken using a Bruker Alpha model instrument. Surface area analyses were carried out using a Quantachrome Quandraorb automatic volumetric measurement system at 77 K using ultra-pure nitrogen gas. Thermogravimetric analyses were carried out by a Perkin Elmer STA 6000 analyser from 50 to 900 °C with 10 °C min<sup>-1</sup> temperature ramp.

### 2A.1.4 Electrochemical studies

Autolab PGSTAT 30 (Ecochemie) was used for all electrochemical studies with a conventional three-electrode test cell from Pine Instruments. Hg/HgO and Pt wire were used as the reference and counter electrodes, respectively. The working electrode was a

glassy carbon (GC) electrode (5 mm diameter) embedded in Teflon, which was polished on a polishing cloth using 0.3 mm alumina slurry followed by washing with water. The catalyst slurry was prepared as follows. 5 mg of the catalyst was dispersed in 1 ml of ethanol : water (3 : 2) solution by ultrasonication. 10 mL from the prepared slurry was drop casted on the GC electrode with the help of a micro syringe, and 2 mL of 0.1% Nafion<sup>®</sup> solution in ethanol was coated to get a uniform layer and to prevent the detachment of the catalyst. This electrode was further dried using an IR lamp and was used as the working electrode. 0.1 M KOH (Aldrich) was used as the electrolyte for all the cyclic voltammetric (CV), chronoamperometric (CA) and rotating disk electrode (RDE) studies. All the RDE experiments were carried out at a scan rate of 10 mV s<sup>-1</sup>. Chronoamperometric (CA) measurements were carried out at a potential of -0.05 V vs. Hg/HgO. Oxygen and nitrogen were used to achieve oxygen rich and oxygen free environments respectively for the RDE and CV experiments.

## 2A.2 Results and discussion

### 2A.2.1 TEM analysis

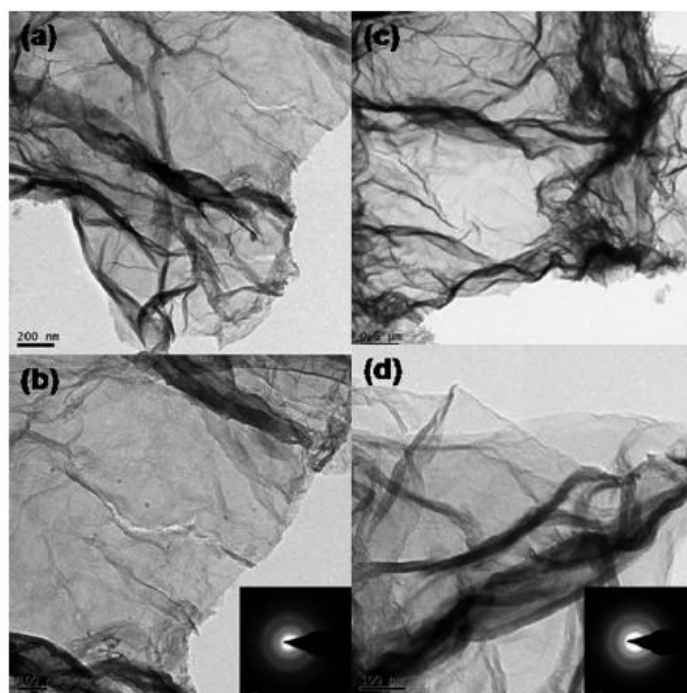


**Figure 2A.1:** TEM images of (a and b) GEPPy and (c and d) NGE-1000. Insets of (b and d) indicate the SAED patterns of the corresponding materials.

Figure 2A.1 (a-b) and Figure 2A.1 (c-d) show respectively the TEM images of GEPPy and NGE-1000. Both the images clearly indicate that the formed graphene sheets have two-dimensional (2-D) buckled morphology with a high surface to volume ratio. The circular pattern of the Selected Area Electron Diffraction (SAED) of GEPPy, as given in the inset of Figure 2A.1(b), clearly depicts the deposition of the oxidized pyrrole molecule on the surface of the graphene sheet. The SAED pattern of the pristine surface of graphene generally gives dotted patterns indicating both the crystalline nature and presence of the six sided honeycomb lattice of the carbon framework.<sup>[17]</sup> Deviation from the pattern expected from a pristine surface clearly indicates the coverage of the graphene surface by the oxidized pyrrole molecules. Heat treatment of GEPPy induces the nitrogen atoms from the oxidized product of pyrrole to get doped into the graphene sheets, which creates defects on the surface. The doping becomes most effective for oxygen reduction at 1000 °C as can be seen from the later sections. Consequently, the SAED pattern of NGE-1000, as given in the inset of Figure 2A.1(d), also shows a similar circular pattern as that of GEPPy due to the defects created during the doping process.

### 2A.2.2 FT-IR analysis

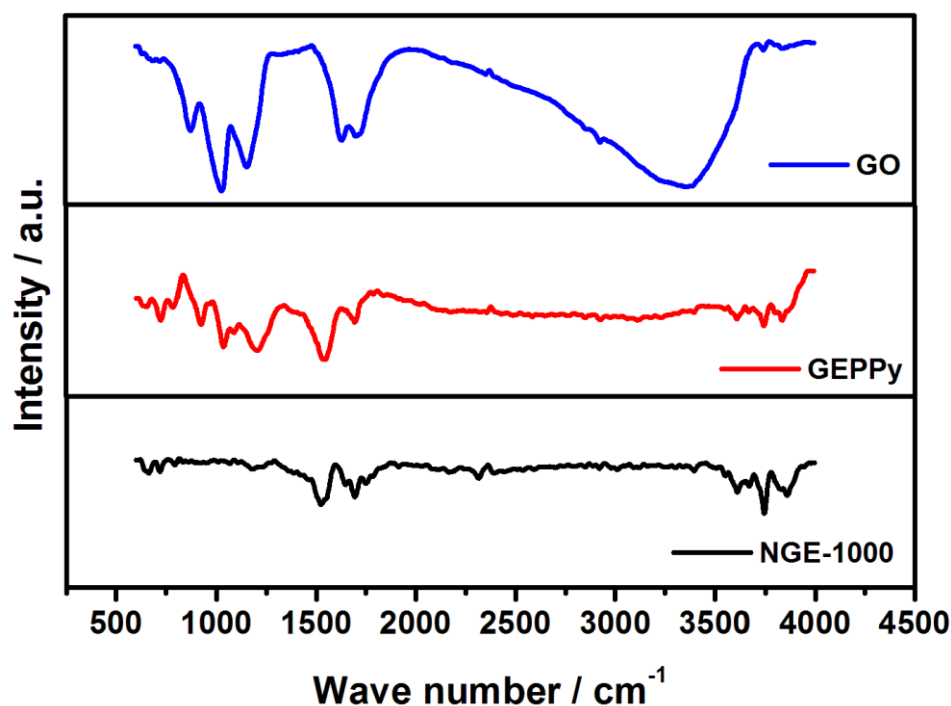


*Figure 2A.2: FTIR spectra of GO, GEPPy and NGE-1000.*

FT-IR spectra (Figure 2A.2) of GO, GEPPy and NGE-1000 clearly give evidence for the reduction of GO using pyrrole followed by nitrogen doping into the carbon framework of graphene during the high temperature heat treatment. GO shows the characteristic peaks corresponding to hydrogen bonded  $\text{-OH}$ ,  $\text{-C=O}$  and  $\text{-C-C-}$  vibrations at  $3357$ ,  $1719$  and  $1612\text{ cm}^{-1}$  respectively. Peaks at  $1151$ ,  $1023$  and  $862\text{ cm}^{-1}$  are related to the vibrations of  $\text{-C-O}$  of ether, alkoxide and epoxide, respectively. Interestingly, the  $\text{-OH}$  stretching and  $\text{-C=O}$  vibrations vanish completely after the reduction using pyrrole and a new peak corresponding to the stretching vibration of the  $\text{-C=C-}$  bond appears at  $1542\text{ cm}^{-1}$ . Peaks at  $956$  and  $790\text{ m}^{-1}$  for pyrrole ring are also observed after the reduction process. The peak at  $1204\text{ cm}^{-1}$  in both GEPPy and NGE-1000 indicates the stretching vibration of the  $\text{-C-N}$  bond. This gives a strong evidence for nitrogen doping into the graphitic framework. Also, at this stage, the characteristic peaks for the pyrrole ring ( $956$  and  $790\text{ cm}^{-1}$ ) vanish due to its decomposition. As another distinct change, the  $\text{-C=C-}$  bond stretching vibration at  $1528\text{ cm}^{-1}$  becomes more prominent after the thermal treatment of GEPPy.<sup>[18]</sup>

### 2A.2.3 TGA analysis

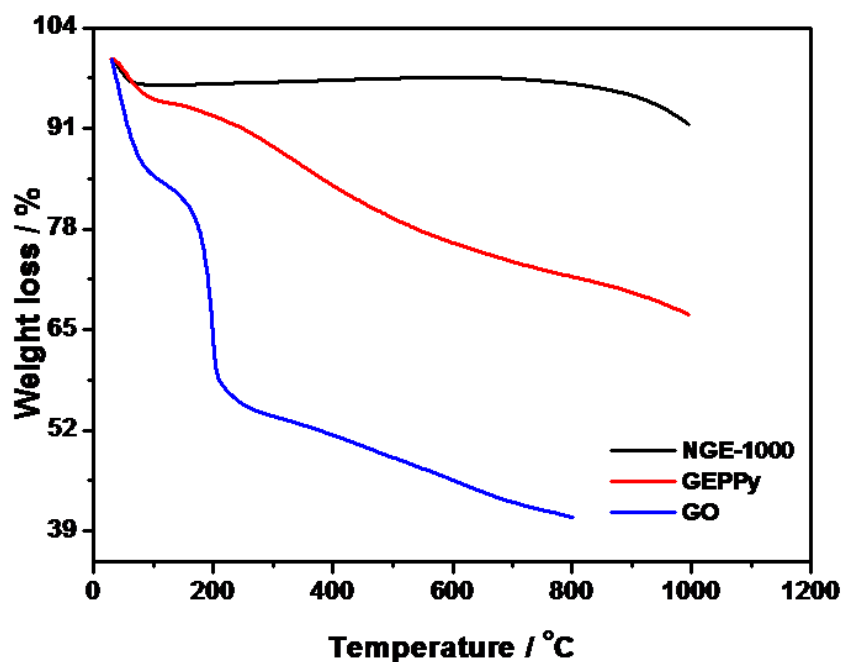


**Figure 2A.3:** Thermogravimetric analysis of GO, GEPPy and NGE-1000 at a temperature range of 25 to 1000 °C by maintaining a heating rate of 10 °C per minute in nitrogen atmosphere.

Thermogravimetric analysis (TGA) gives a direct indication of the level of reduction of graphene oxide and graphitisation at higher temperature. TGA of all the samples is carried out in nitrogen atmosphere at a heating rate of 10 °C per minute and the corresponding TGA profiles are given in Figure 2A.3 It can be seen that GO shows significant weight loss (higher than 60 wt. %) at a temperature slightly more than 100 °C. This is mainly due to the removal of the intercalated water molecules followed by the functional groups such as –COOH as CO and CO<sub>2</sub> from the surface. On the other hand, GEPPy shows only 12 wt. % reduction even up to a higher temperature of 900 °C, indicating the reasonable reduction achieved in GEPPy by the redox reaction between GO and pyrrole. This 12 wt. % weight loss for GEPPy at a higher temperature compared to that in GO can be ascribed to the decomposition of the oxidised pyrrole molecule from the surface of graphene. As expected, in the case of NGE- 1000, only less than 5 wt. % loss is observed even after 900 °C. The higher thermal stability of NGE is mainly due to the better graphitisation and deoxygenation achieved by the system during the thermal treatment process.<sup>[17]</sup>

#### 2A.2.4 Raman analysis

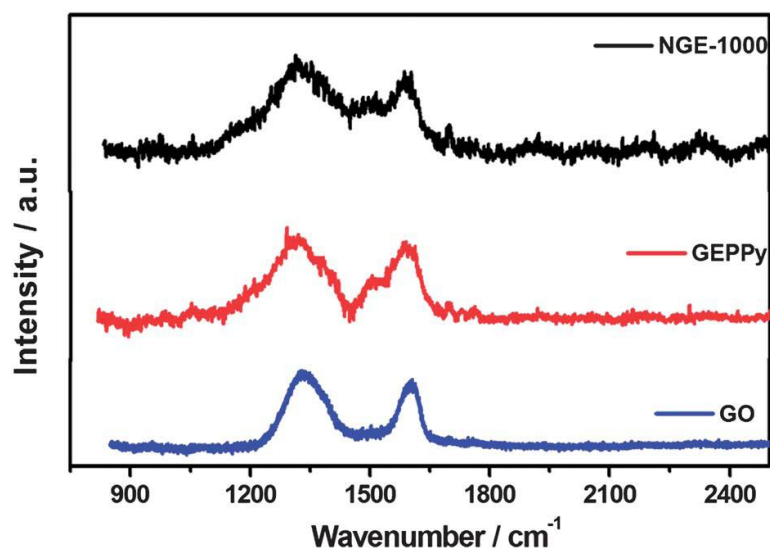


**Figure 2A.4:** Raman spectra of GO, GEPPy and NGE-1000.

The Raman spectrum (Figure 2A.4) of GO displays two peaks at 1327.89 and 1608.32 cm<sup>-1</sup> corresponding to the D- and G-bands respectively.<sup>[19]</sup> On the other hand, the G-band of GEPPy appears at 1587.41 cm<sup>-1</sup>, indicating a recovery of the sp<sup>2</sup> carbon atoms with some apparent defects. Up-shift of the G-band from 1581 cm<sup>-1</sup> (corresponding to

graphite) to  $1587.41\text{ cm}^{-1}$  indicates the charge transfer between the oxidised pyrrole and the graphene layers in GEPPy. The broad band at  $1312.71\text{ cm}^{-1}$  and the bulge at  $1505.15\text{ cm}^{-1}$  confirm the presence of the oxidised products of pyrrole on the surface of graphene.<sup>[16]</sup> The G-band of NGE-1000 appeared at  $1584.41\text{ cm}^{-1}$ , which is close to that of graphite, indicates the major recovery of the hexagonal network of carbon atoms with defects. The ratio of D- and G-band intensities ( $I_D/I_G$ ) is often used to understand the level of chemical modification effected on the surface of graphene. The  $I_D/I_G$  ratios of NGE, GEPPy and GO are respectively 1.24, 1.05 and 1.25. This unambiguously reveals that the reduction of GO to GEPPy leads to an increase of the  $sp^2$  nature of the carbon with some defects on the surface of the graphene sheets. Most importantly, the  $I_D/I_G$  ratio increased as GEPPy was subjected to high temperature heat treatment. This increase in the ratio can be ascribed to the increased defect sites created on graphene upon nitrogen doping. The  $I_D/I_G$  ratio also helps to find out the in plane crystalline size ( $L_a$ ) of the graphene sheets.<sup>[20]</sup> Considering  $L_a$  as an average of the inter defect distances, more defects are expected to create smaller value of  $L_a$ .<sup>[21]</sup> The  $L_a$  value of GO, GEPPy and NGE are 30.75, 36.55 and 30.95 nm respectively. This indicates that the defective sites in the graphene framework are increasing as nitrogen doping takes place in the system.

### 2A.2.5 XRD analysis

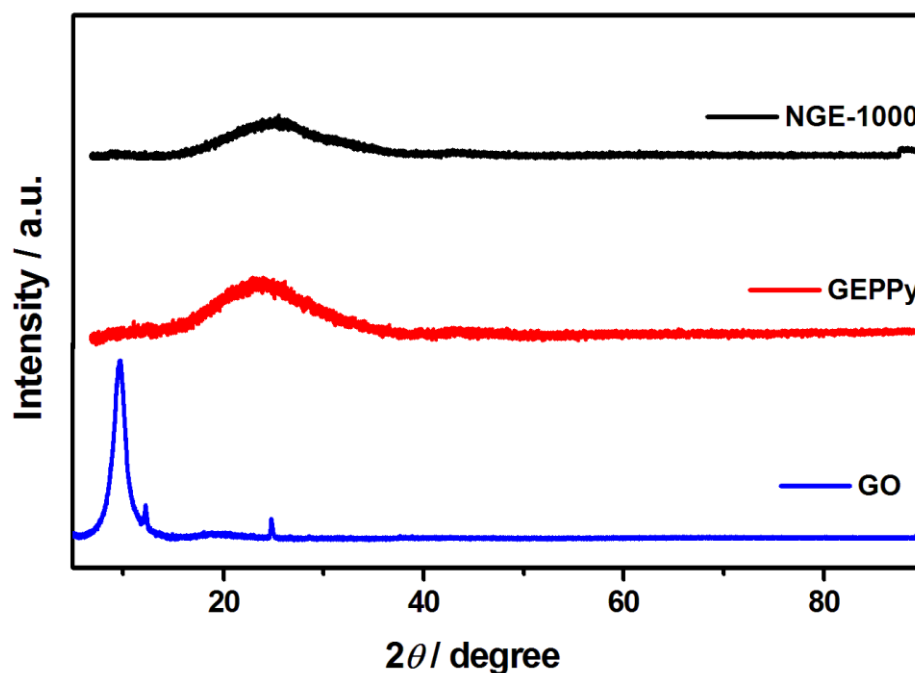


*Figure 2A.5: X-ray diffraction pattern of GO, GEPPy and NGE-1000.*

The powder X-ray diffraction (XRD) of NGE-1000 is compared with that of GEPPy and GO (Figure 2A.5). GO shows a peak at a  $2\theta$  of  $\sim 10^\circ$ , corresponding to a  $d$ -spacing of *ca.* 0.8 nm. After the reduction, the peak corresponding to GO at  $10^\circ$  vanishes and a new broad peak at  $23.4^\circ$  with a  $d$ -spacing of 0.36 nm appears. This indicates the reduction of GO with pyrrole molecules, where most of the  $sp^3$  carbons convert into  $sp^2$  coordination. The  $d$ -spacing of GEPPy is higher compared to graphite (0.33 nm) due to the presence of the attached pyrrole moieties on the surface of the graphene sheets, which is expected to create repulsive force between the neighbouring layers. On the other hand, NGE shows a peak at a  $2\theta$  of  $\sim 2.4^\circ$  higher than GEPPy, leading to a  $d$ -spacing of 0.34 nm which is closer to the  $d$ -spacing of graphite. This indicates the achievement of better graphitization during the process of heat treatment to obtain the NGE samples from their precursor GEPPy. The decrease in the  $d$ -spacing also confirms the degradation of the oxidised pyrrole molecules from the surface of the graphene sheets.

### 2A.2.6 Surface area analysis

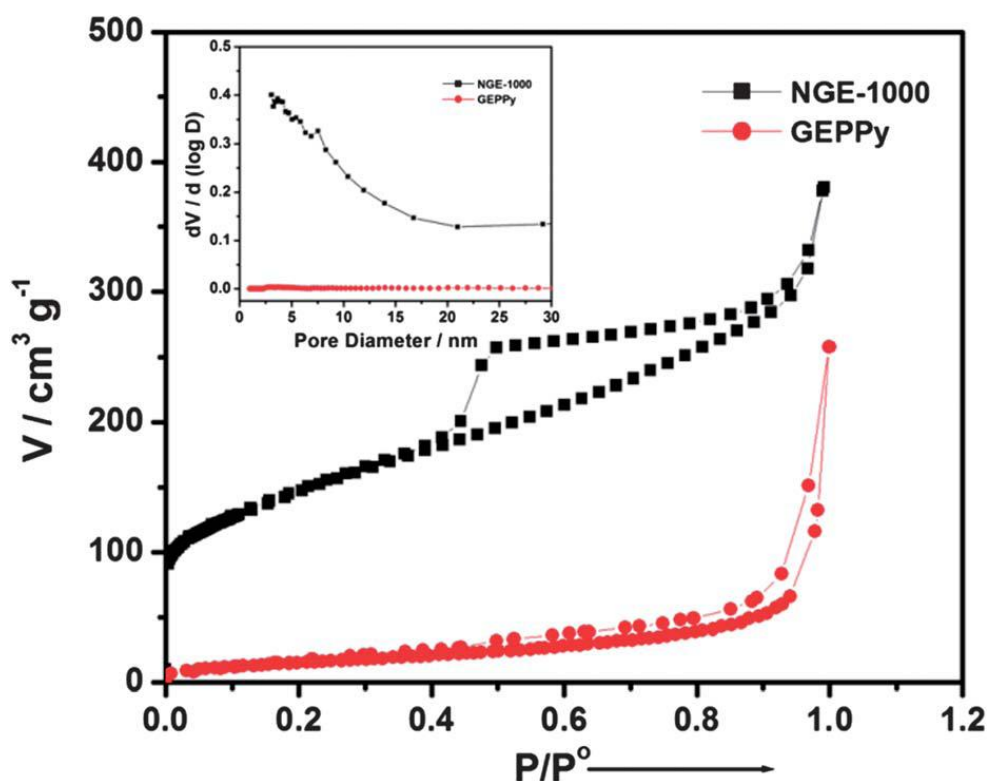


**Figure 2A.6:** Nitrogen adsorption–desorption isotherm of NGE-1000 (Inset: pore size distribution of NGE), demonstrating the mesoporous structure of graphene with a pore size of 3–7 nm and BET surface area of  $528 \text{ m}^2 \text{ g}^{-1}$ .

The Brunauer–Emmett–Teller (BET) surface area of NGE calculated from the nitrogen adsorption–desorption analysis (Figure 2A.6) is  $528 \text{ m}^2 \text{ g}^{-1}$  which is significantly high compared to GEPPy ( $88 \text{ m}^2 \text{ g}^{-1}$ ). Characteristic Type IV isotherm with adsorption in between 0.4 and 0.9 relative pressure ( $P/P_0$ ) clearly indicates the presence of a large number of mesopores with pore size around 3–7 nm in the graphene sheets compared to those in GEPPy (inset of Figure 2A.6). The distinct difference in terms of the pore size distribution between NGE-1000 and GEPPy gives valid evidence for the generation of mesopores during the nitrogen doping process. Thus, a simple method could be developed where the reduction of GO to graphene, creation of mesopores on the surface and doping of the carbon framework with nitrogen could be realized during the course of the process. The surface area of NGE-1000 is comparable to those of the various reported porous N-doped graphene prepared by template assisted synthesis <sup>[22]</sup> and is distinctly higher than that of the materials prepared by template-less methods. <sup>[23]</sup>

### 2A.2.7 XPS analysis

X-ray photoelectron spectroscopy (XPS) was performed to understand the chemical composition of GO, GEPPy and NGE- 1000. XPS analysis reveals the presence of C1s, O1s and N1s without the intervention by any impurities. Deconvoluted XPS spectra of C1s of GO (Figure 2A.7a) show four different peaks. The peaks at 284.58, 286.97, 288.49 and 290.16 eV correspond to the  $sp^2$  carbon ( $-C=C-$ ),  $-C-O$ ,  $-C=O$  and  $-O-C=O$  respectively. After the reduction of GO using pyrrole, the peak corresponding to  $-C=C-$  becomes more intense. The reduction in the peak intensity of the  $sp^3$  carbon clearly indicates the removal of the oxygen moieties from the surface of graphene. C1s spectrum of GEPPy becomes narrow after the reduction process. Importantly, the peak at 285.68 eV confirms the presence of nitrogen atom in GEPPy (Figure 2A.7b). Deconvoluted C1s spectra of NGE-1000 clearly show three different peaks with a high intensity peak at 284.37 eV ( $-C=C-$ ) and other two peaks at 285.87 ( $-C=N$ ) and 287.30 eV ( $-C-N$ ). Narrowing of the broader peak of C1s from GEPPy to NGE-1000 indicates an enhanced degree of graphitization after the pyrolysis. Similarly, the C to O ratio of the samples increases with an increase in the heat treatment temperature. This again confirms the enhanced graphitization of GEPPy at higher temperature.



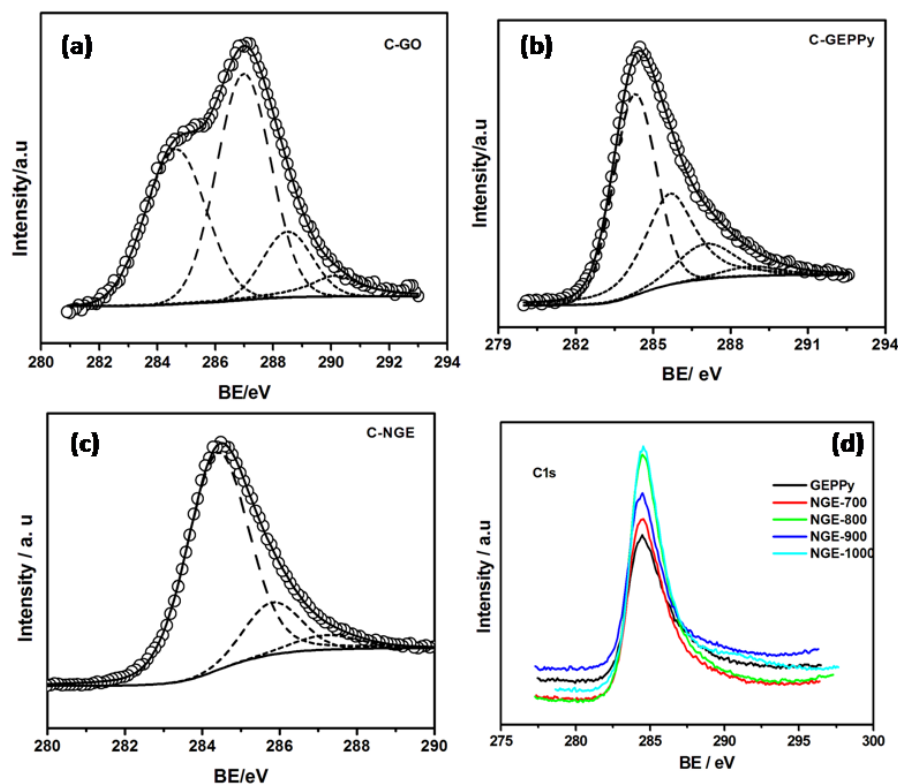


**Figure 2A.7:** Deconvoluted XPS spectra of carbon 1s of (a) GO, (b) GEPPy and C (NGE). (d) C 1s spectra of GEPPy, NGE-700, NGE-800, NGE-900 and NGE-1000. Narrowing of the C1s peak at higher temperature indicates high degree of graphitization as the heat treatment temperature increases.

For understanding the change in the chemical composition and nitrogen environment, the differently heat treated forms of NGE were individually analyzed using XPS. N1s spectra of all the samples were deconvoluted to understand the different types of nitrogen in the samples (Figure 2A.8). GEPPy shows three different types of nitrogen atoms with binding energies of 398.61 (–N=), 399.50 (–N–H) and 400.94 eV (–N<sup>+</sup>) in the oxidised pyrrole ring.<sup>[24]</sup> This clearly supports the presence of the oxidative product of pyrrole on the surface of the graphene sheets prior to the heat treatment process. After the heat treatment at different temperatures, all the four samples are showing three different peaks corresponding to the pyridinic (398.12 eV), pyrrolic (399.8 eV) and graphitic (401.9 eV) nitrogens.<sup>[10a, 11a, 22b, 25]</sup> With an increase in the temperature, the pyrrolic nitrogen content progressively increases as shown in Figure 2A.8f. In NGE-1000, the pyrrolic nitrogen content reached up to 53% compared to 38% obtained for NGE-700. Similarly, the pyridinic nitrogen content decreases with an increase in the temperature, showing a

minimum value of 21% for NGE-1000 compared to 45% detected on NGE-700. On the other hand, the graphitic nitrogen content increases from

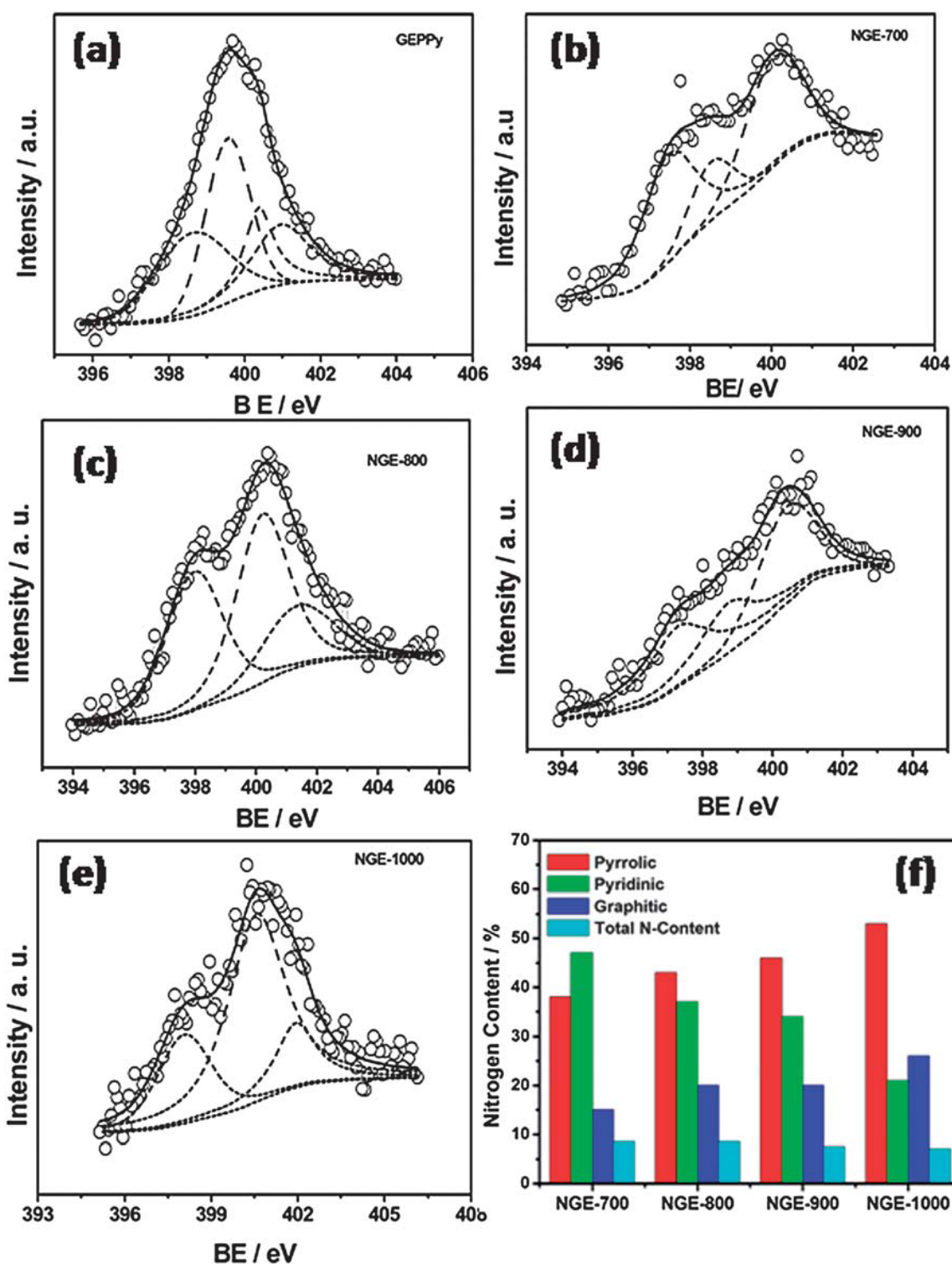


**Figure 2A.8:** Deconvoluted XPS spectra of N1s of (a) GEPPy, (b) NGE-700, (c) NGE-800, (d) NGE-900 and (e) NGE-1000; (f) the estimated values of the different types of nitrogen in all the pyrolysed samples.

16% for NGE-700 to 26% for NGE-1000, indicating a favourable effect of temperature for generating this coordination. In the previous discussion on the BET analysis, we have seen the graphene sheets becoming mesoporous after the heat treatment process. The mesopores are expected to create a large number of defective sites in the graphene sheets. These defective sites during pore generation are responsible for the attainment of the large fraction of pyrrolic nitrogen in the doped systems. Thus, the surface layer of the pyrrole moiety helps to engrave pores, which in turn assists in achieving the most desired pyrrolic form of the doped nitrogen in the graphene matrix. Since both the processes occur simultaneously during the heat treatment step, the selectivity towards the pyrrolic nitrogen as well as the surface area could be increased in one shot. However, the overall nitrogen content in the samples decreases with increasing the pyrolysis temperature. The nitrogen content of 12.5 wt.% in GEPPy has been reduced to 7.0 wt. % in NGE-1000. It is noteworthy that the loading of nitrogen in the graphene sheets after the high temperature pyrolysis is significantly higher compared to some of the reports available for the preparation of nitrogen doped graphene by thermal treatment.<sup>[22a, 26]</sup>

### 2A.2.8 Electrochemical analysis

The different nitrogen bonding environments in the NGE samples must exert significant influence on the electrocatalytic activity towards the oxygen reduction reaction. The kinetics of the oxygen reduction reactions of all the catalysts were studied by using a rotating disk electrode (RDE) by maintaining a catalyst loading of  $0.225 \text{ mg cm}^{-2}$  in the working electrode in 0.1 M KOH. The tests were performed using a three-electrode cell assembly at a scan rate of  $10 \text{ mV s}^{-1}$  and electrode rotation speeds of 900, 1200, 1600, 2000 and 2500 rpm. For Pt/C (40 wt.%), the Pt loading was  $0.106 \text{ mg cm}^{-2}$ . Figure 2A.9 shows the linear sweep voltammograms of the different samples in oxygen saturated 0.1 M KOH at a rotation speed of 1600 rpm. The onset potential of NGE-1000 is more positive compared to NGE-900, NGE-800 and GEPPy. Interestingly, the onset potential of NGE-1000 slightly exceeds the onset potential corresponding to 40 wt.% Pt/C (inset of Figure 2A.9). This matching performance characteristic in terms of the onset potential for both NGE-1000 and 40 wt.% Pt/C is an important development in the pursuit of developing metal-free ORR catalysts for PEMFCs. In terms of the limiting current density ( $j_l$ ), NGE-1000 has the highest  $j_l$  value among all the graphene based catalysts. However, the  $j_l$  value of Pt/C is higher than that of NGE-1000. Thus, overall, the results reveal that the

overpotential for ORR could be brought down by using NGE-1000 to a level comparable to that on Pt/C. At the same time, the number of active sites per unit area in NGE-1000 should be increased further to fill the existing gap in the  $j_1$  values.

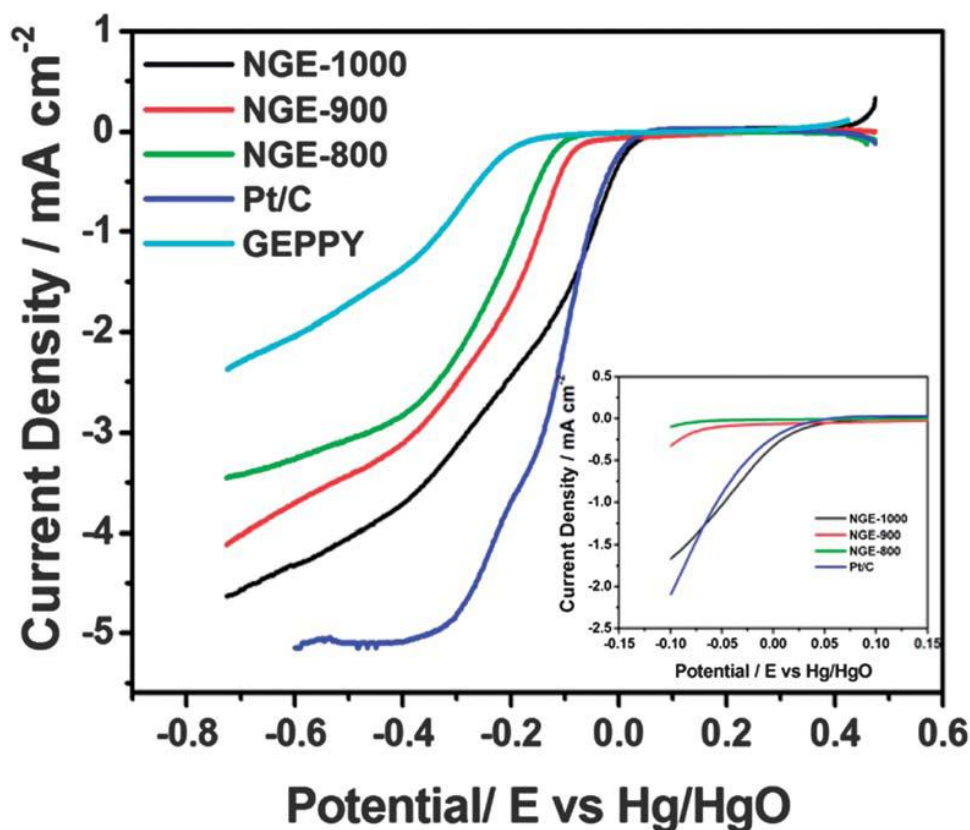


**Figure 2A.9:** Linear sweep voltammogram of NGEs, GEPPy and Pt/C in 0.1 M oxygen saturated KOH at a rotation speed of 1600 rpm and a scan rate of 50 mV s<sup>-1</sup>. Pt wire was used as the counter electrode and Hg/HgO was used as the reference electrode (inset: enlarged area representing the onset potential of the different samples).

The efficiency of a catalyst can be evaluated by using the Koutecky–Levich (K–L) equation, by calculating the kinetic current density and the number of electrons transferred based on the ORR polarization curves. The K–L equation can be represented as follows:

$$\frac{1}{j} = \frac{1}{nFKC_{O_2}} + \frac{1}{0.62nFC_{O_2}D_{O_2}^{2/3}\omega^{-1/6}\nu^{1/2}}$$

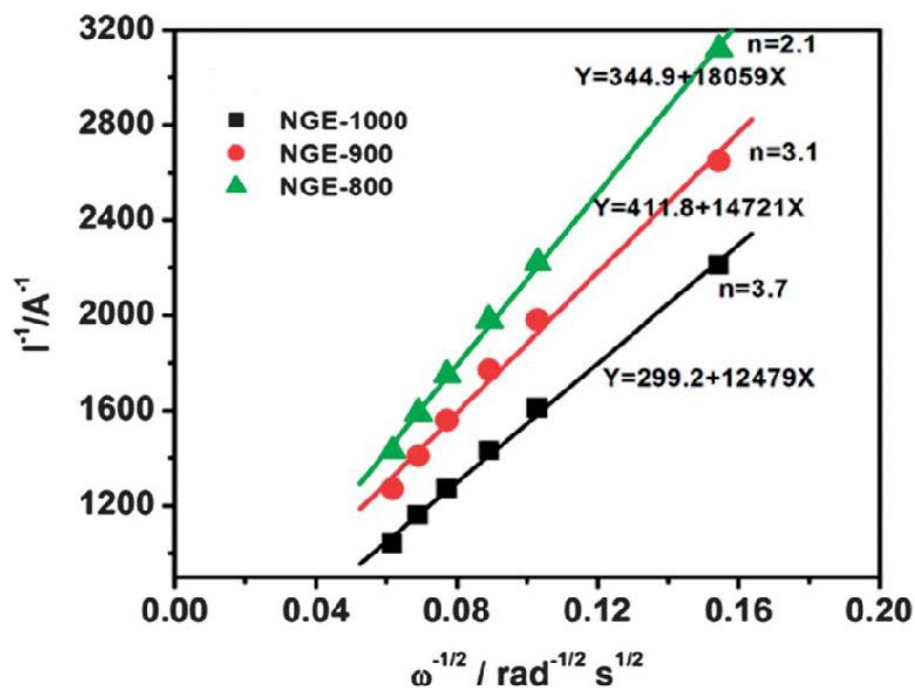


**Figure 2A.10:** *K–L plots of NGE-800, NGE-900 and NGE-1000 at a potential of -0.65 V. The plots are generated from the LSVs of all the three samples conducted in oxygen saturated 0.1 M KOH solution at different rotation speeds.*

where, the kinetic current density,  $j_k = nFkC_{O_2}$ . In these representations,  $n$  is the number of electrons,  $F$  is the Faraday constant ( $96485.5 \text{ C}$ ),  $C_{O_2}$  is the bulk  $O_2$  concentration ( $1.2 \times 10^{-6} \text{ mol cm}^{-3}$ ),  $D_{O_2}$  is the diffusion coefficient of  $O_2$  in the electrolyte ( $1.9 \times 10^{-5} \text{ cm}^2 \text{ s}^{-1}$ ),  $\nu$  is the kinematic viscosity of the electrolyte ( $0.01009 \text{ cm}^2 \text{ s}^{-1}$ ), and  $\omega$  is the rotation rate of the electrode in radians per second ( $2\pi \text{ rpm}/60$ ). The value obtained for the kinetic current is independent of diffusion and can be used to evaluate the intrinsic activity of the catalysts. The plot of  $1/j$  vs.  $\omega^{-1/2}$  gives a linear relationship, with the y-intercept leading to the inverse of the kinetic current. The number of electrons ( $n$ ) transferred during ORR can be calculated from the slope of the plot. Figure 2A.10 shows the linear relationship between  $j_k^{-1}$  versus  $\omega^{-1/2}$  of the different nitrogen doped graphene samples for ORR. Figure 2A.11, which compares the change in  $n$  as a function of the applied potential for the NGE samples, reveals that  $n$  is strongly dependent on the applied potential in the case of NGE-1000 compared to the other two catalysts. With increasingly negative potentials, NGE-1000 approaches towards a  $4e^-$  transfer reaction compared to both NGE-900 and NGE-800. The higher number of electrons transferred observed in the case of NGE-1000 is a clear indication of the better efficiency of the system as more electrons can be generated per mole of the electrode reaction.

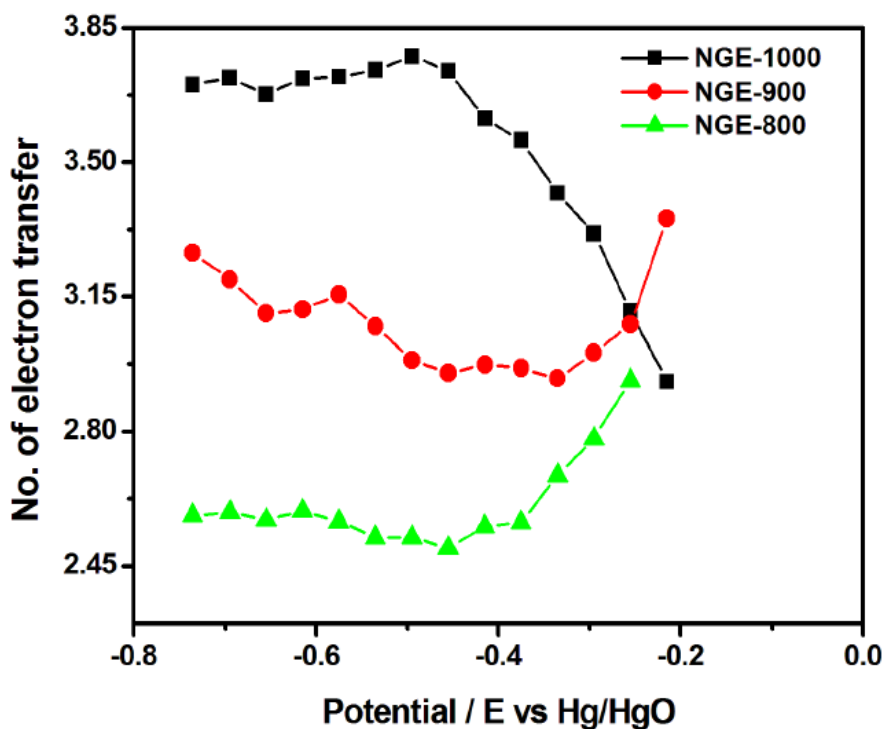


**Figure 2A.11:** The number of electrons transferred versus the potential as calculated from the K-L plots.

It has been realized from the previous sections that the high temperature pyrolysis changes the nitrogen configuration in the NGE samples. The electrochemical ORR activity is found to be strongly a function of the type of nitrogen present in the doped state. With an increase in the pyrolysis temperature from 800 °C to 1000 °C, the kinetic current density ( $j_k$ ) is clearly increasing as evident from Figure 2A.12. At -0.2 V, the  $j_k$  value of NGE-1000 is 6 mA cm<sup>-2</sup> compared to 1.7 and 2.5 mA cm<sup>-2</sup> measured for NGE-800 and NGE-900, respectively. According to recent reports, the electrocatalytic activity of nitrogen doped graphene is strongly dependent on the type of nitrogen content, mainly pyrrolic, pyridinic and graphitic.<sup>[22b, 25]</sup> The XPS analysis has given strong evidence for an increase in the amounts of both pyrrolic and graphitic nitrogen with the pyrolysis temperature.<sup>[5, 27]</sup> The electron withdrawing effect of the pyrrolic and graphitic nitrogen in NGE-1000 can activate the adjacent carbon atoms. This leads to a net positive charge on the neighbouring carbon. This type of charge polarization consequently assists adsorption and reduction of oxygen molecule on the carbon atoms through an energetically favoured association mechanism as reported by Yu *et al.*<sup>[28]</sup> In addition to this effect of charge polarization on ORR, a recent report reveals that mesoporosity in nitrogen doped graphene also induces adsorption and reduction of oxygen molecules. The comparable ORR activity of NGE-

1000 with that of Pt/C clearly gives strong evidence that the pyrrolic nitrogen is essential for oxygen adsorption and reduction to water through a four electron mechanism. This further supports the finding of Yu *et al.* that pyridinic nitrogen alone cannot help for direct four electron pathways for ORR.<sup>[13]</sup>

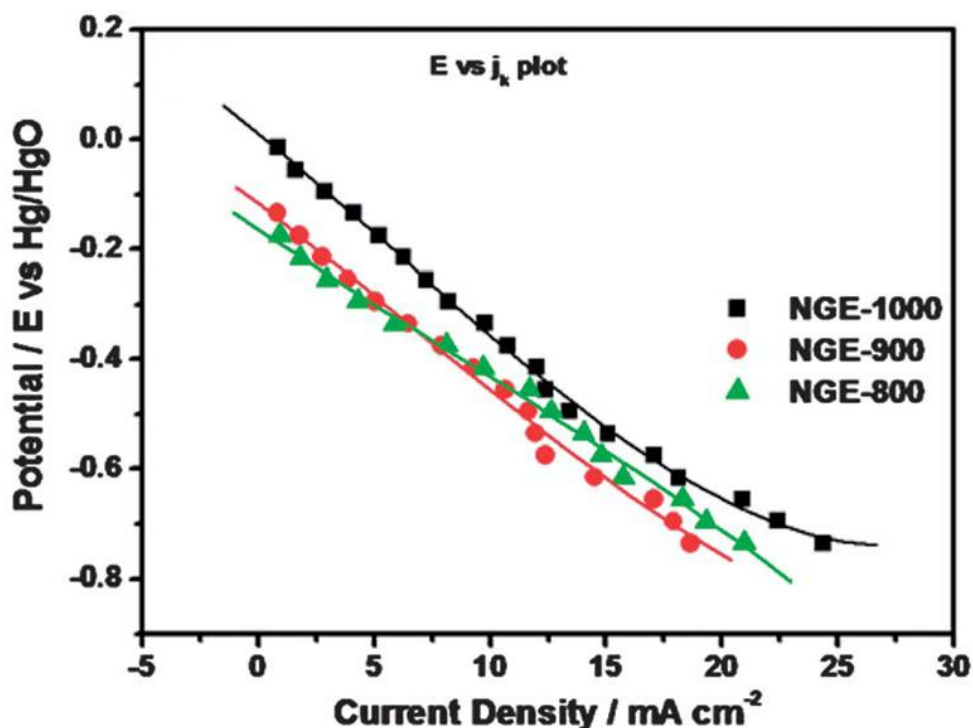


**Figure 2A.12:** *E* versus kinetic current density of all the three catalysts derived from the *K–L* plots.

To examine the possible crossover effect in the presence of other fuel molecules (e.g., methanol), the current–time (*i–t*) chronoamperometric responses for ORR at the NGE-1000 and Pt/C electrodes are obtained. As shown in Figure 2A.13, a sharp decrease in the current was observed for the Pt/C electrode upon addition of 3.0 M methanol. However, the corresponding amperometric response for the NGE-1000 electrode remains almost unchanged even after the addition of methanol. This result explicitly indicates that the NGE-1000 electrocatalyst has higher fuel selectivity towards ORR than the commercial Pt/C electrocatalyst.

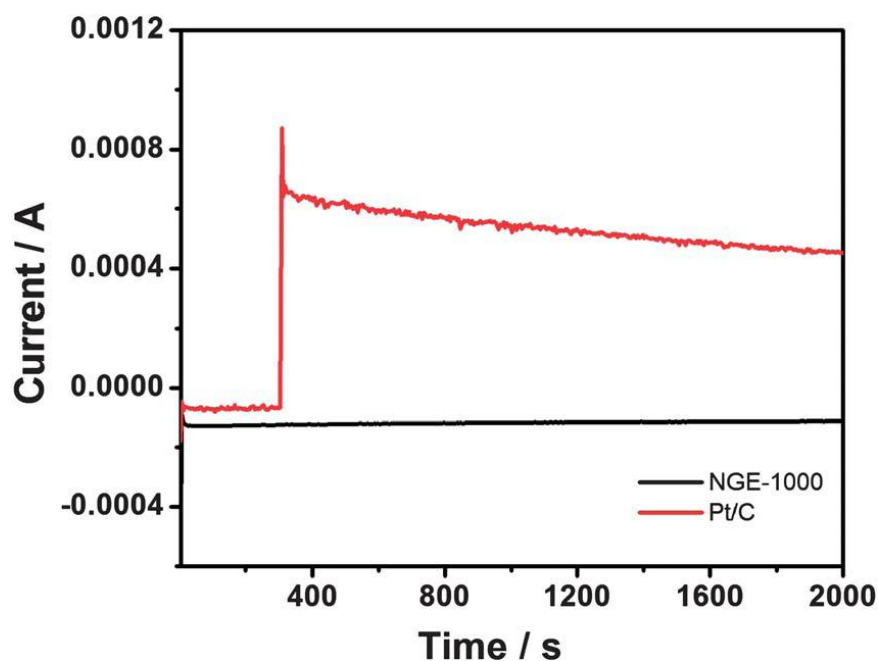


**Figure 2A.13:** Methanol crossover study of NGE-1000 and Pt/C at a rotation speed of 1000 rpm. At 300 s, 3 M methanol was added into the 0.1 M KOH electrolyte to evaluate the crossover effect.

As stability under the electrochemical environment is a mandatory requirement for any electrocatalyst to be considered for realistic applications, an accelerated durability test (ADT) was carried out by using both NGE-1000 and Pt/C catalysts (Figure 2A.14). ADT was carried out by subjecting a potential cycling between -0.37 and 0.37 V vs. Hg/HgO in oxygen saturated 0.1 M KOH at  $100 \text{ mV s}^{-1}$  scan rate at room temperature for 1000 cycle. LSV was taken at different rotation speeds before and after ADT to evaluate the level of performance degradation of the catalyst. The comparison of the LSVs before and after ADT reveals that NGE-1000 clearly outperforms the Pt catalyst in terms of its electrochemical stability. Looking at the plots, it can be inferred that the Pt catalyst suffers from a 35 mV negative shift in the ORR activity at -0.027 V vs. Hg/HgO after ADT whereas NGE-1000 has only 15 mV drop at the same potential. Since ADT involves exposure under drastic electrochemical environment, the result clearly reveals the enhanced cycling stability of NGE-1000. Compared to the Pt catalyst where potential cycling is expected to trigger Pt dissolution and sintering, being metal-free and due to the existence of strong covalent interaction between the active sites and the graphitic lattice, NGE-1000 manages to give an impressive durability profile during the experiment.<sup>[29]</sup>



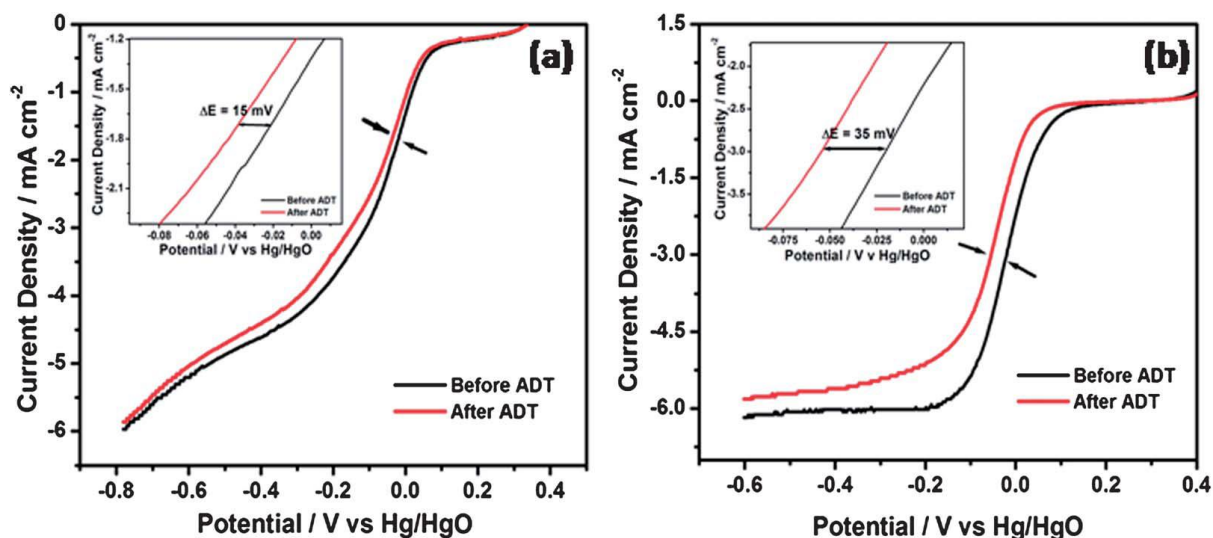


**Figure 2A.14:** Linear sweep voltammogram of (a) NGE-1000 and (b) Pt/C before and after ADT in 0.1M oxygen saturated KOH at a rotation speed of 1600 rpm and a scan rate of  $10 \text{ mV s}^{-1}$ . Pt wire was used as the counter electrode and Hg/HgO was used as the reference electrode. The enlarged portions in the insets of the figure (a) and (b) represent the shift from -0.027 V for the respective catalysts after ADT.

## **Part B: Layer-separated distribution of nitrogen doped graphene by its wrapping on carbon nitride tetrapods for enhanced ORR\***

### **2B.1 Experimental**

#### **2B.1.1 Graphene oxide (GO) synthesis**

In a typical synthesis, a mixture of graphite flakes and potassium permanganate ( $\text{KMnO}_4$ ) was slowly added to a 9:1 mixture of con. sulphuric acid ( $\text{H}_2\text{SO}_4$ ) and phosphoric acid ( $\text{H}_3\text{PO}_4$ ). The mixture was stirred for 12 h at 60 °C. After cooling to room temperature, deionised water (DI water) was added to dilute the mixture followed by the addition of 30% hydrogen peroxide ( $\text{H}_2\text{O}_2$ ) to remove unreacted manganese oxide. While adding the peroxide into the acid mixture, the original pink colour of the mixture turned to yellow. The resulting solution was washed several times with nitric acid ( $\text{HNO}_3$ ), hydrochloric acid ( $\text{HCl}$ ) and ethanol. pH of the solution was reduced using continuous washing with DI water till the pH reaches above 4. The resulting reddish brown viscous solution was washed with diethyl ether and kept for drying at a temperature of 60 °C in a vacuum oven.

#### **2B.1.2 Preparation of $\text{CN}_x$ wrapped nitrogen doped graphene (CNG)**

CNG with different NG loading was synthesised using a simple scalable approach. In a typical synthesis, washed melamine foam was dipped in the GO solution (4 mg/ml) followed by drying using an IR lamp. For different loading of GO in the melamine foam, the number of dipping was changed. Dried GO-melamine foam was annealed at 900 °C for 3 h in argon atmosphere (Scheme 2B.1). The samples are designated as CNG-1, CNG-3 and CNG-6 based on the dipping numbers of the melamine foam in the GO solution as 1 dip, 3 dips and 6 dips, respectively.

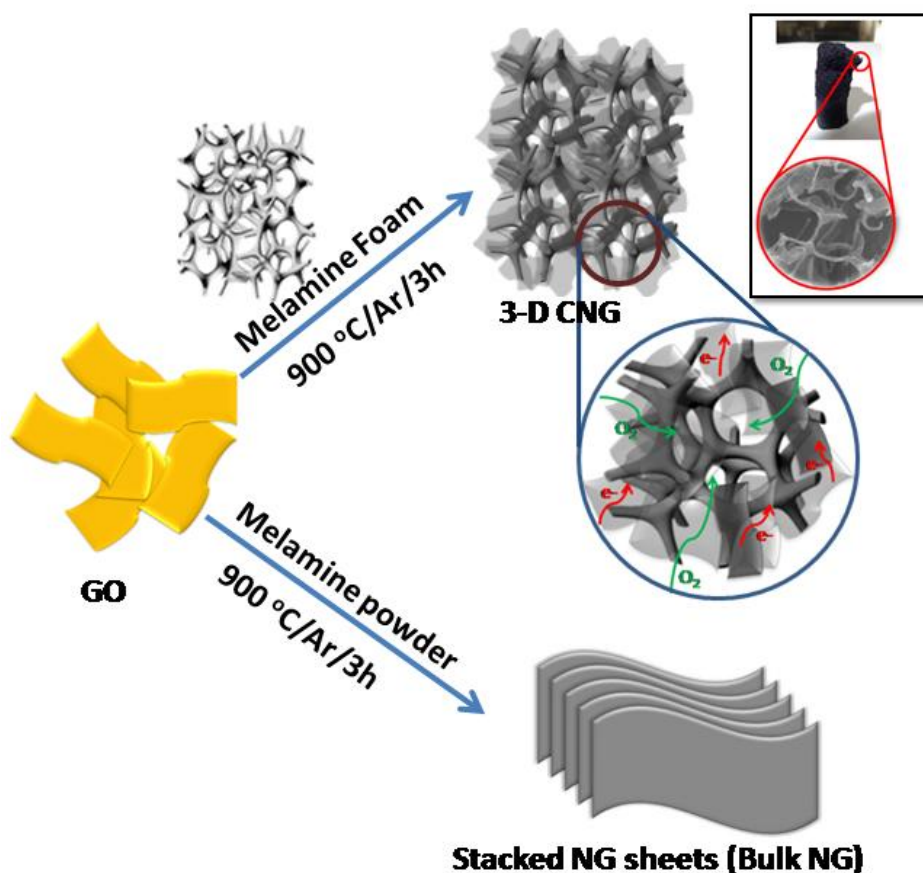
#### **2B.1.3 Preparation of nitrogen doped graphene (Bulk NG)**

Bulk NG was synthesised using a reported procedure. In brief, GO was mixed well with melamine powder followed by annealing at 900 °C for 3 h under argon atmosphere.

*\* Reproduced with permission from Royal Society of Chemistry, Copy right 2014 (Chem. Commun., 2014, 50, 13769-13772)*

### 2B.1.4 Material Characterization

High resolution transmission electron microscopic (HR-TEM) images were recorded using FEI Technai G2 T30 instrument operated at 300 kV. Scanning electron microscopic analysis was carried out using Quanta 200 3D FEI instrument. Raman analysis was performed in LabRam spectrometer (HJY, France) with a laser wavelength of 632 nm. X-ray photoelectron spectroscopic analysis was carried out in VGMicrotech Multilab ESCA 3000 spectrometer employing a monochromatic Mg  $K_{\alpha}$  X-ray source ( $h\nu = 1253.6$  eV). Surface area of all the samples was measured by Brunauer-Emmet-Teller (BET) nitrogen adsorption-desorption experiment on a Quantachrome Quadrasorb automatic volumetric measurement system at 77 K using ultra pure nitrogen gas.



**GO – Graphene oxide, NG – Nitrogen doped graphene,  
3-D CNG – Three dimensional nitrogen doped wrapped carbon nitride**

*Scheme 2B.1: A schematic representation of the preparation of the CNG catalyst having graphene sheets wrapped along the arms of the  $CN_x$  tetrapod units.*

### 2B.1.5 Electrochemical Measurements

All the electrochemical measurements were carried out in a Biologic electrochemical workstation (VMP3) using a conventional three-electrode set-up. 0.1 M HClO<sub>4</sub> was used as the electrolyte for the electrochemical measurements. Catalyst coated glassy carbon rotating ring-disc (Pine Instruments, Inc.) and Ag/AgCl were used as the working electrode and reference electrode, respectively. Potentials given in the manuscript are converted to reference hydrogen electrode scale using an equation,  $E_{\text{RHE}} = E_{\text{Ag/AgCl}} + 0.196 + 0.059 \text{ p}^{\text{H}}$ . To avoid Pt contamination in the working electrode during the potential cycling, a graphite rod was used as the counter electrode. Catalyst ink was prepared by ultrasonically mixing 10 mg of the catalyst in 2 ml of 2:3 ethanol-water mixture for 1 min. 10  $\mu\text{l}$  of the catalyst slurry was drop coated on the glassy carbon electrode, which was polished using 0.05  $\mu\text{m}$  polishing alumina powder. After drying the ink under an IR lamp, 1  $\mu\text{l}$  of 0.01 wt. % Nafion solution in ethanol was applied on the catalyst. The catalyst loading in the electrode is 0.255 mg cm<sup>-2</sup>. For the comparison purpose, the study was also carried out using commercial Pt/C (20 wt.% from Johnson Matthey). 10 mg of Pt/C was mixed well with 2 ml of 2:3 ethanol-water mixture to prepare the catalyst ink. 5  $\mu\text{l}$  of the resulting ink was applied on the glassy carbon electrode in order to get a Pt loading of 25.5  $\mu\text{g}_{\text{Pt}} \text{ cm}^{-2}$ . Cyclic voltammograms of the samples were recorded in 0.1 HClO<sub>4</sub> solution with 5 mV s<sup>-1</sup> scan rate in a potential window of -0.2 to 1 V vs. Ag/AgCl. Linear sweep voltammograms (LSV) were recorded using a rotating ring-disk electrode (RRDE, 0.283 cm<sup>2</sup>, Pine Instruments) at room temperature with a scan rate of 5 mV s<sup>-1</sup> at different electrode rotation speeds in oxygen saturated 0.1 M HClO<sub>4</sub> electrolyte. The ring potential was kept constant at 1.2 V. For the durability and methanol tolerance tests, samples were coated on a glassy carbon electrode (0.196 cm<sup>2</sup>, Pine Instruments) and the measurements were done in 0.1 M HClO<sub>4</sub> at a scan rate of 5 mV s<sup>-1</sup> with an electrode rotation speed of 1600 rpm.

Number of electron transfer and peroxide percentage were determined on the basis of the rotating ring disc electrode (RRDE) voltammogram using the following equations:

$$n = 4 \times \frac{I_d}{I_d + \frac{I_r}{N}} \quad (2.1)$$

$$H_2O_2 \% = 200 \times \frac{\frac{I_r}{N}}{I_d + \frac{I_r}{N}} \quad (2.2)$$

where  $I_d$  is the disc current,  $I_r$  is the ring current, and  $N$  is the collection efficiency of the Pt ring (0.37). In a typical RRDE, the disc electrode is surrounded by a Pt ring with a particular diameter. ORR is occurring on the disc electrode and the produced peroxide, if any, will be oxidized on the ring electrode. Hence, by using both the ring current and disc current, the number of electron transfer and hydrogen peroxide yield can be easily calculated. The collection efficiency ( $N$ ) is the efficiency of the ring electrode to collect the reduced species from the disc electrode. Empirical 'N' can be easily determined using the polarization of potassium ferricyanate redox active species from the equation  $I_r/I_d$ .

Accelerated durability test (ADT) was performed for 5000 cycles to study the electrochemical stability of the catalyst (CNG-3). CV was performed at  $100 \text{ mV s}^{-1}$  scan rate in between a potential window of 0.7 to 1.3 V under oxygen purging. LSV was taken before and after ADT at 1600 rpm with a scan rate of  $5 \text{ mV s}^{-1}$ .

## 2B.2 Results and discussion

### 2B.2.1 SEM and TEM analysis

Figures 2B.1 a and b represent the scanning electron microscope (SEM) images of Bulk NG at different magnifications. From the figure, it is clear that the nitrogen doped graphene layers are stacked together in the Bulk NG. MF derived  $CN_x$  shows tetrapod like interconnecting structures with size more than  $20 \mu\text{m}$  for each unit (Figure 2B.1 c and d). In case of CNG-1,  $CN_x$  is wrapped by a thin layer of NG and it provides a three dimensional architecture to CNG-1. The NG content in CNG-1 is very less and even the  $CN_x$  backbone is clearly visible through the graphene sheets (Figure 2B.1 e and f). CNG-3 also follows similar morphological characteristics to CNG-1 except that the thickness of the NG layer is higher. Compared to CNG-1, the  $CN_x$  backbone is not clearly visible in CNG-3 (Figure 2B.1 g, h and 2B.2). It is evident from the figures that CNG-1 and CNG-3 have many macroporous interconnections due to the peculiar morphology of the  $CN_x$  backbone. Compared to CNG-1 and CNG-3, CNG-6 has high density of the NG nanosheets, which completely hides the  $CN_x$  backbone. The presence of the stacked NG nanosheets on  $CN_x$  is found to disturb the 3-D morphology of the nanostructure in the case

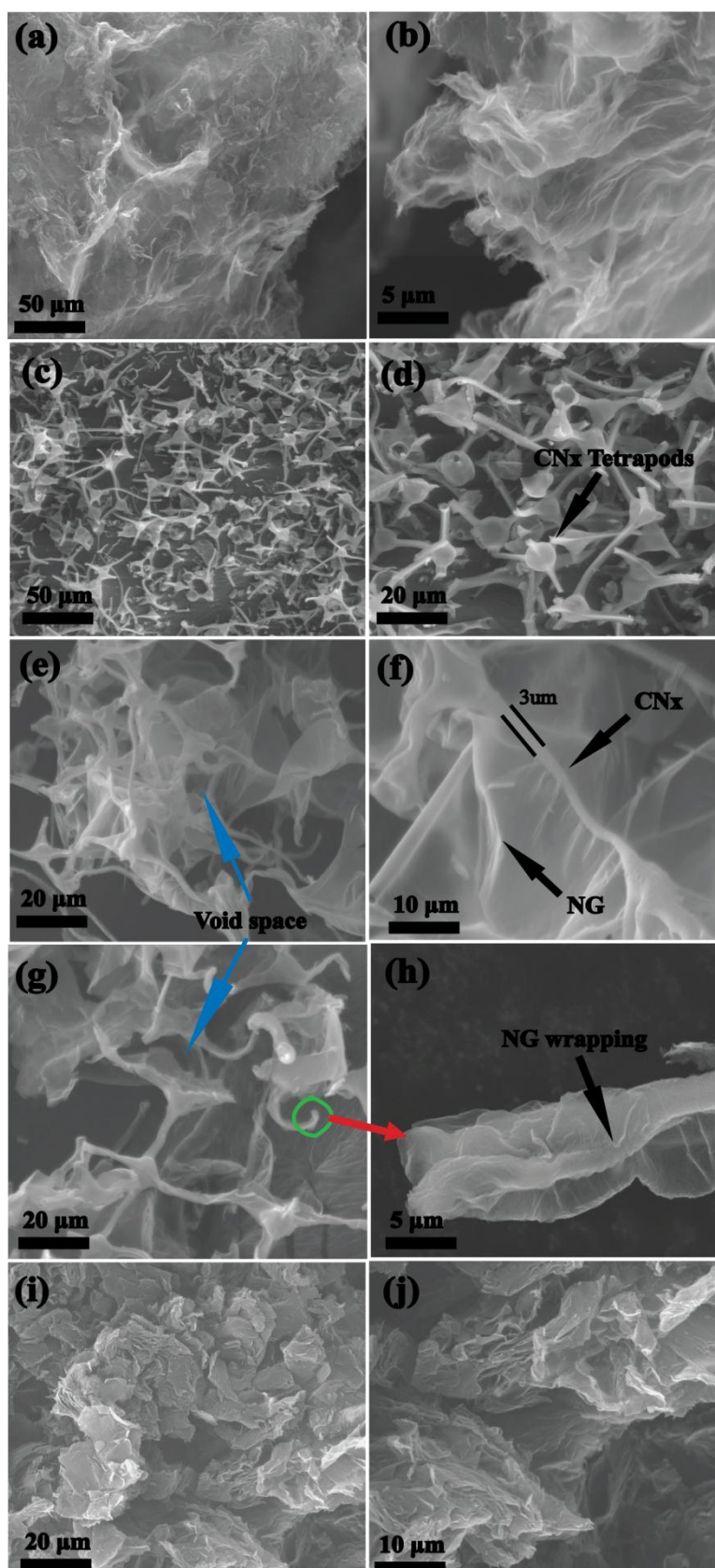


**Figure 2B.1:** SEM images of bulk NG (a and b), CNx (c and d), CNG-1 (e and f), CNG-3 (g and h) and CNG-6 (i and j).

of CNG-6 (Figure 2B.1 i and j). Elemental mapping of CNG-3 indicates that nitrogen atoms are uniformly distributed throughout the material (Figure 2B.3). TEM images of the NG sheets from CNG-3 in Figures 2B. 4 a and b show high quality graphene sheets with disordered lattice fringes. The disorder in the lattice fringes is clearly emphasizing the doping of heteroatom on the graphene sheets during the high temperature annealing. Furthermore, clear selected area electron diffraction pattern indicates the highly crystalline nature of the NG sheets.

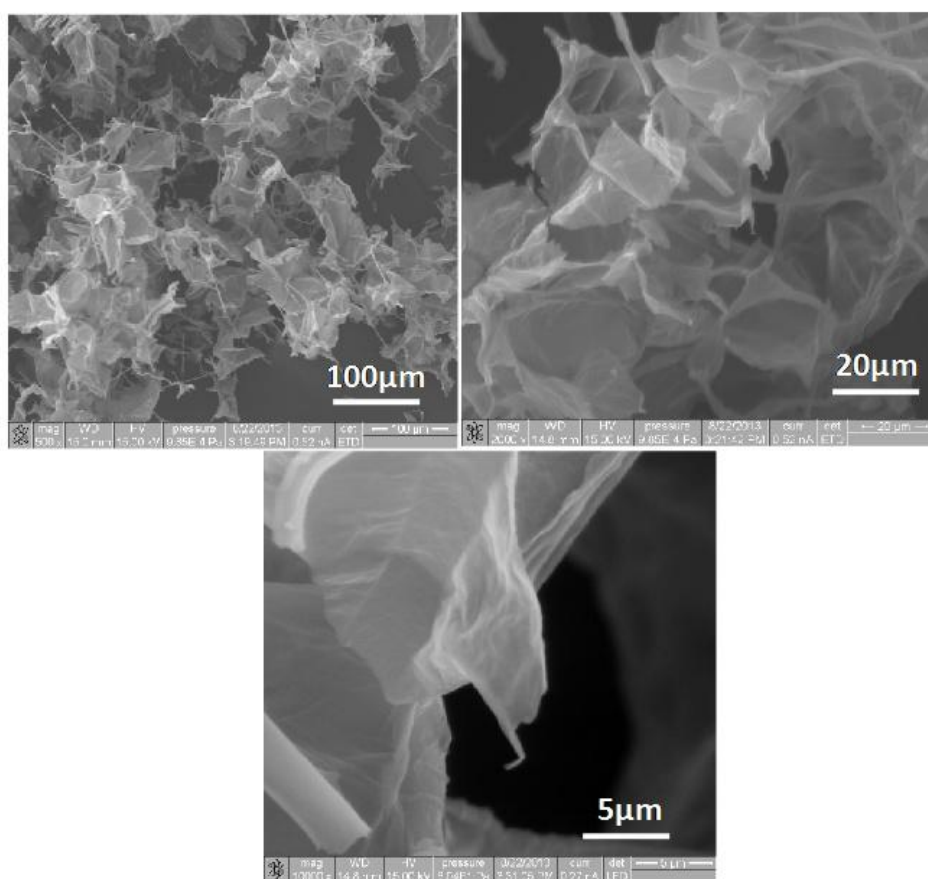


**Figure 2B.2:** FE-SEM images of CNG-3 at different magnifications.

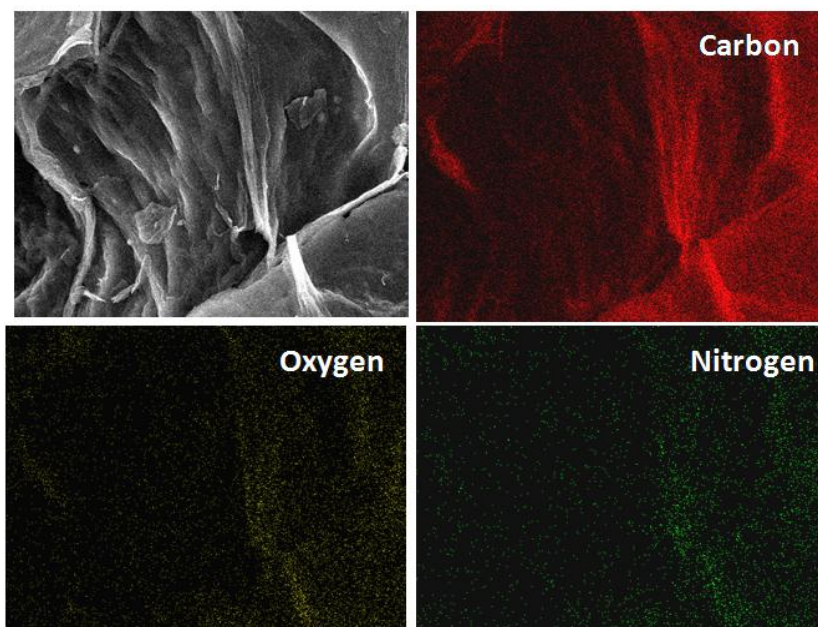


**Figure 2B.3:** Elemental mapping of carbon, oxygen and nitrogen respectively on CNG-3.

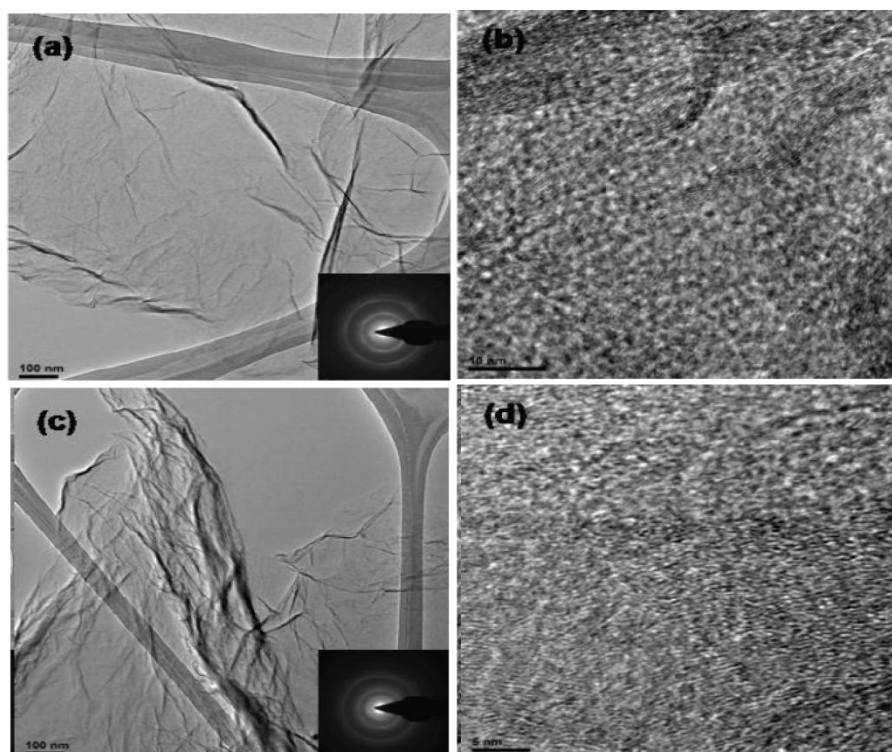


**Figure 2B.4:** TEM images of nitrogen doped graphene in CNG-3 (a and b) and CNG-6 (c and d) at different magnifications.



### 2B.2.2 Raman and XRD analyses

Raman spectroscopic analyses further confirm the nitrogen doping and defects created by nitrogen on CNG during the high temperature annealing. In Figure 2B.5a,  $CN_x$  displays the D-band at  $1318.19\text{ cm}^{-1}$  and the G-band at  $1558.07\text{ cm}^{-1}$ . The down shift of the G-band from  $1581\text{ cm}^{-1}$  (of graphite) indicates that the thermally annealed MF lacks proper  $sp^2$  carbon coordination compared to the CNG samples. For the comparison purpose, bulk NG sample also was prepared separately by annealing GO and melamine mixture at  $900\text{ }^\circ\text{C}$ . Bulk NG shows the G-band at  $1600.26\text{ cm}^{-1}$  with up shift in the G-band position compared to the G-band position of graphite, which gives a clear evidence for n-type doping of nitrogen in the graphene sheets with defects. Compared to  $CN_x$  and bulk NG, the G-band positions of CNG-1 ( $1591.10\text{ cm}^{-1}$ ), CNG-3 ( $1593.03\text{ cm}^{-1}$ ), CNG-6 ( $1594.24\text{ cm}^{-1}$ ) are closer to that of pure graphite. Up shift in the peak position also confirms the nitrogen doping in the CNG samples. The shifting of the peak position towards the high wave number with increase in the dipping number indicates that the defects created by nitrogen moieties are different in the CNG samples. The ratio of the D-band and G-band ( $I_D/I_G$ ) further helps to understand the chemical modifications occur

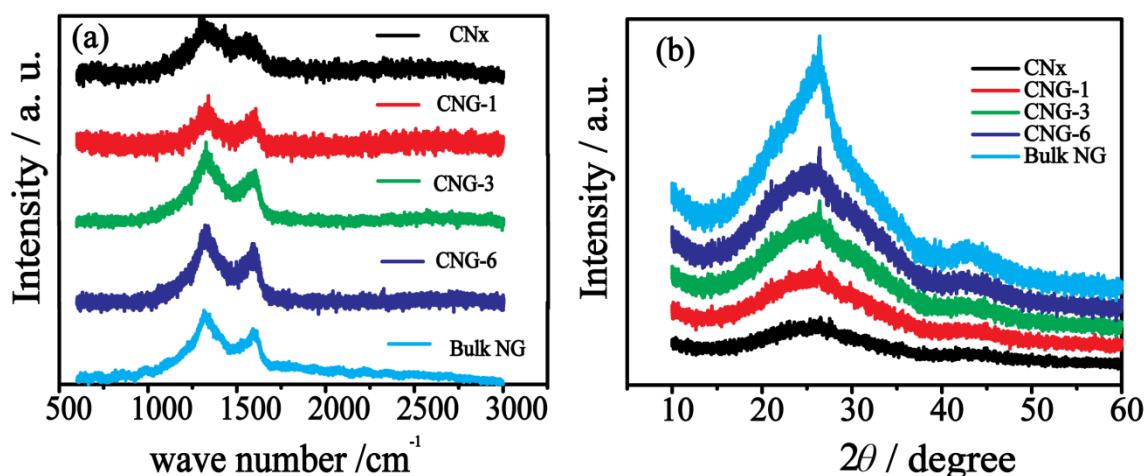


**Figure 2B.5:** (a) Raman spectra of  $CN_x$ , CNG-1, CNG-3, CNG-6 and bulk NG, (b) X-ray diffraction patterns of  $CN_x$ , CNG-1, CNG-3, CNG-6 and Bulk NG sheets.

during the high temperature annealing process.  $CN_x$ , bulk NG, CNG-1, CNG-3 and CNG-6 show an  $I_D/I_G$  ratio of 1.39, 1.46, 1.09, 1.49 and 1.67, respectively. CNG-3 and bulk NG have almost similar  $I_D/I_G$  ratio, indicating the presence of similar defective sites on both the materials. However, the  $I_D/I_G$  ratio is increasing with increase in the NG loading of the

CNG samples, which clearly indicates that the defective sites are getting modified when the NG sheets are wrapped along the  $CN_x$  tetrapods. This may seriously affect the adsorption of dioxygen molecule and its reduction on the CNG samples. The in plane crystalline size ( $L_a$ ) ( $L_a$  is inversely proportional to the  $I_D/I_G$  ratio) of bulk NG and CNG-3 is almost same but it is decreasing with increase in the NG loading on the CNG samples. This indicates that the total nitrogen content is varying with respect to the NG sheets in the CNG samples and simultaneously the defective sites in the CNG samples are also varying. Further evidence for the crystalline nature of the CNG samples has been obtained from X-ray diffraction (XRD) analysis (Figure 2B.5 b). XRD analysis again confirms the amorphous behavior of  $CN_x$  and it also indicates that the crystalline nature is progressively improving by the wrapping of the NG sheets on  $CN_x$ . It is evidenced from the XRD peak at  $2\theta = 26^\circ$ .

### 2B.2.3 Surface area analysis

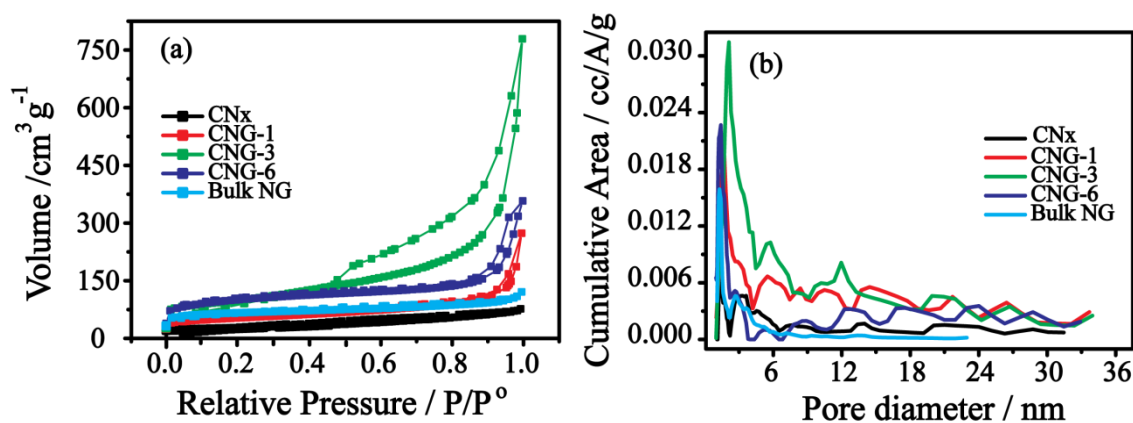


**Figure 2B.6:** (a) Nitrogen adsorption–desorption isotherms and (b) pore size distribution profiles of  $CN_x$ , CNG-1, CNG-3, CNG-6 and Bulk NG.

Surface area measured from nitrogen adsorption-desorption isotherms using Brunauer-Emmett-Teller (BET) method shows that  $CN_x$  possesses a low surface area of 44 m<sup>2</sup>/g (Figure 2B.6). Bulk NG sheets show a surface area of 150 m<sup>2</sup>/g, indicating the stacking of the graphene sheets during the high temperature annealing and this value is comparable to a recently reported value on the thermally treated graphene sheets by Li *et al.*<sup>[30]</sup> The CNG samples show the surface area values in the order of CNG-1 (156 m<sup>2</sup>/g) < CNG-6 (268 m<sup>2</sup>/g) < CNG-3 (276 m<sup>2</sup>/g). It is worth mentioning that the surface area of CNG-1 is higher than that of both  $CN_x$  and bulk NG. This gives a clear evidence for the

reduced restacking of the graphene sheets in presence of MF. CNG-3 shows the highest surface area of 276 m<sup>2</sup>/g, as the number of the NG sheets increases when MF assists restacking of the layers. However, with further increase in the NG loading, a reduction in the surface area has been observed and this is attributed to the enhanced restacking of the graphene sheets when the loading goes beyond a threshold level. This is evidenced from CNG-6 where the surface area is less compared to CNG-3. However, it should be noted that the reduction in the surface area of CNG-6 does not differ much compared to CNG-3, the credit goes to the MF backbone which acts as a template to maintain a loose assembly of the graphene layers. It is interesting to observe that CNG-3 starts adsorbing nitrogen at low relative pressure (0.47 P/P<sub>0</sub>) compared to the other CNG samples, bulk NG and CN<sub>x</sub> (Figure 2B.6 a). This explicitly indicates that CNG-3 consists of pores having a wide range of size distribution. CN<sub>x</sub> and bulk NG have pore size less than 6 nm compared to the wide range of pores observed for the CNG samples (Figure 2B.6 b). CNG-1 and CNG-6 have more micropores compared to CNG-3; on the other hand, the pore size distribution of CNG-3 varies from 3 nm to 35 nm. High surface area and wide range of porosity assist efficient mass transport in CNG-3 sample compared to the other CNG samples and help to make more accessible surface for the reactant moieties.

#### 2B.2.4 XPS analysis

To further confirm the chemical composition of the prepared materials, X-ray Photoelectron Spectroscopic (XPS) analysis was performed. All the samples show the presence of carbon, nitrogen and oxygen.

Deconvoluted C1s spectra (Figure 2B.7) of CN<sub>x</sub> show five distinct binding energy contributions which are indexed as 284.23 (-C=C-), 284.88 (-C-C-), 285.64 (-C-N), 286.82 (-C-O) and 288.59 eV (-C=O). High percentage of -C-C- and -C-O reduces the degree of graphitization of CN<sub>x</sub> and it is evidenced also from the Raman and XRD analyses. The peak at the binding energy of 284.31 eV of C 1s spectra of bulk NG indicates the improved graphitization of the NG sheets and the binding energy at 285.38 eV further confirms the nitrogen doping in the sample. All the CNG samples possess improved graphitization as evidenced from the peak corresponding to the binding energy of 284.36 eV.

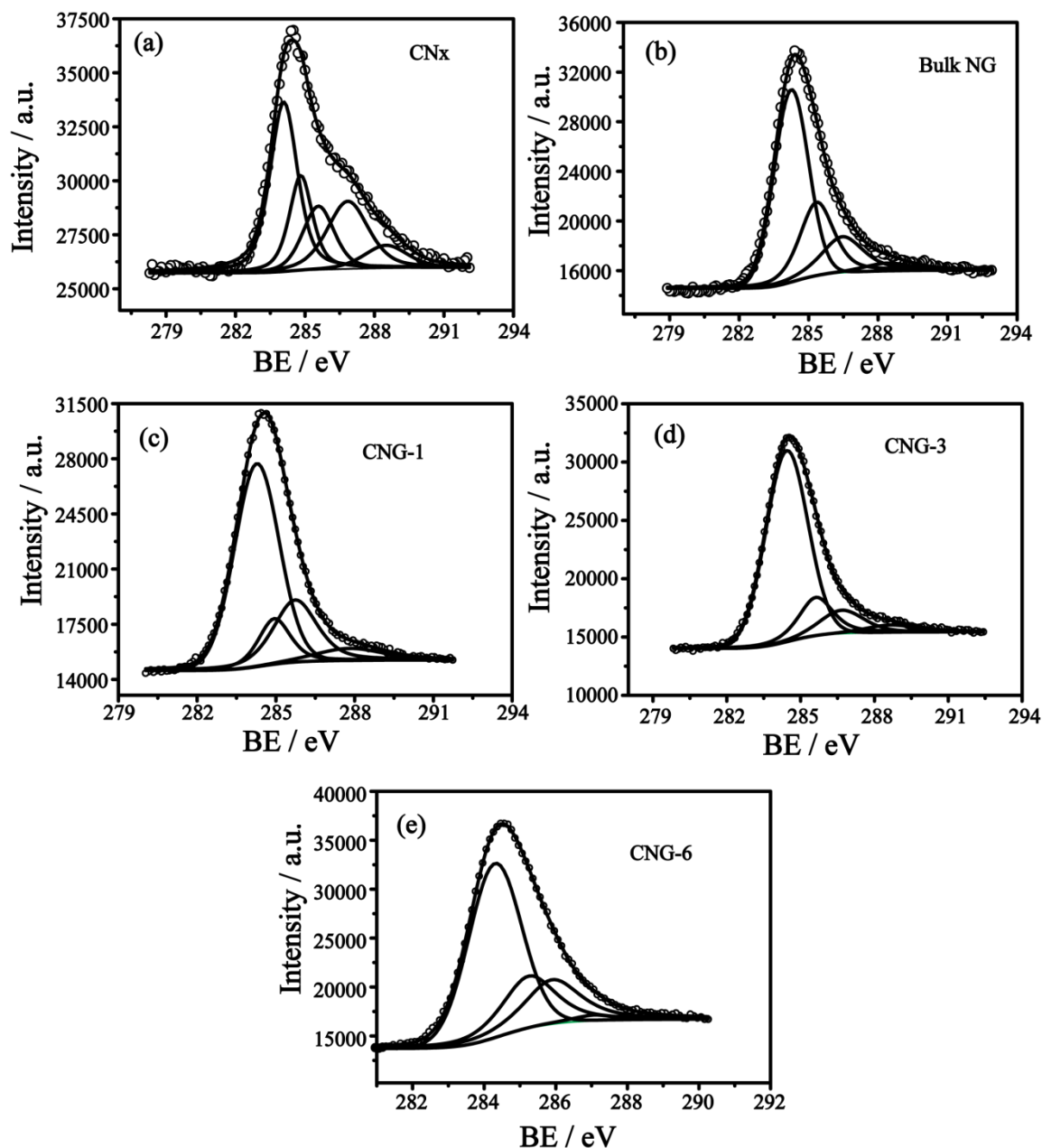


**Figure 2B.7:** Deconvoluted  $C1s$  XPS spectra of (a)  $CN_x$ , (b) bulk NG, (c) CNG-1, (d) CNG-3 and (e) CNG-6 samples.

Similarly, nitrogen doping also has been confirmed from the binding energy peak at around 285.00 eV. Presence of oxygen also could be evidenced from the XPS spectra, which is expected to be generating during the carbonization of MF which exists in the form of the adsorbed state. The wt.% of carbon is in the order of  $CN_x$  (74.26 %) < CNG-3 (80.35 %) < CNG-1 (80.54 %) < Bulk NG (84.71 %) < CNG-6 (85.75 %). More interestingly, the C/O ratio of the CNG samples is increasing with increase in the NG content. The C/O ratio follows the order of  $CN_x$  (3.02) < CNG-1 (4.59) < CNG-3 (4.78) < CNG-6 (8.03) < Bulk

NG (9.52). Lower C/O ratio of CNG-1 and CNG-3 compared to CNG-6 further gives evidence of thin layer coating of the NG sheets on the  $CN_x$  backbone for both CNG-1 and CNG-3.

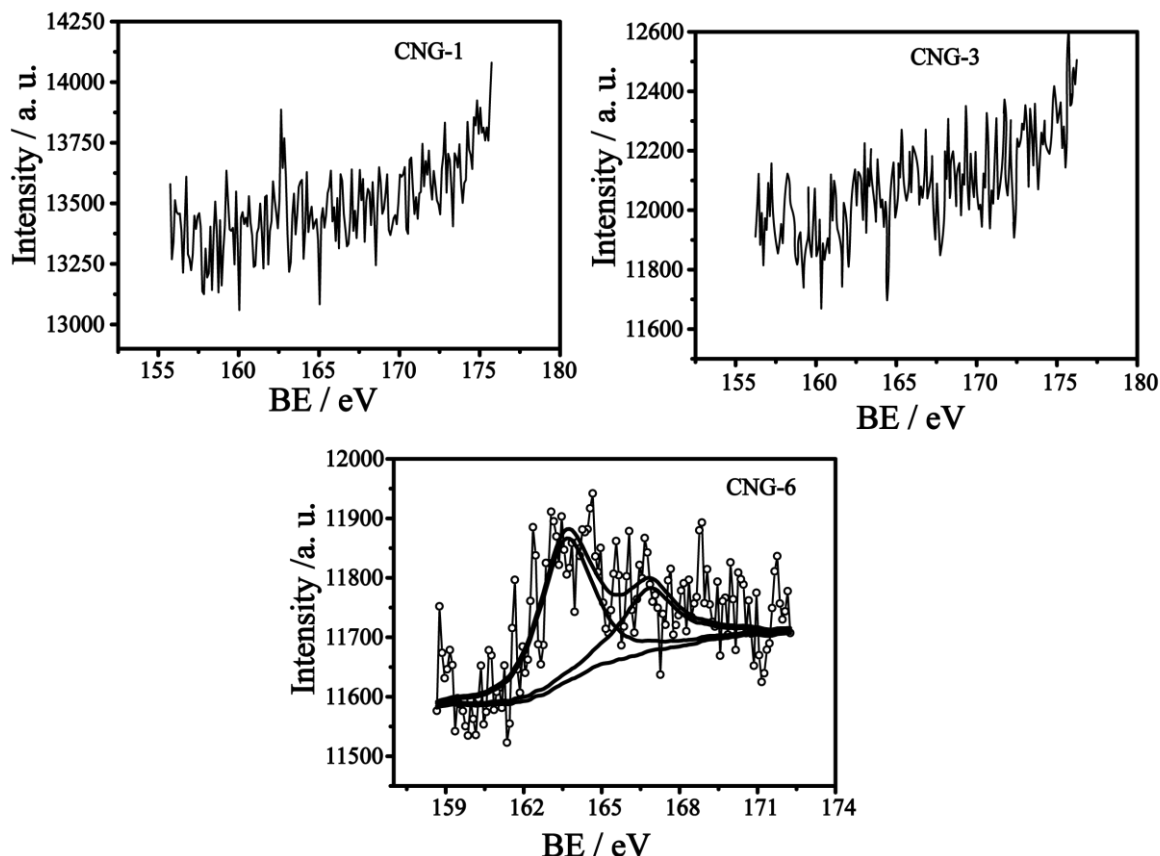


**Figure 2B.8:** XPS spectra of sulphur (S) in the CNG-1, CNG-3 and CNG-6 samples.

More interestingly, CNG-6 shows presence of 0.95 wt.% of sulphur, which is expected to be generated from MF (Figure 2B.8). Since the stability of sulphur at high temperature is very poor, it tends to easily escape from the MF during the high temperature annealing process. In the recent literatures, the amounts of sulphur doped in the carbon morphologies are found to be generally less than 1 wt.%.<sup>[31]</sup> Due to the thin layer wrapping of GO on MF before annealing to generate CNG-1 and CNG-3, sulphur will easily escape from the system at high temperature without incorporating in the carbon matrix. On the other hand, the presence of large amount of GO sheets in CNG-6 helps entrapment of some sulphur and its subsequent doping in the graphene sheets along with the nitrogen atoms.

Deconvoluted N1s spectra (Figure 2B.9) of CNG show that the nitrogen environment varies with the loading of graphene in CNGs.  $CN_x$  shows three different nitrogen environments in it. They are assigned as pyridinic, graphitic and oxides of

nitrogen respectively at the binding energies of 398.00, 400.00 and 405.70 eV. Similarly, Bulk NG also shows pyridinic, pyrrolic and graphitic nitrogen respectively at 398.00, 399.10 and 400.80 eV. Along with the pyridinic, pyrrolic/pyridone and graphitic nitrogens,

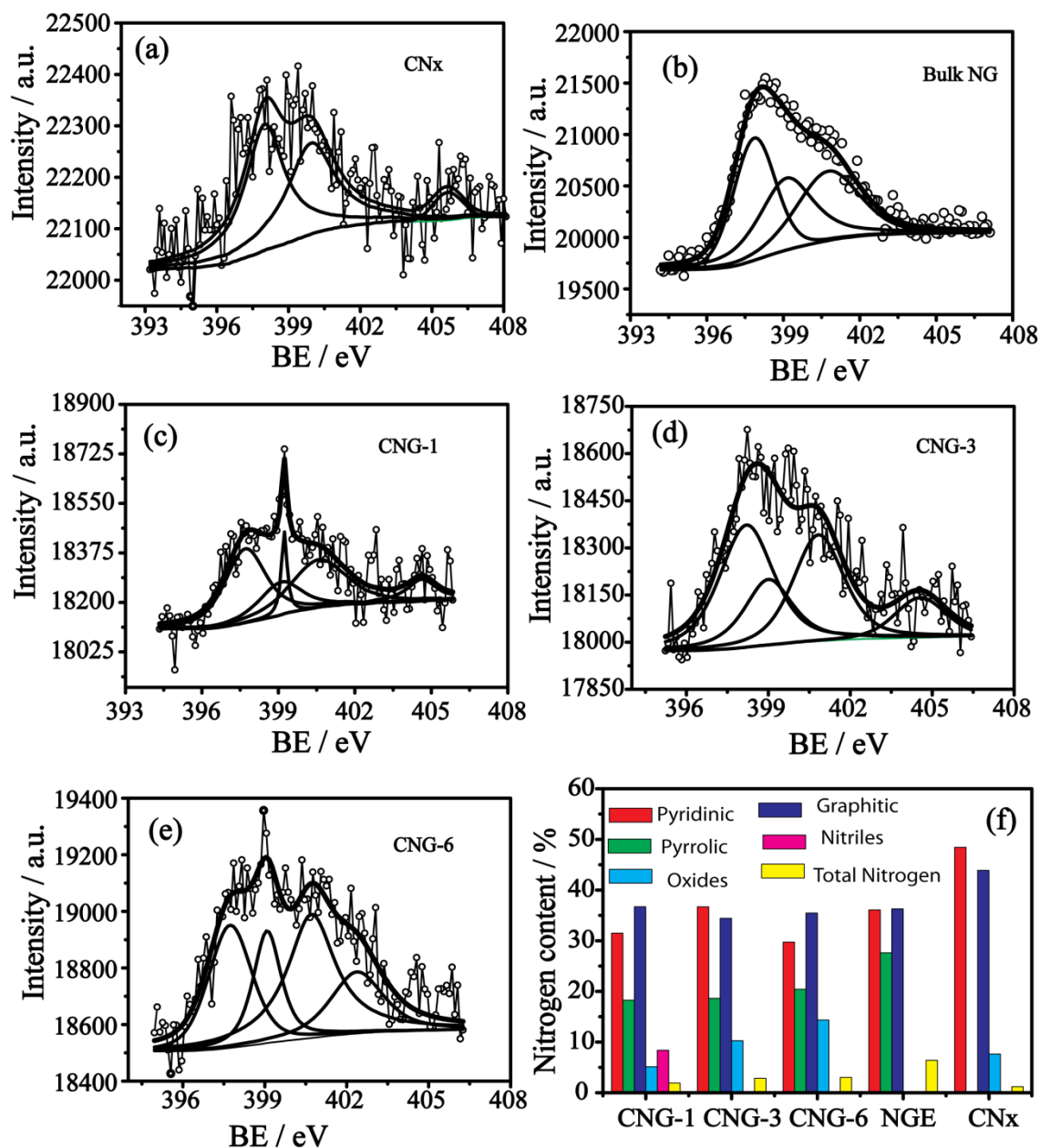


**Figure 2B.9:** Deconvoluted XPS spectra of N1s of (a) CN<sub>x</sub>, (b) Bulk NG, (c) CNG-1, (d) CNG-3 and (e) CNG-6 and (f) percentage of different types of nitrogen content of CN<sub>x</sub>, Bulk NG, CNG-1, CNG-3 and CNG-6.

CNG-1 shows binding energy signatures corresponding to benzenoid amine –NH– type nitrogen (399.54 eV) and oxides of nitrogen (404.54 eV). However, the benzenoid amine type environment is absent in case of CNG-3 and CNG-6. Since the nitrogen environment is seriously changing with the graphene content, the pyridinic nitrogen is found to be highest for CNG-3 (36.69 wt.%) compared to CNG-1 (31.51 wt.%) and CNG-6 (29.73 wt.%). At the same time, the graphitic nitrogen contents in CNG-3 (34.43 wt.%) and CNG-6 (35.3 wt.%) are appeared to be almost same. Pyrrolic/pyridone nitrogen content in the three composites is increasing with increase in the graphene loading and is in the order of CNG-1 (18.26 wt.%) < CNG-3 (18.61 wt.%) < CNG-6 (20.42 wt.%). Asifa *et. al.* reported that the binding energy of the pyridone and pyrrolic nitrogen coordination in deconvoluted N1s spectra is indistinguishable and the pyridone content improves the oxygen adsorption.<sup>[32]</sup> Since the C/O ratio of the CNG samples is less compared to Bulk NG, the chance for formation of pyridone in the CNG samples is evident. The oxide environment of nitrogen also is strongly affected by the graphene content and it is increasing with the graphene loading. CNG-6 (14.36 wt.%) has the highest oxide content whereas CNG-1 (5.13 wt.%) has the lowest. Thus, from the deconvoluted XPS N1s spectra of the CNG samples, it can be unambiguously inferred that the types of nitrogen coordination and their weight percentages differ substantially with respect to the graphene loading. The nitrogen coordination and its oxide will seriously affect the overall electrochemical performance towards dioxygen reduction in acidic medium.

### 2B.2.5 Electrochemical studies

Cyclic voltammetry (CV) of all the electrocatalysts was carried out at a scan rate of 5 mV s<sup>-1</sup> in 0.1 M HClO<sub>4</sub>. For comparing the electrochemical activity of the systems, the testing of the CNG samples was done along with CN<sub>x</sub>, bulk NG and a physical mixture of the both in a ratio of 1:1 under the similar conditions. In Figure 2B.10, bulk NG shows a very broad cathodic peak at 0.59 V with very low double layer charging current. In contrary, the contribution by double layer charging of CN<sub>x</sub> is high in association with a cathodic peak shift towards a more positive value of 0.73 V. CNG-1 shows capacitance in between Bulk NG and CN<sub>x</sub> with the cathodic peak at 0.60 V. CNG-3 and CNG-6 show high double layer charging contribution compared to CNG-1 and CN<sub>x</sub> with the cathodic peaks respectively at 0.72 and 0.62 V. The physical mixture of both CN<sub>x</sub> and Bulk NG also shows the cathodic

peak at a higher potential of 0.72 V compared to  $\text{CN}_x$  and bulk NG. CNG-3 and CNG-6 show high capacitive nature compared to Bulk NG. High capacitive nature of CNG-3 and CNG-6 attributes to the peculiar morphology of the catalysts. Three dimensional (3-D) morphology of CNG-3 provides proper channels for mass transport and, hence, helps to establish maximum electrode-electrolyte interfaces. At the same time, wrapping of the graphene sheets on the  $\text{CN}_x$  tetrapod units helps the system to expose more number of the active reaction sites for effective dioxygen adsorption and its reduction. These structural benefits obtained from the 3-D morphology of CNG is expected to help the system to shift the reduction peak potential towards more positive side compared to Bulk NG.

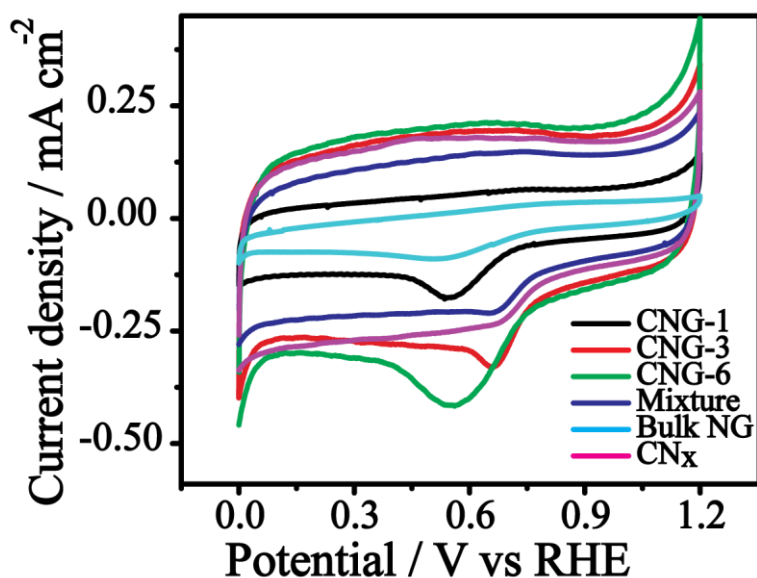


**Figure 2B.10:** Cyclic voltammograms of the non-metal catalysts recorded at a scan rate of  $5 \text{ mV s}^{-1}$  in  $0.1 \text{ M HClO}_4$  solution.

Further insight about ORR activity of these electrocatalysts has been gained through an analysis using rotating disc electrode (RDE), where the linear sweep voltammograms (LSVs) were recorded in oxygen saturated  $0.1 \text{ M HClO}_4$  at a scan rate of  $5 \text{ mV s}^{-1}$  with an electrode rotation speed of 1600 rpm (Figure 2B.11 a). For comparison purpose, the testing was also done by using a standard Pt supported carbon (40 wt.% Pt on carbon, Pt/C) catalyst under the same experimental conditions. From Figure 5b, it is clear that Bulk NG shows substantially poor activity towards ORR in acid medium. The ORR onset potential of bulk NG is more negative (0.72 V) and the reduction current appears to be very low compared to the other electrocatalysts. However,  $\text{CN}_x$  shows a more positive



onset potential (0.87V) compared to the pure NG sheets with improved current density. Unfortunately, due to poor electrical conductivity of  $\text{CN}_x$ , the LSV profile suffers from a greater ohmic contribution. Contrary to both  $\text{CN}_x$  and the NG sheets, CNG-1 shows activity in between that of  $\text{CN}_x$  and NG; this clearly indicates that the active sites are not enough to facilitate oxygen adsorption and its reduction. It is interesting to note that the physical mixture of both  $\text{CN}_x$  and NG shows activity higher than the parent compounds and CNG-1, which further supports the theoretical finding of Qiao *et al.*<sup>[33]</sup> It shows the onset potential at 0.88 V with a maximum reduction current density of  $2.56 \text{ mA cm}^{-2}$  at 0.2 V. This indicates that, just a physical mixing of  $\text{CN}_x$  with NG sheets is favourably tuning the active reaction centres to obtain enhanced ORR activity.

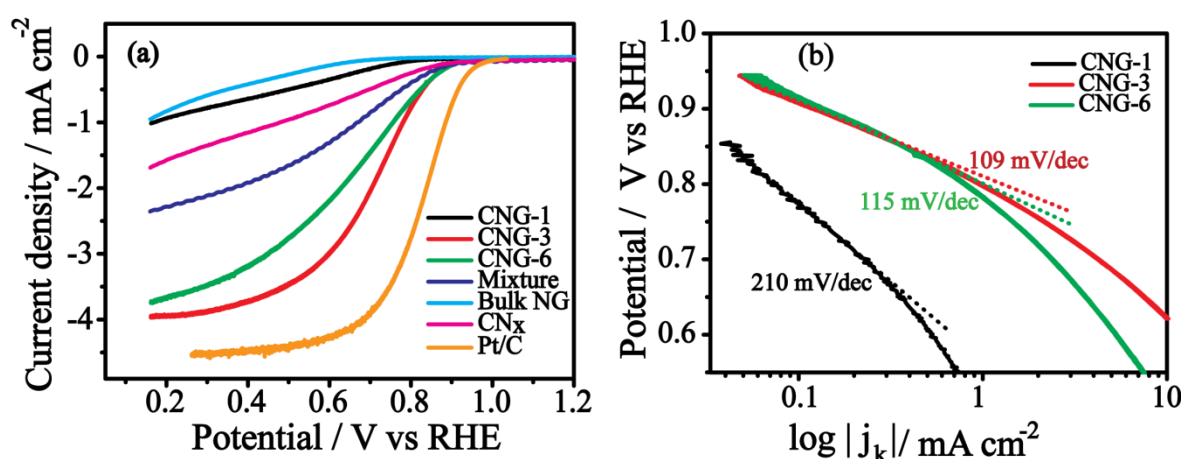


**Figure 2B.11:** (a) Linear sweep voltammograms (LSVs) of the prepared samples and Pt/C taken in 0.1 M oxygen saturated  $\text{HClO}_4$  at an electrode rotation speed of 1600 rpm and a scan rate of  $5 \text{ mV s}^{-1}$  and (b) Tafel slopes of the CNG catalysts at high potential.

A clear advantage in terms of both the ORR onset potential and limiting current density has been observed in the case of CNG-3. The catalyst displays an onset potential at 0.90 V with a maximum current density of  $3.91 \text{ mA cm}^{-2}$  at 0.2 V. With this enhancement in the activity, CNG-3 approaches the activity of the Pt/C catalyst with an overpotential difference as close as 90 mV, which is lower than the overpotential values reported recently for the non-metal electrocatalysts in acidic medium. CNG-6 also shows the same onset potential as CNG-3 but the current density ( $3.67 \text{ mA cm}^{-2}$ ) at 0.2 V is lower compared to CNG-3. However, the half wave potential of CNG-3 is 50 mV higher than that of CNG-6 and 120 mV lower compared to Pt/C. Improved  $E_{1/2}$  of CNG-3 indicates more active reaction centres of CNG-3 compared to CNG-6 even though the intrinsic ORR

activity is same. This is further confirmed from the Tafel plots of the CNG samples in the high potential range (Figure 2B.11 b). CNG-3 displays a Tafel slope of  $109 \text{ mV dec}^{-1}$  in comparison with  $120$  and  $214 \text{ mV dec}^{-1}$  shown by CNG-6 and CNG-1, respectively. This explicitly indicates that the ORR kinetics is varying with respect to the NG loading. The improved ORR activity of CNG-3 is mainly ascribed to the peculiar morphology acquired by the system when NG gets wrapped on  $\text{CN}_x$ . Even though mixing of bulk NG and  $\text{CN}_x$  shows improved activity compared to its parent counterparts, the active reaction sites are not sufficient enough to bring an extensive activity modulation. However, in case of CNG-3, wrapping of NG on  $\text{CN}_x$  provides a more feasible way to achieve a simultaneous modulation of both the active reaction centres and electrical conductivity. This controlled interplay and synergetic effects of both  $\text{CN}_x$  and NG sheets in CNG-3 assist the oxygen adsorption/reduction process. At the same time, the more interconnected morphology and loose distribution of the graphene sheets with the help of the  $\text{CN}_x$  tetrapods provide better accessibility of the active sites to initiate the process.

It should be noted that the ORR mechanism involving the 4-electron pathway leading to water is the preferred one compared to the 2-electron pathway leading the hydrogen peroxide. In order to get an insight into the mechanism and to quantify the formation of peroxide during ORR, Rotating Ring Disk Electrode (RRDE) analysis was carried out. It can be clearly seen from Figure 2B.12a that CNG-3 yields a negligible (3.5 mole %) amount of  $\text{H}_2\text{O}_2$  in the entire potential range. CNG-6, on the other hand, produces almost 7.5 mole % of peroxide during the reaction. Peroxide formation of CNG-1 is found to be higher at more positive potential and it slowly gets decreased at higher negative potentials. At 0.2 V, CNG-1 shows 9.5 mole % of peroxide yield at 0.2 V. The number of electrons participated in the reduction process has been calculated from the RRDE analysis (Figure 2B.12 b), which confirms that both CNG-3 and CNG-6 follow mainly direct 4-electron transfer pathway whereas CNG-1 follows a mixed kinetics involving contributions from both the 2- and 4-electron transfer reactions. Figure 2B.12 c shows Koutcky-Levich plots (K-L plot) of the CNG samples prepared at a potential of 0.34 V. Parallel behaviour of the straight lines of CNG-3 and CNG-6 indicates similar electrode reactions with 4-electron transfer pathway for ORR. CNG-1, on the other hand, shows a slight deviation from the parallel nature of CNG-3 and CNG-6. This indicates contributions by other side reactions in CNG-1. Apart from the peculiar morphology of CNG-3, the ORR activity is strongly influenced by the active reaction centre formation during the high temperature

annealing. Theoretical studies clearly emphasize that defect as well as nitrogen coordination are playing vital roles in the active site modulation to reduce oxygen molecule through the 4-electron pathway. The XPS analysis unambiguously confirms that the nitrogen coordination in the CNG samples is influenced strongly by the NG loading. Compared to CNG-1 and CNG-6, the pyridinic nitrogen content is high in CNG-3. Similarly, the pyrrolic/pyridone content in the CNG samples is also found to be increasing with the NG loading.

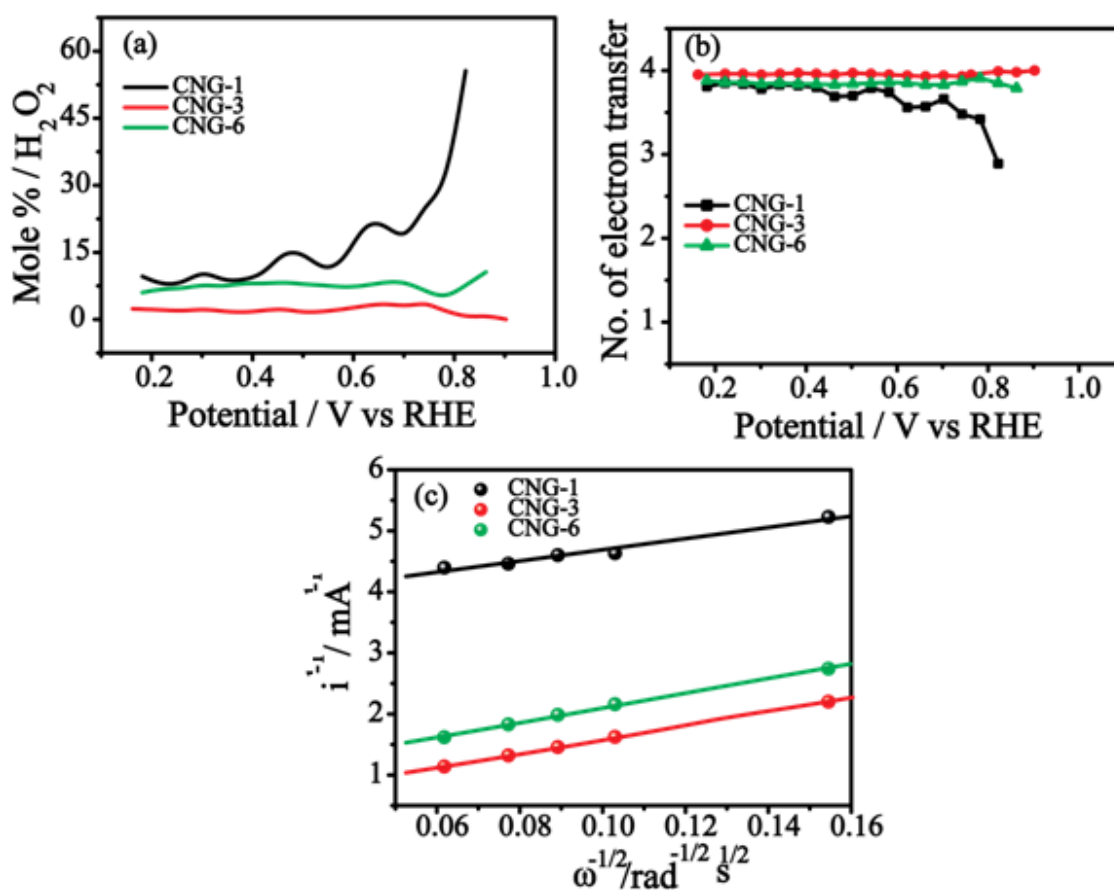


**Figure 2B.12:** (a) The percentage of hydrogen peroxide formation calculated by using a rotating ring disc electrode (RRDE) in 0.1 M HClO<sub>4</sub> at an electrode rotation speed of 1600 rpm and a voltage scan rate of 5 mV s<sup>-1</sup>, (b) the plot representing the number of electrons transferred vs. the potential as calculated from RRDE and (c) K–L plots of the CNG electrocatalysts obtained at a potential of 0.34 V vs. RHE.

It is well known that the pyridinic as well as the pyrrolic/pyridone nitrogen content improves the ORR activity.<sup>[30, 32]</sup> In CNG-1 and CNG-3, the chances for the formation of the pyridinic nitrogen is more compared to the pyrrolic nitrogen because of the lower

loading of the NG sheets and lower C/O ratio in these materials. In contrary, CNG-6 has almost similar C/O ratio compared to the bulk NG sheets, which reduces the chance for the creation of more pyridone type nitrogen but it has a mixed distribution of the pyrrole/pyridone type nitrogen coordination. Similarly, trace amount of sulphur detected in CNG-6 is not expected to influence the ORR activity significantly. The enhanced ORR activity of CNG-3 can easily connect to the improved coordination of the stable pyridinic and pyridine type nitrogens. It is reported that the hydroxypyridine a tautomeric form of pyridone forms an adduct with dioxygen.<sup>[34]</sup> This stable adduct has an oxygen chemisorption geometry similar to that of Pt.<sup>[35]</sup> From this, we believe that the co-presence of both N and O in CNG-3 and the stable adduct formation between the oxygen molecule and pyridone along with the high pyridinic nitrogen content help the system to achieve high ORR activity.

Along with the improved ORR activity, CNG-3 shows excellent tolerance towards methanol (Figure 2B.13 a) compared to Pt/C (Figure 2B.13 b). Further, to get more information about the electrochemical stability of CNG-3, accelerated durability test (ADT) was performed for 5000 cycles. CV was performed at  $100 \text{ mV s}^{-1}$  scan rate in between a potential window of 0.7 to 1.3 V under oxygen purging. LSV was taken before and after ADT at 1600 rpm with a scan rate of  $5 \text{ mV s}^{-1}$ . From Figure 2B.14 a, the ORR activity of CNG-3 is found to be increased after 1000 stability cycling with more positive shift in both the onset potential as well as  $E_{1/2}$ .

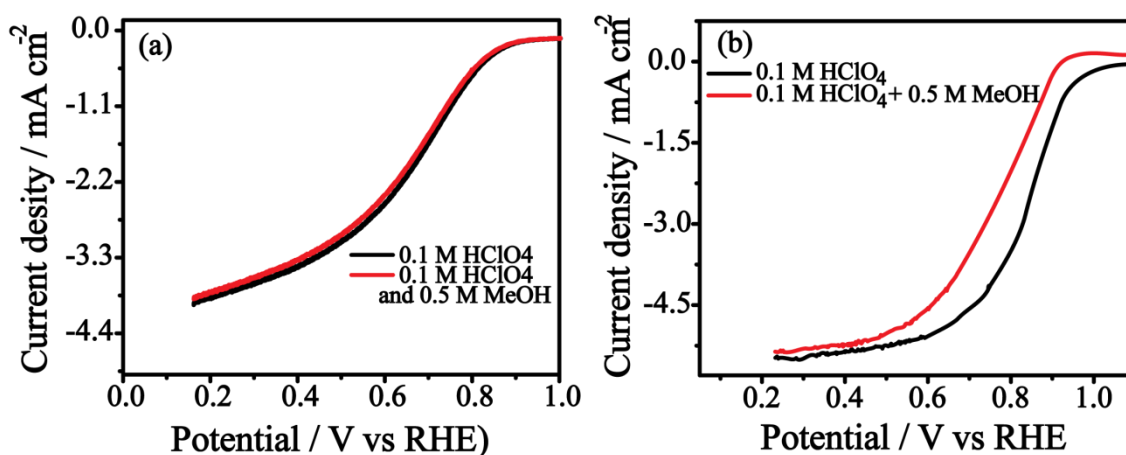


**Figure 2B.13:** (a) Methanol crossover study of (a) CNG-3 and (b) Pt/C with an electrode rotation rate of 1600 rpm at a scan rate of  $5 \text{ mV s}^{-1}$ . 0.5 M methanol was added into 0.1 M  $\text{HClO}_4$  electrolyte to evaluate the crossover effect.

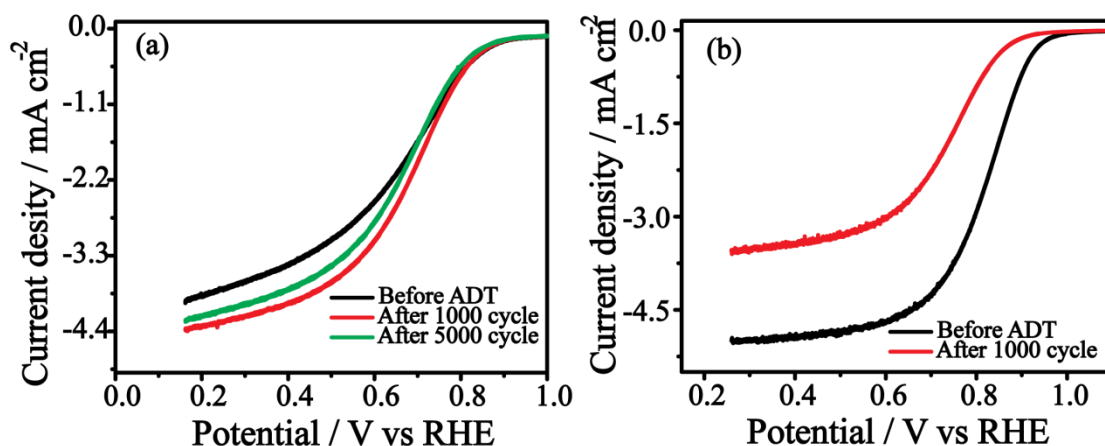


**Figure 2B.14:** LSVs of (a) CNG-3 and (b) Pt/C before and after ADT at 1600 rpm with 5  $\text{mV s}^{-1}$  scan rate in oxygen saturated 0.1 M  $\text{HClO}_4$ .

This clearly indicates that the intrinsic ORR activity is getting modulated simultaneously as the system passes through the potential cycling. However, it is found that the benefit of the potential induced active site modulation is not happening continuously. This is evident from the fact that, after 5000 cycles, the intrinsic ORR activity is slightly getting decreased as evident from the negative shift in the onset potential without changing the reduction current density. This type of behaviour was recently reported by Zelanay *et. al.* in their work based on carbon nanotube-carbon particle composite.<sup>[36]</sup> Contrary to CNG-3, Pt/C shows negative shift in the onset potential as well as  $E_{1/2}$  after 5000 cycles (Figure 2B.14 b). This is mainly due to the reduction in the catalytic centre due to carbon corrosion at higher positive potential. These studies, thus, clearly show that CNG-3 is a promising electrocatalyst with improved fuel tolerance and electrochemical stability along with higher ORR activity in acidic medium.

## 2.2 Conclusion

Two different approaches have been carried out to synthesize NGE with improved active reaction centre density by modifying its surface area, nitrogen coordination and morphology.

NGE prepared by the high temperature heat-treatment of pyrrole reduced graphene oxide in an inert atmosphere shows high surface area of  $528 \text{ m}^2 \text{ g}^{-1}$ . The high surface area of the prepared NGE is attributed to the prevention of restacking by the oligomeric form of

pyrrole formed during the redox reaction between pyrrole and GO. The formed oligomeric form of pyrrole acts as a nitrogen source for NGE. The study reveals the fact that the enhanced proportions of the pyrrolic nitrogen along with the mesoporous structure of graphene are the main reasons for the enhanced catalytic activity towards ORR. Most importantly, NGE-1000 catalyst shows comparable onset potential (0.05 V vs. Hg/HgO) with 40 wt.% Pt/C, which involves a 4- electron pathway for ORR in alkaline medium. Moreover, the fuel tolerance and durability under the electrochemical environment of the NGE catalyst are found to be superior to that of the Pt/C catalyst.

In another approach, a 3-dimensional (3D) form of NGE was prepared by one-step thermal treatment of melamine foam soaked with graphene oxide at 900 °C in inert atmosphere. During the high temperature annealing, MF gets converted into carbon nitride (CN<sub>x</sub>) with concomitant conversion of GO to nitrogen doped graphene (NG). The nitrogen liberated from MF is trapped by the graphene sheets and the thus formed nitrogen doped graphene (NG) subsequently gets wrapped onto CN<sub>x</sub>, which has maintained an interconnected porous structure through the tetrapod units. The peculiar interconnected morphology of the prepared materials provides high specific surface area by essentially reducing the restacking of the graphene sheets with the help of the CN<sub>x</sub> backbone. The interconnected morphology also maintains accessible channels and pores throughout the material and this helps NG to effectively expose the active centres for the reactants. More interestingly, with the number of dip-coating of MF in the GO solution, a significant difference in the nature of the doped nitrogen sites is observed after the thermal treatment process. The sample prepared after the annealing of MF with three dipping cycles in the GO solution (CNG-3) shows improved ORR activity with 90 mV overpotential compared to Pt/C and it reduces dioxygen molecule to water through the preferred 4-electron transfer mechanism. XPS analysis clearly shows the presence of pyridinic and pyridone type nitrogens, which are found to be contributing efficiently for ORR. More interestingly, CNG-3 shows improved electrochemical stability with efficient fuel selectivity.

## 2.3 Reference

- [1] a)Y. Sun, Q. Wu, G. Shi, *Energy Environ. Sci.* **2011**, *4*, 1113-1132; b)M. Liu, R. Zhang, W. Chen, *Chem. Rev.* **2014**, *114*, 5117-5160.
- [2] D. Chen, H. Feng, J. Li, *Chem. Rev.* **2012**, *112*, 6027-6053.

- [3] C. Mattevi, G. Eda, S. Agnoli, S. Miller, K. A. Mkhoyan, O. Celik, D. Mastrogiovanni, G. Granozzi, E. Garfunkel, M. Chhowalla, *Adv. Function. Mater.* **2009**, *19*, 2577-2583.
- [4] a)H. Wang, T. Maiyalagan, X. Wang, *ACS Catal.* **2012**, *2*, 781-794; b)J. P. Paraknowitsch, A. Thomas, *Energy Environ. Sci.* **2013**, *6*, 2839-2855; c)K. N. Wood, R. O'Hayre, S. Pylypenko, *Energy Environ. Sci.* **2014**, *7*, 1212-1249.
- [5] D. Wei, Y. Liu, Y. Wang, H. Zhang, L. Huang, G. Yu, *Nano Lett.* **2009**, *9*, 1752-1758.
- [6] L. S. Panchakarla, K. S. Subrahmanyam, S. K. Saha, A. Govindaraj, H. R. Krishnamurthy, U. V. Waghmare, C. N. R. Rao, *Adv. Mater.* **2009**, *21*, 4726-4730.
- [7] R. Imran Jafri, N. Rajalakshmi, S. Ramaprabhu, *J. Mater. Chem.* **2010**, *20*, 7114-7117.
- [8] a)D. Geng, Y. Chen, Y. Chen, Y. Li, R. Li, X. Sun, S. Ye, S. Knights, *Energy Environ. Sci.* **2011**, *4*, 760-764; b)Z.-H. Sheng, L. Shao, J.-J. Chen, W.-J. Bao, F.-B. Wang, X.-H. Xia, *ACS Nano* **2011**, *5*, 4350-4358.
- [9] Y. Zhang, K. Fugane, T. Mori, L. Niu, J. Ye, *J. Mater. Chem.* **2012**, *22*, 6575-6580.
- [10] a)J. Casanovas, J. M. Ricart, J. Rubio, F. Illas, J. M. Jiménez-Mateos, *J. Am. Chem. Soc.* **1996**, *118*, 8071-8076; b)C. P. Ewels, M. Glerup, *Journal of Nanoscience and Nanotechnology* **2005**, *5*, 1345-1363.
- [11] a)Y. Shao, S. Zhang, M. H. Engelhard, G. Li, G. Shao, Y. Wang, J. Liu, I. A. Aksay, Y. Lin, *J. Mater. Chem.* **2010**, *20*, 7491-7496; b)S. Kundu, T. C. Nagaiah, W. Xia, Y. Wang, S. V. Dommele, J. H. Bitter, M. Santa, G. Grundmeier, M. Bron, W. Schuhmann, M. Muhler, *J. Phy. Chem. C* **2009**, *113*, 14302-14310.
- [12] a)K. Gong, F. Du, Z. Xia, M. Durstock, L. Dai, *Science* **2009**, *323*, 760-764; b)L. Feng, Y. Yan, Y. Chen, L. Wang, *Energy Environ. Sci.* **2011**, *4*, 1892-1899.
- [13] Z. Luo, S. Lim, Z. Tian, J. Shang, L. Lai, B. MacDonald, C. Fu, Z. Shen, T. Yu, J. Lin, *J. Mater. Chem.* **2011**, *21*, 8038-8044.
- [14] L. Lai, J. R. Potts, D. Zhan, L. Wang, C. K. Poh, C. Tang, H. Gong, Z. Shen, J. Lin, R. S. Ruoff, *Energy Environ. Sci.* **2012**, *5*, 7936-7942.
- [15] D. C. Marcano, D. V. Kosynkin, J. M. Berlin, A. Sinitskii, Z. Sun, A. Slesarev, L. B. Alemany, W. Lu, J. M. Tour, *ACS Nano* **2010**, *4*, 4806-4814.
- [16] C. A. Amarnath, C. E. Hong, N. H. Kim, B.-C. Ku, T. Kuila, J. H. Lee, *Carbon* **2011**, *49*, 3497-3502.

- [17] I. K. Moon, J. Lee, R. S. Ruoff, H. Lee, *Nat Commun* **2010**, *1*, 73.
- [18] Y. Ma, S. Jiang, G. Jian, H. Tao, L. Yu, X. Wang, X. Wang, J. Zhu, Z. Hu, Y. Chen, *Energy Environ. Sci.* **2009**, *2*, 224-229.
- [19] K. N. Kudin, B. Ozbas, H. C. Schniepp, R. K. Prud'homme, I. A. Aksay, R. Car, *Nano Lett.* **2008**, *8*, 36-41.
- [20] a)B. Guo, Q. Liu, E. Chen, H. Zhu, L. Fang, J. R. Gong, *Nano Lett.* **2010**, *10*, 4975-4980; b)L. G. Cançado, K. Takai, T. Enoki, M. Endo, Y. A. Kim, H. Mizusaki, A. Jorio, L. N. Coelho, R. Magalhães-Paniago, M. A. Pimenta, *Applied Physics Letters* **2006**, *88*, 163106.
- [21] C. Zhang, L. Fu, N. Liu, M. Liu, Y. Wang, Z. Liu, *Adv. Mater.* **2011**, *23*, 1020-1024.
- [22] a)S. Yang, L. Zhi, K. Tang, X. Feng, J. Maier, K. Müllen, *Adv. Function. Mater.* **2012**, *22*, 3634-3640; b)S. Yang, X. Feng, X. Wang, K. Müllen, *Angew. Chem. Int. Ed.* **2011**, *50*, 5339-5343.
- [23] a)Y. Sun, C. Li, Y. Xu, H. Bai, Z. Yao, G. Shi, *Chem. Commun.* **2010**, *46*, 4740-4742; b)S. Stankovich, D. A. Dikin, R. D. Piner, K. A. Kohlhaas, A. Kleinhammes, Y. Jia, Y. Wu, S. T. Nguyen, R. S. Ruoff, *Carbon* **2007**, *45*, 1558-1565; c)K. R. Lee, K. U. Lee, J. W. Lee, B. T. Ahn, S. I. Woo, *Electrochem. Commun.* **2010**, *12*, 1052-1055.
- [24] M. Pumera, B. Šmíd, X. Peng, D. Golberg, J. Tang, I. Ichinose, *Chemistry – A European Journal* **2007**, *13*, 7644-7649.
- [25] E. Yoo, J. Nakamura, H. Zhou, *Energy Environ. Sci.* **2012**, *5*, 6928-6932.
- [26] a)X. Li, H. Wang, J. T. Robinson, H. Sanchez, G. Diankov, H. Dai, *J. Am. Chem. Soc.* **2009**, *131*, 15939-15944; b)T. N. Huan, T. Van Khai, Y. Kang, K. B. Shim, H. Chung, *J. Mater. Chem.* **2012**, *22*, 14756-14762.
- [27] L. Zhang, Z. Xia, *J. Phy. Chem. C* **2011**, *115*, 11170-11176.
- [28] L. Yu, X. Pan, X. Cao, P. Hu, X. Bao, *J. Catal.* **2011**, *282*, 183-190.
- [29] Z. Lin, G. Waller, Y. Liu, M. Liu, C.-P. Wong, *Adv. Energy Mater.* **2012**, *2*, 884-888.
- [30] L. Li, A. Manthiram, *Adv. Energy Mater.* **2014**, DOI: 10.1002/aenm.201301795.
- [31] a)Z. Yang, Z. Yao, G. Li, G. Fang, H. Nie, Z. Liu, X. Zhou, X. a. Chen, S. Huang, *ACS Nano* **2011**, *6*, 205-211; b)S. Some, Y. Kim, Y. Yoon, H. Yoo, S. Lee, Y. Park, H. Lee, *Sci. Rep.* **2013**, *3*.



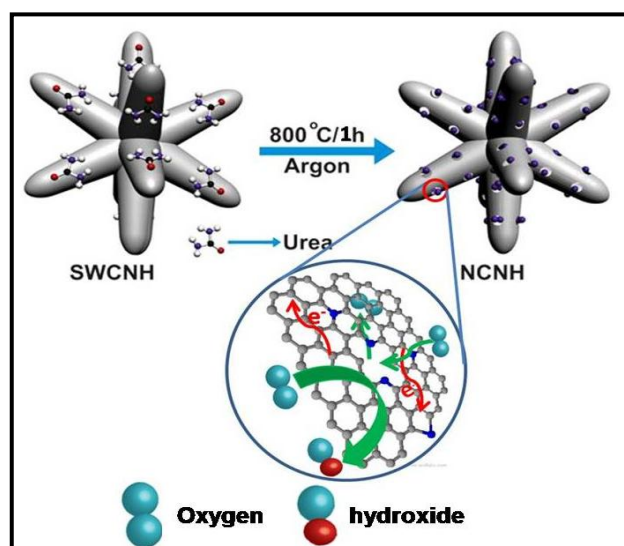
- [32] R. Silva, D. Voiry, M. Chhowalla, T. Asefa, *J. Am. Chem. Soc.* **2013**, *135*, 7823-7826.
- [33] Y. Zheng, Y. Jiao, J. Chen, J. Liu, J. Liang, A. Du, W. Zhang, Z. Zhu, S. C. Smith, M. Jaroniec, G. Q. Lu, S. Z. Qiao, *J. Am. Chem. Soc.* **2011**, *133*, 20116-20119.
- [34] J. R. Pels, F. Kapteijn, J. A. Moulijn, Q. Zhu, K. M. Thomas, *Carbon* **1995**, *33*, 1641-1653.
- [35] P. B. Balbuena, D. Altomare, L. Agapito, J. M. Seminario, *J. Phys. Chem. B* **2003**, *107*, 13671-13680.
- [36] H. T. Chung, J. H. Won, P. Zelenay, *Nat Commun* **2013**, *4*, 1922.



## Chapter 3

### *Nitrogen doped carbon nanohorn and its metal chalcogenide composite as ORR electrocatalysts\**

This chapter focuses on the development of nitrogen doped carbon nanohorn (NCNH) and its metal chalcogenide composite for achieving improved ORR activity in alkaline medium. Nitrogen doping in single walled carbon nanohorn (SWCNH) was carried out by the high temperature annealing of SWCNH and urea mixture in an inert atmosphere. Surface area and electrical conductivity of SWCNH could be easily modulated during the nitrogen doping. More positive half wave potential ( $E_{1/2}$ ) of NCNH indicates that the active reaction centre density has been improved drastically by modifying the physical properties. Moreover, NCNH shows excellent electrochemical stability and fuel tolerance for ORR. Furthermore,  $\text{CoSe}_2$  nanoparticles were dispersed on the surface of NCNH to study the substrate effect of a non-precious catalyst towards ORR. Experimental results show that the nitrogen atoms in NCNH improve the ORR activity of  $\text{CoSe}_2$  and help to display more positive  $E_{1/2}$  by the system, which is even better than that displayed by the current *state-of-the-art* Pt/C catalysts. This further proved that the substrate also has a very critical role in a system in modulating the reaction centre density.  $\text{CoSe}_2$  supported NCNH ( $\text{CoSe}_2/\text{NCNH}$ ) shows excellent tolerance towards methanol and the system provides high power density ( $15 \text{ mW cm}^{-2}$ ) in micro-laminar flow fuel cells.



\* Contents of this chapter was published in the following research articles:

*S. M. Unni et al., Small, 2015, 11, 352-360.*

*S. M. Unni et al., ECS Trans., 2015, 64, 1-9.*

*S. M. Unni et al., ChemElectroChem, 2015, DOI:10.1002/celec.201500154.*

*A part of the studies discussed in this chapter was carried out at Universite de Poitiers, France, during the tenure of Raman-Charpak Fellowship – 2013.*

### 3.1 Introduction

Recently, heteroatom doped carbon morphologies have been identified as promising cathode materials for PEMFCs. Nevertheless, the activity towards dioxygen reduction is still lower compared to Pt in terms of the onset potential.<sup>[1]</sup> To reduce the energy required for oxygen reduction reaction (ORR), it is necessary to create more active sites on the electrocatalysts for high density chemisorptions of dioxygen.<sup>[2]</sup> Along with electron density and spin density changes around the carbons as induced by the heteroatom, creation of more and more active centres for ORR impart a proper solution for enhanced activity of these type of non-metal electrocatalysts.<sup>[1d]</sup> Since edges of carbon morphologies are more active towards doping, active site modulation is possible only by the incorporation of more edges or by improving the porosity on the surface.<sup>[1b]</sup> Porosity on the surface ultimately improves the surface area of the electrocatalyst. Many efforts have been given to enhance the surface area of carbon materials which include hard and soft template assisted syntheses, hydrothermal methods and annealing of high surface area materials like metal organic framework (MOF).<sup>[1d,3]</sup> However, all these synthetic strategies gravely affect the electronic conductivity of the materials.<sup>[4]</sup> Both high surface area and high electronic conductivity are prerequisites of any material targeting for energy device applications.

It is well-known that simple surface modification of carbon nanohorn (CNH) enhances its surface area from 350 to 1700 m<sup>2</sup> g<sup>-1</sup>.<sup>[5]</sup> As synthesised single walled carbon nanohorn (SWCNH) possesses surface area ranging from 300 – 400 m<sup>2</sup> g<sup>-1</sup>.<sup>[5]</sup> Surface area of nanohorn can be tuned by simple oxidation methods.<sup>[5-6]</sup> Since high surface area carbon morphologies have low electrical conductivity, heteroatom doping appears as an efficient strategy to enhance the conductivity as the process leads to a favourable change in the electron density of the material.<sup>[7]</sup> In this scenario, nitrogen doped carbon nanohorn with surface area more than 1500 m<sup>2</sup> g<sup>-1</sup>, holds unique benefits and the material deserves exploration for its application towards electrochemical oxygen reduction.

Very less number of studies has been carried out on the application of SWCNH in renewable energy sector. Few reports are available for the use of CNH as catalyst support for Pt in PEMFCs, supercapacitor electrodes and dye sensitized solar cells.<sup>[8]</sup> Recently, Zhao *et al* reported a composite of SWCNH and SnO<sub>2</sub> for lithium ion battery electrode.<sup>[9]</sup> Also, there are reports related to SWCNH based drug delivery systems with less cytotoxicity.<sup>[10]</sup> Even though few reports are available for nitrogen doped nanohorn

(NCNH) synthesis using arc discharge method<sup>[16]</sup>, there are no reports on the exploration of high surface area NCNH as an electrocatalyst for PEMFC cathode.

Nitrogen doping on SWCNH can bring in interesting modulations in the ORR activity of the system. Apart from this, the heteroatom doping can induce more favourable changes in the electrical conductivity of the material all the while retaining the high surface area of the morphology. Hence, NCNH can also be employed as a potential substrate for creating other ORR active sites based on non-precious metal based moieties. Basically, the theme of the present chapter is essentially an exploration of these two advantages of NCNH (*i.e.*, NCNH as an ORR catalyst as such and utilization of NCNH as a substrate for dispersing other potential non-precious metal based ORR active sites) with an aim to develop noble metal-free electrocatalysts with the ability to reduce oxygen at a substantially reduced overpotential. In this scenario, *Part A* of the present chapter mainly focuses on the nitrogen doping of SWCNH by simple thermal treatment in the presence of urea as a nitrogen source and *Part B* deals with the influence of NCNH to improve the electrochemical activity of a non-precious cobalt selenide (CoSe<sub>2</sub>) based active sites to enable the system to function as an efficient electrocatalyst towards oxygen reduction reaction.

## **Part A. Nitrogen doped carbon nanohorn as an efficient oxygen reduction electrocatalyst\***

### **3A.1 Experimental**

#### **3A.1.1 Materials**

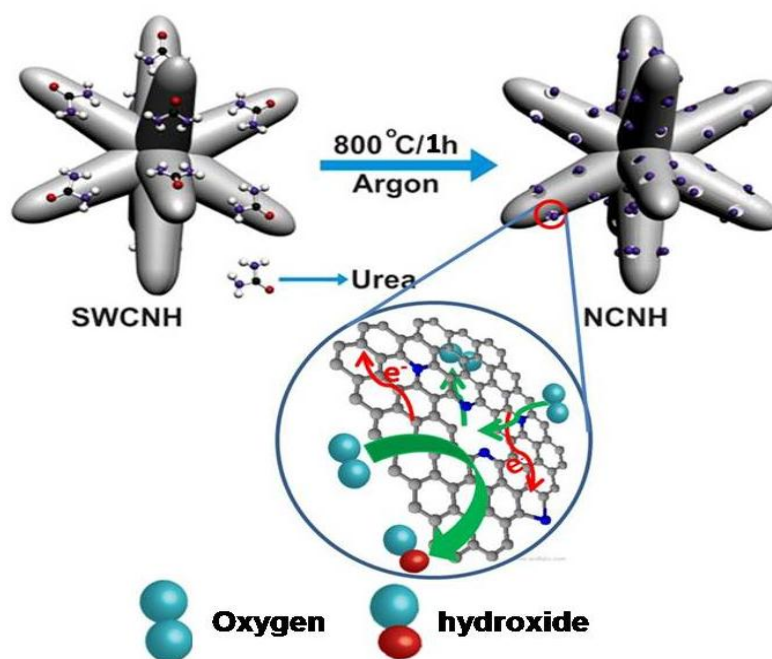
Single wall carbon nanohorn (SWCNH) was purchased from J K Impex. Urea, methanol, ethanol and hydrogen peroxide (30%) were purchased from Rankem Chemicals, India. All the chemical were used without further purification.

#### **3A.1.2 Functionalization and nitrogen doping of SWCNH**

Initially, SWCNH was mixed well with methanol solution in order to remove its puffy nature. After filtrating this mixture, the black powder obtained was dried under vacuum at a temperature of 80 °C for complete removal of methanol and the resulting sample was treated as pure SWCNH. 2 g of the resulting SWCNH was mixed with 250 ml of hydrogen peroxide in a round bottom flask and was refluxed for 5 h at 60 °C. After functionalization, the resulting solution was filtered and washed several times with deionised water for the complete removal of hydrogen peroxide. The resulting carbon

\* Reproduced with permission from 'Small 2015, 11, 352-360. Copyright © 2015 Wiley-VCH Verlag GmbH & Co. KGaA, Weinheim

nanohorn cake was dried under vacuum for overnight at a temperature of 80 °C. This material was treated as functionalized single wall carbon nanohorn (FCNH). 50 mg of FCNH was mixed with 250 mg of urea using a mortar and pestle followed by annealing at different temperatures (600, 800 and 1000 °C) for 1 h in argon atmosphere. The resulting nitrogen doped CNH derived at 600, 800 and 1000 °C are designated as N-600, N-800 and N-1000, respectively. For comparison, FCNH was also annealed at 800 and 1000 °C for 1 h without urea and the corresponding samples are named as C-800 and C-1000, respectively.



**Scheme 3A.1:** Schematic representation of the synthesis of nitrogen doped single walled nanohorn (NCNH) through urea treatment at high temperature. The inset shows the active centres formed around the pore opening, which facilitate ORR.

### 3A.1.3 Materials characterization

PANalytical X'pert Pro instrument was used to analyze the materials for X-ray diffraction (XRD) patterns. Data collection was done at a scan rate of 0.5° using Cu K $\alpha$  (1.5418 Å) radiation. HR 800 Raman spectrometer (Jobin Yvon, Horiba, France) using 632.8 nm green laser (NRS 1500 W) was used for Raman analysis of the samples. Morphology of the synthesized materials was analyzed using High Resolution Transmission Electron Microscope (HR-TEM) FEI model TECNAI G2 F30 instrument operated at an accelerating voltage of 300 kV (Cs = 0.6 mm, resolution 1.7 Å). 200 mesh copper grid coated with carbon film (Ted Pella) was used to coat the samples for TEM analysis. Samples were dispersed in methanol and coated on the TEM grid followed by drying under an IR lamp for complete removal of methanol. X-ray Photoelectron

Spectroscopy (XPS) analysis was carried out using VG Microtech Multilab ESCA 3000 spectrometer equipped with an Al K $\alpha$  X-ray source ( $h\nu = 1253.6$  eV).

### 3A.1.4 Electrochemical measurements

All the electrochemical analyses were carried out using an Autolab PGSTAT30 (Ecochemie) with conventional three-electrode test cell from Pine Instruments. Hg/HgO and glassy carbon rod were used as the reference and counter electrodes, respectively. Glassy carbon (GC) electrode (5 mm diameter) which is embedded in Teflon was used as the working electrode (WE) after drop coating the samples. Glassy carbon electrode was cleaned on a polishing cloth using alumina powder and washed using deionized water before the CV and RDE analyses. Catalyst slurry for the electrochemical analysis was prepared by dispersing 5 mg of the material in 1 ml of methanol water (3:2) solution by sonication. 10  $\mu$ L catalyst slurry was drop-casted on the electrode followed by 1.5  $\mu$ L of 0.1 % Nafion<sup>®</sup> solution in ethanol was applied on the surface of the catalyst layer. This electrode was dried using an IR lamp. Total catalyst loading on the electrode was 50  $\mu$ g. All the RDE experiments were carried out at a scan rate of 10 mV s<sup>-1</sup> in 0.1 M KOH solution at different electrode rotation, which was varied from 400 to 2500 rpm. Oxygen and nitrogen were used for creating oxygen rich and oxygen free environments respectively in 0.1 M KOH for the RDE analysis.

The Koutecky-Levich (K-L) plot, a plot of inverse of the electrode rotation speed and inverse of the current at different potential, was used to calculate the number of electrons. Linear fit of K-L plot gives intercept corresponding to the inverse of kinetic current whereas the slope of the plot leads to the calculation of the number of electron transfer using the equation:

$$B = 0.62nFC_{O_2}D_{O_2}^{2/3}\nu^{-1/6}\omega^{1/2} \text{-----} (1)$$

where 'n' is the number of electron transfer, 'F' is the Farady constant (96486 C mol<sup>-1</sup>), 'C<sub>O<sub>2</sub></sub>' is the concentration of oxygen in 0.1 M KOH (1.2 X 10<sup>-3</sup> mol l<sup>-1</sup>), 'D<sub>O<sub>2</sub></sub>' is the diffusion coefficient of oxygen in 0.1 M KOH solution (1.9 X 10<sup>-5</sup> cm s<sup>-1</sup>) and 'v' is the kinematic viscosity.

The number of electron transfer and peroxide percentage were determined on the basis of the rotating ring disc electrode (RRDE) voltammogram using the following equations:

$$n = 4 \times \frac{I_d}{I_d + \frac{I_r}{N}} \text{-----} (2)$$

$$H_2O_2 \% = 200 \times \frac{\frac{I_r}{N}}{I_d + \frac{I_r}{N}} \text{-----} (3)$$

where  $I_d$  is the disc current,  $I_r$  is the ring current, and  $N$  is the collection efficiency of the Pt ring (0.37). Area of the glassy carbon electrode used for the RRDE analysis is  $0.24 \text{ cm}^2$ .

Chronoamperometric (CA) measurements were carried out at a potential of  $-0.05 \text{ V}$  vs Hg/HgO in oxygen saturated  $0.1 \text{ M KOH}$  solution. After  $300 \text{ s}$  of the analysis,  $2 \text{ ml}$  of  $3 \text{ M}$  methanol was applied in order to understand the methanol tolerance of the materials.

### 3A.1.5 Anion exchange membrane fuel cell test

#### 3A.1.5.1 Membrane pretreatment

Fumapem FAA membrane (FumaTech, Germany) was used for MEA preparation for an alkaline exchange membrane fuel cell testing. Fumapem FAA membrane was soaked in  $1 \text{ M KOH}$  solution for  $24 \text{ h}$  to replace the bromide ion by  $\text{OH}^-$  form followed by washing the membrane using DI water for several times. The wet form of the membrane with a thickness of  $65 \mu\text{m}$  was used for MEA making.

#### 3A.1.5.2 Electrode preparation

Conventional brush coating method was used for making the electrodes. The cathode layer was prepared by coating a slurry of N-800 and  $10 \text{ wt. \%}$  Fumion in N-methyl pyrrolidone (NMP) with a Fumion to carbon ratio (F/C) of  $0.8$  in isopropyl alcohol (IPA) and a catalyst loading of  $3 \text{ mg cm}^{-2}$  on a gas diffusion layer (GDL, SGL CC, Germany). At the anode,  $40\% \text{ Pt/C}$  (E-TEC) was used with a loading  $0.5 \text{ mg cm}^{-2}$  (F/C is  $0.8$ ). For comparison, the cathode layer was also made with  $40 \text{ wt. \% Pt/C}$  (E-TEC) with a Pt loading of  $0.8 \text{ mg cm}^{-2}$  and a F/C ratio of  $0.4$ .

#### 3A.1.5.3 MEA fabrication

For making MEA, the wet form of the membrane was kept between the electrodes and applied  $0.5 \text{ ton}$  pressure for  $30 \text{ seconds}$  at room temperature.

#### 3A.1.5.4 Test Station Details

The fuel cell performance was evaluated using an MEA with an active area of  $4 \text{ cm}^2$ . A standard test fixture received from Fuel Cell Technologies, Inc, USA, was used for the testing purpose. The testing was done by using a fuel cell test station (Fuel Cell Technologies, Inc, USA) by purging  $\text{H}_2$  with a flow rate of  $50 \text{ sccm}$  at the anode and  $\text{O}_2$  with a flow rate of  $100 \text{ sccm}$  at the cathode by maintaining a relative humidity of  $100 \%$  and a cell operating temperature of  $50 \text{ }^\circ\text{C}$ .



### 3A.2 Results and discussion

Simple thermal treatment of functionalized SWCNH (FCNH) and urea at higher temperature was used for the synthesis of NCNH. Functionalization of nanohorn creates large number of pores in it and the surface area increases dramatically from 300 to 1500 m<sup>2</sup> g<sup>-1</sup>. This highly porous nanostructure provides exceptionally reactive edges to improve doping on the edges. During the high temperature reaction, urea decomposes to form ammonia which induces the doping of nitrogen.<sup>[11]</sup> The functional groups present on the surface of SWCNH assist the doping process by interacting with the intermediate ammonia molecules. SWCNH samples annealed in presence of urea at 600, 800 and 1000 °C are designated as N-600, N-800 and N-1000 respectively. Similarly, functionalized SWCNH (FCNH) was annealed at 800 °C without urea for the purpose of comparison (C-800).

#### 3A.2.1 TEM and EDAX analysis

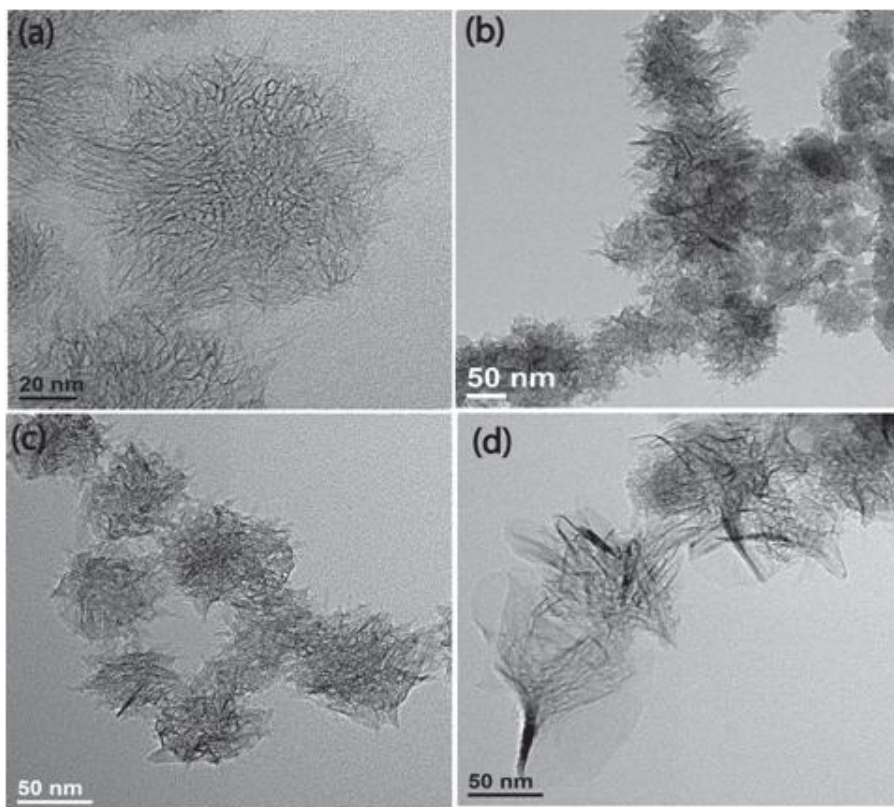


**Figure 3A.1:** HR-TEM images of a) SWCNH, b) FCNH, and c-d) N-800 under different magnifications.

Morphology of SWCNH was analysed using high resolution transmission electron microscopy (HR-TEM) which is shown in Figure 3A.1. From Figure 3A.1a, it can be seen that bundles of SWCNH are assembled to form a “dahlia” like morphology, having a size of around 60-80 nm. After functionalization, some morphology variations, even though not so prominent, occur due to the formation of functional groups as well as the generation of micro and mesopores (Figure 3A.1b). Moreover, no coalescence is observed after the functionalization and the individual bundles and their petals remain intact like untreated SWCNH. From Figure 3A.1c and d, it is clear that, after high temperature annealing, morphology of NCNH remains exactly similar to FCNH. This clearly indicates that the annealing at higher temperature in the presence of argon atmosphere doesn't make an apparent deformation in the inherent morphology of SWCNH. Further, EDAX (Figure 3A.2) analysis clearly shows the presence of nitrogen in the samples. Amount of nitrogen is varying with the annealing temperature. N-600 shows the highest weight percentage of nitrogen (9.31 wt. %) and the nitrogen content reduces with increase in the temperature. The nitrogen contents in N-800 and N-1000 are 7.42 and 6.37 wt. %, respectively.

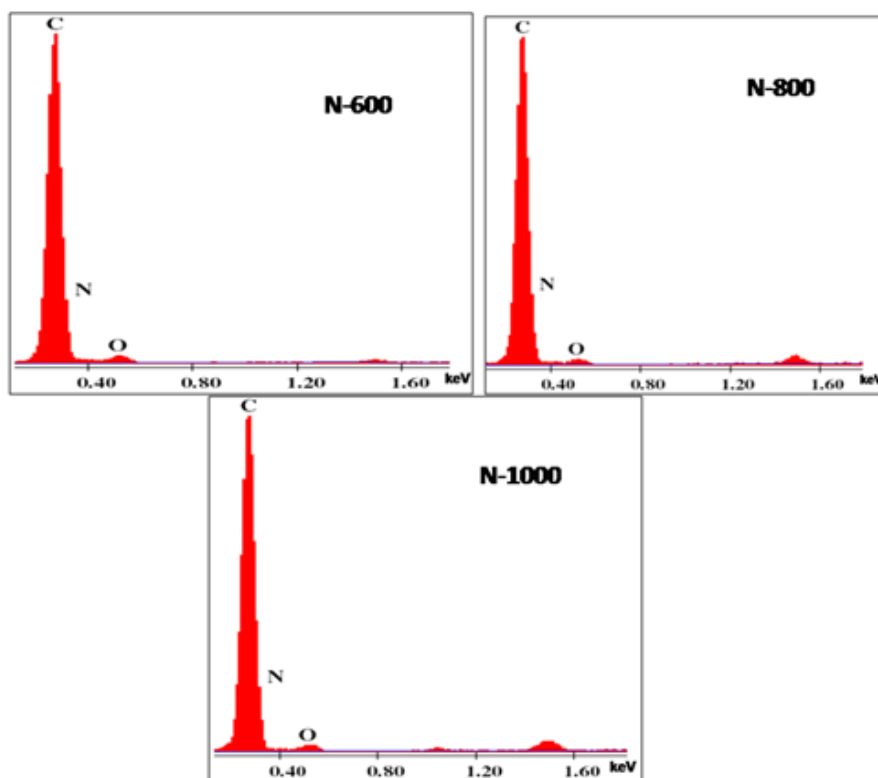


**Figure 3A.2:** EDAX spectra of N-600, N-800 and N-1000.

### 3A.2.2 Raman analysis

Raman spectroscopy gives a clear evidence for the defects created on the surface of nanohorns and nitrogen doping (Figure 3A.3a). Raman spectrum of SWCNH shows two peaks, *viz.*  $\sim 1310$  and  $\sim 1583$   $\text{cm}^{-1}$ , which are assigned to the D and G bands of the graphene framework (Figure S6).<sup>[12]</sup> Usually, the D band of nanohorns will have higher intensity due to large number of  $\text{sp}^3$  hybridized carbon atoms compared to graphene or carbon nanotubes.<sup>[13]</sup> A close inspection of the G-band position in FCNH indicates a shift to higher wave number by  $5$   $\text{cm}^{-1}$  ( $1590$   $\text{cm}^{-1}$ ), in comparison with SWCNH, due to the electron withdrawing effects of the functional groups. After annealing of FCNH at higher temperature in the

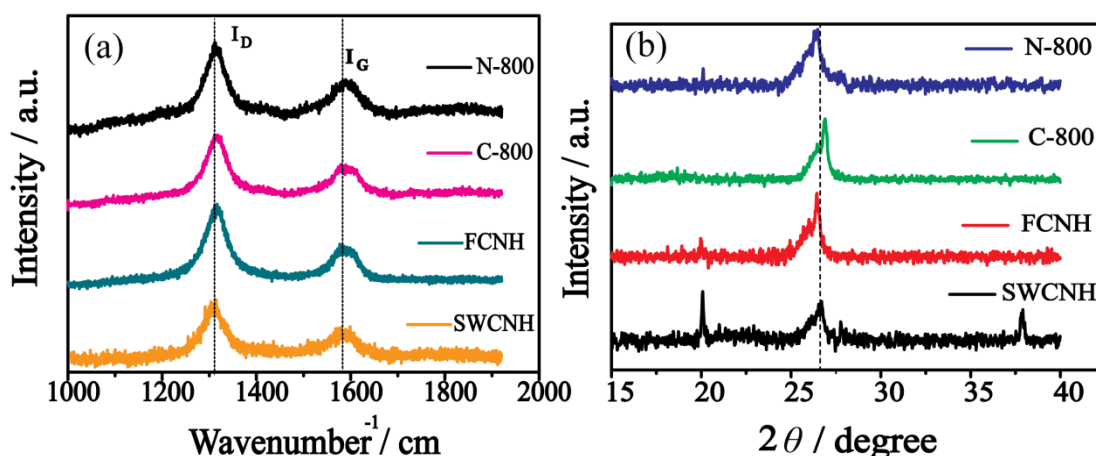


**Figure 3A.3:** (a) Raman spectra and (b) X-ray diffraction of SWCNH, FCNH, C-800 and N-800.

presence of argon, the G band of C-800 is shifted towards a lower wave number of  $1587.62$   $\text{cm}^{-1}$ , which is still higher than the corresponding value for SWCNH. This clearly indicates the removal of functional groups from the surface of FCNH by leaving back more defective sites on the surface of C-800. In the case of N-800, an up shift in the G-band position ( $1594.13$   $\text{cm}^{-1}$ ) indicates the doping of nitrogen into the carbon matrix along with the defects generated through the high temperature annealing. It is reported that the electron withdrawing effect of nitrogen doping in carbon nanotubes and graphene may cause the up shift in the G-band position.<sup>[14]</sup> Electron density changes in the carbon atom due to the neighbouring heteroatom can change the electrochemical properties of nanohorn, which in turn can assist the ORR activity. The powder X-ray diffraction (XRD) of N-800 is compared with that of SWCNH, FCNH and C-800 (Figure 3A.3b). It can be

seen that the  $2\theta$  value of all the four samples are more or less same (the  $2\theta$  values are, SWCNH:  $26.57^\circ$ , FCNH:  $26.42^\circ$ , C-800:  $26.8^\circ$  and N-800:  $26.37^\circ$ ).

### 3A.2.3 Surface area analysis

In order to understand the nature of porosity of the materials, nitrogen adsorption isotherms were taken (Figure 3A.4a). Two different types of nitrogen adsorption isotherms (77 K) are observed. FCNH and C-800 show Type-IV behaviour, while all the nitrogen doped

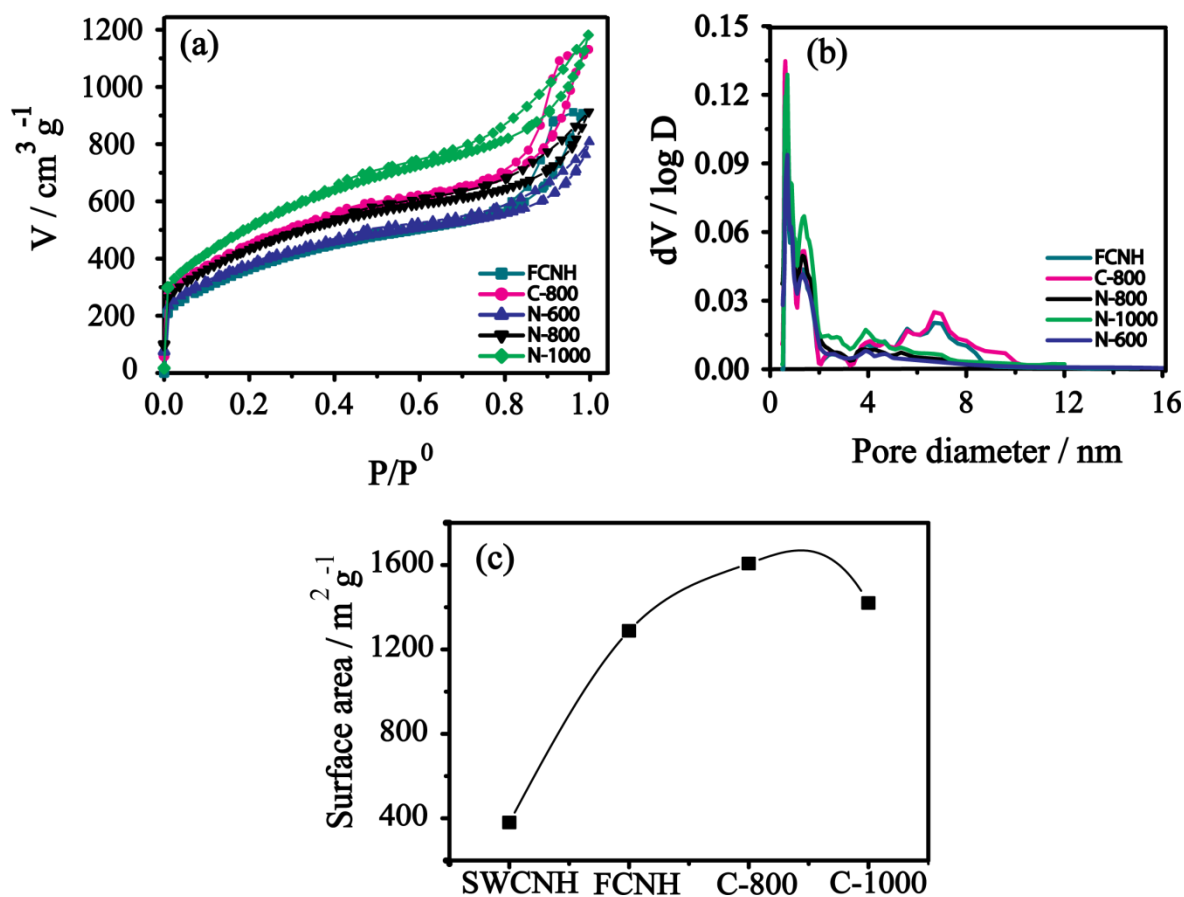


**Figure 3A.4:** (a) Nitrogen adsorption–desorption isotherm of FCNH, C-800, N-600, N-800 and N-1000. All the nitrogen doped samples show Type-II isotherms whereas CNH without doping shows Type-IV isotherm. (b) Pore size distribution of FCNH, C-800, N-600, N-800 and N-1000. (c) Plots corresponding to the changes in surface area of the prepared carbon nanohorn samples without nitrogen doping (SWCNH, FCNH) annealed at different temperatures (C-800 and C-1000 corresponds to the FCNH samples annealed at 800 and 1000 °C respectively). Knotting of “nanowindow” of FCNH is happening at 1000 °C, which leads to the reduction in the surface area.

nanohorns show Type-II isotherms. From these isotherms, a clear transformation of the mesoporous behaviour of the undoped systems into the microporous nature upon nitrogen doping is evident. Similarly,  $N_2$  adsorption shows an increasing trend as we go from N-600 to N-1000. On the other hand, nitrogen adsorption rate is higher for C-800 than FCNH and this is ascribed to the surface area enhancement as a result of the high temperature annealing process. With increasing the temperature, the gas adsorption capacity of the nanohorns reduces (Figure 3A.4c) but in the case of NCNH, the gas adsorption capacity increases even up to 1000 °C. The nitrogen adsorption isotherms lead to the quantification of the surface area of the materials and this follows the order: N-600 ( $1384 \text{ m}^2 \text{ g}^{-1}$ ) < N-800 ( $1534 \text{ m}^2 \text{ g}^{-1}$ ) < N-1000 ( $1836 \text{ m}^2 \text{ g}^{-1}$ ). The surface area of  $1836 \text{ m}^2 \text{ g}^{-1}$  obtained for N-1000 is higher than the recently reported value of  $1720 \text{ m}^2 \text{ g}^{-1}$  by Yuge *et. al.* for carbon nanohorns.<sup>[8g]</sup> Surface area of FCNH ( $1289 \text{ m}^2 \text{ g}^{-1}$ ) has also increased after the annealing at 800 °C (C-800,  $1600 \text{ m}^2 \text{ g}^{-1}$ ). This value is almost comparable to that of N-800. Pores of N-600, N-800 and N-1000 are having a size range between 0.5 to 2 nm. However, the pore size of FCNH and C-800 is varied from 0.5 to 10 nm. From the nitrogen sorption studies, it is clear that the heteroatom doping is important to get high surface area and it is found to be increasing with increasing the temperature. Nitrogen atoms on nanohorns prevent knotting of carbon atoms at higher temperature as observed in the case of pure SWCNH and graphene.<sup>[6a, 15]</sup>

### 3A.2.4 Four-probe electrical conductivity measurement

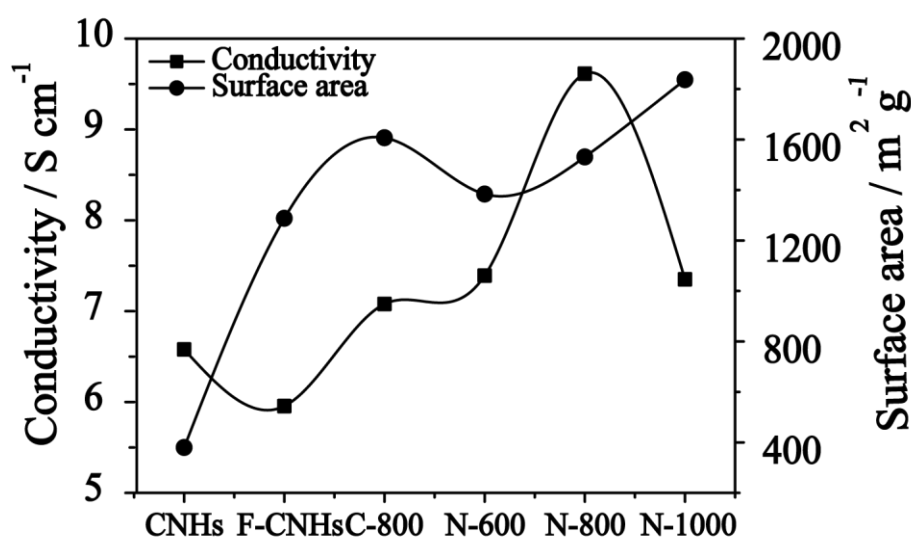


**Figure 3A.5:** Plots corresponding to the changes in the electrical conductivity and surface area of the prepared carbon nanohorn samples.

It is well reported that increasing the surface area of porous carbon material reduces the electrical conductivity. Electrical conductivity is strongly related to the porous nature of the materials and it is an inevitable requirement of those materials proposing for energy device applications. From the four-probe conductivity measurement (Figure 3A.5), it is observed that the conductivity of nanohorn is increasing with the nitrogen doping. Among the different nitrogen doped systems, N-800 shows the highest conductivity ( $9.60 \text{ S cm}^{-1}$ ) compared to N-600 ( $7.40 \text{ S cm}^{-1}$ ) and N-1000 ( $7.35 \text{ S cm}^{-1}$ ). The lower conductivity of N-1000 compared to N-800 may be attributed to its high surface area, but still this value is higher than that of C-800, FCNH and SWCNH. The conductivity of nanohorn without doping is in the order of C-800 ( $7.07 \text{ S cm}^{-1}$ ) > SWCNH ( $6.57 \text{ S cm}^{-1}$ ) > FCNH ( $4.95 \text{ S cm}^{-1}$ ). This indicates that FCNH along with the enhancement in the surface area decreases the conductivity of the material but its annealed product (C-800) attains enhanced conductivity due to the removal of the functional moieties. In the case of the nitrogen doped systems, the conductivity enhancement is credited to the electronic changes in the carbon atoms due to the interactions from the doped nitrogen atoms.<sup>[21]</sup> Both high conductivity as well as high surface area of the NCNH samples helps to enhance the electrocatalytic activity towards ORR.

### 3A.2.5 XPS analysis

Chemical composition of the nitrogen doped carbon nanohorn samples was analysed using X-ray photoelectron spectroscopy (XPS). In all the three samples, a major peak of C1s spectrum appears at 284.5 eV, which indicates the existence of the  $\text{sp}^2$  carbon of graphene. The peak at 285.7 eV indicates the presence  $-\text{C}-\text{C}-$  single bonds ( $\text{sp}^3$  carbon) (Figure 3A.6). Oxygen contents are mainly from the moisture, adsorbed oxygen, carbon dioxide or from the residual functional groups containing oxygen. Weight percentage of carbon is found to be increasing in the order of N-600 < N-800 < N-1000. This clearly indicates that the graphitization is increasing with increase in the annealing temperature. Similarly, the oxygen weight percentage decreases dramatically with increasing the annealing temperature, which follows the order: N-600 > N-800 > N-1000. The nitrogen content in the samples also is decreasing with the increase in the annealing temperature. N-600 has the highest nitrogen content of *ca.* 10.9 %, whereas N-800 and N-1000 show nitrogen contents of 8.7 and 3.2 %, respectively. To further understand the different types of the

nitrogen coordinations in the samples, which are determining the efficiencies towards ORR, the N1s spectra is deconvoluted.

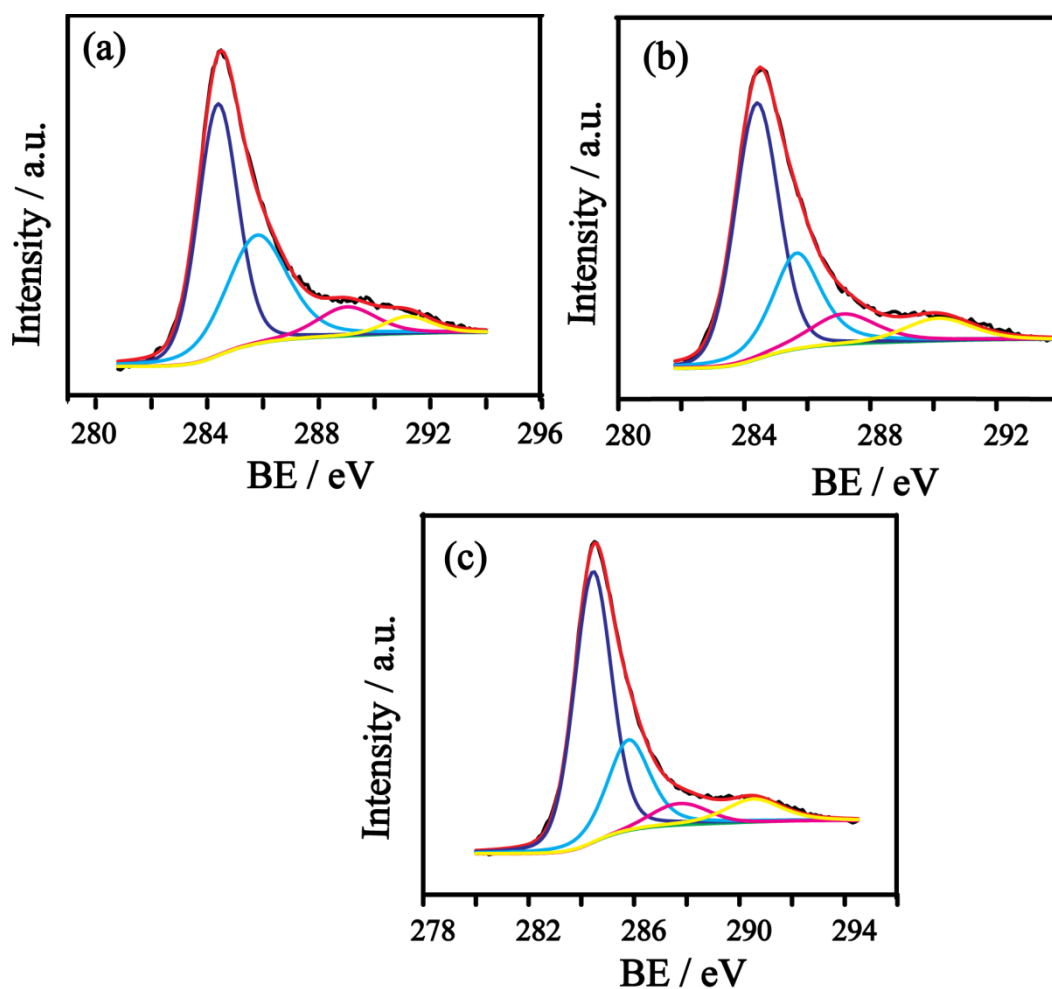


**Figure 3A.6:** Deconvoluted XPS spectra of N1s of (a) N-600, (b) N-800 and (c) N-1000.

The deconvoluted N1s spectra of N-600, N-800 and N-1000 show three different types of nitrogens as pyridinic, pyrrolic and graphitic (Figure 3A.7 a-c). The peak at around 398 eV represents the pyridinic nitrogen, 399 eV represents the pyrrolic nitrogen and the one at around 401 eV stands for the graphitic nitrogen.<sup>[16]</sup> More interestingly, N-800 shows the highest proportion of the pyridinic nitrogen compared to N-600 and N-1000. The 49 % pyridinic nitrogen present on N-800 is far better than that in N-600 (30 %) and N-1000 (39 %) (Figure 3A.7 d). The pyrrolic nitrogen content in the samples is in the order of N-600 (47.0 %) > N-1000 (42.2 %) > (N-800 (27.1 %) and the graphitic nitrogen content follows the order: N-800 (23.6 %) > N-600 (22.5 %) > N-1000 (18.5 %). It is also reported that the annealing temperature also converts the pyridinic nitrogen into the

pyrrolic and graphitic nitrogens.<sup>[17]</sup> This is the main reason for the decrease in the pyridinic nitrogen content from 49 % of N-800 to 39 % of N-1000 after the annealing at 1000 °C. It is well reported that the pyridinic nitrogen helps to improve the ORR activity.<sup>[23]</sup> Hence, the higher pyridinic nitrogen containing N-800 is expected to be a better electrocatalyst for ORR in alkaline medium.

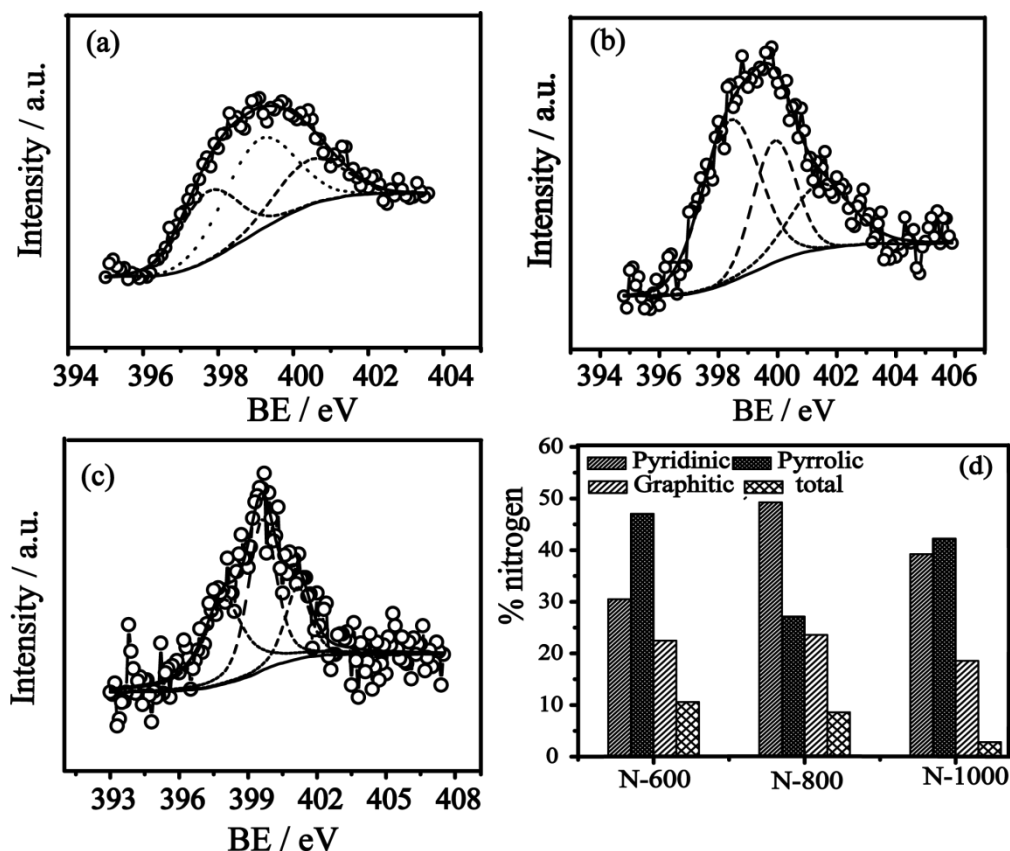


**Figure 3A.7:** Deconvoluted XPS spectra of N1s of (a) N-600, (b) N-800 and (c) N-1000; (d) the estimated values of the different types of nitrogen in all the annealed samples.

### 3A.2.6 Electrochemical analysis

Electrocatalytic activity of NCNH was performed using Cyclic Voltammetry (CV) and Rotating Disk Electrode (RDE). Figure 3A.8 shows the cyclic voltammograms of N-800 in oxygen and nitrogen saturated 0.1 M KOH solution at a rotation rate of 900 rpm in a potential window of -0.8 to 0.6 V vs. Hg/HgO. In the nitrogen saturated solution, a rectangular behaviour of the voltammogram originates due to double layer charging. However, the oxygen reduction current increases dramatically after the oxygen purge, which indicates the presence of potential oxygen reduction sites on N-800.



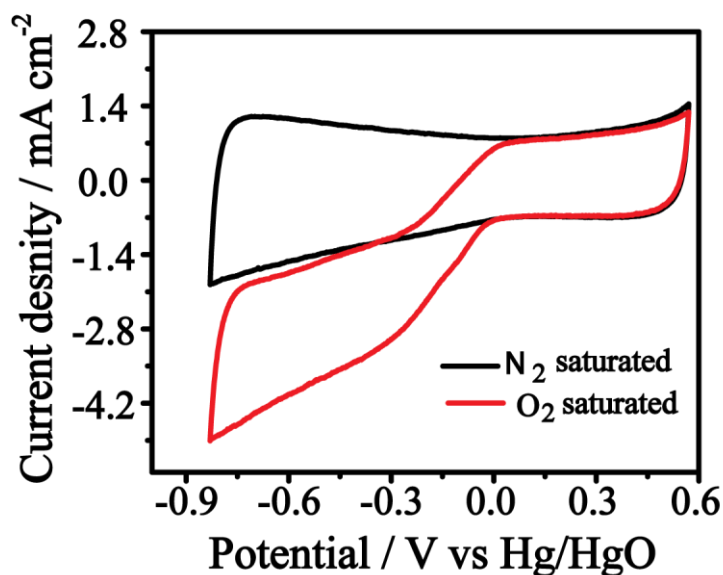


**Figure 3A.8:** Cyclic voltammograms of N-800 recorded in nitrogen and oxygen saturated 0.1 M KOH solution at a scan rate of  $50 \text{ mV s}^{-1}$  at an electrode rotation rate of 900 rpm. Glassy carbon electrode and Hg/HgO were used as the counter and reference electrodes respectively

A detailed electrode kinetic evaluation and a comparative study were carried out using RDE with Hg/HgO and glassy carbon as the reference and counter electrodes, respectively, in oxygen saturated 0.1 M KOH at different electrode rotation rates (Figure 3A.9a) in a potential window of -0.8 to 0.5 V vs. Hg/HgO. Clearly, N-800 shows a more positive onset potential of 0.026 V compared to SWCNH, FCNH, C-800 and the other nitrogen doped systems (N-600 and N-1000). It is important to note that the ORR onset potential of N-800 is only 50 mV lower than that of the state-of-the-art 40 wt.% Pt/C (0.076 V). The obtained onset potential of N-800 is comparatively higher than some of the recently reported onset potentials of nitrogen doped graphene, nitrogen doped carbon nanotubes and functionalized graphene (Table S 1). N-600 and N-1000 show the onsets at 0.019 and 0.018 V respectively. Pure SWCNH shows the onset at -0.09 V, which has more negative potential compared to FCNH (-0.067 V) and C-800 (-0.069 V). More positive onset potential of N-800 indicates that its intrinsic ORR activity is higher compared to N-600 and N-1000. Similarly, N-800 shows only 16 mV negative shift in the half wave potential ( $E_{1/2}$ ) compared to Pt/C (-0.020 V).  $E_{1/2}$  of N-1000 (-0.056 V) and N-600 (-0.074 V) got shifted to more negative direction compared to N-800 (-0.036 V). This further indicates that the active reaction site density of N-800 is higher compared to N-600 and N-1000.<sup>[6]</sup>  $E_{1/2}$  of the nanohorn without the nitrogen doping possesses the more negative value

compared to Pt/C and the N-doped nanohorns, indicating the poor reaction centre density on the material. All these undoped nanohorns show two stage reductions as reported by Dai *et. al.* in vertically aligned carbon nanotubes.<sup>[18]</sup> However, the linear sweep voltammogram (LSV) of C-800 shows lesser ohmic resistance compared to FCNH. This is mainly attributed to the removal of functional groups from the surface at higher temperature. Diffusion limited current density ( $j_L$ ) of FCNH and C-800 is  $-3.65$  and  $-3.75$   $\text{mA cm}^{-2}$  respectively. The  $j_L$  value of SWCNH is 1.5 times lower than that of FCNH and C-800. These results clearly show that simple functionalization itself modifies the electronic properties of nanohorns. Comparatively higher degree of functional groups on FCNH slightly reduces the  $j_L$  value compared to C-800.

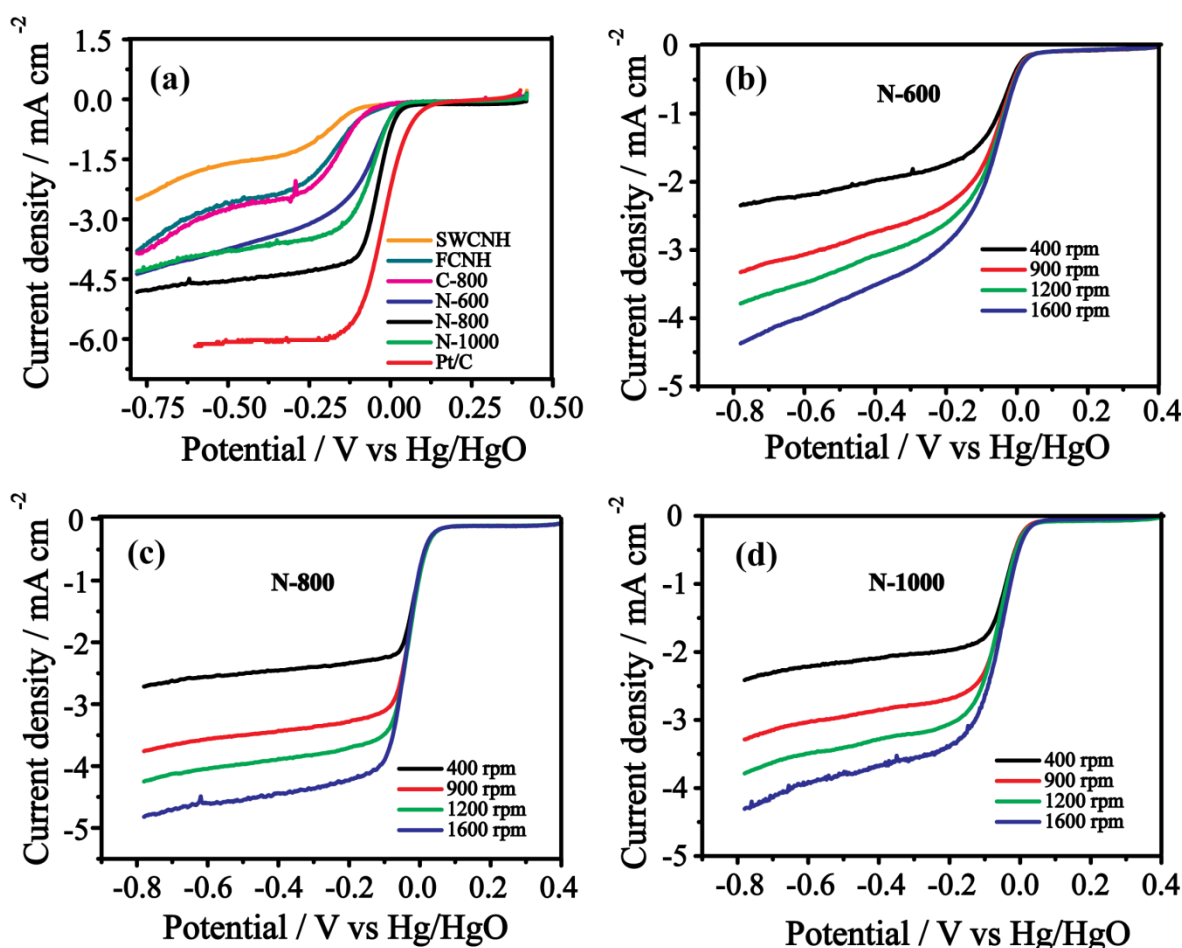


**Figure 3A.9:** (a) Linear sweep voltammograms of the CNH samples and Pt/C with a platinum loading on  $102 \mu\text{g cm}^{-2}$  in  $0.1 \text{ M}$  oxygen saturated KOH at a rotation speed of  $1600 \text{ rpm}$  and a scan rate of  $10 \text{ mV s}^{-1}$ . LSVs of (b) N-600, (c) N-800 and (d) N-1000 at different rotation speeds in  $0.1 \text{ M}$  oxygen saturated KOH at a scan rate of  $10 \text{ mV s}^{-1}$ . Glassy carbon electrode and Hg/HgO were used as the counter and reference electrode, respectively.

N-800 shows a  $j_L$  value of  $-4.69 \text{ mA cm}^{-2}$ , which is higher than the other doped nanohorn samples ( $j_L$  value of N-600 and N-1000 are  $4.28$  and  $-4.19 \text{ mA cm}^{-2}$ , respectively). Ohmic resistance of N-1000 is lower compared to N-600, due to partial removal of functional moieties from the surface of N-1000. Compared to SWCNH, the onset potential of N-800 is  $116 \text{ mV}$  more positive with a  $2.3$  times higher  $j_L$ . The onset potential and  $j_L$  of N-800 are respectively  $8 \text{ mV}$  and  $0.50 \text{ mA cm}^{-2}$  higher than N-1000 and are respectively  $7 \text{ mV}$  and  $0.40 \text{ mA cm}^{-2}$  higher than N-600. Such small difference in the onset and reduction current was reported by Wang *et. al.* for nitrogen doped graphene synthesised from graphene oxide and urea.<sup>[11]</sup> High surface area, high conductivity and nitrogen active sites facilitate fast mass transport, electron transport and oxygen adsorption on N-800, which is the main reason for its enhanced activity towards ORR. Similarly, to perform enhanced reduction activity, nitrogen doping is necessary and LSV is giving a clear evidence for this with a substantial reduction in the oxygen reduction overpotential by around  $80 \text{ mV}$  for N-800 compared to C-800.

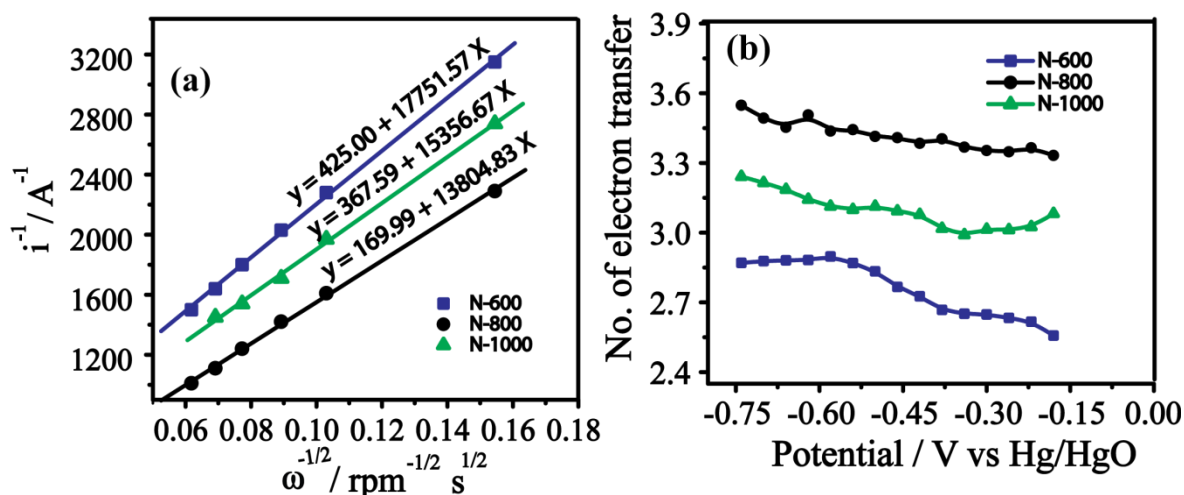


**Figure 3A.10:** (a) K–L plots of N-600, N-800 and N-1000 at a potential of  $-0.22 \text{ V}$  vs.  $\text{Hg/HgO}$ . The plots are generated from the LSVs of all the three samples conducted in oxygen saturated  $0.1 \text{ M KOH}$  solution at different rotation speeds. Theoretical K-L plots for  $n = 4$  and  $n = 2$  are also given in the plot. (b) The number of electrons transferred versus the potential as calculated from the K-L plots.

From the Koutecky-Levich (K-L) plot, which is the plot of the inverse of the square root of the electrode rotation rate ( $\omega^{-1/2}$ ) vs inverse of the current ( $i^{-1}$ ), it is clear that slope of the plots is decreasing from N-600 to N-800 (Figure 3A.10a). This is giving a clear evidence for the shift from the 2-electron ( $2e^-$ ) to the desired 4-electron ( $4e^-$ ) transfer

kinetics from N-600 to N-800. The number of electrons calculated from the slopes of the K-L plots at different potentials is given in Figure 3A.10b. The Figure 3A.10b indicates that in the case of N-800, the electron transfer number is increasing slightly from 3.4 to 3.6 while the potential goes more towards the negative direction. This implies that N-800 follows nearly a  $4e^-$  reduction pathway for the entire potential range. N-1000, on the other hand, is following a mixed kinetics involving both peroxide and hydroxide pathways, leading to an electron transfer number which lies in between 3.1 and 3.3. N-600 is showing a dominant  $2e^-$  reduction pathway where peroxide forms as the major reduction product. To further understand the amount of peroxide forming during ORR, we performed Rotating Ring Disk Electrode (RRDE) analysis (Figure 3A.11a)

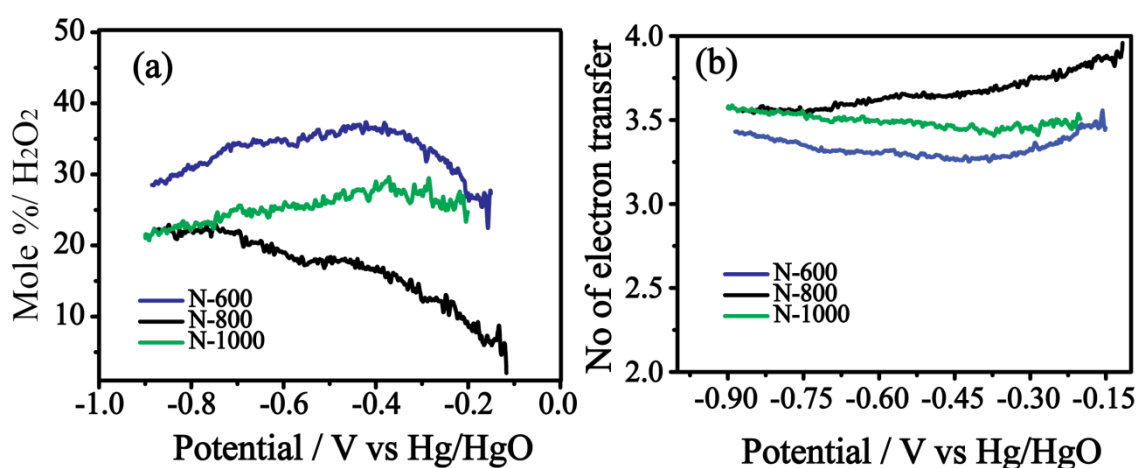


**Figure 3A.11:** (a) the percentage of hydrogen peroxide formation calculated from the rotating ring disc electrode (RRDE) in 0.1 M KOH at a rotation of 1600 rpm and scan rate of  $10 \text{ mV s}^{-1}$  and (b) the plot indicating the number of electrons transferred vs. the potential as calculated from RRDE.

of all the three catalysts and found that the peroxide yield of N-800 slowly increases from 10 % to 20 % at more negative potentials. Similarly, N-1000 shows the peroxide yield in between 20 and 25% and N-600 shows around 30 % of the peroxide yield at higher negative potentials. From the number of electron transfer as calculated from the H<sub>2</sub>O<sub>2</sub> percentage, it could be confirmed that N-800 shows contributions mainly from the direct 4-electron pathway with the electron transfer number lies in between 3.9 and 3.5. At higher negative potentials, the electron transfer number is found to be reaching to nearly 3.5, as obtained from the K-L plot. However, the electron transfer numbers of N-1000 and N-600

are showing less deviation with potential and are estimated to be around 3.5 and 3.2 respectively.

Nitrogen dopant in the nanohorns induces charge delocalization of carbon atom which in turn improves the adsorption of oxygen molecules on nanohorns and facilitates the reduction process.<sup>[25]</sup> Moreover, the type of nitrogen also plays an important role in the electrocatalytic activity towards ORR. In recent literatures, both pyridinic and pyrrolic nitrogen are reported to be contributing for enhancing the activity of the system towards ORR.<sup>[19]</sup> In the study for exploring the structure of the active centre of nitrogen doped graphene, Ruoff *et al* explained the importance of pyridinic and graphitic nitrogen towards ORR.<sup>[17]</sup> According to Ruoff *et al*, pyridinic nitrogen shifts the  $2e^-$  reduction pathway to the  $4e^-$  process and the graphitic nitrogen enhances the limiting current. In the present case, N-800 has the highest pyridinic nitrogen content compared to N-600 and N-1000. Graphitic nitrogen content is in the order of N-600 (22.5 %) < N-800 (23.6 %) < N-1000 (18.5 %). The graphitic nitrogen content in these nitrogen doped nanohorns differs slightly. Hence, the contribution from the graphitic nitrogen for the observed differences in the performance between the samples can be omitted. Interestingly, the pyridinic nitrogen content in N-800 is the highest (~50 %) among all the samples, and it is found to be promoting the reaction to the  $4e^-$  transfer process. N-1000 and N-600 have 39.2 % and 30.5% pyridinic nitrogen, respectively, so the ORR kinetics of N-1000 is higher compared to N-6000. The Tafel plots of the nitrogen doped samples (Figure 3A.12A) further substantiate these arguments. Tafel plots derived from the diffusion corrected kinetic current density indicate that N-800 has the minimum slope of  $81.2 \text{ mV decade}^{-1}$  compared to Pt/C ( $104.8 \text{ mV decade}^{-1}$ ). This further supports that the oxygen reduction kinetics in N-800 is better than that in Pt/C. N-1000 ( $83.72 \text{ mV decade}^{-1}$ ) shows less Tafel slope compared to N-600 ( $100.62 \text{ mV decade}^{-1}$ ) and it is very close to N-800, indicating a very similar reduction kinetics involved in N-800 and N-1000.

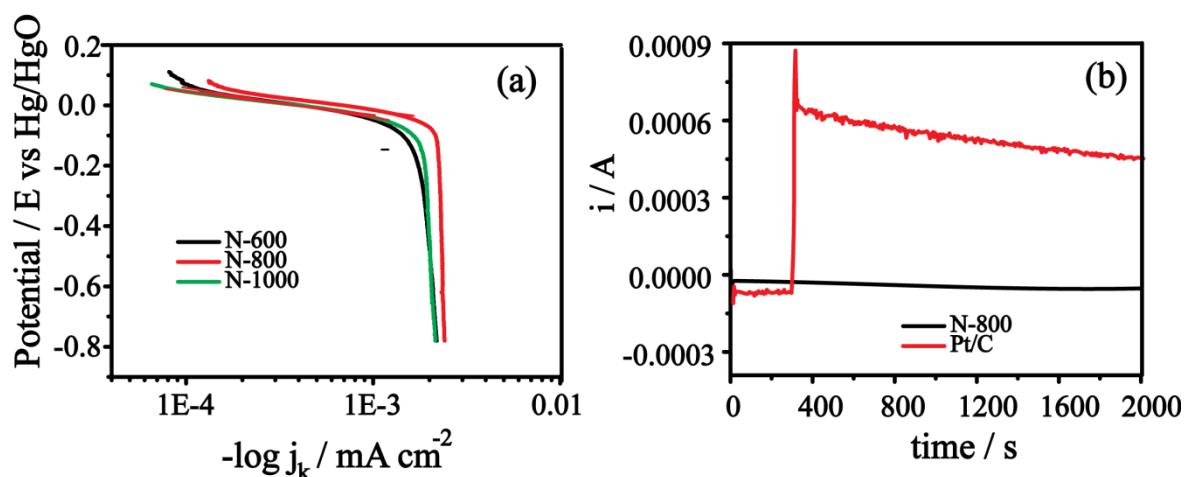


**Figure 3A.12:** (a) Tafel plots of the different catalysts and (b) methanol crossover study of N-800 and Pt/C at a rotation speed of 1000 rpm at  $-0.05$  V. At 300 s, 3 M methanol was added into 0.1 M KOH electrolyte to evaluate the crossover effect.

In order to understand the tolerance of N-800 towards the methanol crossover effect compared to Pt/C, we have carried out chronoamperometric study in oxygen saturated 0.1 M KOH solution at 1000 rpm for 2000 s. During the reaction, at 300 s, 2 ml of 3 M methanol was added (Figure 3A.12b). In the case of Pt/C, subsequent to the addition of methanol, the oxygen reduction current of Pt/C decreases, which indicates the oxidation of methanol on the surface of Pt followed by the poisoning of the surface by the by-product of the reaction. Contrary to this, in the case of N-800, there is no change in the reduction current even after the addition of methanol indicating that N-800 is completely resistant towards methanol. The higher methanol tolerance is a characteristic feature of the nitrogen doped ORR catalysts and also is a distinct advantage over their Pt based counterparts.

Similarly, to understand electrochemical stability of the catalyst, we carried out accelerated durability test (ADT) for both N-800 and Pt/C. ADT was carried out by potential cycling at  $100 \text{ mV s}^{-1}$  scan rate in between  $-0.37$  to  $0.30$  V in oxygen saturated 0.1 M KOH. LSV was taken both before and after ADT. From Figures 3A.13a, it is clear that N-800 shows enhanced electrochemical stability and there is no apparent change in the onset potential but the  $j_L$  value decreases slightly. On the other hand, Pt/C shows a clear negative shift in the onset potential and fall in the  $j_L$  value after the 1000 cycles (Figure 3A.13b). This negative shift in the onset potential and decreased  $j_L$  are mainly due to the dissolution or agglomeration of Pt during the forced oxidation of carbon support by ADT.

Enhanced stability of N-800 clearly depicts that the nanohorns are more resistant towards carbon corrosion even though the test induces some changes in the active sites.

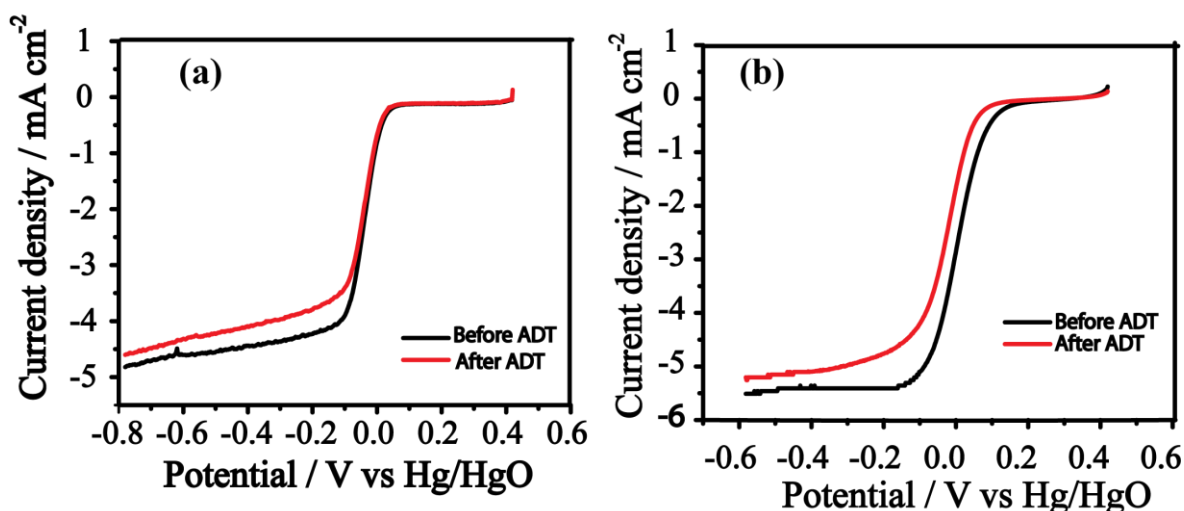


**Figure 3A.13:** Linear sweep voltammograms of (a) N-800 and (b) Pt/C before and after ADT in 0.1 M oxygen saturated KOH at a rotation speed of 1600 rpm and a scan rate of 10  $\text{mV s}^{-1}$ .

Figure 3A.14a shows steady state polarization plot of anion exchange membrane fuel cell (AEMFC) using N-800 as the cathode catalyst. The Membrane Electrode Assembly (MEA) was prepared by sandwiching the anode (made from Pt/C) and cathode (made from N-800) electrodes with a Fumapem FAA anion exchange membrane. The MEA derived from N-800 as the cathode shows an open circuit voltage (OCV) of 0.75 V. For comparison purpose, a similar test under identical test condition was also performed by using Pt/C in place of N-800 as the cathode catalyst. The Pt/C system shows an OCV of 1 V (Figure 3A.14b) but features of the polarization curve of N-800 is similar to that of Pt/C. N-800 delivered a maximum current density of  $91 \text{ mA cm}^{-2}$  and a maximum power density of  $30 \text{ mW cm}^{-2}$  with oxygen as the oxidant and hydrogen as the fuel. Pt/C shows the maximum current density and power density of  $180 \text{ mA cm}^{-2}$  and  $60 \text{ mW cm}^{-2}$ , respectively. Even though Pt/C displayed higher single cell performance, it should be noted that the performance of N-800 is comparable to the recently reported value using NCNT.<sup>[27]</sup> Further optimization with respect to the electrode binder composition and the testing parameters such as temperature, pressure and anion conducting membranes etc. is expected to improve the single cell performance of N-800.

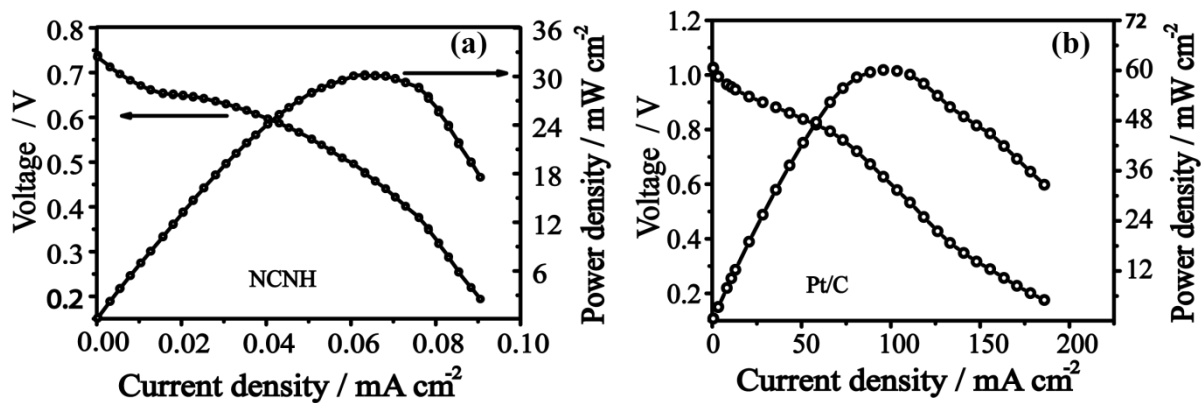


**Figure 3A.14:** Steady state polarization plot of anion exchange membrane fuel cell (AEMFC) with (a) N-800 and (b) Pt/C as cathode catalyst taken at 50 °C.



## **Part B: CoSe<sub>2</sub> supported nitrogen-doped carbon nanohorn for ORR**

Apart from precious metal chalcogenides, early transition metal (Co, Mn, Ni, Fe etc) chalcogenides (selenides and sulphides) perform very well towards various electrode reactions such as ORR,<sup>[20]</sup> oxygen evolution (OER)<sup>[21]</sup> and hydrogen evolution (HER)<sup>[22]</sup>. Among different metal chalcogenides, cobalt selenide as well as cobalt sulphides are the only 3d-transition metal chalcogenides which perform well in the ORR.<sup>[20a, 20b, 20d-g, 23]</sup> However, the activity performance of these catalysts is far away from the Pt based catalysts in both acidic and alkaline conditions.<sup>[24]</sup> This is mainly due to the instability of selenide and sulphide at higher positive potentials.<sup>[24]</sup>

Catalytic activity and stability of cobalt selenide/sulphide can be improved by tuning the support materials because the catalyst support plays an important role for the modulation of the intrinsic ORR activity and active reaction center density of the electrocatalysts.<sup>[25]</sup> Usually, carbon nanoparticle of size 60 nm are used as the catalyst support due to their high electrical conductivity.<sup>[26]</sup> As this support material lacks high surface area and corrosion resistance, performance of the cobalt selenide or sulphide supported catalyst loses its activity by time.<sup>[27]</sup> There have been some attempts to change the support materials from carbon to graphene to improve the activity performance of electrocatalysts.<sup>[21c]</sup> Recently, Chao *et al* used Fe and nitrogen coordinated carbon nanoparticle as a catalyst support for CoSe<sub>2</sub> and found that it improves the activity of the prepared catalysts.<sup>[20e]</sup> However, the actual activity enhancement of CoSe<sub>2</sub> in this catalyst is not clear since the nitrogen coordinated iron moiety itself shows ORR activity in both acid and alkaline conditions. Moreover, stability of this material was found to be poor after prolonged reaction.

This section of Chapter 3 focuses on the improvement of the active reaction centre of NCNH by dispersing CoSe<sub>2</sub> on it. This section also provides an insight about the influence of the substrate materials for the improved ORR activity of CoSe<sub>2</sub> based non-precious metal centres. High surface area and good electrical conductivity of NCNH create more anchoring sites for CoSe<sub>2</sub> without any agglomeration. This assists to attain better dispersion of the non-precious metal chalcogenide catalytic centres. Since NCNH is free

from metal impurities compared to other carbon allotropes, the effect of substrate on ORR on  $\text{CoSe}_2$  metal centers can be easily evaluated.

### 3B.1 Experimental section

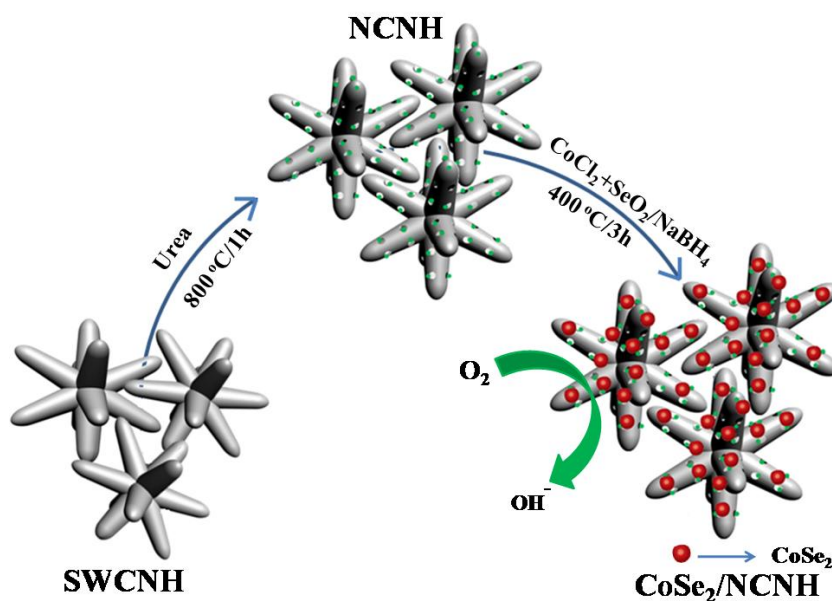
#### 3B.1.1 Materials

SWCNH was purchased from Global nanotech, India. Urea, Ethanol,  $\text{H}_2\text{O}_2$ , KOH,  $\text{NaBH}_4$ ,  $\text{CoCl}_2$  and  $\text{SeO}_2$  were purchased from Aldrich and these chemicals were used without further purification.

#### 3B.1.2 Synthesis of nitrogen doped nanohorn (NCNH)

1.8 g of urea was dissolved in 20 ml of water followed by the addition of 300 mg of SWCNH. The resulting mixture bath was sonicated for one hour and allowed to dry at  $60^\circ\text{C}$  with stirring. After the drying for overnight, the resulting material was pulverised thoroughly using a mortar and pestle and was subsequently annealed at  $800^\circ\text{C}$  for 1 h in argon atmosphere. The final black coloured powder was washed with water and ethanol and the wet cake was dried at  $60^\circ\text{C}$  for overnight.

#### 3B.1.3 Synthesis of 40 wt.% $\text{CoSe}_2$ supported nitrogen doped nanohorn ( $\text{CoSe}_2/\text{NCNH}$ )



*Scheme 3B.1: Schematic representation of the synthesis of  $\text{CoSe}_2/\text{NCNH}$ .*

170 mg of NCNH was dispersed well in 180 ml of ethanol for 30 min. 0.051 g of  $\text{CoCl}_2$ , 0.088 g of  $\text{SeO}_2$  and 2.133 g of sodium acetate were added into the NCNH suspension and the mixture was stirred for overnight in nitrogen atmosphere. 0.186 g of  $\text{NaBH}_4$  was dissolved in 20 ml of ethanol and this was added to the above solution drop-wise and the mixture was kept for stirring for 4 h. The resulting mixture was filtered using a PTFE filter paper having a pore size of 0.2  $\mu\text{m}$  and the residue was washed well using ethanol. Thus obtained black cake was dried at 60  $^\circ\text{C}$  for 48 h. The black solid material was pulverized well and finally annealed at 400  $^\circ\text{C}$  for 4 h in nitrogen atmosphere to remove amorphous selenium. The same method was used for the preparation of  $\text{CoSe}_2/\text{C}$  and  $\text{CoSe}_2/\text{CNH}$ . Here, instead of NCNH, carbon and SCNH were used as the catalyst support.

### 3B.1.4 Electrochemical characterization

Electrochemical studies of all the catalysts were carried out in a  $\mu$ -Autolab Potentiostat using conventional three-electrode test cell. Oxygen saturated 0.1 M KOH was used in the electrochemical experiments as the electrolyte. Home-made reversible hydrogen electrode was used as the reference electrode and a glassy carbon was used as the counter electrode. A glassy carbon (GC) electrode (3 mm diameter) was used as the working electrode (WE) after drop coating the samples. To prepare the catalyst slurry for the electrochemical analysis, 5 mg of the catalyst was dispersed in 1 ml of water and isopropyl alcohol mixture in the ratio of 3:1 along with 40  $\mu\text{l}$  of 5 wt.% Nafion solution (Sigma Aldrich), and the mixture was dispersed by sonication. 3  $\mu\text{L}$  of the catalyst slurry was drop-coated on the glassy carbon electrode. Total catalyst loading on the electrode was 214  $\mu\text{g cm}^{-2}$  and the  $\text{CoSe}_2$  loading was 85  $\mu\text{g cm}^{-2}$ . Linear sweep voltammogram (LSV) was recorded in oxygen saturated 0.1 M KOH solution at a scan rate of 5  $\text{mV s}^{-1}$  at different electrode rotation rates varied from 400 to 2500 rpm. Pt/C (20 wt. %, Johnson and Matthey) coated electrode, having a catalyst loading of 25  $\mu\text{g cm}^{-2}$ , was also tested in the same way for comparison purpose. The Koutecky-Levich (K-L) plot, a plot of  $j^{-1}$  versus  $\omega^{-1/2}$  (electrode rotation speed) at different potentials, was used to calculate the number of electrons involved in the reduction process.

The number of electron transfer during ORR was calculated using the equation:

$$B = 0.6 nFv^{-1/2}C_{\text{O}_2}D_{\text{O}_2}^{2/3}$$

where 'n' is the electron transfer number, 'F' is the Faraday constant ( $96,486 \text{ C mol}^{-1}$ ), ' $C_{O_2}$ ' is the concentration of oxygen in 0.1 M KOH ( $1.2 \times 10^{-3} \text{ mol L}^{-1}$ ), ' $D_{O_2}$ ' is the diffusion coefficient of oxygen in 0.1 M KOH solution ( $1.9 \times 10^{-5} \text{ cm}^2 \text{ s}^{-1}$ ) and ' $\nu$ ' is the kinematic viscosity.

### 3B.1.5 Air breathing micro laminar flow fuel cell

#### 3B.1.5.1 Electrodes fabrication

Cathode of microlaminar flow fuel cell was prepared by spray coating of the suspension of  $\text{CoSe}_2$  supported on different substrate on carbon paper (AvCarb T P75T) and dried at  $60^\circ\text{C}$ . Suspension of catalyst was prepared by sonicating 10 mg of  $\text{CoSe}_2$  supported on different substrate with ultra pure water ( $125 \mu\text{l}$ ) and Nafion solution (5 wt. %,  $300 \mu\text{l}$ , Sigma Aldrich) in a bath sonicator for 2 h. For anode, PtRu/C (20 wt.%, HP fuel cell store) was used. Additionally, a cathode using Pt/C (20 wt. %, Johnson Matthey) was also prepared for comparison purpose. The metal loadings were  $0.7 \text{ mg cm}^{-2}$  for all the electrocatalysts.

#### 3B.1.5.2 Air breathing micro laminar flow fuel cell testing

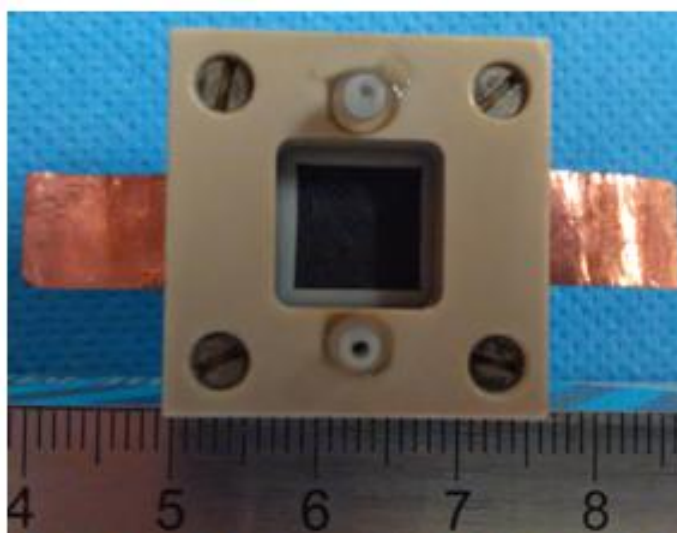


**Figure 3B.1:** Digital photograph of the air breathing micro laminar flow fuel cell assembly.

Two TK-PEEK plates, 6 mm height and 25 mm width, served as the end plates to maintain the all fuel cell parts together. Each plate had two holes: the inlet and the outlet. The anode and cathode were “sandwiched” between the two plates. The cathode plate was

opened to air by means of a window or a small compartment and the fuel was feeding through anode. Two sheets of copper, in contact with the electrodes, served as the current collectors (see the photograph of  $\mu$ LFFC cell assembly, Figure. 3B.1). Between the electrodes, there were two pieces of SU-8 structures with an array of 10 micro-channels arranged in parallel. Each channel was having 250  $\mu\text{m}$  height, 500  $\mu\text{m}$  width and 20 mm length. A sheet of nanoporous polycarbonate filter Cyclopore (0.1  $\mu\text{m}$  pore size) was put between the two SU-8 structures to prevent initial mixing of the streams in the micro-channels. The fabrication of the structures with micro-channels was achieved on Si wafers covered by a 400 nm thermally grown  $\text{SiO}_2$  layer as substrates.<sup>[28]</sup>

In order to begin with the direct methanol  $\mu$ LFFC operation, the cell was assembled using  $\text{CoSe}_2/\text{X}$  (X= C, CNH and NCNH) as the cathode and PtRu/C as the anode. 3 M KOH was used as the supporting electrolyte to the cathode and 3 M KOH + 5 M  $\text{CH}_3\text{OH}$  was used as the fuel for the anode. Current–potential measurements were carried out by connecting the positive and negative wires of the cell to a 2611A Keithley Sourcemeter. It served as an electronic load, whereas the current and the voltage produced by the fuel cell were measured with the same device. To measure the potential of each electrode separately, a 2100 Keithley digital multi-meter and an RHE with a Luggin micro-capillary were used; this was plunged into the cathode reservoir. The anode and cathode streams were introduced into the cell at 7  $\text{cm}^3/\text{min}$ , using a micro-pump (miniplus 3 Gilson) with 2 supply channels.

For calculating  $iR$  drop, resistance of the cell was measured using the PEIS method with a Potentiostat/Galvanostat (SP-300 Biologic Science Instruments) by applying a frequency of 10 kHz in a punctual measurement of the assembled cell. The working electrode of the Potentiostat was connected to the cathode in the  $\mu$ LFFC meanwhile the counter electrode connection was given to the anode. To separately measure the  $iR$  losses of the cathode and anode, a RHE was placed in the flowing electrolyte at the exit of the  $\mu$ LFFC. The obtained resistance values were 0.780  $\Omega$  and 0.885  $\Omega$  for the cathode and anode, respectively.

Current–potential measurements were carried out with a 2611A Keithley Sourcemeter which served as an electronic power source, whereas, the current and the voltage produced by the micro fuel cell were measured with the same device. To measure

the potential of each electrode separately, it was necessary to use a 2100 Keithley digital multimeter and an RHE with a Luggin microcapillar plunged into the cathode reservoir.

### 3B.2 Results and discussion

#### 3B.2.1 XRD analysis

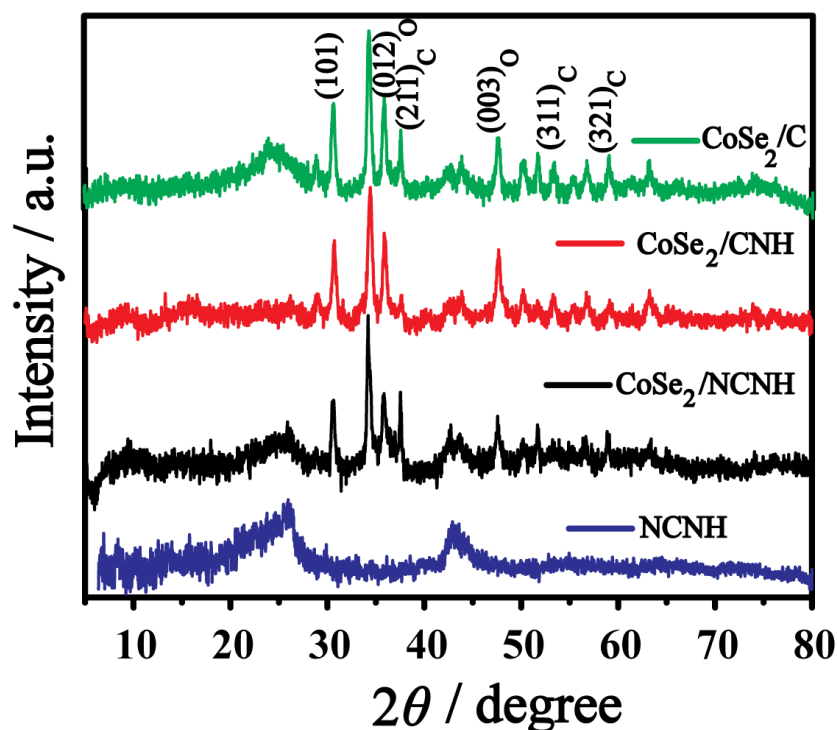


**Figure 3B.2:** Powder X-ray diffraction of the different samples prepared.

CoSe<sub>2</sub> supported on various carbon supports were synthesized through a simple surfactant-free chemical route (Scheme 3B.1). Figure 3B.2 shows the powder X-ray diffraction (PXRD) patterns of CoSe<sub>2</sub>/NCNH, CoSe<sub>2</sub>/CNH, CoSe<sub>2</sub>/C and NCNH. NCNH shows a broad diffraction peak at a  $2\theta$  of  $\sim 26^\circ$  indicates the (002) plane of the graphitic carbon. The peaks appeared at  $35.96^\circ$  and  $47.7^\circ$  correspond to the presence of orthorhombic phase of the CoSe<sub>2</sub> nanocrystals<sup>[20e]</sup> whereas the ones appeared at  $37.5^\circ$ ,  $53.2^\circ$  and  $59.1^\circ$  represent the (211), (311) and (312) Bragg planes, respectively, of the cubic phase of the CoSe<sub>2</sub> nanocrystals.<sup>[24a, 24b]</sup> It is interesting to note that orthorhombic Bragg plane intensity of CoSe<sub>2</sub> nanocrystals supported on NCNH decreased as compared to CoSe<sub>2</sub>/CNH and CoSe<sub>2</sub>/C. This further indicates that CoSe<sub>2</sub> supported on NCNH mainly exists in the cubic form.

### 3B.2.2 Raman analysis

Figure 3B.3 shows the Raman spectra of  $\text{CoSe}_2$  samples supported on different substrates. Two prominent peaks were observed for all the samples at 1313.9 and 1581.5  $\text{cm}^{-1}$  and these are attributed to the D and G bands of the disordered and graphitic carbon, respectively.<sup>[29]</sup> It is well known that CNH itself contains defects on it due to the presence of the  $\text{sp}^3$  carbon.<sup>[5]</sup> The  $I_D/I_G$  ratio of  $\text{CoSe}_2/\text{CNH}$  was found to be 1.7 and this value is lower than that of  $\text{CoSe}_2/\text{NCNH}$  (1.9) and NCNH (2.1). The increased  $I_D/I_G$  ratios of NCNH and  $\text{CoSe}_2/\text{NCNH}$  further confirm the defects generated by the nitrogen atoms. However, the  $I_D/I_G$  ratio of  $\text{CoSe}_2/\text{C}$  is an indicative of the reduced defects on the surface of the carbon.

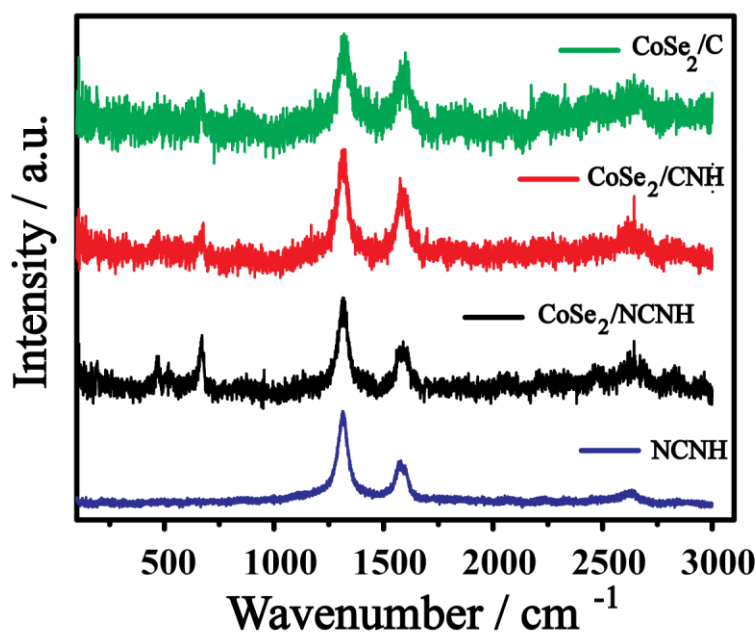


**Figure 3B.3:** Raman spectra of the  $\text{CoSe}_2$  supported samples.

Furthermore, Raman spectroscopy reveals the different phases of  $\text{CoSe}_2$  present in the samples. The Raman spectra of  $\text{CoSe}_2/\text{NCNH}$  has peaks at 663.6, 467.3, 516.4 and 188.5  $\text{cm}^{-1}$  which are corresponding to the cubic structure of  $\text{CoSe}_2$ .<sup>[30]</sup> These Raman peaks are consistent with the results obtained from the XRD experiments. It is important to note that peaks corresponding to the hexagonal cobalt (137, 486 and 695  $\text{cm}^{-1}$ ) and trigonal selenium (144 and 235  $\text{cm}^{-1}$ ) are absent in the Raman spectra.<sup>[30]</sup> This further confirms the presence of cubic  $\text{CoSe}_2$  nanoparticles on NCNH. The peak centered at 663.6  $\text{cm}^{-1}$  is also

present in the case of  $\text{CoSe}_2/\text{C}$  and  $\text{CoSe}_2/\text{CNH}$ . However, the other characteristic peaks are not prominent in the latter materials.

### 3B.2.3 TEM analysis

Figures 3B.4a-d, show the transmission electron microscopic (TEM) images of NCNH (Figure 3B.4a),  $\text{CoSe}_2/\text{CNH}$  (Figure 3B.4b),  $\text{CoSe}_2/\text{NCNH}$  (Figure 3B.4c) and  $\text{CoSe}_2/\text{C}$  (Figure 3B.4d). A spherical morphology with an average  $\text{CoSe}_2$  particle size of 20 nm was revealed for  $\text{CoSe}_2/\text{NCNH}$ .  $\text{CoSe}_2$  is better dispersed on NCNH than on carbon and SWCNH. This clearly indicates that the dahlia-like morphology of the self-assembled nanohorn is beneficial for the effective dispersion of  $\text{CoSe}_2$  nanoparticles compared to carbon. The better dispersion of  $\text{CoSe}_2$  on NCNH compared to SWCNH further confirms the important role played by the nitrogen atoms for facilitating the nucleation and dispersion of  $\text{CoSe}_2$  nanostructures on NCNH.

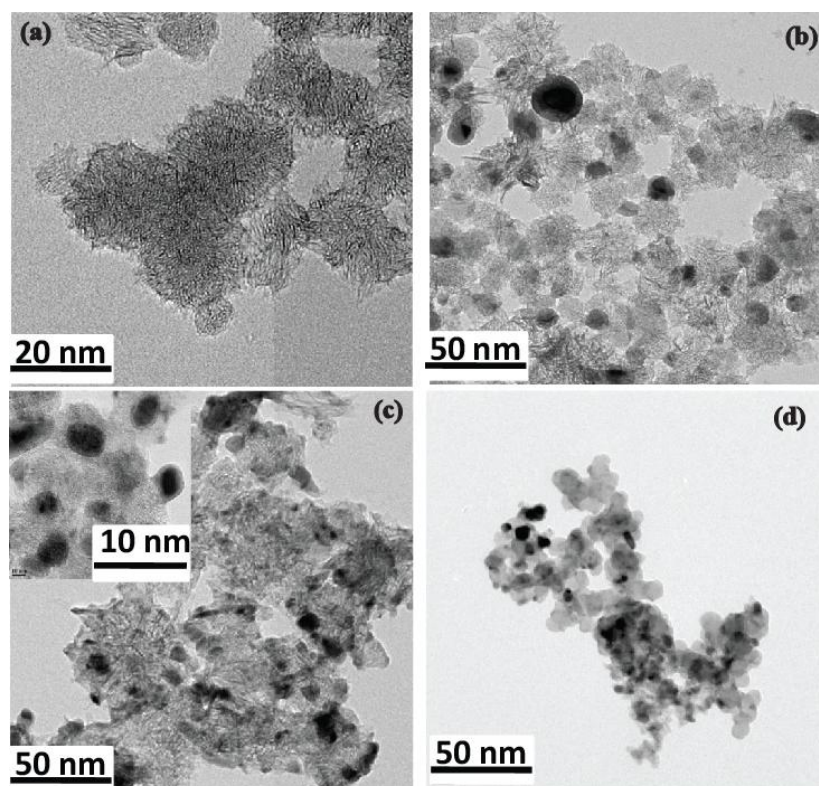


**Figure 3B.4:** TEM images of (a) NCNH, (b)  $\text{CoSe}_2/\text{CNH}$ , (c)  $\text{CoSe}_2/\text{NCNH}$  (the inset represents the image taken at higher magnification) and (d)  $\text{CoSe}_2/\text{C}$ .



### 3B.2.4 Surface area analysis

Nitrogen adsorption isotherm was measured at 77 K to understand the surface area as well as the nature of porosity of CoSe<sub>2</sub> supported samples and NCNH (Figure 3B.5a). BET surface area obtained from the isotherm follows the order of NCNH (1167 m<sup>2</sup>/g) > CoSe<sub>2</sub>/NCNH (772 m<sup>2</sup>/g) > CoSe<sub>2</sub>/CNH (321 m<sup>2</sup>/g) > CoSe<sub>2</sub>/C (88 m<sup>2</sup>/g). It is important to note that surface area of NCNH is lesser compared to a recently reported value.<sup>[29]</sup> The lower surface area of NCNH is mainly due to the absence of functionalisation of SWCNH before the annealing process. However, it is interesting to note that the nitrogen doping further increases the surface area of SWCNH without subjecting to oxidative treatment prior to the high-temperature annealing. Even though NCNH has high surface area, after the CoSe<sub>2</sub> decoration, the surface area is found to be reduced to 772 m<sup>2</sup> g<sup>-1</sup>. This further confirms the proper dispersion of CoSe<sub>2</sub> on NCNH. It is interesting to note that the surface area of CoSe<sub>2</sub>/C is lower than that of the SWCNH-based systems. Pore size distributions (Figure 2b) calculated using DFT analysis of the isotherms clearly indicate that the NCNH-based samples contain a majority of micropores (pore diameter 0–2 nm). Along with the micropores, they also contain some amount of mesopores (pore diameter 2–15 nm); however, a wide range of porosity was also observed for the SWCNH-supported CoSe<sub>2</sub>.

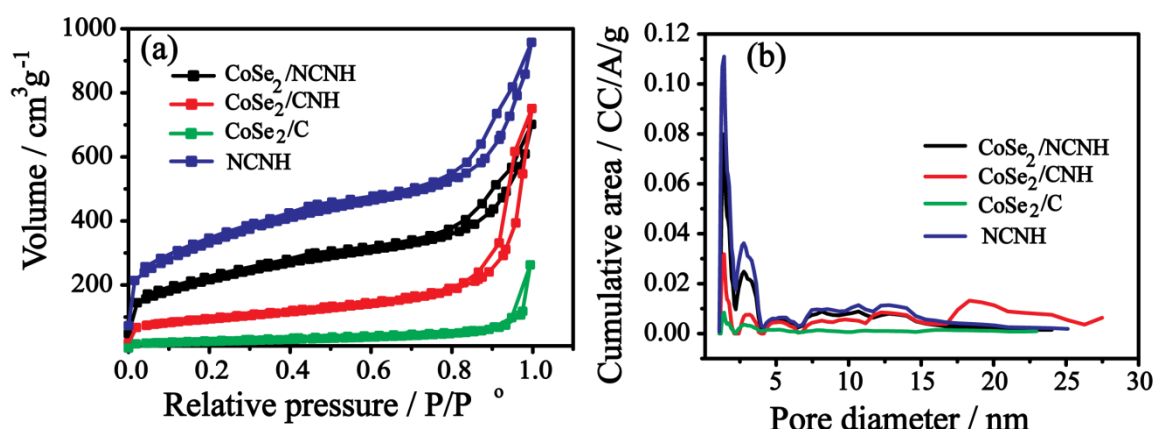


**Figure 3B.5:** (a) Nitrogen adsorption-desorption isotherms of the different samples and (b) the pore size distribution profiles of the samples.

The porosity of the carbon is found to be drastically reduced after the CoSe<sub>2</sub> dispersion on its surface. The unusual morphology, high surface area and porosity of the SWCNH-supported CoSe<sub>2</sub> are expected to contribute to the accessibility of the interfacial area of the system to the reactant along with the attainment of a favourable organisation of water

molecules, which are the essential criteria of an electrocatalyst for ensuring its performance.

### 3B.2.5 XPS analysis

X-ray photoelectron spectroscopy (XPS) was used to reveal the chemical signature of the elements present in the  $\text{CoSe}_2$  samples. Apart from cobalt, selenium, carbon and oxygen, the presence of nitrogen was also detected in the  $\text{CoSe}_2$  supported NCNH sample. Pure NCNH also shows the presence of nitrogen, carbon and oxygen. The presence of oxygen in all the prepared samples might be due to the adsorbed oxygen or impurities. From the XPS analysis (Figure 3B.6a), it was found that binding energy of Co  $2p_{3/2}$  of  $\text{CoSe}_2/\text{NCNH}$  is negatively shifted to 778.1 eV compared to  $\text{CoSe}_2/\text{CNH}$  (778.4 eV).<sup>[31]</sup> However, compared to  $\text{CoSe}_2/\text{C}$  this negative shift is only 0.1 eV and the Co  $2p_{3/2}$  peak of  $\text{CoSe}_2/\text{C}$  is centered at 778.2 eV. If we compare the binding energy shift in Co  $2p_{3/2}$  of the CNH based catalyst, the presence of nitrogen lowered the binding energy of Co  $2p_{3/2}$ . This is a strong indication that electron can be transferred from the nitrogen moieties in the carbon nanohorn to the catalytic center in  $\text{CoSe}_2$ . The same change was also observed for Se  $3d_{3/2}$  (Figure 3B.6b). Binding energy values of Se  $3d_{3/2}$  for  $\text{CoSe}_2/\text{NCNH}$ ,  $\text{CoSe}_2/\text{CNH}$  and  $\text{CoSe}_2/\text{C}$  are 55.2, 55.6 and 55.3 eV, respectively.

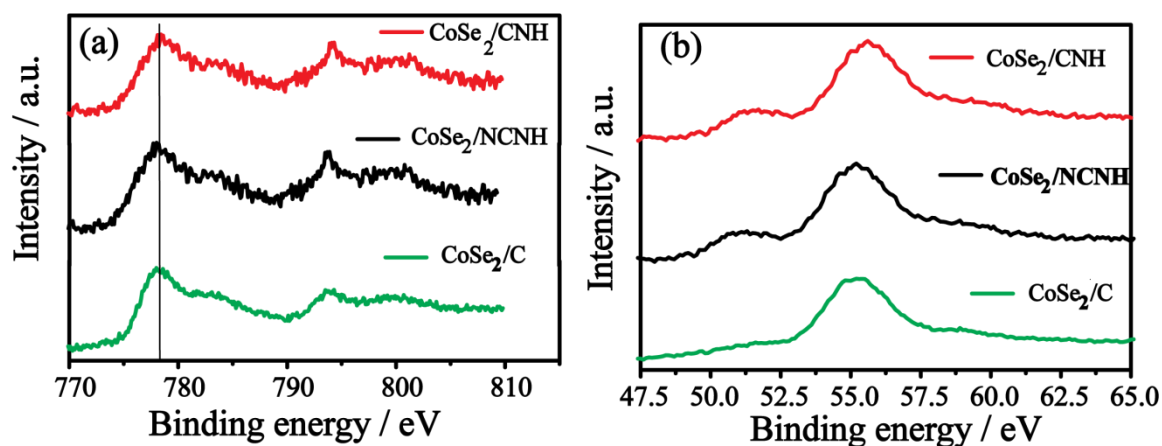
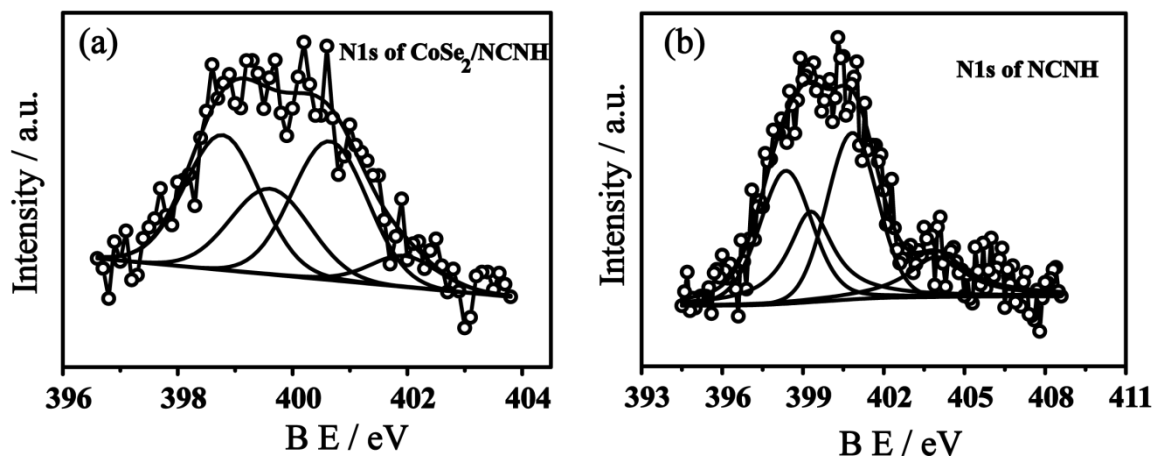


Figure 3B.6: XPS spectra of (a) Co 2p and (b) Se 3d.

Deconvoluted N1s spectra of  $\text{CoSe}_2/\text{NCNH}$  (Figure 3B.7a), and NCNH (Figure 3B.6b) show four different nitrogen coordinations in the samples, mainly pyridinic (~ 398 eV), pyrrolic (~ 399 eV), graphitic (400 eV) and oxide of nitrogen at higher binding energy.<sup>[16, 19a]</sup>



**Figure 3B.7:** (a) Deconvoluted XPS spectra of N 1s in (a)  $\text{CoSe}_2/\text{NCNH}$  and (b)  $\text{NCNH}$ .

From the XPS analysis, it is apparent that the nitrogen atoms induce a charge transfer from nanohorn to the  $\text{CoSe}_2$  nanocrystals. It is well known that the d electron configuration of metal cations in metal chalcogenides plays an important role in its electrocatalytic activity.<sup>[22e]</sup> The low spin electronic configuration of the 3d electrons in Co make  $\text{CoSe}_2$  a metallic conductor.<sup>[32]</sup> The modified electronic structure in Co, which is induced by nitrogen atoms, further expected to enhance the ORR through the preferred 4-electron charge transfer path.

### 3B.2.6 Electrochemical analysis

Electrocatalytic activity of all the materials was measured using a rotating disc electrode (RDE) set-up. Linear sweep voltammetry (LSV) was performed in an oxygen saturated 0.1 M KOH with an electrode rotation rate of 1600 rpm at a scan rate of  $5 \text{ mV s}^{-1}$ . Commercial Pt/C was also tested, in the same experimental condition, for comparison purpose. From Figure 3B.8a, it is clear that  $\text{CoSe}_2$  supported NCNH system outperforms  $\text{CoSe}_2/\text{C}$  and  $\text{CoSe}_2/\text{CNH}$ . The more positive onset potential, and half-wave potential of  $\text{CoSe}_2/\text{NCNH}$  indicate the improvement in both intrinsic activity as well as active reaction center density induced by the support modification. It is notable that  $\text{CoSe}_2$  supported carbon and CNH catalysts show a similar electrochemical activity in terms of the onset potential and half-wave potential.

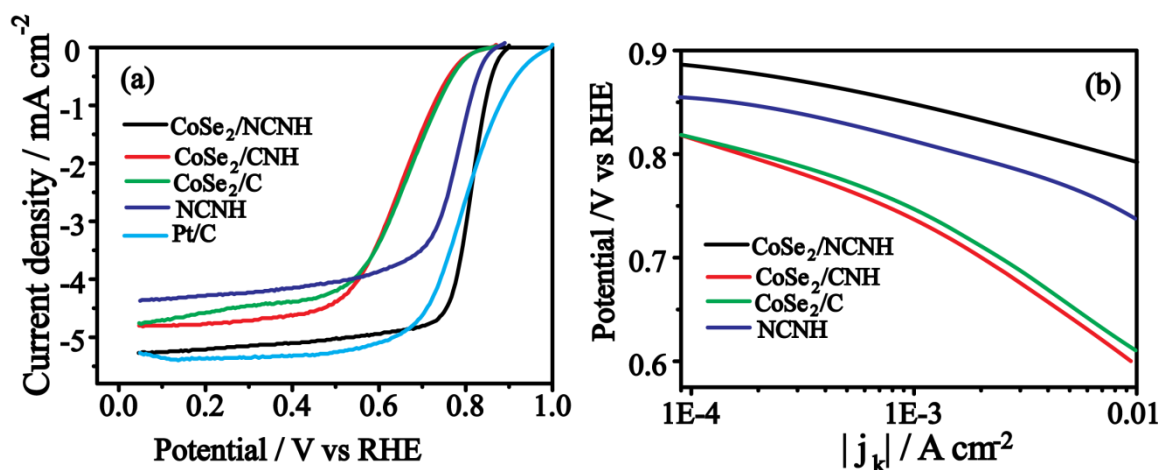


**Figure 3B.8:** (a) Linear sweep voltammograms (LSVs) of the prepared samples and Pt/C in 0.1 M oxygen-saturated KOH at a rotation speed of 1600 rpm and a scan rate of 5 mV s<sup>-1</sup> and (b) Tafel slopes of the catalysts obtained at high potential.

CoSe<sub>2</sub>/NCNH shows an onset potential at 0.90 V vs RHE which is 50 mV higher than both CoSe<sub>2</sub>/C and CoSe<sub>2</sub>/CNH. Similarly, E<sub>1/2</sub> of CoSe<sub>2</sub>/NCNH is found to be 0.81 V vs RHE, which is 160 and 150 mV higher than that of CoSe<sub>2</sub>/CNH and CoSe<sub>2</sub>/C, respectively. As NCNH alone will contribute towards ORR, the onset potential and E<sub>1/2</sub> of NCNH are found to be 23 mV and 40 mV less compared to CoSe<sub>2</sub>/NCNH. This further confirms the synergetic effects of CoSe<sub>2</sub> and NCNH in attaining improved ORR in the composite as compared to the individual counterparts in the system. More interestingly, CoSe<sub>2</sub>/NCNH shows a much improved E<sub>1/2</sub> compared to Pt/C even though its intrinsic activity is much higher as expected. The improvement in activities of CoSe<sub>2</sub>/NCNH is further confirmed from Tafel slope at higher positive potential, Figure 3B.8b. CoSe<sub>2</sub>/NCNH shows a Tafel slope of 52 mV decade<sup>-1</sup> which is 10 mV decade<sup>-1</sup> less compared to NCNH (63 mV decade<sup>-1</sup>) and 20 mV decade<sup>-1</sup> less compared to both CoSe<sub>2</sub>/CNH (72 mV decade<sup>-1</sup>) and CoSe<sub>2</sub>/C (72 mV decade<sup>-1</sup>). These results emphasize that the oxygen adsorption as well as its reduction strongly depends on the electrocatalyst support. SWCNH alone cannot boost the activity of CoSe<sub>2</sub> and, hence, it is having a similar activity performance with CoSe<sub>2</sub>/C. This clearly suggests that the nitrogen atom in NCNH together with the high surface area play a major role in improving the active reaction site density of CoSe<sub>2</sub>. The nitrogen dopant attached to SWCNH modifies the electron density of CoSe<sub>2</sub> in CoSe<sub>2</sub>/NCNH and reduces oxygen molecule more efficiently compared to the other catalyst supports.

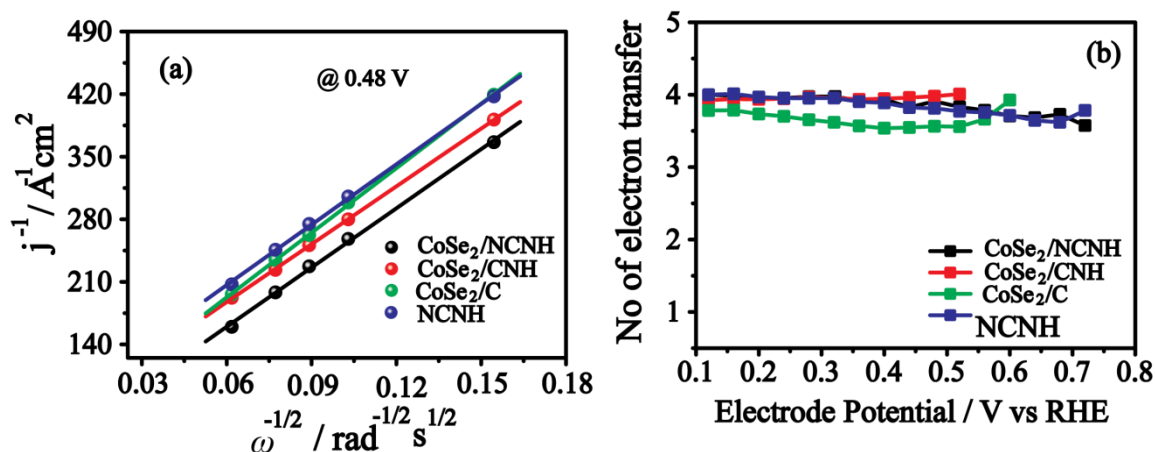


**Figure 3B.9:** (a) K–L plots of the electrocatalysts obtained at a potential of 0.48 V vs. RHE and (b) the plot indicating the number of electrons transferred vs. the potential as calculated from the slope of the K–L plot.

Koutecky–Levich (K–L) plots can be used to provide further kinetic parameters for ORR. Figure 3B.9a shows the K–L plot of the different catalysts recorded at 0.48 V, in which, CoSe<sub>2</sub>/NCNH, CoSe<sub>2</sub>/CNH and NCNH show similar slopes, suggesting a similar mode of oxygen reduction in these samples. However, the slope of CoSe<sub>2</sub>/C deviates slightly from those of the other catalysts, indicating that the mode of oxygen reduction varies marginally from the other catalysts. The number of electrons transferred, calculated from the slope, gives a clearer idea about the mode of oxygen reduction (Figure 3B.9b). CoSe<sub>2</sub>/NCNH, CoSe<sub>2</sub>/CNH and NCNH follow a direct 4-electron pathway for the reduction of molecular oxygen over the potential range measured. Contrary to this, the results reveal an electron transfer number of 3.5 for CoSe<sub>2</sub>/C at 0.48 V, which is found to be approaching towards the values of 4 at more-negative potentials. Similarly, the kinetic current density  $j_k$ , which is directly correlated to the rate constant of the ORR, is also calculated from the intercept of the K–L plot (Figure 3B.10a). At 0.80 V, the  $j_k$  value of CoSe<sub>2</sub>/NCNH is found to be 8.08 mA cm<sup>-2</sup>, which is much higher compared to the values obtained for the other catalysts. The  $j_k$  values of CoSe<sub>2</sub>/NCNH at 0.80 V are 5.0, 4.5 and 4.0 times higher than that of NCNH (1.62 mA cm<sup>-2</sup>), CoSe<sub>2</sub>/CNH (1.78 mA cm<sup>-2</sup>) and CoSe<sub>2</sub>/C (2.04 mA cm<sup>-2</sup>), respectively. Figure 3B.10b shows the mass activity of the different catalysts with respect to the total loading of the sample and with respect to the

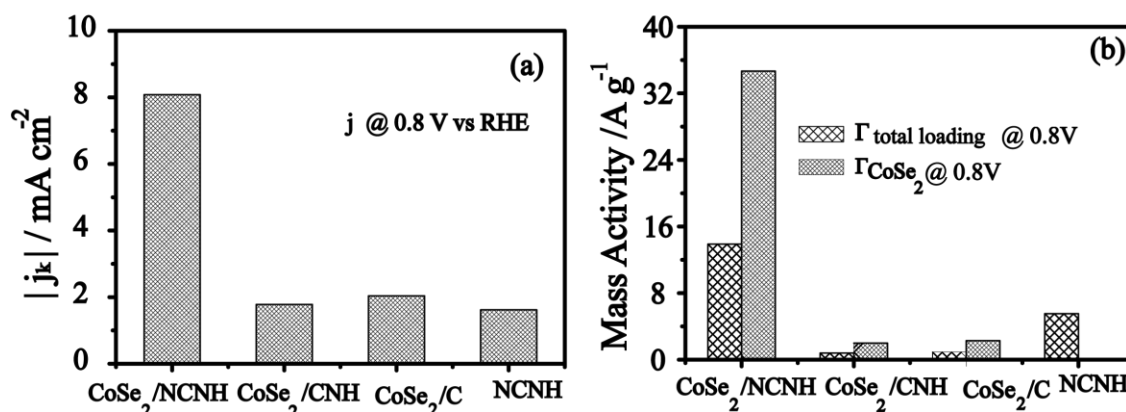


**Figure 3B.10:** (a) Kinetic current density and oxygen reduction current density measured at 0.80 V of the different electrocatalysts and (b) mass activity of the different electrocatalysts measured at 0.80 V.

loading of CoSe<sub>2</sub> alone. From the data shown in Figure 3B.10b, it is apparent that the mass activity of CoSe<sub>2</sub>/NCNH (13.8 A g<sup>-1</sup>) with respect to the total catalyst loading is 2.5 times higher than that of NCNH (5.4 A g<sup>-1</sup>) and 17.8 times higher than both CoSe<sub>2</sub>/CNH (0.78 A g<sup>-1</sup>) and CoSe<sub>2</sub>/C (0.78 A g<sup>-1</sup>). Similarly, the mass activity with respect to the loading of CoSe<sub>2</sub> in the samples follows the order: CoSe<sub>2</sub>/NCNH (34.6 A g<sup>-1</sup>) > CoSe<sub>2</sub>/C (2.3 A g<sup>-1</sup>) > CoSe<sub>2</sub>/CNH (1.8 A g<sup>-1</sup>). From the above electrochemical activity data, it is clear that the support NCNH improves the activity of CoSe<sub>2</sub> compared to SWCNH and carbon. Moreover, the nitrogen atoms in NCNH modify the electronic structure of CoSe<sub>2</sub>, thus increasing the intrinsic oxygen reduction activity and improving the reaction centre density. From this improvement in activity, one can conclude that the activity of the non-platinum electrocatalysts can also be improved by tuning the support materials. The morphology as well as the nitrogen content of SWCNH influences the catalytic activity of CoSe<sub>2</sub>.

Furthermore, the stability of the electrocatalysts was studied by accelerated durability test (ADT), Figure 3B.11. Cyclic voltammograms were performed for 2000 cycles with 50 mV s<sup>-1</sup> scan rate between a potential window of 0.40 - 0.90 V under oxygen purging. LSV was carried out before and after ADT. From Figure 3B.11a, it is clear that there is no change in the onset potential of CoSe<sub>2</sub>/NCNH even after ADT. Contrary to CoSe<sub>2</sub>/NCNH, Pt/C shows a 20 mV decrease in the onset potential after ADT. Similarly, after ADT, E<sub>1/2</sub> of CoSe<sub>2</sub>/NCNH decreased by 10 mV from its initial value compared to a

drop of 20 mV in the case of Pt/C (Figure 3B.11b). A reduction current density by  $0.256 \text{ mA cm}^{-2}$  at 0.40 V has also been observed for CoSe<sub>2</sub>/NCNH after ADT. This value is less compared to Pt/C ( $0.271 \text{ mA cm}^{-2}$ ). The reduction in the performance of Pt/C compared to CoSe<sub>2</sub>/NCNH is attributed to the corrosion of the catalyst support and agglomeration of the Pt nanoparticles. This clearly indicates that NCNH not only improves the activity of CoSe<sub>2</sub> but it also prevents the catalyst from agglomeration and corrosion.

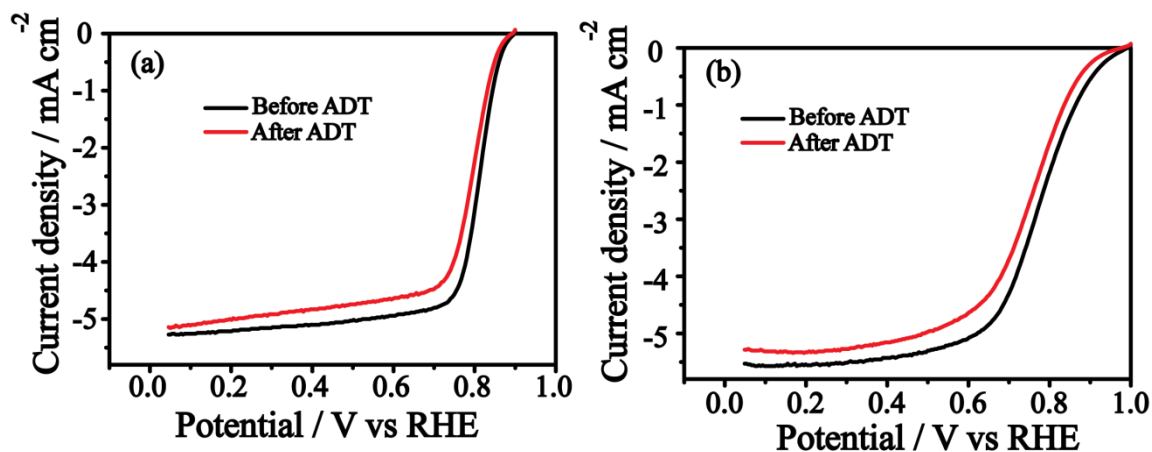


**Figure 3B.11:** LSVs of (a) CoSe<sub>2</sub>/NCNH and (b) Pt/C before and after ADT at 1600 rpm with  $5 \text{ mV s}^{-1}$  scan rate.

**Table 3B.1.** Open circuit potential of the cathode ( $E_{\text{Cathode}}$ ) and the anode ( $E_{\text{Anode}}$ ), maximum current density ( $j_{\text{Max}}$ ) at short circuit and maximum power density ( $P_{\text{Max}}$ ) of the  $\mu\text{LFFC}$  based on CoSe<sub>2</sub> supported on different substrates.

Sample	$E_{\text{Cathode}}$ [V vs RHE]	$E_{\text{Anode}}$ [V vs RHE]	$j_{\text{Max}}$ [ $\text{mA cm}^{-2}$ ]	$P_{\text{Max}}$ [ $\text{mW cm}^{-2}$ ]
CoSe <sub>2</sub> /NCNH	0.95	0.47	124.20	10.04
CoSe <sub>2</sub> /CNH	0.89	0.47	79.28	4.53
CoSe <sub>2</sub> /C	0.89	0.47	79.79	5.33
NCNH	0.92	0.49	72.40	4.41
Pt/C	0.80	0.40	59.87	5.75

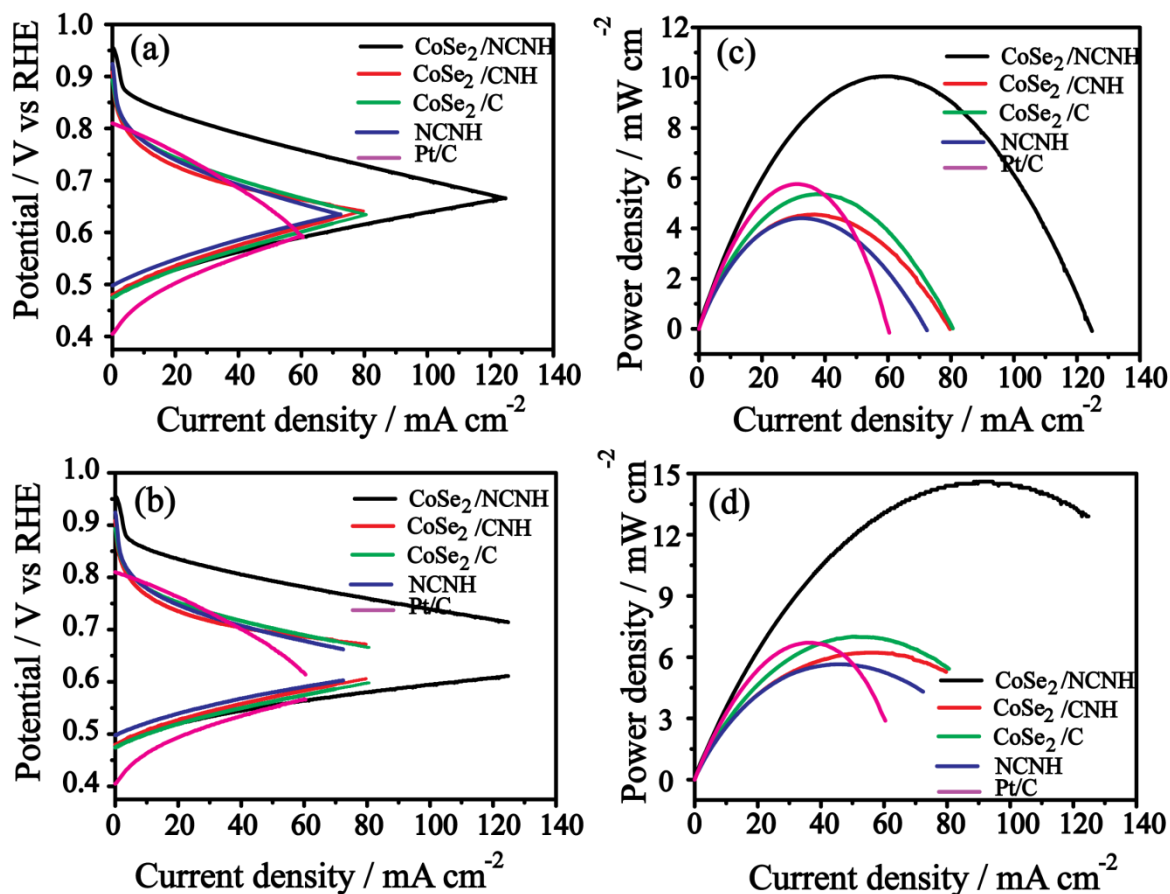


**Figure 3B.12:** (a & c) *iR* correction-free and (b & d) *iR* corrected current-potential and power density curves of  $\mu$ LFFC with CoSe<sub>2</sub>/NCNH, CoSe<sub>2</sub>/CNH, CoSe<sub>2</sub>/C, NCNH and Pt/C as the cathode catalysts. Pt-Ru/C was used as the anode catalyst. 5 M methanol was used as the fuel in alkaline solution.

CoSe<sub>2</sub> supported on the different substrates were further used as the cathode catalysts for the air breathing direct methanol multichannel micro-laminar flow fuel cell ( $\mu$ LFFC) in order to study the real fuel cell activity of these catalysts. The current-potential, *j-E*, characteristics of  $\mu$ LFFC are given in Figure 3B.12, in which it is clear that the cathodic onset potential of the system based on CoSe<sub>2</sub>/NCNH is more positive as compared to the ones based on CoSe<sub>2</sub>/C, CoSe<sub>2</sub>/CNH and Pt/C. The maximum current density as well as power density of CoSe<sub>2</sub>/NCNH based system is far better compared to the rest of the systems at a concentration of 5 M methanol. Compared to NCNH, the chalcogenide on SWCNH and carbon enhances the ORR rate (Table 3B.1). However, better activity is obtained when this catalytic centre electronically interacts with NCNH (Figure 3B.12 c). The maximum current density, at short circuit of CoSe<sub>2</sub>/NCNH (124.20



$\text{mA cm}^{-2}$ ) is 1.5 times higher than that of both  $\text{CoSe}_2/\text{C}$  ( $79.79 \text{ mA cm}^{-2}$ ) and  $\text{CoSe}_2/\text{CNH}$  ( $79.28 \text{ mA cm}^{-2}$ ). Interestingly,  $\text{CoSe}_2/\text{NCNH}$  outperforms  $\text{Pt}/\text{C}$ . The maximum current density on  $\text{Pt}/\text{C}$  ( $59.87 \text{ mA cm}^{-2}$ ) is 2 times less compared to that of  $\text{CoSe}_2/\text{NCNH}$ . Moreover, the maximum power density of the catalysts is in the order of  $\text{CoSe}_2/\text{NCNH}$  ( $10.04 \text{ mW cm}^{-2}$ ) >  $\text{Pt}/\text{C}$  ( $5.75 \text{ mW cm}^{-2}$ ) >  $\text{CoSe}_2/\text{C}$  ( $5.33 \text{ mW cm}^{-2}$ ) >  $\text{CoSe}_2/\text{C}$  ( $4.53 \text{ mW cm}^{-2}$ ). It is also important to note that after the  $iR$  correction, the power density of  $\text{CoSe}_2/\text{NCNH}$  is found to be increased to  $14.8 \text{ mW cm}^{-2}$  (Figure 3B.12d). It is very important to note that on the  $\text{CoSe}_2/\text{NCNH}$  system, the concentration of methanol has no effect in the cathodic performance of the fuel cell (Figure 3B.13a). Contrary to the  $\text{CoSe}_2/\text{NCNH}$  based system, the cathodic performance of the  $\text{Pt}/\text{C}$  based system is found to be decreasing with increasing the methanol concentration as expected (Figure 3B.13b). Similarly, the maximum power density as well as the current density of the  $\text{CoSe}_2/\text{NCNH}$  based system is not decreasing much compared to the  $\text{Pt}/\text{C}$  based cell under different concentrations of the methanol feed (Figure 3B.13 b). These results further emphasize that  $\text{CoSe}_2/\text{NCNH}$  is a suitable alternate to the Pt based catalyst in direct methanol fuel cells.

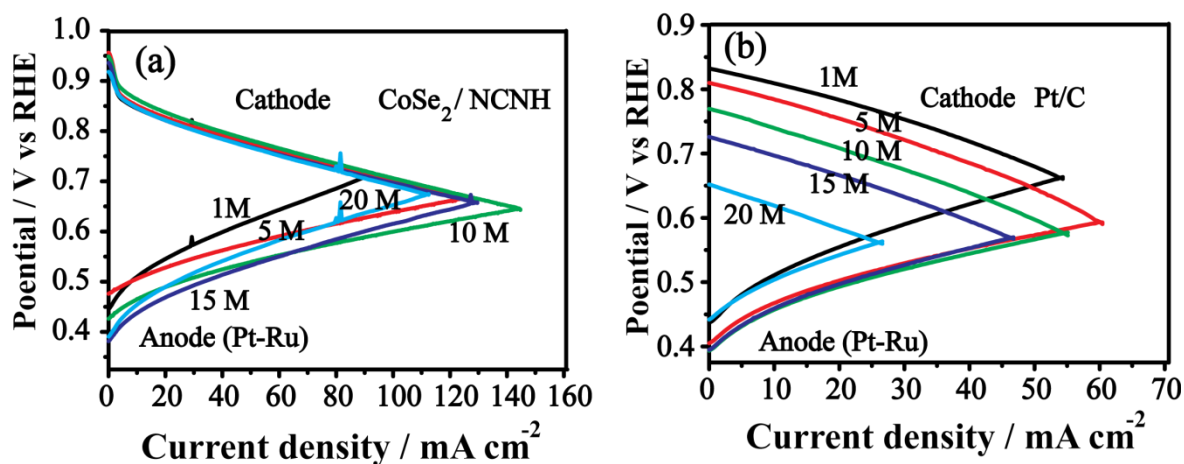


**Figure 3B.13:** Non-ohmic corrected current-potential characteristics of (a)  $\text{CoSe}_2/\text{NCNH}$  and (b)  $\text{Pt}/\text{C}$  cathode of  $\mu\text{LFFC}$  at different concentrations of methanol in alkaline solution.

## 3.2 Conclusion

The present chapter discloses the synthesis of nitrogen doped carbon nanohorn and its metal chalcogenide supported form as two potential non-precious electrocatalysts for facilitating dioxygen reduction in alkaline medium.

A simple synthesis method was adopted for preparing nitrogen doped carbon nanohorn to boost the active reaction centre for ORR by high temperature treatment of functionalized nanohorns and urea. The nitrogen doped nanohorn shows significantly high surface area up to  $1836 \text{ m}^2 \text{ g}^{-1}$ . The nitrogen doping also enhances the electrical conductivity of nanohorn by changing the electronic density of the carbon atoms. Most importantly, the sample designated as N-800 shows more positive onset potential (0.026 V vs. Hg/HgO) compared to N-600 and N-1000. Interestingly, the onset potential of N-800 is only 50 mV lower than that of the *state-of-the-art* 40 wt.% Pt/C catalyst. N-800 follows the preferred  $4e^-$  pathway for the oxygen reduction reaction. Similarly, the kinetic current density of N-800 is higher than that of N-600 and N-1000, indicating that the ORR activity is strongly depending on the pyrolysis temperature. N-800 shows high durability and fuel tolerance compared to the commercial Pt/C. Moreover, an MEA fabricated with N-800 as the cathode catalyst provides a maximum power density of  $30 \text{ mW cm}^{-2}$  in AEMFC testing at  $50^\circ\text{C}$ . Thus, with these sets of enhanced electrochemical properties, nitrogen doped nanohorn turns out to be a potential cost effective, metal-free cathode catalyst for polymer electrolyte membrane fuel cells.

Furthermore, The ORR activity of  $\text{CoSe}_2$  nanoparticles supported on different substrates was studied to understand the ability of the support materials to tune the ORR activity of the non-platinum electrocatalysts. PXRD, Raman spectroscopy and XPS studies support the formation of  $\text{CoSe}_2$  nanoparticles on various carbon supports. Spherical  $\text{CoSe}_2$  nanoparticles with an average size of 20 nm supported on NCNH are observed by TEM. Moreover, NCNH provides high surface area and the nitrogen atoms aid the distribution of  $\text{CoSe}_2$  nanoparticles on the surface of NCNH. From the XPS analysis, it was found that the nitrogen atoms modify the electronic structure of  $\text{CoSe}_2$  nanoparticles through a strong substrate–catalyst interaction, which in turn assists efficient molecular oxygen adsorption and its reduction. The intrinsic activity and active-site density of  $\text{CoSe}_2$  is found to be improved significantly when these nanoparticles are supported on NCNH. A positive shift in the onset potential by 50 mV and a shift by 150 mV in  $E_{1/2}$  of  $\text{CoSe}_2/\text{NCNH}$  compared to  $\text{CoSe}_2/\text{C}$  indicate that the morphology of NHCH and the nitrogen doping play important roles in modulating the reaction centres of  $\text{CoSe}_2$ . From the K–L plot, it is found that  $\text{CoSe}_2/\text{NCNH}$  reduces molecular oxygen to hydroxide ions through a 4-electron charge transfer. The kinetic current density of  $\text{CoSe}_2/\text{NCNH}$  at 0.80 V is 4.5 and 4.0 times higher than  $\text{CoSe}_2/\text{CNH}$  and  $\text{CoSe}_2/\text{C}$ , respectively. The mass activity with respect to the total

loading of CoSe<sub>2</sub>/NCNH at 0.80 V is found to be 17.8 times higher than that of CoSe<sub>2</sub>/C and CoSe<sub>2</sub>/CNH. Furthermore, compared to Pt/C, CoSe<sub>2</sub>/NCNH shows improved stability during ADT. The performance of a CoSe<sub>2</sub>/NCNH-based cathode in a  $\mu$ -LFFC indicates that CoSe<sub>2</sub>/NCNH is a better choice than CoSe<sub>2</sub>/CNH, CoSe<sub>2</sub>/C and Pt/C for the cathode application. The maximum current density obtained for the CoSe<sub>2</sub>/NCNH based cell is estimated to be twice that of the one based on Pt/C at a methanol concentration of 5 M. The maximum power density in this case is found to be 1.7 times higher than that of the system based on Pt/C. Similarly, the cathodic performance of CoSe<sub>2</sub>/NCNH is unaffected by the concentration of methanol. Considering the interesting activity characteristics of CoSe<sub>2</sub>/NCNH as evident from this study, this material can be considered as a potential cathode electrocatalyst for fabricating cost-effective and active air-breathing direct methanol microlaminar flow fuel cells.

### 3.3 Reference

- [1] a)H. Wang, T. Maiyalagan, X. Wang, *ACS Catal.* **2012**, *2*, 781-794; b)T. Palaniselvam, H. B. Aiyappa, S. Kurungot, *J. Mater. Chem.* **2012**, *22*, 23799-23805; c)D. Yu, Y. Xue, L. Dai, *J. Phys. Chem. Lett.* **2012**, *3*, 2863-2870; d)Y. Zheng, Y. Jiao, J. Chen, J. Liu, J. Liang, A. Du, W. Zhang, Z. Zhu, S. C. Smith, M. Jaroniec, G. Q. Lu, S. Z. Qiao, *J. Am. Chem. Soc.* **2011**, *133*, 20116-20119.
- [2] H. T. Chung, J. H. Won, p. Zelenay, *Nat. Commun.* **2013**.
- [3] a)H. Jiang, P. S. Lee, C. Li, *Energy Environ. Sci.* **2013**, *6*, 41-53; b)B. Liu, H. Shioyama, T. Akita, Q. Xu, *J. Am. Chem. Soc.* **2008**, *130*, 5390-5391; c)C. Li, G. Shi, *Nanoscale* **2012**, *4*, 5549-5563.
- [4] a)P. Simon, Y. Gogotsi, *Acc. Chem. Res.* **2012**, *46*, 1094-1103; b)M. A. Worsley, P. J. Pauzauskie, T. Y. Olson, J. Biener, J. H. Satcher, T. F. Baumann, *J. Am. Chem. Soc.* **2010**, *132*, 14067-14069; c)L. Zhang, F. Zhang, X. Yang, G. Long, Y. Wu, T. Zhang, K. Leng, Y. Huang, Y. Ma, A. Yu, Y. Chen, *Scientific Reports* **2013**, *3*, 1408.
- [5] S. Zhu, G. Xu, *Nanoscale* **2010**, *2*, 2538-2549.
- [6] a)C. M. Yang, H. Noguchi, K. Murata, M. Yudasaka, A. Hashimoto, S. Iijima, K. Kaneko, *Adv. Mater.* **2005**, *17*, 866-870; b)C. Cioffi, S. Campidelli, F. G. Brunetti,

- M. Meneghetti, M. Prato, *Chem. Commun.* **2006**, 2129-2131; c)J. Fan, M. Yudasaka, J. Miyawaki, K. Ajima, K. Murata, S. Iijima, *J. Phys. Chem. B* **2006**, *110*, 1587-1591; d)K. Murata, K. Kaneko, W. A. Steele, F. Kokai, K. Takahashi, D. Kasuya, K. Hirahara, M. Yudasaka, S. Iijima, *J. Phys. Chem. B* **2001**, *105*, 10210-10216; e)S. Utsumi, J. Miyawaki, H. Tanaka, Y. Hattori, T. Itoi, N. Ichikuni, H. Kanoh, M. Yudasaka, S. Iijima, K. Kaneko, *J. Phys. Chem. B* **2005**, *109*, 14319-14324.
- [7] X. Li, H. Wang, J. T. Robinson, H. Sanchez, G. Diankov, H. Dai, *J. Am. Chem. Soc.* **2009**, *131*, 15939-15944.
- [8] a)L. Brandão, C. Passeira, D. Mirabile Gattia, A. Mendes, *J Mater Sci* **2011**, *46*, 7198-7205; b)E. Bekyarova, A. Hashimoto, M. Yudasaka, Y. Hattori, K. Murata, H. Kanoh, D. Kasuya, S. Iijima, K. Kaneko, *J. Phys. Chem. B* **2005**, *109*, 3711-3714; c)M. Kosaka, S. Kuroshima, K. Kobayashi, S. Sekino, T. Ichihashi, S. Nakamura, T. Yoshitake, Y. Kubo, *J. Phys. Chem. C* **2009**, *113*, 8660-8667; d)T. Yoshitake, Y. Shimakawa, S. Kuroshima, H. Kimura, T. Ichihashi, Y. Kubo, D. Kasuya, K. Takahashi, F. Kokai, M. Yudasaka, S. Iijima, *Physica B: Condensed Matter* **2002**, *323*, 124-126; e)L. Zhang, N. Zheng, A. Gao, C. Zhu, Z. Wang, Y. Wang, Z. Shi, Y. Liu, *J. Power Sources* **2012**, *220*, 449-454; f)A. Izadi-Najafabadi, T. Yamada, D. N. Futaba, M. Yudasaka, H. Takagi, H. Hattori, S. Iijima, K. Hata, *ACS Nano* **2011**, *5*, 811-819; g)R. Yuge, T. Manako, K. Nakahara, M. Yasui, S. Iwasa, T. Yoshitake, *Carbon* **2012**, *50*, 5569-5573; h)C.-M. Yang, Y.-J. Kim, M. Endo, H. Kanoh, M. Yudasaka, S. Iijima, K. Kaneko, *J. Am. Chem. Soc.* **2006**, *129*, 20-21.
- [9] Y. Zhao, J. Li, Y. Ding, L. Guan, *RSC Adv.* **2011**, *1*, 852-856.
- [10] a)S. Zhu, G. Xu, in *Nanotechnologies for the Life Sciences*, Wiley-VCH Verlag GmbH & Co. KGaA, **2007**; b)M. Nakamura, Y. Tahara, Y. Ikehara, T. Murakami, K. Tsuchida, S. Iijima, I. Waga, M. Yudasaka, *Nanotechnology* **2011**, *22*, 465102.
- [11] Z. Lin, G. Waller, Y. Liu, M. Liu, C.-P. Wong, *Adv. Energy Mater.* **2012**, *2*, 884-888.
- [12] S. Bandow, A. M. Rao, G. U. Sumanasekera, P. C. Eklund, F. Kokai, K. Takahashi, M. Yudasaka, S. Iijima, *Appl Phys A* **2000**, *71*, 561-564.
- [13] S. Utsumi, H. Honda, Y. Hattori, H. Kanoh, K. Takahashi, H. Sakai, M. Abe, M. Yudasaka, S. Iijima, K. Kaneko, *J. Phys. Chem. C* **2007**, *111*, 5572-5575.

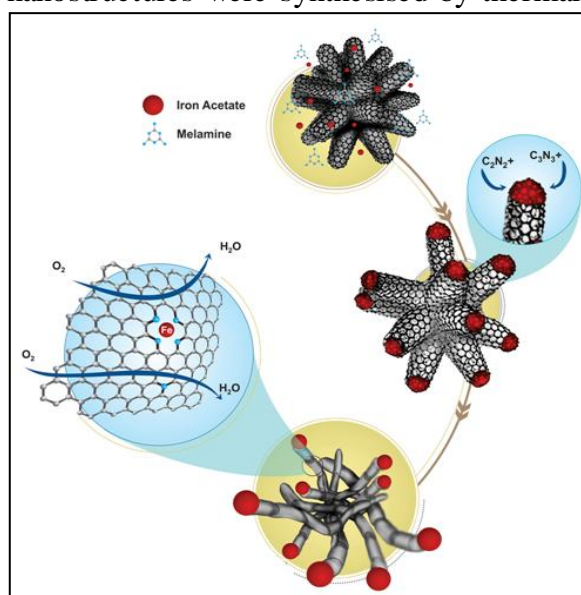
- [14] a)L. S. Panchakarla, A. Govindaraj, C. N. R. Rao, *ACS Nano* **2007**, *1*, 494-500; b)L. Zhao, R. He, K. T. Rim, T. Schiros, K. S. Kim, H. Zhou, C. Gutiérrez, S. P. Chockalingam, C. J. Arguello, L. Pálová, D. Nordlund, M. S. Hybertsen, D. R. Reichman, T. F. Heinz, P. Kim, A. Pinczuk, G. W. Flynn, A. N. Pasupathy, *Science* **2011**, *333*, 999-1003; c)F. Niu, J.-M. Liu, L.-M. Tao, W. Wang, W.-G. Song, *J. Mater. Chem. A* **2013**, *1*, 6130-6133.
- [15] J. Fan, R. Yuge, J. Miyawaki, T. Kawai, S. Iijima, M. Yudasaka, *J. Phys. Chem. C* **2008**, *112*, 8600-8603.
- [16] J. Casanovas, J. M. Ricart, J. Rubio, F. Illas, J. M. Jiménez-Mateos, *J. Am. Chem. Soc.* **1996**, *118*, 8071-8076.
- [17] L. Lai, J. R. Potts, D. Zhan, L. Wang, C. K. Poh, C. Tang, H. Gong, Z. Shen, J. Lin, R. S. Ruoff, *Energy Environ. Sci.* **2012**, *5*, 7936-7942.
- [18] K. Gong, F. Du, Z. Xia, M. Durstock, L. Dai, *Science* **2009**, *323*, 760-764.
- [19] a)S. M. Unni, S. Devulapally, N. Karjule, S. Kurungot, *J. Mater. Chem.* **2012**, *22*, 23506-23513; b)S. Yang, X. Feng, X. Wang, K. Müllen, *Angew. Chem. Int. Ed.* **2011**, *50*, 5339-5343.
- [20] a)H. Wang, Y. Liang, Y. Li, H. Dai, *Angew. Chem. Int. Ed.* **2011**, *50*, 10969-10972; b)N. Mahmood, C. Zhang, J. Jiang, F. Liu, Y. Hou, *Chemistry – A European Journal* **2013**, *19*, 5183-5190; c)G. A. Tritsarlis, J. K. Nørskov, J. Rossmeisl, *Electrochimi. Acta* **2011**, *56*, 9783-9788; d)D. Zhao, S. Zhang, G. Yin, C. Du, Z. Wang, J. Wei, *Electrochimi. Acta* **2013**, *91*, 179-184; e)Y.-S. Chao, D.-S. Tsai, A.-P. Wu, L.-W. Tseng, Y.-S. Huang, *International Journal of Hydrogen Energy* **2013**, *38*, 5655-5664; f)E. Vayner, R. A. Sidik, A. B. Anderson, B. N. Popov, *J. Phys. Chem. C* **2007**, *111*, 10508-10513; g)M.-R. Gao, J. Jiang, S.-H. Yu, *Small* **2012**, *8*, 13-27.
- [21] a)M.-R. Gao, Y.-F. Xu, J. Jiang, Y.-R. Zheng, S.-H. Yu, *J. Am. Chem. Soc.* **2012**, *134*, 2930-2933; b)Y.-R. Zheng, M.-R. Gao, Q. Gao, H.-H. Li, J. Xu, Z.-Y. Wu, S.-H. Yu, *Small* **2015**, *11*, 182-188; c)M.-R. Gao, X. Cao, Q. Gao, Y.-F. Xu, Y.-R. Zheng, J. Jiang, S.-H. Yu, *ACS Nano* **2014**, *8*, 3970-3978.
- [22] a)H. Zhang, B. Yang, X. Wu, Z. Li, L. Lei, X. Zhang, *ACS Appl. Mater. Inter.* **2015**; b)Y.-F. Xu, M.-R. Gao, Y.-R. Zheng, J. Jiang, S.-H. Yu, *Angew. Chem. Int. Ed.* **2013**, *52*, 8546-8550; c)D. Kong, J. J. Cha, H. Wang, H. R. Lee, Y. Cui, *Energy Environ. Sci.* **2013**, *6*, 3553-3558; d)M.-R. Gao, Z.-Y. Lin, T.-T. Zhuang, J.

- Jiang, Y.-F. Xu, Y.-R. Zheng, S.-H. Yu, *J. Mater. Chem.* **2012**, *22*, 13662-13668; e)D. Kong, H. Wang, Z. Lu, Y. Cui, *J. Am. Chem. Soc.* **2014**, *136*, 4897-4900; f)D.-Y. Wang, M. Gong, H.-L. Chou, C.-J. Pan, H.-A. Chen, Y. Wu, M.-C. Lin, M. Guan, J. Yang, C.-W. Chen, Y.-L. Wang, B.-J. Hwang, C.-C. Chen, H. Dai, *J. Am. Chem. Soc.* **2015**; g)J. Xie, J. Zhang, S. Li, F. Grote, X. Zhang, H. Zhang, R. Wang, Y. Lei, B. Pan, Y. Xie, *J. Am. Chem. Soc.* **2013**, *135*, 17881-17888; h)M.-R. Gao, J.-X. Liang, Y.-R. Zheng, Y.-F. Xu, J. Jiang, Q. Gao, J. Li, S.-H. Yu, *Nat Commun* **2015**, *6*.
- [23] Y. Feng, T. He, N. Alonso-Vante, *Chem. Mater.* **2007**, *20*, 26-28.
- [24] a)Y. Feng, N. Alonso-Vante, *Electrochimi. Acta* **2012**, *72*, 129-133; b)Y. J. Feng, T. He, N. Alonso-Vante, *Fuel Cells* **2010**, *10*, 77-83; c)Y. Feng, T. He, N. Alonso-Vante, *Electrochimi. Acta* **2009**, *54*, 5252-5256.
- [25] S. Sharma, B. G. Pollet, *J. Power sources* **2012**, *208*, 96-119.
- [26] H. Huang, X. Wang, *J. Mater. Chem. A* **2014**, *2*, 6266-6291.
- [27] a)Y.-J. Wang, D. P. Wilkinson, J. Zhang, *Chem. Rev.* **2011**, *111*, 7625-7651; b)Z. Zhang, J. Liu, J. Gu, L. Su, L. Cheng, *Energy Environ. Sci.* **2014**, *7*, 2535-2558; c)L. Zhang, L. Wang, C. M. B. Holt, B. Zahiri, Z. Li, K. Malek, T. Navessin, M. H. Eikerling, D. Mitlin, *Energy Environ. Sci.* **2012**, *5*, 6156-6172.
- [28] A. S. Gago, Y. Gochi-Ponce, Y.-J. Feng, J. P. Esquivel, N. Sabaté, J. Santander, N. Alonso-Vante, *ChemSusChem* **2012**, *5*, 1488-1494.
- [29] S. M. Unni, S. N. Bhange, R. Illathvalappil, N. Mutneja, K. R. Patil, S. Kurungot, *Small* **2015**, *11*, 352-360.
- [30] C. E. M. Campos, J. C. de Lima, T. A. Grandi, K. D. Machado, P. S. Pizani, *Physica B: Condensed Matter* **2002**, *324*, 409-418.
- [31] H. van der Heide, R. Hemmel, C. F. van Bruggen, C. Haas, *Journal of Solid State Chemistry* **1980**, *33*, 17-25.
- [32] K. Adachi, M. Matsui, Y. Omata, *Journal of the Physical Society of Japan* **1981**, *50*, 83-89.

## Chapter 4

### *Nitrogen and iron co-doped carbon nanohorn for ORR\**

This chapter elaborates on the synthesis of nitrogen and iron co-doped carbon nanohorns and their ORR activity. Here, influence of the relative loading of nitrogen and iron precursor on the morphology of the resultant co-doped carbon nanohorn is studied along with its effect in the ORR activity accomplished by the modification of the active reaction centre density. Nitrogen and iron co-doped nanostructures were synthesised by thermal annealing of the materials in an inert atmosphere. At lower loading of the nitrogen and iron precursor, morphology of nanohorn (FeNCNH) remains intact after the annealing. This material shows excellent ORR activity and electrochemical stability in alkaline medium and outperforms the commercial Pt/C catalyst. However, the ORR performance of FeNCNH is relatively poor in acidic conditions. When the iron and nitrogen precursor loadings are higher, the morphology of carbon nanohorn transforms to graphene nanotube with the iron oxide nanoparticles encapsulated at the tip (FeGNT). These materials perform well towards ORR in both alkaline and acidic conditions. An overpotential of 100 mV was observed for ORR in the case of FeGNT, as compared to Pt/C in acidic condition and it also outperforms Pt/C in alkaline medium. Moreover, the electrochemical stability of FeGNT is far better in comparison with Pt/C. Single cell performance of FeGNT as the cathode catalyst provides a maximum power density of  $200 \text{ mW cm}^{-2}$  using Nafion<sup>®</sup> 212 as a proton conducting membrane.



\*Contents of this chapter was published in the following research article:

S.M. Unni *et al.*, J. Mater. Chem. A, 2015, 3, 4361 – 4367.

S.M. Unni *et al.*, ACS Appl. Mater. Interfaces, 2015, 10.1021/acsami.5b07802

## 4.1 Introduction

Fe and Co have been identified as the proper non-precious metal counterparts for the heteroatoms as their mutual coordinations and synergistic interactions have the ability to narrow down the overpotential for ORR.<sup>[1]</sup> Recently, few reports have appeared on Fe based electrocatalysts, which have shown activity comparable to that of the Pt based systems.<sup>[1c, 2]</sup> Most of these works in this direction are mainly giving emphasis on tuning the ways to improve the active reaction centres in order to attain efficient chemisorption of dioxygen molecules so as to improve the ORR activity. Dodelet *et al* introduced a new concept to improve the active site of iron coordinated nitrogen doped carbon materials by creating micropores on carbon using pore filler.<sup>[1d]</sup> Similar kind of work is also reported by Dai *et al* using partially unzipped carbon nanotubes, which possess active centres with improved characteristics to reduce dioxygen molecule.<sup>[2c]</sup> Also, there are reports to utilize high surface area carbons derived from metal organic frame works (MOFs) to create more active centres.<sup>[3]</sup> Xu *et al* used a high surface area carbon to create more active centres which contains coordinated moieties of Fe based complexes.<sup>[2a]</sup> Most of these Fe coordinated nitrogen doped carbon materials require either template or multiple annealing procedures for creating high surface area with high microspores as well as nitrogen doping. Similarly, harsh oxidation treatment of carbon morphology to improve the active reaction centre, adversely affects its physico-chemical characteristics.

Higher activity can be achieved if one can tune the surface area and micro-porosity to create more number of metal-nitrogen coordinated ( $M-N_x$ ) sites in order to improve the active reaction centre density without compromising the physico-chemical properties of the carbon matrix. In this regard, single wall carbon nanohorn (SWCNH) can be a suitable candidate among the different carbon morphologies due to its easily tuneable surface area as well as microporosity, which can be achievable without seriously affecting its physico-chemical properties.<sup>[4]</sup> Similarly, the peculiar dahlia like morphology of these materials is expected to help for fast mass transport compared to reduced graphene oxide as well as carbon nanotubes. Single wall nanohorn projections in the carbon morphology even help to trap reactant molecules and improve the activity. Even though some reports are available for SWCNH as catalyst support for PEMFC, this material as such has not yet been used as a catalyst for fuel cells.<sup>[5]</sup> Three times higher surface area with micro-meso pores can be easily achieved by simple thermal annealing of SWCNH. Apart from this, the three



dimensional 'dahlia' like morphology of SWCNH with high density of micro-mesopores can also assist to improve the active reaction site density by facilitating effective coordination of nitrogen and iron.

First part (*Part A*) of the chapter explains a one-step thermal treatment of a mixture of single wall carbon nanohorn (SWCNH), melamine and  $\text{FeCl}_3$  at different temperatures, followed by acid wash to synthesize Fe coordinated nitrogen doped carbon nanohorn. Here, a mixture of SWCNH, melamine and  $\text{FeCl}_3$  was taken in a ratio of 1:3:0.1. This ratio provides Fe and N co-doped SWCNH, without any deformation in the SWCNH morphology. Second part (*Part B*) of the chapter introduces a facile synthesis of Fe and N doped graphene nanotube with high surface area and higher density of active sites by annealing a mixture of SWCNH, melamine and iron salt in a ratio of 1:10:2.5 in an inert atmosphere.

## Part A. Surface-modified single wall carbon nanohorn as an effective electrocatalyst for platinum-free fuel cell cathodes\*

In this part of the present chapter, a simple one-step process involving thermal treatment of a mixture containing single wall carbon nanohorn (SWCNH), melamine and  $\text{FeCl}_3$  at different temperatures (800, 900 and 1000 °C) followed by acid washing to synthesize the Fe coordinated nitrogen doped carbon nanohorns (FeNCNH-800, FeNCNH-900 and FeNCNH-1000) is illustrated. High temperature annealing of SWCNH with melamine and ferric chloride creates more number of micropores along the surface. These fertile regions ensure high density of doped nitrogen atoms which simultaneously coordinate with iron to create efficient active centres for adsorption and reduction of dioxygen. The synthesised material shows an ORR activity higher than that of the commercial Pt/C, all the while maintaining high electrochemical stability and tolerance towards poisoning.

### 4A.1 Experimental

#### 4A.1.1 Functionalization of SWCNH

Preparation of functionalized SWCNH (FCNH) is as follows: 2 g of SWCNH was mixed with  $\text{H}_2\text{O}_2$  in a round-bottom flask and the mixture refluxed 5 h at 60 °C. After cooling to room temperature, the product was filtered off and washed a number of times with deionised water to ensure complete removal of  $\text{H}_2\text{O}_2$ . The resulting sample was dried overnight under vacuum at 80 °C.

#### 4A.1.2 Synthesis of FeNCNH

Initially 300 mg of melamine was dissolved in 20 ml deionized water with sonication and stirring. After complete dissolution, 100 mg of FCNH was added and the mixture was sonicated a further 30 min. 6 mg of  $\text{FeCl}_3$  was added to the resulting solution and the mixture stirred at 60 °C. The resulting black powder was annealed for 3 h at various temperatures in an argon atmosphere. The samples prepared at different temperatures were separately mixed with concentrated hydrochloric acid and stirred overnight, followed by bath sonication for 1 h to ensure removal of the iron impurities. The samples were finally washed several times with deionized water. For comparison,

\* *Reproduced with permission from Royal Society of Chemistry (J. Mater. Chem. A 2015, 3, 4361-4367)*

nitrogen-doped single-walled carbon nanohorn (NCNH) was similarly prepared by annealing a mixture of FCNH and melamine, without addition of  $\text{FeCl}_3$ , at  $900\text{ }^\circ\text{C}$  for 3 h.

#### 4A.1.3 Synthesis of FeNC

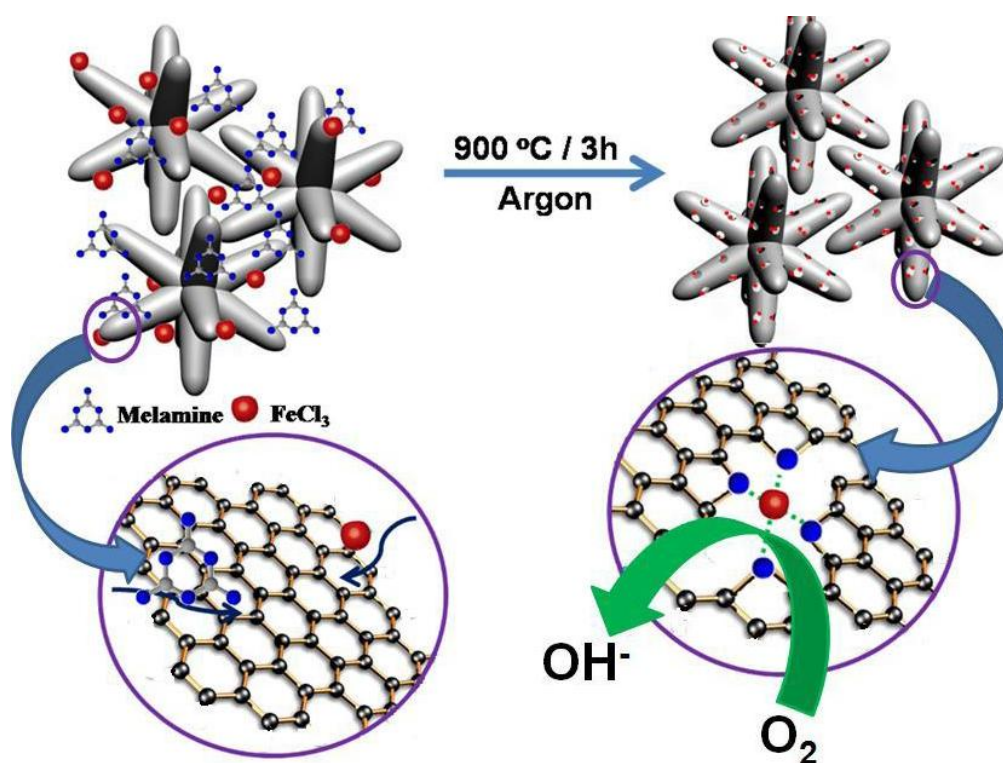
For the preparation of the Fe coordinated nitrogen doped carbon (FeNC) samples, we have used Vulcan carbon mixed with melamine and  $\text{FeCl}_3$  (amounts were taken as similar to the case of FeNCNH). The adopted synthesis procedures were similar to that used for preparing FeNCNH. The annealing was done at  $900\text{ }^\circ\text{C}$  under argon atmosphere for 3 h.

#### 4A.1.4 Synthesis of Fe complex on SWCNH

For the Fe complex synthesis, we have followed the procedure reported by Thorum *et al* (Angew. Chem. Int. Ed, 2009, 48, 165). In a typical synthesis, FCNH and  $\text{FeCl}_3$  were mixed well in deionized water. 0.159 g of 3,5-diamino-1,2,4-triazole in 10 ml solution was added slowly into the above mixture and the mixture was stirred for 18 h. After stirring, the solid material was collected using filtration and it was dried under vacuum at  $80\text{ }^\circ\text{C}$  for overnight.

#### 4A.1.5 Physical characterizations

X-ray diffraction (XRD) patterns were obtained from PANalytical X'pert Pro instrument.  $\text{Cu K}\alpha$  ( $1.5418\text{ \AA}$ ) radiation was used for the X-ray radiation. Raman analyses of the samples were carried out using HR 800 Raman spectrometer (Jobin Yvon, Horiba, France) using 632.8 nm green laser (NRS 1500 W). High resolution transmission electron microscope (HR-TEM) FEI model (TECNAI G2 F30) operated at an accelerating voltage of 300 kV ( $C_s = 0.6\text{ mm}$ , resolution  $1.7\text{ \AA}$ ) and field emission scanning electron microscope (FE-SEM) model NOVA Nano SEM 450, were used for analyzing morphology of the synthesized materials. X-ray photoelectron spectroscopy (XPS) analysis was carried out using a VG Microtech Multilab ESCA 3000 spectrometer equipped with an  $\text{Al K}\alpha$  X-ray source. Electrical conductivity of SWCNH and NCNH were measured using the four probe technique. The measured values are respectively 6.5 S/cm and 9.2 S/cm.



**Scheme 1:** Schematic representation of the preparation of Fe- and N-doped carbon nanohorns.

#### 4A.1.6 Electrochemical Characterization

Electrochemical studies of the samples were carried out in a Biologic electrochemical work station with a three-electrode test cell from Pine Instruments. Oxygen and nitrogen saturated 0.1 M KOH was used in the electrochemical experiments as the electrolyte. Hg/HgO was used as the reference electrode and a glassy carbon rod was used as the counter electrode. A glassy carbon (GC) electrode (5 mm diameter) from Pine Instruments was used as the working electrode (WE) after drop coating the samples. To prepare the catalyst slurry for the electrochemical analysis, 5 mg of the catalyst was dispersed in 1 ml of N, N-dimethyl acetamide solution by sonication. 20  $\mu\text{L}$  of the catalyst slurry was drop-coated on the electrode. Followed by this, 2  $\mu\text{L}$  of 0.1 % Nafion® solution was applied on the catalyst layer. 100  $\mu\text{g}$  was the total catalyst loading on the electrode. Linear sweep voltammogram (LSV) was recorded in oxygen saturated 0.1 M KOH solution at a scan rate of 5  $\text{mV s}^{-1}$  at different electrode rotation rates from 400 to 2500 rpm.

The Koutecky-Levich (K-L) plot, a plot of inverse of the current versus inverse of electrode the rotation at different rotation speed at different potential, was used to calculate

the number of electrons. Slope and Y-intercept were used to calculate the kinetic current density and number of electron transfer respectively.

The number of electron transfer during ORR was calculated using the equation:

$$B = 0.6 nFv^{-1/2}C_{O_2}D_{O_2}^{2/3}$$

where, 'n' is the electron transfer number, 'F' is the Farady constant (96486 C mol<sup>-1</sup>), 'C<sub>O<sub>2</sub></sub>' is the concentration of oxygen in 0.1 M KOH (1.2 x 10<sup>-3</sup> mol l<sup>-1</sup>), 'D<sub>O<sub>2</sub></sub>' is the diffusion coefficient of oxygen in 0.1 M KOH solution (1.9 x 10<sup>-5</sup> cm s<sup>-1</sup>) and 'v' is the kinematic viscosity.

#### 4A.1.7 Anion exchange membrane fuel cell test

Fumapem FAA membrane (FumaTech, Germany) was used as the anion exchange membrane. The membrane was pretreated using the following procedure. The membrane was soaked in 1 M KOH for 24 h to replace bromide by OH<sup>-</sup>. Subsequently, the membrane was washed by using deionized water. The thickness of the membrane at wet condition was 65 μm. Conventional brush coating method was applied to make the cathode layer using a slurry of FeNCNH-900 and 10 wt. % Fumion in N-methyl pyrrolidone (NMP) with a Fumion to carbon ratio (F/C) of 0.8 in isopropyl alcohol (IPA). A catalyst loading of 4 mg cm<sup>-2</sup> was used on a gas diffusion layer (GDL, SGL CC, Germany). At the anode, 40 wt. % Pt/C (E-TEC) was used with 0.5 mg cm<sup>-2</sup> (F/C is 0.4) catalyst loading. For comparison, the cathode layer was also made with 40 wt. % Pt/C (E-TEC) with a Pt loading of 0.8 mg cm<sup>-2</sup> and an F/C ratio of 0.4. Membrane electrode assembly (MEA) was prepared by keeping the membrane in between the cathode and anode followed by applying 0.5 ton pressure for 30 sec at room temperature. Active electrode area of the MEA was 4 cm<sup>2</sup>. A standard test fixture from Fuel Cell Technologies, Inc, USA, was used for the single cell analysis. The testing was done by using a fuel cell test station (Fuel Cell Technologies, Inc, USA) by purging H<sub>2</sub> with a flow rate of 50 sccm at the anode and O<sub>2</sub> with a flow rate of 100 sccm at the cathode by maintaining a relative humidity of 100 % and a cell operating temperature of 50 °C.

## 4A.2 Results and Discussion

### 4A.2.1 TEM and SEM analysis

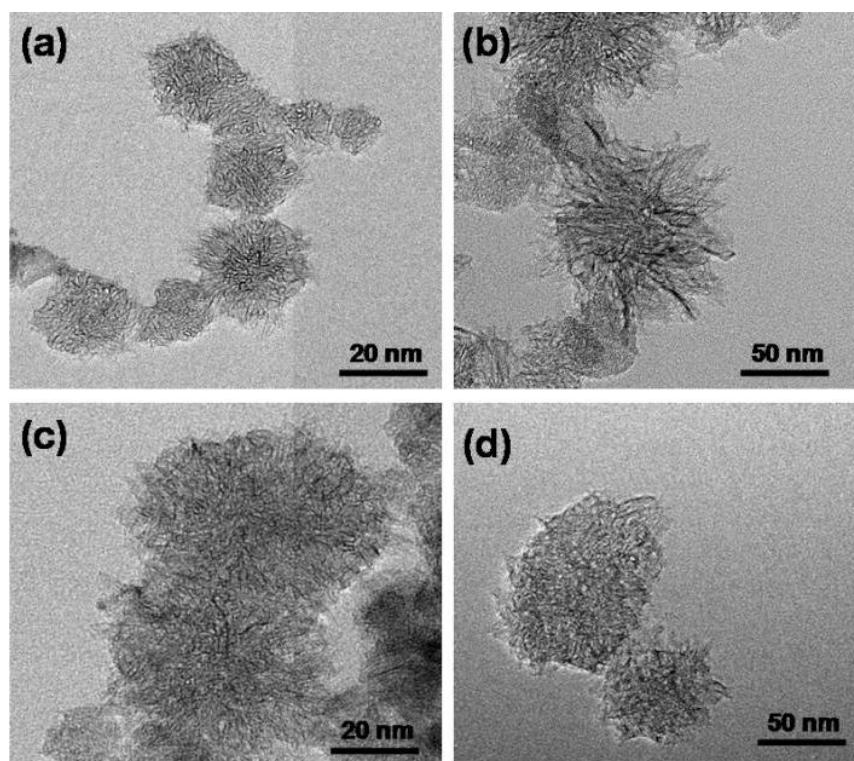


**Figure 4A.1:** HR-TEM images of (a) SWCNH, (b) NCNH and (c) & (d) FeNCNH-900 under different magnifications.

Figure 4A.1 shows high resolution transmission electron microscopic (HR-TEM) images of SWCNH, nitrogen doped nanohorn (NCNH) and the Fe coordinated nitrogen doped carbon nanohorn prepared at 900 °C (FeNCNH-900). It should be noted that the flower like morphology of NCNH and FeNCNH-900 is intact even after the high temperature annealing process compared to some recent reports on functionalized SWCNH.<sup>[6]</sup> Retention in morphology improves active mass transport, hence concomitantly results into improved ORR activity. More importantly, absence of iron particle in FeNCNH-900 indicates that the acid washing is effective and it removed unwanted iron oxides and carbides from the nanohorn. Field emission scanning electron microscopic (FE-SEM) investigation of FeNCNH-900 shows presence of nanohorn aggregates with non-uniform morphology (Figure 4A.2). Further, elemental mapping clearly shows the presence of carbon, nitrogen, oxygen and iron in FeNCNH-900.

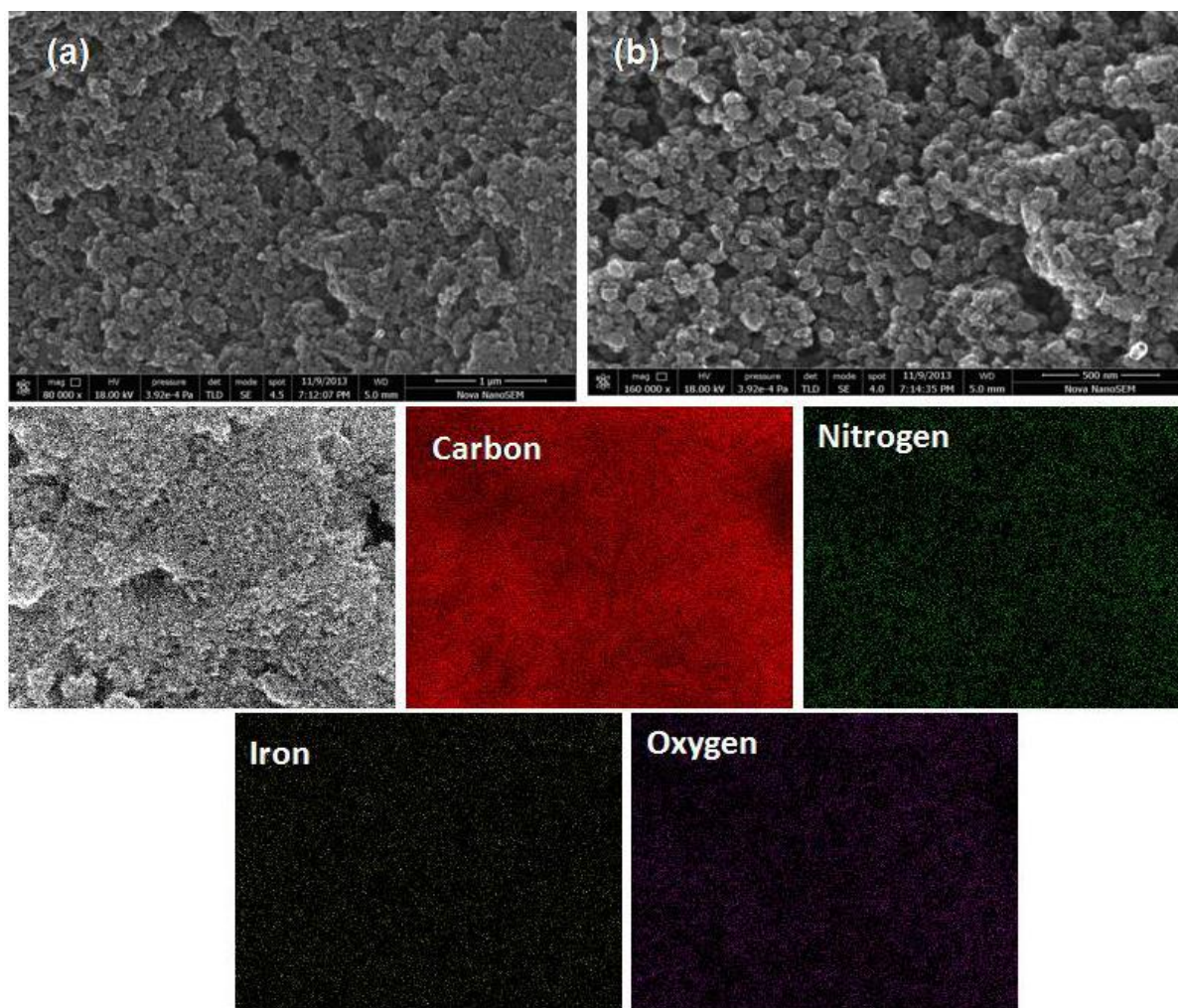


**Figure 4A.2:** FE-SEM images (a & b) and the corresponding elemental mapping of carbon, nitrogen, iron and oxygen in FeNCNH-900.

#### 4A.2.2 Raman and XRD analysis

Raman analysis further confirms the doping of nitrogen in the carbon matrix (Figure 4A.3a). The G band position of SWCNH ( $1579.8\text{ cm}^{-1}$ ) is up shifted to higher wave number ( $1583.9\text{ cm}^{-1}$ ) after nitrogen doping. The G band position of FeNCNH ( $1584.4\text{ cm}^{-1}$ ) is almost similar to that of NCNH. This indicates that the morphology of nanohorn remains intact after the nitrogen and Fe doping. Moreover, the nitrogen doping on SWCNH is further confirmed by the change in the 2D band position. SWCNH shows the 2D band at  $2602.7\text{ cm}^{-1}$  which is shifted to a higher wave number ( $2609.2\text{ cm}^{-1}$ ) for NCNH but the 2D band of FeNCNH-900 is shifted to much higher wave number ( $2620.7\text{ cm}^{-1}$ ) which clearly indicates the changes in the electron density around the carbon moiety responsible for oxygen adsorption and ORR. Further, the doping was confirmed from the

$I_D/I_G$  ratio, which is increasing in the order of SWCNH (1.64) < NCNH (1.83) < FeNCNH-900 (1.94). X-ray diffraction (XRD) analysis (Figure 4A.3b) also emphasises the absence of oxides and carbides of Fe in FeNCNH-900 with its similar XRD features of SWCNH and NCNH.

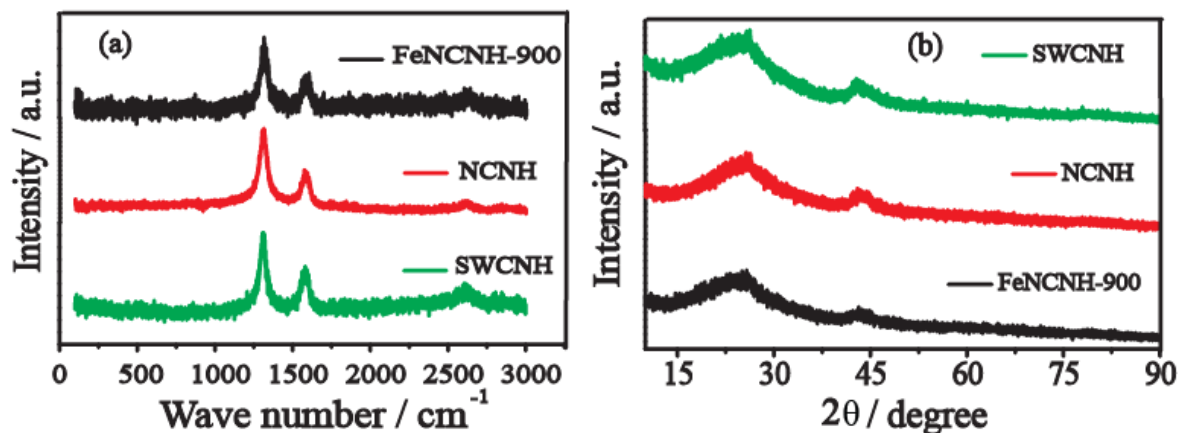


**Figure 4A.3:** (a) Raman spectra and (b) X-ray diffraction patterns of FeNCNH-900, NCNH and SWCNH.

#### 4A.2.3 Surface area analysis

Nitrogen adsorption isotherms were taken to understand the nature of the porosity of the materials, (Figure 4A.4 a & b). FeNCNH-900 and NCNH show Type-II isotherms. An increasing trend of N<sub>2</sub> adsorption can be observed for FeNCNH-900 and NCNH compared to SWCNH, which indicates a drastic enhancement in the surface area after the thermal annealing. A recent report reveals that mild functionalization of SWCNH improves the surface area of the material.<sup>[7]</sup> However, the high temperature annealing will normally assist the knotting of the pores on the surface of SWCNH. In the present case, nitrogen doping prevents the knotting and enhances the surface area without affecting its electrical conductivity.<sup>[7]</sup> The isotherms lead to the quantification of the surface area of the materials, which follows the order: SWCNH (340 m<sup>2</sup> g<sup>-1</sup>) < FeNCNH (1315 m<sup>2</sup> g<sup>-1</sup>) < NCNH (1327 m<sup>2</sup> g<sup>-1</sup>). The surface areas of FeNCNH-900 and NCNH are almost comparable but is 4 times higher than that of SWCNH. However, compared to the recent reports, the surface areas of NCNH and FeNCNH are found to be lower, which is assumed to be due to the deposition of carbon on the surface of nanohorn during the decomposition of melamine.<sup>[8]</sup> The pores of NCNH and FeNCNH-900 are having a size range between 0.5 to 20 nm with maximum density of pores lying in between 0.5 to 3 nm. This clearly



indicates that most of the pores on FeNCNH and NCNH are micropores. The amount of mesopores on FeNCNH-900 is less compared to that on NCNH. However, the pore size of SWCNH is varied from 10 to 70 nm. From the nitrogen sorption studies, it is clear that FeNCNH-900 has high density of micropores, which can essentially act as a contributing factor to improve the active reaction site density to promote ORR by creating proper Fe-N<sub>x</sub> active sites.

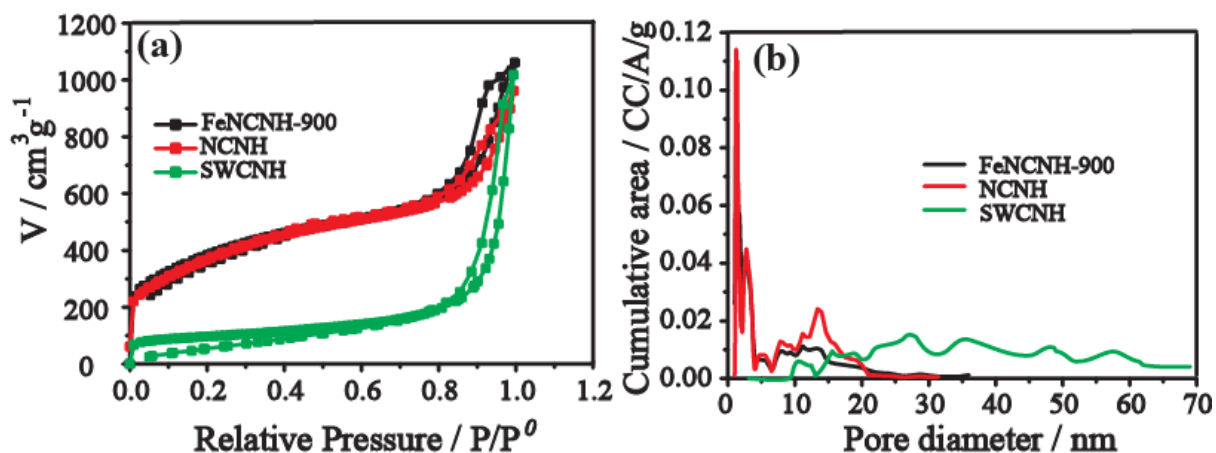


**Figure 4A.4:** (a) Nitrogen adsorption–desorption isotherms and (b) pore size distribution of FeNCNH-900, NCNH and SWCNH.

#### 4A.2.4 XPS analysis

To fully understand different nitrogen environments of the samples annealed at different temperatures and their effect in the overall ORR activity, X-ray photoelectron spectroscopy (XPS) was used. XPS spectra of NCNH, FeNCNH-800, FeNCNH-900, FeNCNH-1000 show the presence of carbon (Figure 4A.5), nitrogen and oxygen in the samples. Since the surface concentration of Fe in the samples is relatively low, a proper spectrum for Fe 2p is not observed. (Figure 4A.6). All the samples show nearly 96 % of carbon. Deconvoluted C1s spectra of carbon for the samples corresponding to different annealing temperatures are shown in Figure S8. NCNH, FeNCNH-800 and FeNCNH-900 show four different types of nitrogen environments which are pyridinic at  $\sim 398.15$  eV, pyrrolic at  $\sim 399.59$  eV, graphitic at  $\sim 400.97$  eV and oxides of nitrogen at  $\sim 405.48$  eV (Figure 4A.7).<sup>[9]</sup> NCNH possesses a total nitrogen loading of 2.24 wt. % and this value is less in the respective Fe based nanohorns. FeNCNH-900 shows high wt.% of pyridinic and pyrrolic nitrogen compared to rest of the samples.

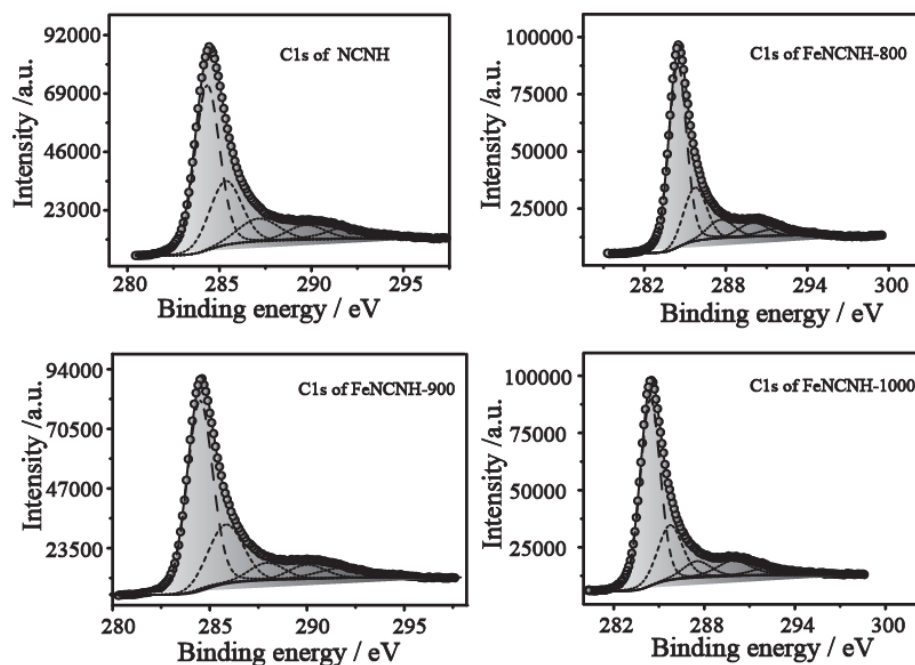


**Figure 4A.5:** Deconvoluted XPS profiles of C 1s in NCNH, FeNCNH-800, FeNCNH-900 and FeNCNH-1000.

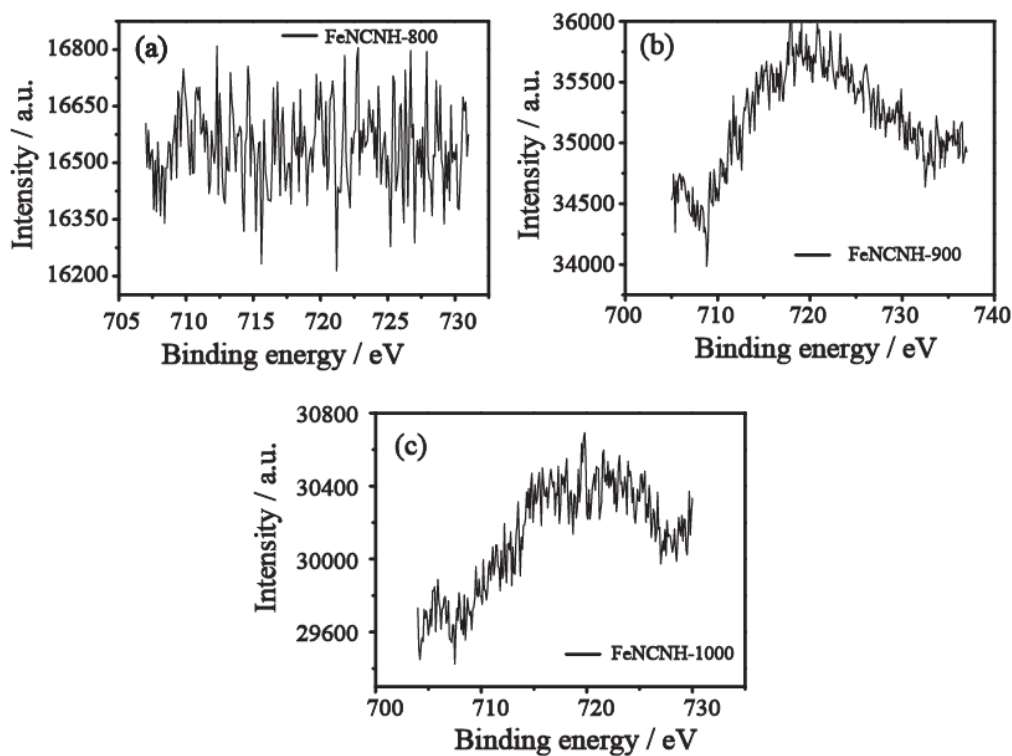


**Figure 4A.6:** XPS profiles of Fe in FeNCNH-800, FeNCNH-900 and FeNCNH-1000.

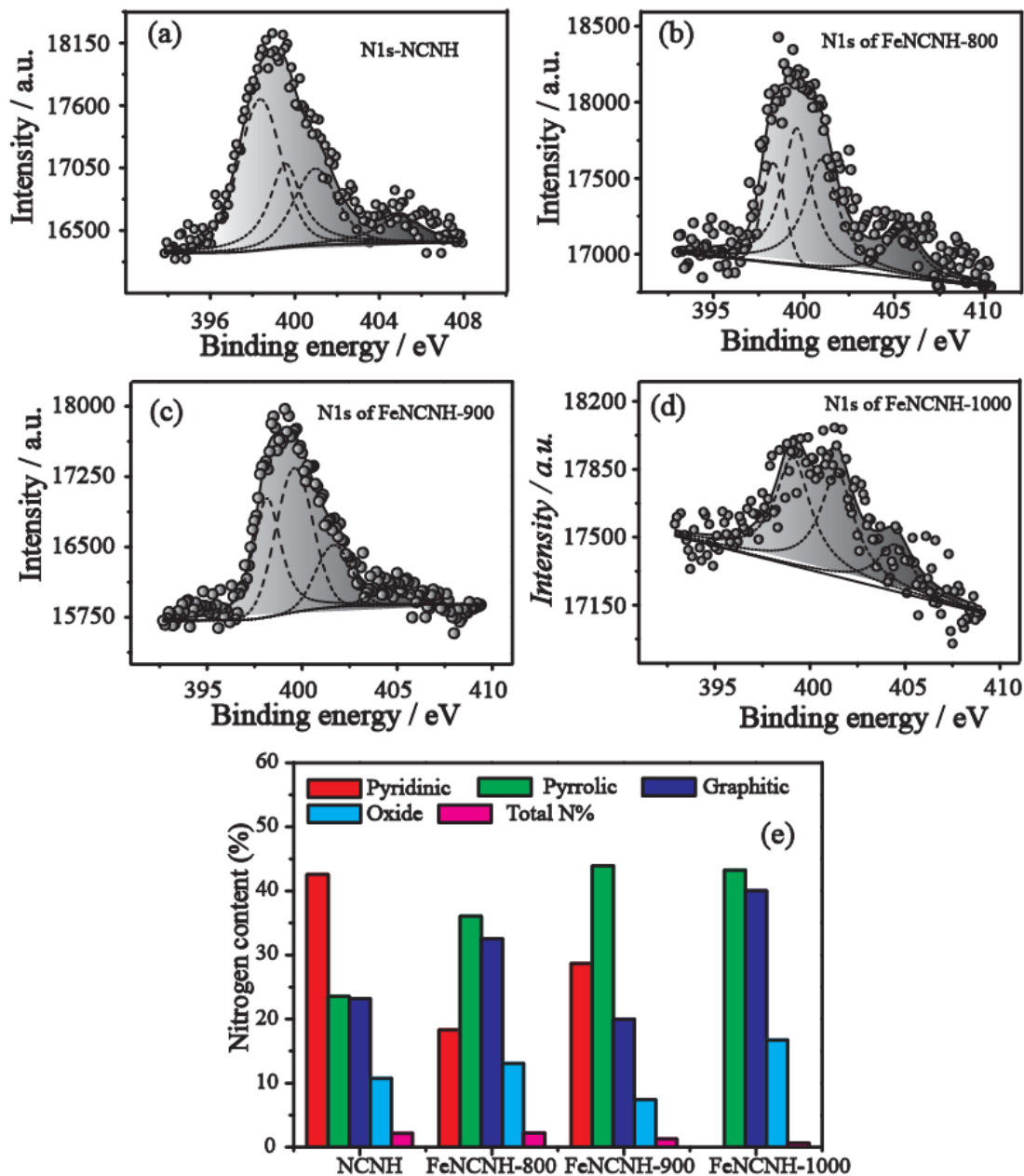


**Figure 4A.7:** Deconvoluted XPS spectra of N 1s of (a) NCNH, (b) FeNCNH-800, (c) FeNCNH-900 (d) FeNCNH-1000 and (e) percentage of the different types of nitrogen as well as the total nitrogen content of NCNH, FeNCNH-800, FeNCNH-900 and FeNCNH-1000.

The pyrrolic nitrogen content in the different samples is in the order of FeNCNH-900 (44.0 wt. %) > FeNCNH-800 (36.1 wt. %) > FeNCNH-1000 (43.2 wt. %) > NCNH (23.5 wt. %). In the case of FeNCNH-1000, the pyridinic nitrogen is absent because, at higher temperature, the pyridinic nitrogen gets converted into the pyrrolic and graphitic

nitrogens.<sup>12</sup> The total nitrogen content is decreasing with increasing the treatment temperature (Figure 4A.7e).

#### 4A.2.5 Electrochemical studies

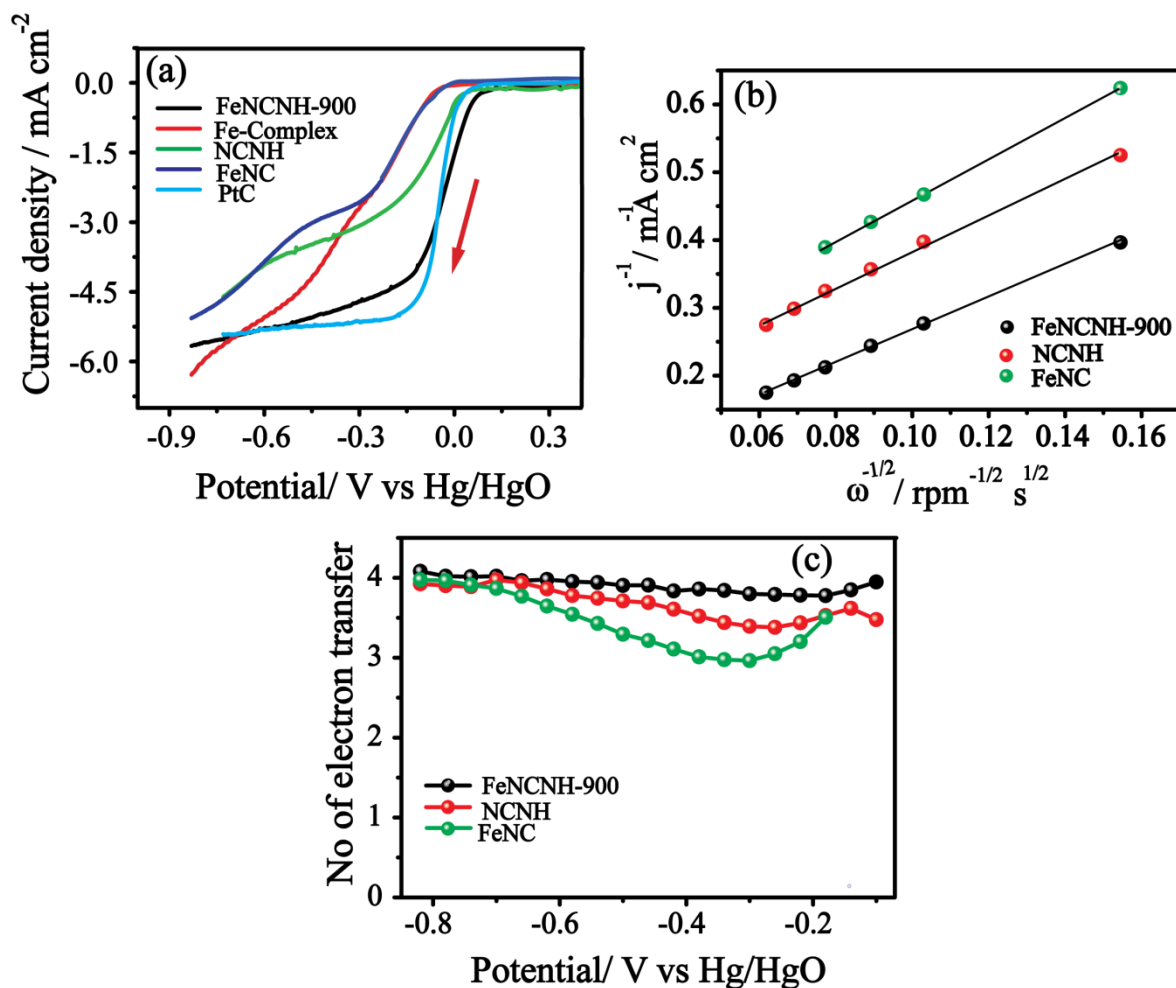


**Figure 4A.8:** (a) Linear sweep voltammograms (LSVs) of the carbon nanohorn samples and Pt/C in 0.1 M oxygen-saturated KOH at a rotational speed of 1600 rpm and scan rate of  $5\text{ mV s}^{-1}$ . (b) K–L plots of FeNCNH-900, NCNH and FeCN at a potential of  $-0.30\text{ V vs. Hg/HgO}$  and (c) the plots of the number of electrons transferred vs. the potential as calculated from the K-L plots for the different samples.

Electrocatalytic activity of FeNCNH-900 was studied using a Rotating Disc Electrode (RDE) system in 0.1 M KOH solution with an electrode rotation rate of 1600 rpm at  $5\text{ mV s}^{-1}$  scan rate. From Figure 4A.8a, it is clear that, at a current density of  $-0.2\text{ mA cm}^{-2}$ , FeNCNH-900 has much higher positive potential of 0.09 V, which is 40 mV more positive compared to the commercial Pt/C catalyst ( $60\text{ }\mu\text{g cm}^{-1}\text{ Pt}$ ) at the same current

density. Similarly, the half wave potential ( $E_{1/2}$ ) of FeNCNH-900 (-0.026V) is 20 mV higher than that of Pt/C (-0.046V). The improved positive onset potential as well as  $E_{1/2}$  of FeNCNH-900 clearly indicates that the intrinsic ORR activity as well as the active reaction centre density of the system is higher compared to the commercial Pt/C system.<sup>[2b]</sup>

To further understand the active reaction centre in FeNCNH-900, we synthesised NCNH with the similar procedure as adopted for preparing the FeNCNH counterparts without adding  $\text{FeCl}_3$ . From Figure 3a, it is clear that, at  $j = -0.2 \text{ mA cm}^{-2}$ , NCNH displays a potential of 0.05 V, which is comparable to that obtained with Pt/C, but 40 mV lower than that of FeNCNH-900. On the other hand, the oxygen reduction current density is lower than that of both Pt/C and FeNCNH-900. Comparative ORR performance of both NCNH and FeNCNH-900 clearly indicates that Fe- $\text{N}_x$  is an essential ingredient to enhance ORR. Similarly, the favourable effect of nanohorn morphology in bringing in the desired performance characteristics is proved by comparing the ORR activity of FeNCNH-900 and FeNC (prepared by annealing the mixture of Vulcan carbon, melamine and  $\text{FeCl}_3$  at 900 °C in Ar atmosphere). FeNC shows a potential (at  $j = -0.2 \text{ mA cm}^{-2}$ ) more negative (-0.04 V) as well as the reduction current lower compared to both NCNH and FeNCNH-900. The activity of the reaction centre is expected to be due to the existence of a preferred coordination of Fe with the doped nitrogen on the edges of the micropores of nanohorns. Number of electrons calculated from the Koutkey–Levich plot (K-L plot) shows (Figure 4A.8 b & c) that both FeNCNH-900 as well as NCNH follow direct 4-electron pathway for dioxygen reduction in the entire potential range. Contrary to this, the electron transfer number in the case of FeNC displays a lower value initially, which increases gradually as the potential sweeps to higher negative values and approaches to the 4-electron pathway as reported by Dai et al.<sup>[2f]</sup> This explicitly indicates that FeNC is following a mixed kinetics in the lower negative potentials and it is approaching towards a direct 4-electron reduction pathway in the higher negative potentials. From this analysis, it is apparent that Fe- $\text{N}_x$  along with the micropores present in the nanohorn morphology attributes a controlled interplay and creates more active centres through efficient coordination of iron with the nitrogen present at the edges of the pores.

In order to understand the effect of Fe content in NCNH towards ORR, different mass loadings of  $\text{FeCl}_3$  with the total Fe percentage in the salt to SWCNH, *ca.* 1, 2 and 5 %, were also maintained for annealing by keeping the temperature at 900 °C. Figure 4A.9 shows that the system with 2 % Fe is outperforming the samples corresponding to the 1

and 5 % Fe samples. Both the potential (at  $j = -0.2 \text{ mA cm}^{-2}$ ) as well as  $E_{1/2}$  for ORR is varying with the iron percentage. 1 and 5 % of Fe result into a potential of 0.067 V and 0.069 V at  $-0.2 \text{ mA cm}^{-2}$ , for both the samples whereas the corresponding values of  $E_{1/2}$  are -0.045 and -0.042 V. The ORR current density measured at -0.3 V for the samples corresponding to the different content of Fe follows the order of 2 % > 1 % > 5 %. This clearly indicates that an optimum

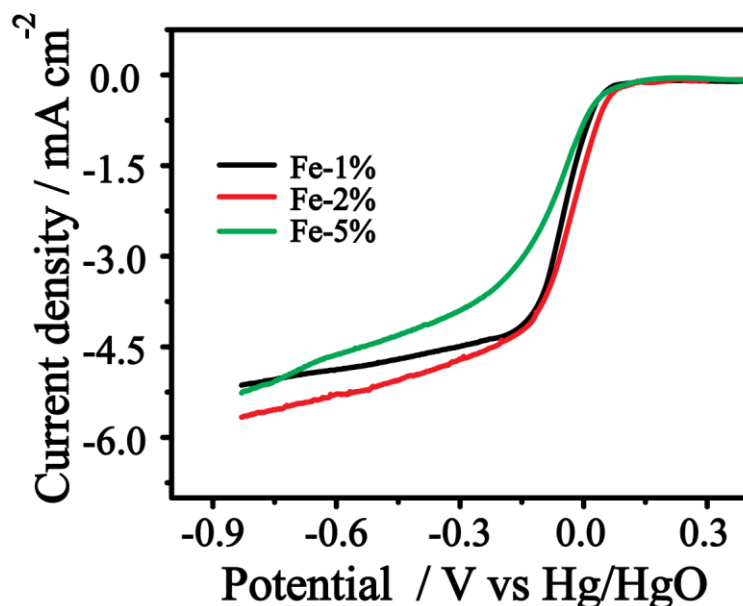


**Figure 4A.9:** LSVs of the FeNCNH samples at different Fe content.

Fe content is necessary to boost the intrinsic ORR activities as well as the active reaction centre density. 2 % of Fe shows improved number of active reaction sites as well as ORR activity compared to the other two cases. Moreover, all the Fe based catalysts with different Fe content show ORR activities higher than NCNH. This finding thus substantiates the important role played by Fe as a partner with nitrogen to catalyse the dioxygen reduction.

To further evaluate the effect of annealing temperature on modulating the activity of the catalytic sites, along with FeNCNH-900, we prepared two other catalysts by annealing the sample corresponding to the 2% Fe at 800 and 1000 °C. These samples are designated as FeNCNH-800 and FeNCNH-1000, respectively. It is well known that the annealing temperature is expected to tune the coordination of nitrogen, which will be eventually reflected in ORR. From Figure 4A.10a, it can be seen that the onset potential of FeNCNH-900 is clearly more positive compared to both FeNCNH-800 and FeNCNH-

1000. The potential of FeNCNH-800 at  $-0.2 \text{ mA cm}^{-2}$  is  $0.08 \text{ V}$  which is  $10 \text{ mV}$  lower than that of FeNCNH-900 and  $22 \text{ mV}$  higher than that of FeNCNH-1000.

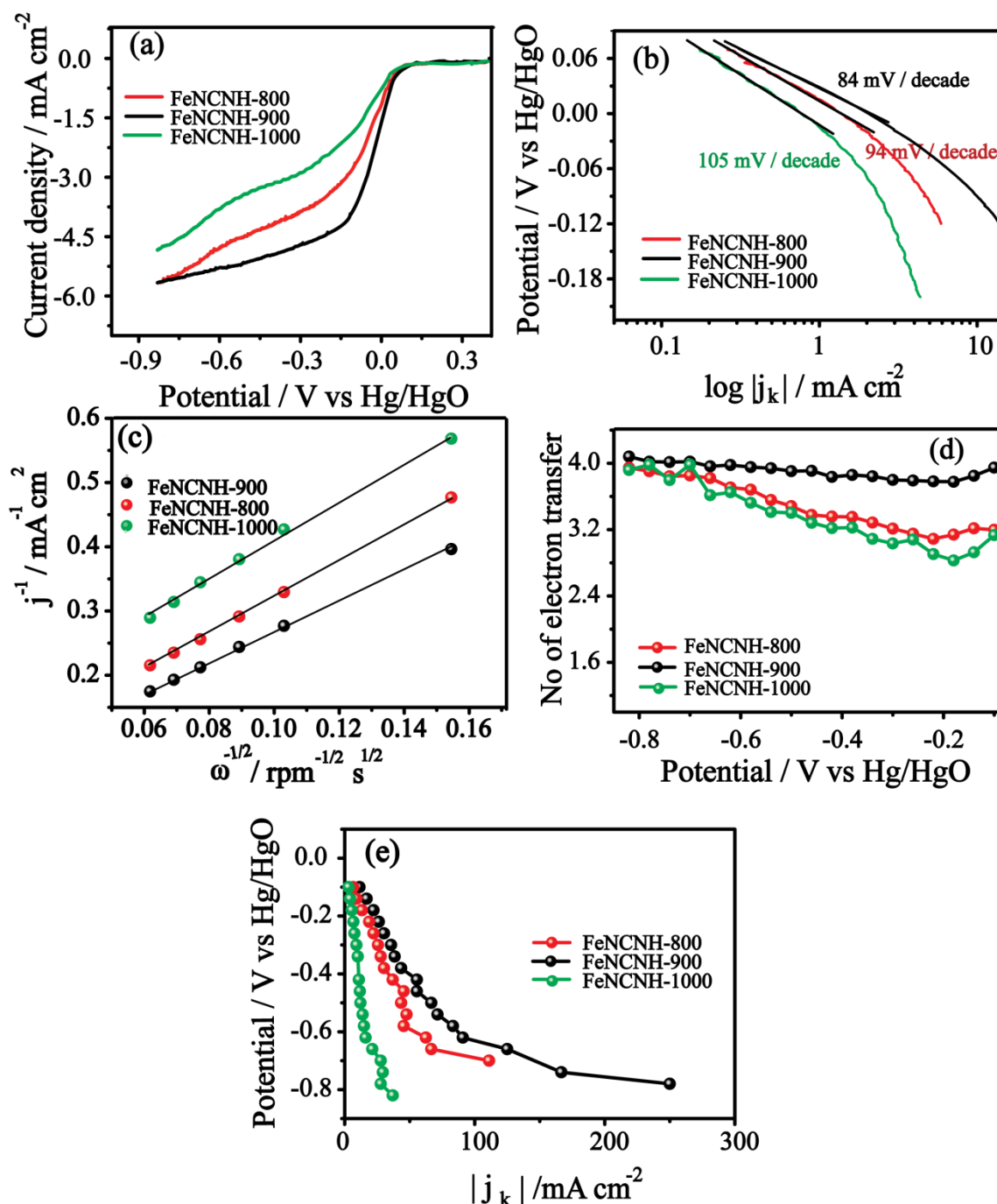


**Figure 4A.10:** (a) LSVs of FeNCNH-800, FeNCNH-900 and FeNCNH-1000; (b) Tafel slopes of the catalysts; (c) K–L plots of FeNCNH-800, FeNCNH-900 and FeNCNH-1000 at a potential of  $-0.30 \text{ V}$  vs Hg/ HgO; (d) the calculated values of the electron transfer numbers of the catalysts from the K–L plots as a function of the applied potential and (e)  $j_k$

vs.  $E$  plot where  $j_k$  was calculated from the intercept of the K-L plots of FeNCNH-800, FeNCNH-900 and FeNCNH-1000.

Similarly,  $E_{1/2}$  of these samples is in the order of FeNCNH-900 (-0.026V) > FeNCNH-800 (-0.028 V) > FeNCNH-1000 (-0.030V). Likewise, the ORR current density at -0.30 V also follows the order of FeNCNH-900 > FeNCNH-800 > FeNCNH-1000. Decrease in the dioxygen reduction current density is mainly attributed to the lowering of the density of the active reaction centre. The measured value of the Tafel slope of FeNCNH-900 is 81 mV decade<sup>-1</sup> which is significantly lower than of the values calculated for FeNCNH-800 (94 mV decade<sup>-1</sup>) and FeNCNH-1000 (104 mV decade<sup>-1</sup>) (Figure 4A.10b). Higher values of Tafel slope of the later two samples indicate that the ORR mechanism in these two cases is different compared to that for FeNCNH-900 and Pt/C. The number of electron transfer derived from the slopes of the K-L plots (Figure 4A.10c & d) shows that FeNCNH-900 follows a 4-electron pathway in the entire potential range. This clearly indicates that oxygen molecules are directly getting converted into hydroxide on FeNCNH-900. On the other hand, both FeNCNH-800 and FeNCNH-1000 show the electron transfer number lower than 3.2 at higher positive potentials and close to 4 at higher negative potentials. Kinetic current density values calculated from the Y-intercepts of the K-L plots (Figure 4A.10e) are also found to be higher for FeNCNH-900 in the entire potential range compared to FeNCNH-800 and FeNCNH-1000.

The nitrogen coordination in the sample is seriously affecting the overall performance of the catalyst towards dioxygen reduction.<sup>[10]</sup> It is well known that, instead of the total wt.% of nitrogen, the specific coordination of the nitrogen is important to promote ORR.<sup>[10]</sup> NCNH has high wt.% of nitrogen with high pyridinic contribution. Rouff *et. al.* clearly mentioned that the pyridinic nitrogen shifts the ORR onset potential towards more positive but it does not promote the overall reduction current density.<sup>[11]</sup> In accordance with this, NCNH shows an onset potential comparable to Pt/C, but its oxygen reduction current density is very poor compared to Pt/C. On the other hand, in the case of the FeNCNH samples, the pyridinic nitrogen content is in the order of FeNCH-900 (28.7 wt.%) > FeNCNH-800 (18.3 wt.%) > FeNCNH-1000 (0.0 wt.%) with an explicit influence on the onset potential. FeNCNH-800 shows an onset potential close to that of FeNCNH-900, which is higher than that of FeNCNH-1000. On the basis of the onset potential shift, one can clearly note that, not only the pyridinic nitrogen but the Fe coordination is also imparting a crucial role in ORR. Since FeNCNH-900 has higher weight percentage of



pyrrolic as well as pyridinic nitrogen, it shows higher performance compared to the rest of the electrocatalysts as expected. Even though FeNCNH-1000 has almost comparable pyrrolic nitrogen content, the total nitrogen percentage is too less to improve the active reaction site density. This clearly retards the ORR performance. It is reported that, pure oxidised form of iron shows poor oxygen reduction activity.<sup>[12]</sup> Hence, the much enhanced ORR activity of FeNCNH-900 could be due to contributions from other factors such as the synergistic effects of both iron and nitrogen in the catalyst.<sup>17,33</sup> It has been reported recently that in ORR catalysts possessing Fe and N moieties, the coordinated Fe, N and C active reaction centre plays a crucial role in shifting the onset potential as well as  $E_{1/2}$  towards more positive direction.<sup>31</sup> From the XPS analysis, it is evident that FeNCNH-900 possesses high wt.% of pyrrolic nitrogen, which is responsible for establishing the coordination with the iron moiety.<sup>27,31</sup> Thus generated new active reaction centres in FeNCNH-900 improve the intrinsic catalytic activity towards ORR compared to NCNH. Due to the relatively higher pyrrolic coordination in FeNCNH-900, it is expected that the main active reaction centre is the in-plane Fe-N<sub>4</sub> coordinated site.<sup>52</sup> Since FeNCNH-900 has higher density of micropores as evident from the porosity data, the graphene matrix of the nanohorn acts as a fertile region for accommodating more number of the in-plane Fe-N<sub>4</sub> active reaction centres, leading to facile reduction of oxygen through the 4-electron pathway. However, even though the pyrrolic nitrogen percentage is higher for FeNCNH-1000, due to the fewer amounts of the overall nitrogen atoms in the system, the active

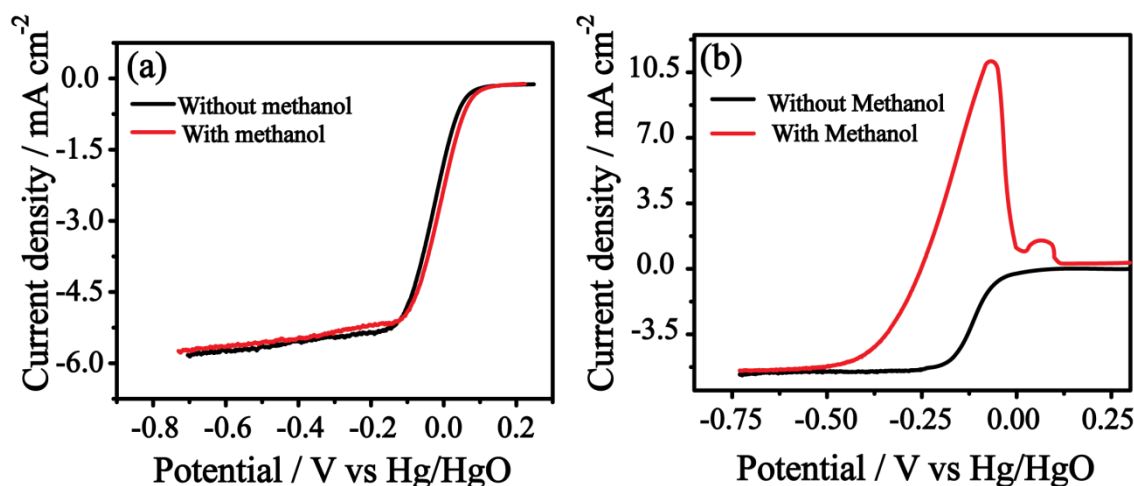


**Figure 4A.11:** Methanol crossover study of FeNCNH-900 (a) and Pt/C (b) with an electrode rotation rate of 1600 rpm at and a scan rate of 5 mV s<sup>-1</sup>. 3 M methanol was added into 0.1 M KOH electrolyte to evaluate the crossover effect.

reaction centre density is less compared to that in FeNCNH-900. Thus, along with high surface area ( $1315 \text{ m}^2/\text{g}$ ) and higher density of micropores (pore diameter less than 3 nm) of FeNCNH-900, maximum density of Fe-N<sub>4</sub> active sites present in the system enables it to position itself as a potential ORR catalyst to replace Pt/C from fuel cell cathode.

FeNCNH-900 shows excellent tolerance towards methanol (Figure 4A.11a & b) compared to Pt/C. To study the stability of the materials, we performed accelerated durability test (ADT) for 5000 cycles. Cyclic voltammetry was performed in between a potential window of -0.40 to 0.20 V at  $100 \text{ mV s}^{-1}$  scan rate under oxygen purging. LSV was taken before and after ADT at 1600 rpm with a scan rate of  $5 \text{ mV s}^{-1}$ . It is clear from Figure

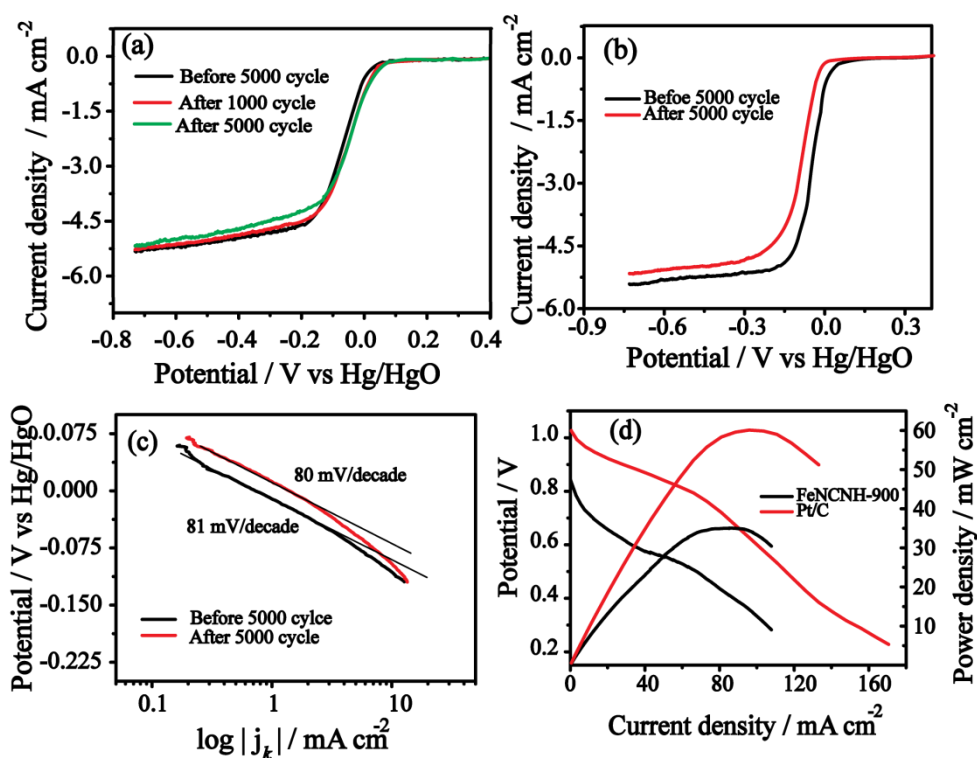


**Figure 4A.12:** (a) LSVs of FeNCNH-900 before and after ADT, at 1600 rpm and a scan rate of  $5 \text{ mV s}^{-1}$ , (b) LSVs of Pt/C before and after ADT in oxygen saturated 0.1 M KOH at an electrode rotation speed of 1600 rpm and a scan rate of  $5 \text{ mV s}^{-1}$  respectively. Hg/HgO and glassy carbon were used as the reference and counter electrode respectively, (c) Tafel plots of FeNCNH-900 at low current density before and after ADT and (d) single cell performance at 50 °C of an AEMFC with FeNCNH-900 and Pt/C as the cathode catalyst in the membrane electrode assembly (MEA).

4A.12a that after 1000 stability cycling, the ORR activity of FeNCNH-900 is increased. Both onset potential as well as  $E_{1/2}$  are shifted towards more positive potential initially and remained as such even after 5000 cycles. This explicitly indicates that the electrocatalytic activity of FeNCNH-900 is increasing with respect to the number of the potential cycles, at least in the initial 1000 cycles. This type of behaviour was recently reported by Zelanay *et. al.* in their work based on the carbon nanotube-carbon particle composite.<sup>[2b]</sup> Contrary to FeNCNH-900, Pt/C shows negative shift in the onset potential as well as  $E_{1/2}$  after the 5000 cycles (Figure 4A.12b). Further, a reduction in the value of the Tafel slope after the 5000 cycles in the case of FeNCNH-900 substantiates the potential cycle depended improvement in the ORR activity of the system (Figure 4A.12c). These studies, thus, clearly show that FeNCNH-900 is an excellent electrocatalyst with enhanced fuel tolerance and electrochemical stability along with higher ORR activity as compared to Pt/C.

Figure 4A.12d shows single cell anion exchange membrane fuel cell (AEMFC) polarization plot recorded at 50 °C using FeNCNH-900 as the cathode catalyst in the membrane electrode assembly (MEA). Fumapem FAA anion exchange membrane was used as electrolyte and commercial 40 wt.% Pt/C catalyst was employed as the anode. The measurements were carried out by passing humidified hydrogen and oxygen in the anode and cathode of the cell respectively. The MEA displays an open circuit voltage (OCV) of 0.83 V. Compared to FeNCNH-900, when a similar experiment was carried out by using an MEA having commercial 40 wt.% Pt/C as the cathode, a higher OCV of 1.0 V is obtained. Except this, the features of the polarization plots of both the MEAs remain more or less same. FeNCNH-900 based MEA delivered a current density of 30 mA cm<sup>-2</sup> at 0.60 V with a maximum a power density of 35 mW cm<sup>-2</sup>. Pt based MEA outperformed FeNCNH-900 in terms of the power density and current density, but the performance of FeNCNH-900 is higher than the recently reported value of NCNT.<sup>[13]</sup> However, the electrode preparation involves very sensitive parameters such as the optimum ionomer to catalyst ratio. In the present case, we have followed same protocols for making both the Pt/C and FeNCNH based electrodes, which actually need to be optimized looking at the significant differences in the morphology of the carbons and nature of the active sites between the samples. Such optimization studies, which are being progressed in our group, are expected to further improve the performance characteristics of the MEA derived from our Pt-free system.

## Part B: Carbon Nanohorn-derived Graphene Nanotube System as a Platinum-free Fuel Cell Cathode

This section of the chapter explains a facile synthesis of a nitrogen doped graphene nanotube (FeGNT) possessing high surface area and higher density of active sites by annealing a mixture of single walled carbon nanohorn (SWCNH), melamine and iron salt in an inert atmosphere. Unlike the work discussed in *Part A*, the present section discloses the influence of nitrogen and iron precursor loading in transforming the morphology of SWCNH to graphene nanotube. Even though reports are available on the structural modification of nanohorns at high temperature in presence of iron moieties,<sup>[14]</sup> an approach towards the formation of graphene nanotube like morphology has not been explored so far. Compared to the CVD grown graphene nanotubes, the present synthesis approach is simple and cost effective. Since the catalytic activity as well as the stability of an electrocatalyst strongly depends on the *in situ* formed structure and carbon morphology at high temperatures, FeGNT prepared from SWCNH paves the way for a new synthesis strategy for an efficient electrocatalyst for a variety of electrochemical reactions.

### 4B.1 Experimental section

#### 4B.1.1 Materials

Melamine powder, iron acetate, potassium hydroxide, sulphuric acid and perchloric acid were purchased from Sigma Aldrich Chemicals and used without any further purification. Single walled carbon nanohorn was purchased from Global nanotech, India. H<sub>2</sub>O<sub>2</sub> (30 % w/v), Ethanol (99 % ) and PTFE filter paper with pore size 0.45 µm were purchased from Thomas Baker Chemicals, India. Nafion 5% in water was purchased from Dupont Inc, USA. Deionised water (18 mΩ) from the milli-Q set-up was used for performing all the electrochemical measurements.

#### 4B.1.2 Functionalization of SWCNH (FCNH)

Carbon nanohorn (CNH) is less porous in its natural form.<sup>[15]</sup> Hence, functionalization of carbon nanohorn is pretty much unavoidable.<sup>[15-16]</sup> Mild functionalizations is preferred so that the conductivity and structure of the nanohorn are not hampered. Functionalization takes place only in defect concentrated regions like tip of

the horns where the  $sp^3$  bonds are prominent.<sup>[4a]</sup> Functionalization makes CNH highly porous.<sup>[15]</sup>

Functionalization of nanohorn was performed as reported earlier.<sup>[15]</sup> 2 g of CNH was dispersed in 200 ml  $H_2O_2$  and the mixture was kept for reflux at 60 °C for 6 h. Temperature of the reaction mixture was controlled as the reaction was carried out in a silicon-oil bath. The resultant mixture was subjected to thorough washing with distilled water and then the mixture was filtered out. The filtrate was dried at 60 °C.

#### **4B.1.3 Preparation of graphene nanotube from single wall carbon nanohorn (FeGNT)**

200 mg of FCNH was added to 25 mL of water and the mixture was kept for bath sonication for 30 min. to get a uniform dispersion. To the resulting solution, 0.58 g of iron acetate was added and the mixture was kept under stirring for overnight. To this mixture, 2 g of melamine was added and the mixture was kept for drying overnight with stirring at 60 °C. The resulting black colored powder was loaded in an alumina boat, which was mounted in a quartz tube and was kept in a tubular furnace at 900 °C for 1 h in Ar atmosphere, which led to a dark black colored catalyst sample. This powder was dispersed in 0.5 M  $H_2SO_4$  for 12 h at 80 °C followed by filtration and drying. It was collected and subjected to annealing under the Ar atmosphere at 900 °C for 1 h.

#### **4B.1.4 Preparation of nanotube from melamine powder (FeNCNT)**

2 g of melamine and 0.58 g of iron acetate were mixed together in 25 mL water and the resulting solution was kept for stirring overnight at 60 °C. The resulting orange red colored powder was placed in a tubular furnace at 900 °C and was kept under argon atmosphere for 1 h, which was later allowed to cool back to room temperature under Ar flow. The resulting dark black colored catalyst sample was dispersed in 0.5 M  $H_2SO_4$  for 12 h at 80 °C. The sample was filtered, dried and kept again for annealing under Ar atmosphere at 900 °C for 1 h.

#### **4B.1.5 Preparation of nano oyster type morphology from CNH and iron (FeCNO)**

200 mg of CNH was uniformly dispersed in 25 mL water and 0.58 g of iron acetate was added into this solution. The resulting solution was kept under stirring for overnight at 60 °C for drying. The resulting powder was subjected to annealing under Ar atmosphere at

900 °C for 1 h. The sample was filtered, dried and kept again for annealing under Ar atmosphere at 900 °C for 1 h.

#### **4B.1.6 Preparation of nitrogen doped nanohorn (NCNH)**

200 mg of FCNH was added to 25 mL water and was kept for bath sonication for 30 min. to get a uniform dispersion. To the resulting solution, 2 g of melamine was added and the mixture was kept for overnight stirring at 60 °C for drying. The dried precursor mixture was kept for annealing under Ar atmosphere for 1 h at 900 °C. After cooling, the resulted catalyst was dispersed in 0.5 M H<sub>2</sub>SO<sub>4</sub> for 12 h at 80 °C followed by filtration and drying. The sample was filtered, dried and kept again for annealing under Ar atmosphere at 900 °C for 1 h.

#### **4B.1.7 Material characterization**

FEI Technai G2 T30 operated at 300 kV and Quanta 200 3D FEI were used respectively for high resolution transmission electron microscopic (HR-TEM) and scanning electron microscopic (SEM) analysis. LabRam spectrometer (HJY, France) was used for Raman analysis with a laser wavelength of 632 nm. VGMicrotech Multilab ESCA 3000 spectrometer was used for X-ray photoelectron spectroscopic analysis by employing a monochromatic Mg K<sub>α</sub> X-ray source ( $h\nu = 1253.6$  eV). Brunauer-Emmet-Teller (BET) nitrogen adsorption-desorption experiment was performed on Quantachrome Quadrasorb automatic volumetric measurement system at 77 K using ultra pure nitrogen gas.

#### **4B.1.8 Electrochemical measurements**

Biologic electrochemical workstation (VMP3) was used for all the electrochemical measurements by using a three-electrode set-up. 0.1 M HClO<sub>4</sub>, 0.5 M H<sub>2</sub>SO<sub>4</sub> and 0.1 M KOH were used as the electrolytes for the electrochemical measurements. Catalyst coated glassy carbon disc (0.196 cm<sup>2</sup> area, Pine Instruments. Inc.) was used as the working electrode. Different reference electrodes were used for the electrochemical measurements which are Ag/AgCl in 0.1 M HClO<sub>4</sub>, Hg/HgSO<sub>4</sub> in 0.5 M H<sub>2</sub>SO<sub>4</sub> and Hg/HgO in 0.1 M KOH. For the purpose of comparison, all the potentials are converted to the reference hydrogen electrode scale and used in the manuscript. A graphite rod was used as the counter electrode in all the three electrolytes. For the preparation of the catalyst ink, 10 mg of the catalyst was ultrasonically dispersed in a mixture of 1 ml of water-isopropyl alcohol (3:1) and 40 μl of 5 wt. % Nafion solution for 1 h. 20 μl of the catalyst slurry was drop

coated on the glassy carbon electrode to get a total catalyst loading of  $1 \text{ mg cm}^{-2}$ . The glassy carbon electrode was polished using  $0.05 \text{ }\mu\text{m}$  polishing alumina powder prior to drop coating of the catalyst ink. The catalyst ink was dried under an IR lamp for electrochemical analysis. Commercial Pt/C (40 wt. % from Johnson Matthey (Alpha Acessar)) was also studied for the comparison purpose. Catalyst ink for Pt/C was prepared by dispersing 10 mg of Pt/C in 1 ml of water and  $40 \text{ }\mu\text{l}$  of Nafion (5 wt. % in water) using an ultrasonic bath for 1 h.  $5 \text{ }\mu\text{l}$  of the resulting ink was drop coated on the glassy carbon electrode in order to get a total Pt loading of  $100 \text{ }\mu\text{g}_{\text{Pt}} \text{ cm}^{-2}$ . Linear sweep voltammograms (LSVs) were recorded using a rotating disk electrode (RDE,  $0.196 \text{ cm}^2$ , Pine Instruments) at different electrode rotation speeds (400, 900, 1200, 1600 and 2500 rpm) in an oxygen saturated electrolyte with a scan rate of  $5 \text{ mV s}^{-1}$  at room temperature. For the durability analysis, accelerated durability test (ADT) was performed for 5000 cycles for FeGNT in all the three electrolytes. CV was performed at  $100 \text{ mV s}^{-1}$  scan rate in between a potential window of 0.60 to 1.0 V under oxygen purging. LSV was taken before and after ADT at 1600 rpm with a scan rate of  $5 \text{ mV s}^{-1}$ .

Hydrogen peroxide percentage and number of electron transfer during the oxygen reduction reaction were measured using a rotating ring disc electrode (RRDE,  $0.245 \text{ cm}^2$ , Pine Instruments) voltammogram using the following equations:

$$n = 4 \times \frac{I_d}{I_d + \frac{I_r}{N}} \dots\dots\dots (1)$$

$$H_2O_2(\%) = 200 \times \frac{\frac{I_r}{N}}{I_d + \frac{I_r}{N}} \dots\dots\dots (2)$$

where,  $I_d$  is the disc current,  $I_r$  is the ring current, and  $N$  is the collection efficiency of the Pt ring (0.37).

#### 4B.1.9 Single cell analysis

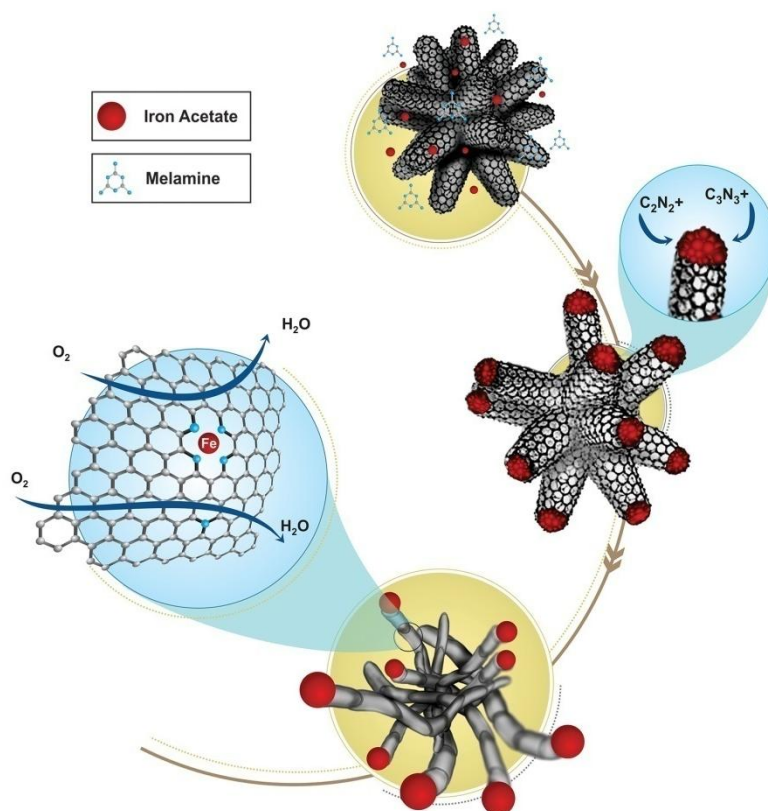
Nafion 212 membrane (DuPont, USA) was used as the proton exchange membrane. Initially, the Nafion membrane was boiled in con.  $\text{HNO}_3$  for 1 h. This was followed by boiling the membrane in DI water, 1 M  $\text{H}_2\text{SO}_4$ , and DI water for another 1 h each. This pretreated membrane was used for the membrane electrode assembly (MEA) fabrication.

Electrodes were prepared by conventional brush coating method. For the cathode layer, a slurry of FeGNT and 20 wt. % Nafion (dispersion in water, DuPont, USA) with a

Nafion to carbon ratio (N/C) of 0.50 in isopropyl alcohol (IPA) was used.  $2 \text{ mg cm}^{-2}$  of the catalyst loading was used on a gas diffusion layer (GDL, SGL CC, Germany). The anode electrode comprises of 40 wt. % Pt/C with a catalyst loading of  $0.50 \text{ mg cm}^{-2}$  (N/C is 0.5). For comparison, the Pt/C cathode layer was also made with a Pt loading of  $0.50 \text{ mg cm}^{-2}$  and an N/C ratio of 0.50.

MEA was prepared by keeping the Nafion membrane in between the cathode and anode followed by applying 0.25 ton pressure for 1 min. at  $130 \text{ }^\circ\text{C}$ .  $4 \text{ cm}^2$  is the active electrode area of the MEA. A standard test fixture (Fuel Cell Technologies Inc, USA) was used for the MEA performance analysis. The testing was done by using a fuel cell test station (Fuel Cell Technologies Inc, USA) by purging  $\text{H}_2$  and  $\text{O}_2$  with a flow rate of 50 sccm and 100 sccm respectively at the anode and cathode by maintaining a relative humidity of 100 % and a cell operating temperature of  $65 \text{ }^\circ\text{C}$ .

#### 4B.2 Results and discussion



**Scheme 4B.1:** Schematic representation of the formation of Fe-N<sub>x</sub> doped graphene nanotube from single wall carbon nanohorn during its reaction with iron acetate and melamine.



Peroxide treated SWCNH with ‘nanowindows’ is beneficial for the effective distribution of ferric ions and nitrogen sources for the synthesis of FeGNT with high density of active sites. In a typical synthesis, iron acetate was added to the dispersion of the peroxide treated SWCNH and the mixture was kept for overnight stirring. After the addition of melamine, the resulting mixture was dried and subjected to annealing at 900 °C in an inert atmosphere. The resulting black powder was washed with sulphuric acid and annealed again at 900 °C (Scheme 4B.1). Similar procedure was followed to prepare two control samples, *viz.* (i) iron encapsulated nanotube (FeNCNT) which was prepared by annealing of a mixture of melamine and iron salt without any SWCNH, and (ii) nitrogen doped nanohorn (NCNH), which was prepared by annealing of a mixture of SWCNH and melamine without any iron salt.

#### 4B.2.1 XRD and Raman analysis

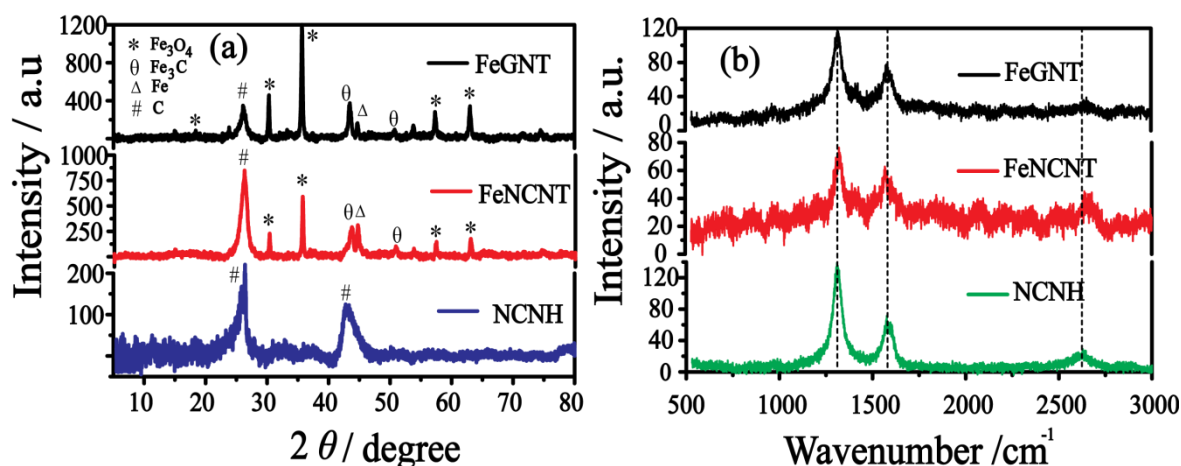


Figure 4B.1: (a) X-ray diffraction patterns of FeGNT, FeNCNT and NCNH and (b) Raman spectra of FeGNT, FeNCNT and NCNH.

X-ray diffraction (XRD) (Figure 4B.1a) pattern of FeGNT shows peaks which corresponds to the graphitic carbon (26.5°), Fe<sub>3</sub>O<sub>4</sub> (35.4°, 30.1°, 57.3°, 62.9°, 18.2° (JCPDS No. 65-3107)) Fe<sub>3</sub>C (43.3°, 50.7° (JCPDS, No. 89-2867)) and Fe (44.8°, JCPDS, No. 87-0722). Similar peaks are also observed in the case of FeNCNT. However, the FWHM of the graphitic peak of FeNCNT is higher than that of FeGNT, which indicates the formation of thick graphitic carbon walls in FeNCNT. Decreased Fe peak intensity of FeGNT compared to FeNCNT indicates that majority of the iron nanoparticles in the nanostructure is Fe<sub>3</sub>O<sub>4</sub> and Fe<sub>3</sub>C. According to a recent report, Fe<sub>3</sub>O<sub>4</sub> encapsulation within the carbon matrix also improves the ORR activity.<sup>[17]</sup> A reduced intensity ratio of the D

and G bands in Raman spectra (Figure 4B.1b) further confirms the reduction in the defective sites or surface impurities of FeGNT ( $I_D/I_G \sim 1.7$ ) compared to NCNH ( $I_D/I_G \sim 2.3$ ); however, the  $I_D/I_G$  ratio is even less for FeNCNT (1.2) compared to the rest. More interestingly, the prominent peak of the metal oxide at around  $678 \text{ cm}^{-1}$  in Raman spectra<sup>[18]</sup> is absent in the case of FeGNT. This clearly indicates that all the metal nanoparticles are well encapsulated within the carbon shell and possibly none of the metal oxide nanoparticles is present on the carbon surface.

#### 4B.2.2 FE-SEM and Elemental mapping

Field emission scanning electron microscope (FE-SEM) images clearly indicate existence of highly dense tubular morphology of FeGNT (Figure 4B.2 a-c). The diameter of FeGNT lies in between 100-150 nm with length of several micrometers. Compared to

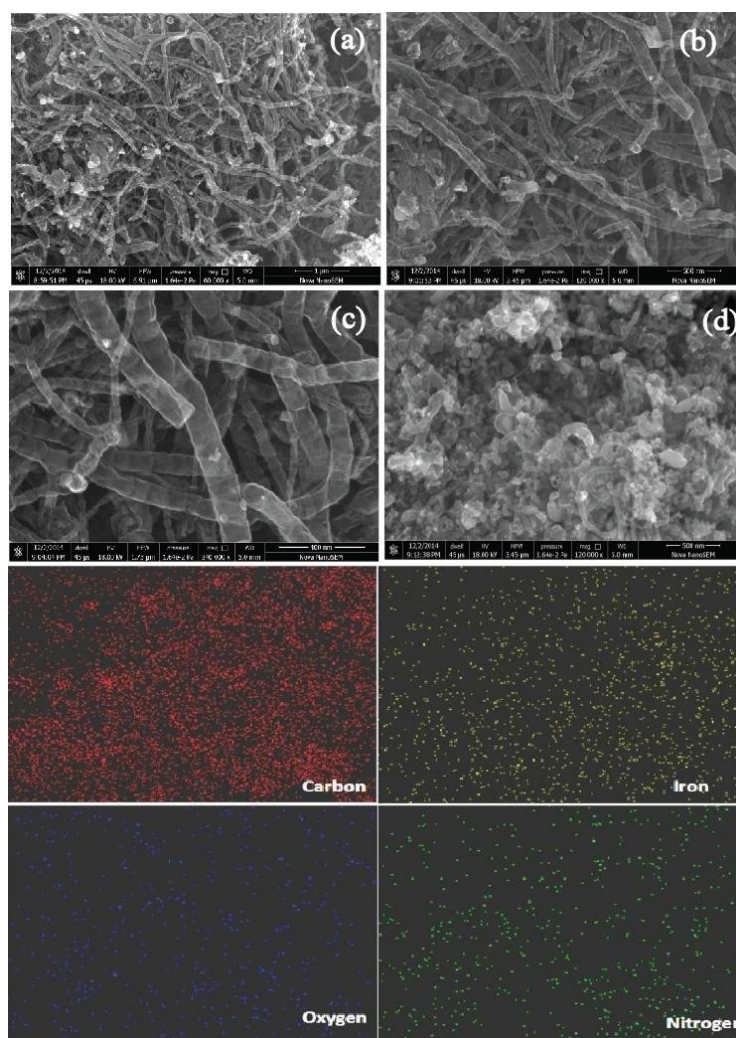


**Figure 4B.2:** FESEM images of (a-c) FeGNT and (d) FeNCNT. Images representing the elemental mapping of FeGNT using FE-SEM are also presented.

FeGNT, FeNCNT (Figure 4B.2d) is highly agglomerated with carbon particles which indicates the importance of SWCNH for the effective conversion of the nanotube like morphology. The uniform distribution of nitrogen and iron atoms on FeGNT (Figure 4B.2) ultimately improves the density of the active reaction center, which later helps to facilitate higher electrocatalytic activity during the oxygen reduction experiments.

#### 4B.2.3 HR-TEM analysis

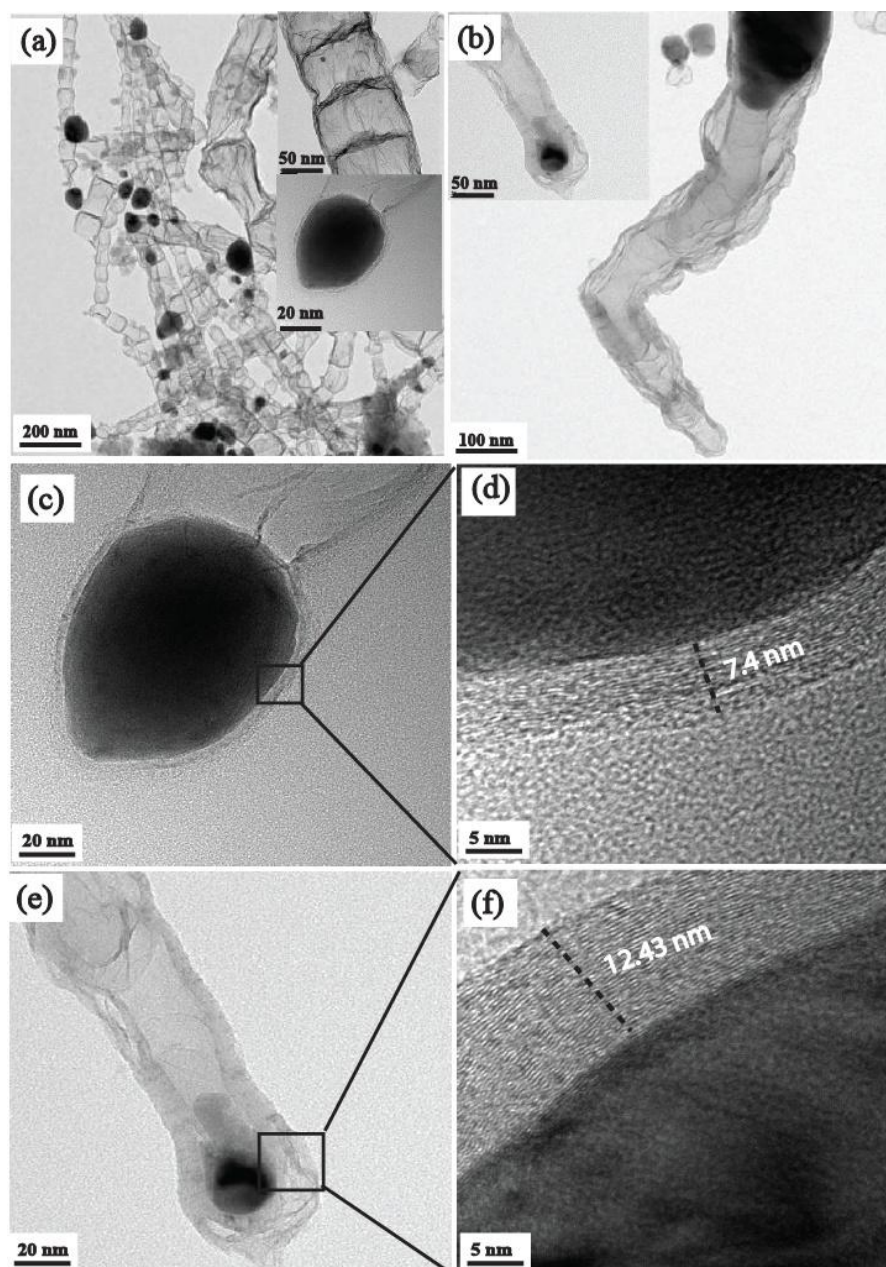


**Figure 4B.3:** HR-TEM images of FeGNT (a, c, d) and FeNCNT (b, e, f). Higher magnification images are given in the insets.

Transmission electron microscopic (TEM) images of FeGNT (Figure 4B.3a) show the tubular morphology of graphene where the metal nanoparticles are loosely bounded within the graphene sheets. The tubular morphology in the present case appears like originated by the loose rolling of the graphene sheets. Hence, the present nanostructure has been named as graphene nanotube, a terminology used by Li *et al.*<sup>[19]</sup> However, the wall thickness of FeNCNT is found to be higher compared to FeGNT (Figure 4B.3 c & d) and is evidenced by the narrow FWHM of the (002) plane in XRD. The distortion in the graphitic plane of the carbon shell of FeGNT compared to the flat graphitic plane in FeNCNT indicates the effective doping of 'Fe-N<sub>x</sub>' and nitrogen moieties into the carbon layers.<sup>[20]</sup> More interestingly, the annealed product of SWCNH (Figure 4B.4a) and the iron salt mixture

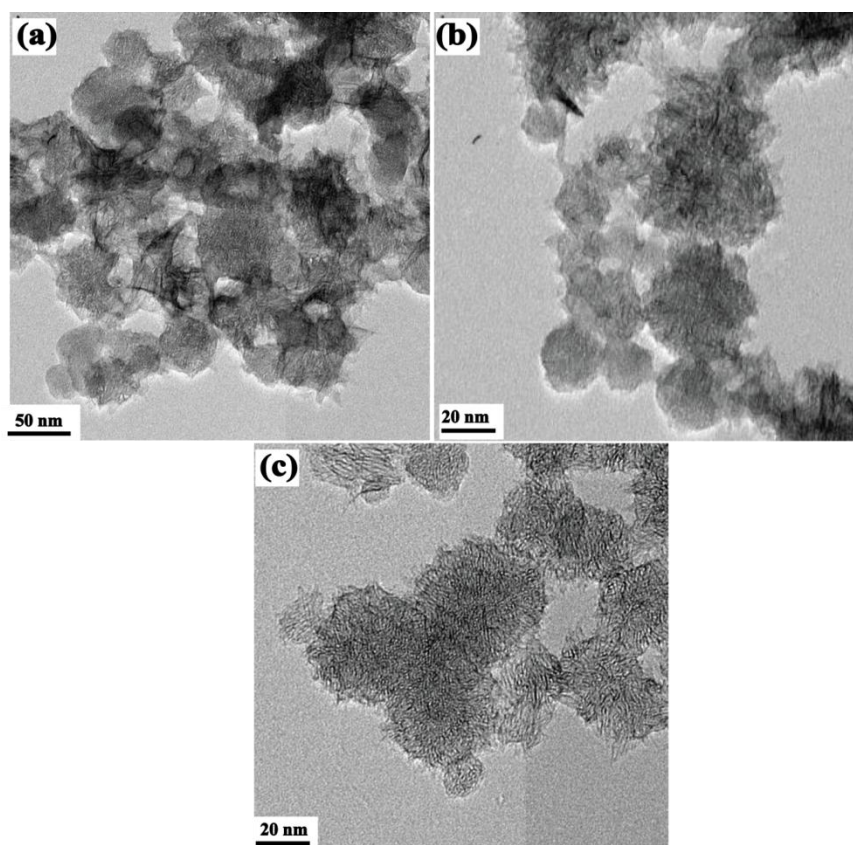


**Figure 4B.4:** HR-TEM images of (a) FeCNO, (b) NCNH and (c) SWCNH.

(FeCNO) shows that the SWCNH morphology is collapsing during the thermal treatment in presence of the iron salt. This further emphasizes the possibility of the morphology changes of SWCNH in the presence of the iron salt. The morphology of NCNH (Figure

4B.4b) is found to be slightly deteriorated from that of SWCNH due to the deposition of the carbon derived from melamine at higher temperature.<sup>[21]</sup>

In order to understand a clear mechanism of the graphene nanotube growth, the mixture of SWCNH, melamine and iron salt is annealed at different temperatures (Figure 4B.5). At 500 °C, there is no noticeable difference in the morphology of SWCNH. However, when the temperature is increased to 700 °C, the SWCNH changes its morphology to nanoyster type and with further increase in temperature (900 °C), the carbon nanohorn aggregates are completely transformed to graphene nanotube morphology. Presence of some carbon nanoparticles is also observed at 900 °C; however, the amount of such carbon nanoparticles is comparatively less. Further increase in the temperature does not change the tubular morphology of the graphene sheets which indicates that the optimum temperature for the nanotube formation is 900 °C.

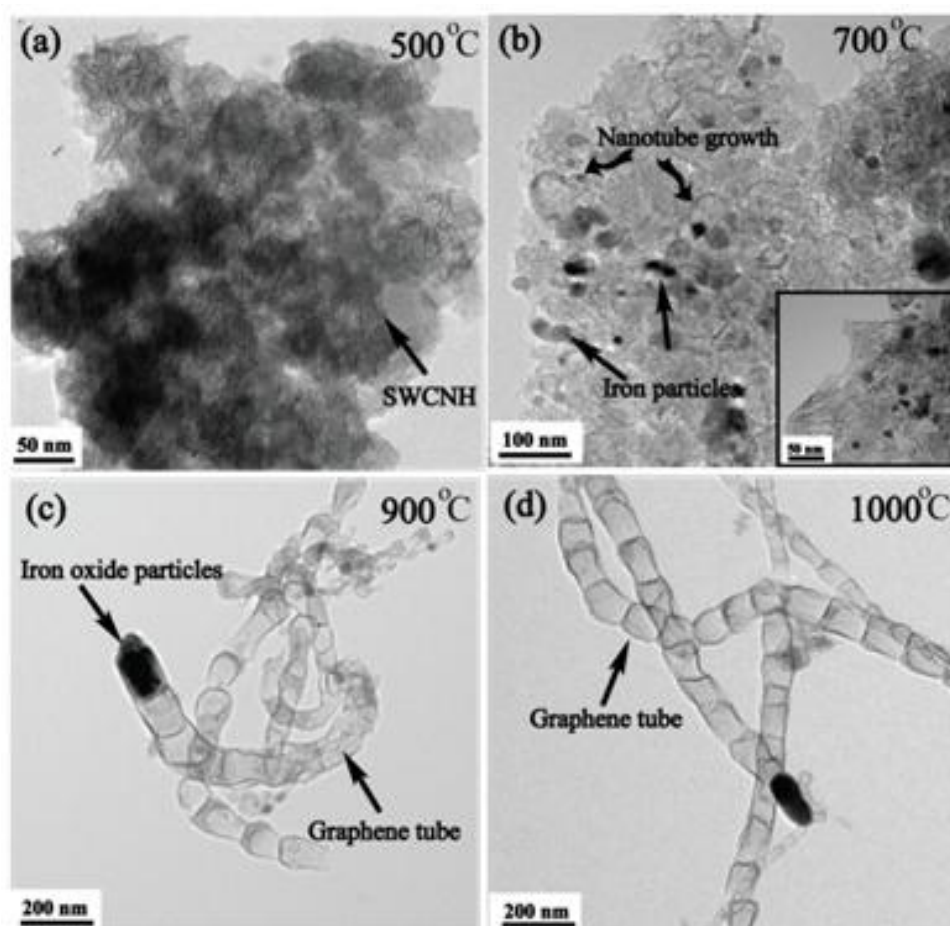


**Figure 4B.5:** HR-TEM images of FeGNT at different annealing temperatures during the synthesis: (a) 500 °C, (b) 700 °C, (c) 900 °C and (d) 1000 °C. Images of higher magnifications are given in the inset.

It is also interesting to observe that the SWCNH to melamine ratio also plays a crucial role towards the formation of graphene nanotube (Figure 4B.6). By keeping the iron salt content constant, a SWCNH to melamine ratio of 1:2.5 does not generate the tubular morphology even at 900 °C. The tubular morphology slowly grows from SWCNH at a ratio of 1:7.5 and the complete conversion of SWCNH to the graphene nanotube is found to be occurring at a ratio of 1:10. From these experimental evidences, the proposed growth mechanism of graphene nanotube is as follows: At high temperature, the iron particle diffuses

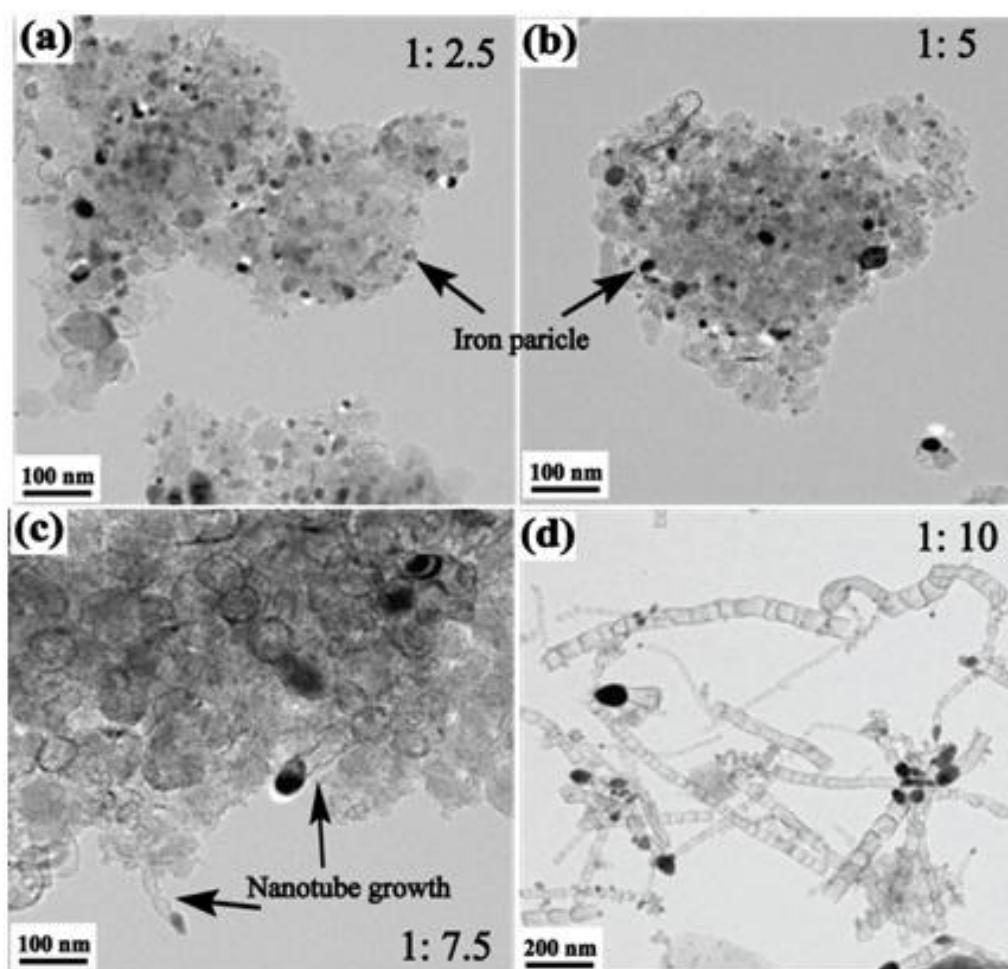
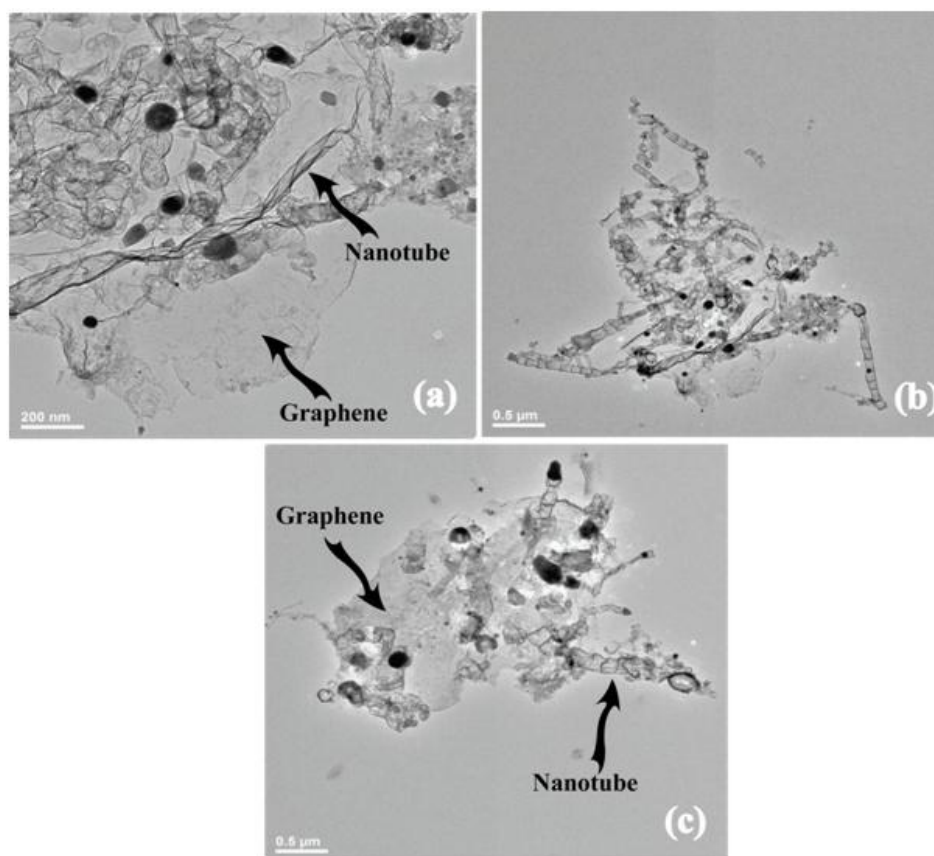


Figure 4B.7: HR-TEM images of FeGNT with different ratios of SWCNH and melamine powder.

into the nanohorns by unzipping the graphene wall of individual nanohorns and forms an oyster type morphology.<sup>[14]</sup> Simultaneously generated carbon nitride gases (e.g.,  $C_2N_2^+$ ,  $C_3N_2^+$ ,  $C_3N_3^+$ ) from melamine will dissolve in these nanoparticles.<sup>[22]</sup> After super saturation of these feed gases in the nanoparticles, precipitation of carbon occurs under the

thermal treatment conditions and this in turn results in the initiation of the nanotube growth catalyzed by the iron particle, a mechanism which is nearly similar to the one as suggested by Gagotsi *et al.*<sup>[23]</sup> From Figure 4B.7, it is clear that the nanohorn plays a pivotal role in maintaining the concentration of the carbon nitride feed gas from melamine to initiate the tubular growth from the nanohorn. This ultimately leads to reduction in the thickness of the wall of the nanotubes and improvement in the surface area of the nanotubes. If melamine amount is less, only core-shell type nanostructure forms on SWCNH. Since XRD analysis gives a clear evidence for the presence of  $\text{Fe}_3\text{O}_4$  or  $\text{Fe}_3\text{C}$  particles, it is expected that these particles are catalyzing the nanotube growth in a root growth manner.<sup>[19, 23-24]</sup> The formation of  $\text{Fe}_3\text{O}_4$  is expected from the reaction between the iron nanoparticles and trapped oxygen species in the nanohorns at high temperature. The lower FWHM of  $\text{Fe}_3\text{O}_4$  peak at a  $2\theta$  of  $\sim 35.6^\circ$  and higher FWHM of Fe peak at a  $2\theta$  of  $\sim 44.6^\circ$  of FeGNT support this possibility. Since such trapping effect of the oxygenated species is lower in the FeNCNT samples, both  $\text{Fe}_3\text{C}$  and Fe phases are dominant along with  $\text{Fe}_3\text{O}_4$



**Figure 4B.8:** HR-TEM images of the nanotube grown on graphene sheets at different magnifications.

in this sample. To serve as a supplementary evidence, the effect of SWCNH in the nanotube formation was studied by replacing it with graphene oxide (Figure 4B.8). However, in this case, the material obtained comprises of both nitrogen doped graphene and carbon nanotube, as reported by Zhang *et al.*<sup>[25]</sup> This further supports the importance of SWCNH for the generation of graphene nanotube.

#### 4B.2.4 Surface area analysis

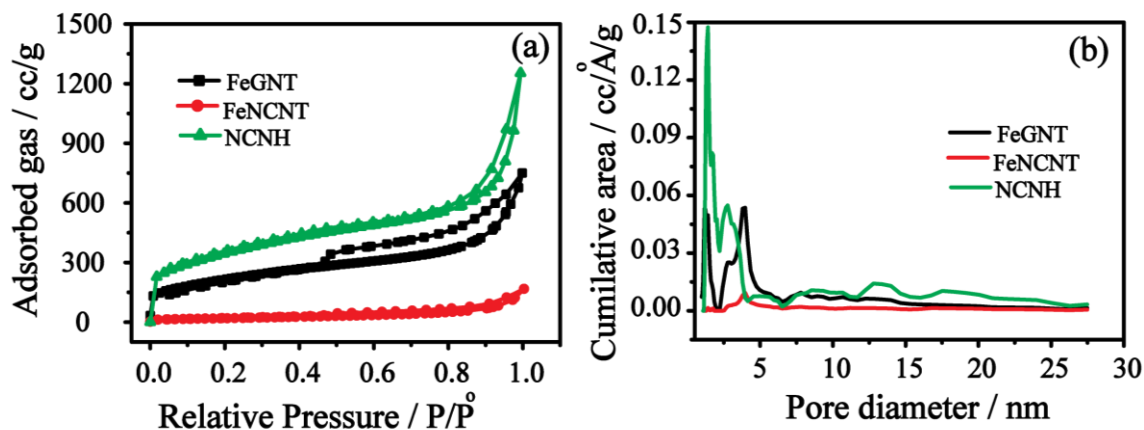


**Figure 4B.9:** (a) Nitrogen adsorption–desorption isotherms and (b) pore size distribution profiles of FeGNT, FeNCNT and NCNH.

Transformation of SWCNH to graphene nanotube is further confirmed from the Brunauer Emmet Teller (BET) surface area analysis. Normally, peroxide treated nanohorn provides high surface area of around  $1200 \text{ m}^2 \text{ g}^{-1}$ . BET surface area of NCNH in the present case is  $1520 \text{ m}^2 \text{ g}^{-1}$ , which is reduced to half ( $759 \text{ m}^2 \text{ g}^{-1}$ ) in the case of FeGNT. This is a clear evidence for the complete transformation of SWCNH to graphene nanotube and, to the best of our knowledge, is the highest surface area ever reported in the metal encapsulated nanotubes prepared from nitrogen source like melamine and metal salt.<sup>[19]</sup> More interestingly, the surface area of FeNCNT is found to be  $71 \text{ m}^2 \text{ g}^{-1}$ , which is similar to the recently reported Co encapsulated nanotube by Asefa *et al.*<sup>[26]</sup> The nitrogen adsorption isotherm of NCNH resembles a Type II characteristic whereas this behavior is found to be modified in the case of FeGNT (Figure 4B.9a). This indicates the transformation of the microporous nature of NCNH into mesoporous when SWCNH changes to graphene nanotube with the attainment of larger pores having sizes in the range of 2-6 nm (Figure 4B.9b). Apart from the surface area, electric conductivity of FeGNT is found to be  $7.8 \text{ S cm}^{-1}$ , which is  $\sim 4$  times higher than that of FeNCNT ( $2.1 \text{ S cm}^{-1}$ ). High



surface area with mesoporosity is necessary to improve the active reaction site density and efficient reactant transport. This along with the modulated electric conductivity and one dimensional morphology of FeGNT give great prospect for the material to evolve as an active electrocatalyst for ORR.

#### 4B.2.5 XPS analysis

X-ray photoelectron spectroscopy (XPS) is further employed to analyse the surface elements which are responsible for bringing the electrocatalytic activity. As shown in the elemental analysis data (Table 4B.1), the total nitrogen content is increasing when SWCNH is converted into FeGNT (3.09 at. %). The respective nitrogen contents in NCNH and FeNCNT are 1.07

**Table 4B.1:** Elemental composition of the different samples calculated from XPS.

Sample	C (At.%)	O (At.%)	N (At.%)	Fe (At.%)
FeGNT	88.87	7.64	3.10	0.39
FeNCNT	91.95	6.18	1.42	0.45
NCNH	88.67	10.26	1.10	0.00

and 1.42 at. %. This clearly indicates that SWCNH plays an important role to trap the nitrogen atoms during the graphene nanotube formation. Fitted N1s spectra of NCNH shows (Figure 4B.10) two peaks at 398.50 eV and 400.64 eV assigned for the pyridinic and quaternary nitrogen respectively; however, FeGNT shows the peaks corresponding to pyridinic (398.28 eV), pyrrolic (399.36 eV), quaternary (400.84 eV) and different forms of oxides (402.54, 404.09, 405.13 and 406.50 eV). Similar peaks are also observed in FeNCNT, where 398.32 eV corresponds to the pyridinic, 399.53 eV for the pyrrolic, 401.13 eV for the quaternary and 402.80 and 404.29 eV for the oxides of nitrogen.<sup>[9]</sup> Atom percentage of different nitrogen content is given in Figure 4B.10d. It is interesting to observe that the quaternary to pyridinic nitrogen ratio is increasing in the order of FeGNT (1.29) > FeNCNT (1.19) > NCNH (0.90). Stimulatingly, the recent literature shows the significant role of the quaternary nitrogen in promoting the ORR activity of the N-doped carbon systems.<sup>[10-11]</sup> Since the doping of quaternary nitrogen into the carbon layers reduces the C-N bond length, which is comparable to the O-O bond length, adsorption and

reduction of dioxygen is expected to be more facile in FeGNT.<sup>[27]</sup> This ultimately leads to improved ORR activity. Oxidised nitrogen species do not have any major role in the ORR activity.<sup>[2e]</sup>

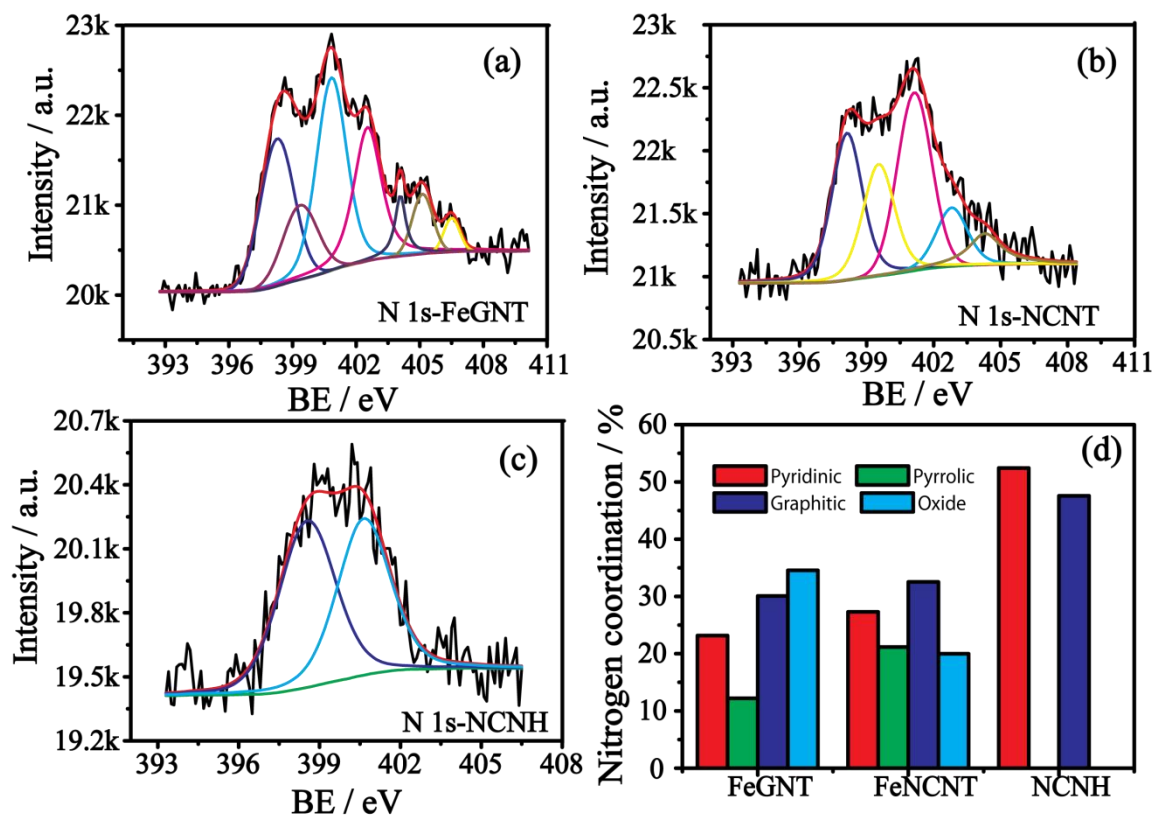


Figure 4B.10.: Deconvoluted N1s X-ray photoelectron spectra of (a) FeGNT, (b) FeNCNT, (c) NCNH and (d) different types of nitrogen coordinations calculated from the deconvoluted N 1s spectra of nitrogen in FeGNT, FeNCNT and NCNH.

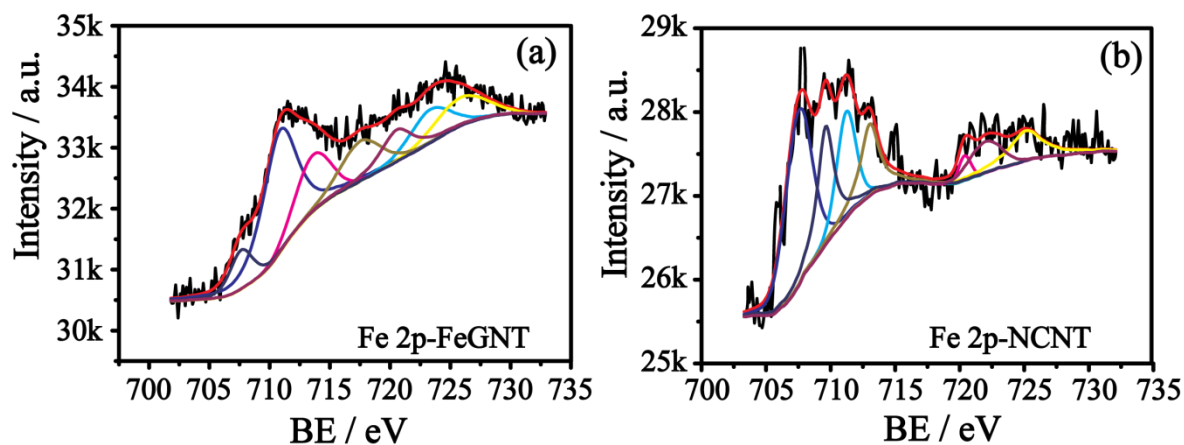


Figure 4B.11.: Deconvoluted Fe 2p spectra of (a) FeGNT and (b) FeNCNT.

Apart from nitrogen, the peaks corresponding to the iron moiety also give an evidence for the surface iron species (Figure 4B.11). FeGNT shows peaks at 711.10 and 714.02 eV correspond to the  $2p_{3/2}$  orbital of  $\text{Fe}^{\text{II}}$  and  $\text{Fe}^{\text{III}}$ , respectively.<sup>[28]</sup> Similarly, peaks at 724.08 and 726.09 eV correspond to the  $2p_{1/2}$  orbitals of  $\text{Fe}^{\text{II}}$  and  $\text{Fe}^{\text{III}}$ , respectively. Satellite peaks are also observed for the deconvoluted Fe 2p spectra of Fe in FeGNT. Fitted Fe 2p spectra of FeNCNT also show similar kinds of peaks. Apart from the above mentioned peaks as observed in FeGNT, two additional peaks at 707.75 and 709.61 eV are also observed in FeNCNT, which are attributed to the  $\text{Fe}^0$  and  $\text{FeO}_x$  moieties respectively.<sup>[29]</sup> It is well known that  $\text{Fe-N}_x$  improves the ORR activity of the electrocatalysts.<sup>[27a, 30]</sup> Also, the pyridinic as well as pyrrolic nitrogen easily coordinates with the iron species to form the  $\text{Fe-N}_x$  active sites.<sup>[31]</sup> According to some of the recent literatures, a peak at  $398.6 \pm 0.3$  eV of the fitted N 1s spectra is assigned to the  $\text{Fe-N}_x$  coordination.<sup>[32]</sup> In the present case, both FeGNT and FeNCNT showing a clear peak at 398.28 and 398.32 eV respectively, can also associate with the  $\text{Fe-N}_x$  interaction along with the pyridinic nitrogen. From the XPS analysis, it is clear that both the quaternary nitrogen content and  $\text{Fe-N}_x$  coordination simultaneously can play a determining role to improve the oxygen reduction activity of FeGNT. More or less uniform distribution of iron and nitrogen species obtained from the elemental mapping also supports this conclusion.

#### 4B.2.6 Electrochemical studies

**Table 4B.2:** Electrochemical performance of the different catalysts including Pt/C in 0.1 M  $\text{HClO}_4$ , 0.5 M  $\text{H}_2\text{SO}_4$  and 0.1 M KOH.

	Onset potential (V vs RHE)	Half wave potential (V vs RHE)	Tafel slope (mV decade <sup>-1</sup> )	Peroxide yield at 0.5 V vs RHE	Number of electron transfer at 0.5 V vs RHE
0.1 M $\text{HClO}_4$					
Pt/C	0.99	0.87	66.84	2.80	3.95
FeGNT	0.90	0.71	77.40	5.30	3.89
FeNCNT	0.77	0.46	132.21	6.03	3.88
NCNH	0.80	0.49	146.04	6.02	3.88

0.5 M H <sub>2</sub> SO <sub>4</sub>					
Pt/C	0.98	0.85	64.23	1.47	3.97
FeGNT	0.90	0.75	77.94	2.30	3.95
FeNCNT	0.77	0.48	114.98	7.37	3.85
NCNH	0.71	0.41	211.19	7.37	3.85
0.1 M KOH					
Pt/C	1.00	0.86	91.00	3.45	3.94
FeGNT	1.00	0.85	84.84	5.01	3.90
FeNCNT	0.92	0.75	84.86	9.95	3.80
NCNH	0.92	0.75	91.14	3.01	3.94

Electrocatalytic activity of FeGNT and other control samples was analysed by linear sweep voltammetry (LSV) using a rotating disc electrode (RDE) in oxygen saturated both acid (0.5 M H<sub>2</sub>SO<sub>4</sub> and 0.1 M HClO<sub>4</sub>) and alkaline (0.1 M KOH) conditions. For the purpose of comparison, commercial 40 wt.% Pt/C was also tested by maintaining a catalyst loading of 100 μgPt cm<sup>-2</sup> on the electrode. In 0.1 M HClO<sub>4</sub> (Figure 4B.12a), FeGNT shows an onset potential ( $E_{\text{onset}}$ ) of 0.90 V which is only 0.09 V lower than that of Pt/C (0.99 V); similarly, the half wave potential ( $E_{1/2}$ ) of FeGNT (0.71 V) is 0.15 V lower than that of Pt/C (0.86 V). More importantly, NCNH shows more positive  $E_{\text{onset}}$  and  $E_{1/2}$  compared to FeNCNT; however, compared to FeGNT, the ORR activity of these materials is very less in 0.1 M HClO<sub>4</sub>. 40 mV positive shifts in  $E_{\text{onset}}$  as well as  $E_{1/2}$  are observed for NCNH compared to FeNCNT. In 0.5 M H<sub>2</sub>SO<sub>4</sub> (Figure 4B.12b), FeGNT shows an  $E_{\text{onset}}$  of 0.90 V which is only 0.08 V lower than that of Pt/C (0.98 V). Similarly,  $E_{1/2}$  of FeGNT (0.75 V) is 0.10 V lower than that of Pt/C (0.85 V). In 0.5 M H<sub>2</sub>SO<sub>4</sub>, FeNCNT outperformed NCNH in terms of  $E_{\text{onset}}$  as well as  $E_{1/2}$  (Table 4B.2). Also the LSV feature of NCNH is found to be changed with respect to the acid used. From Figure 4B.12c, it is clear that FeGNT shows comparable performance in terms of  $E_{\text{onset}}$  as well as  $E_{1/2}$  with Pt/C in alkaline condition. FeNCNT and NCNH show comparable ORR activity in alkaline medium; however, both  $E_{\text{onset}}$  as well as  $E_{1/2}$  are found to be shifted towards more negative

compared to FeGNT. From LSV, it is clear that both intrinsic as well as active reaction centre density are improved during the *in-situ* graphene nanotube growth from SWCNH.

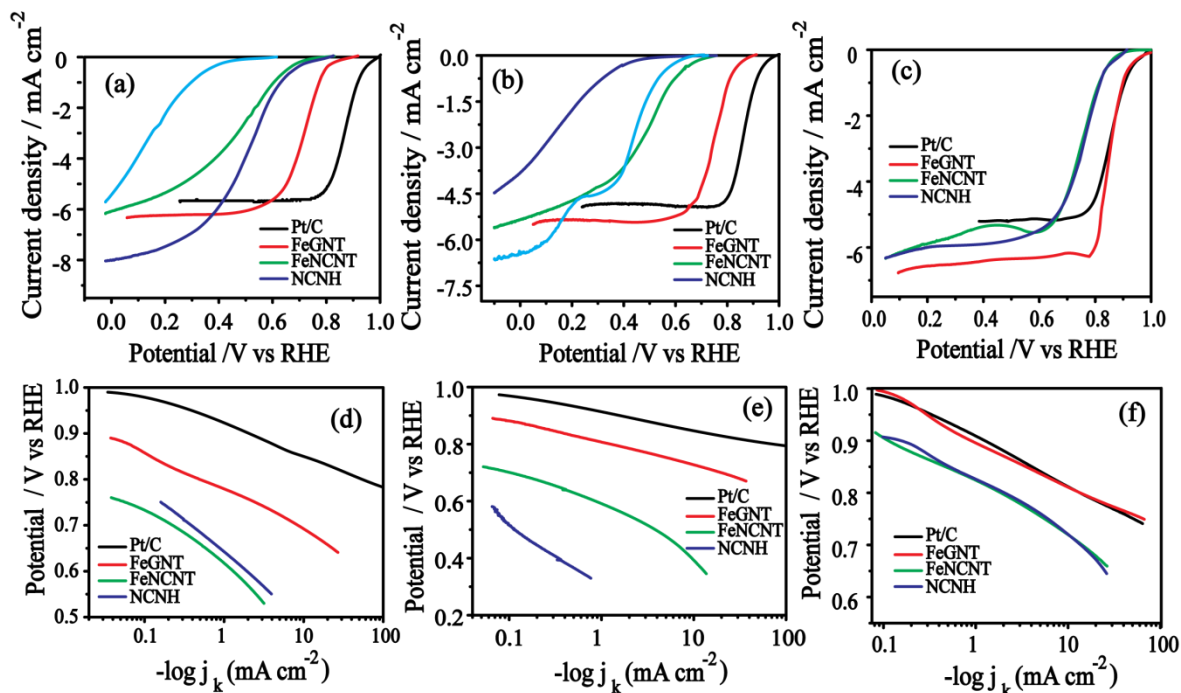


**Figure 4B.12.** Linear sweep voltammograms (LSVs) of the prepared samples and Pt/C in oxygen saturated (a) 0.1 M HClO<sub>4</sub>, (b) 0.5 M H<sub>2</sub>SO<sub>4</sub> and (c) 0.1 M KOH at an electrode rotation speed of 1600 rpm and a scan rate of 5 mV s<sup>-1</sup> and the corresponding Tafel slopes of the catalysts ((d) 0.1 M HClO<sub>4</sub>, (e) 0.5 M H<sub>2</sub>SO<sub>4</sub> and (f) 0.1 M KOH)).

From Table 4B.2, it is clear that the Tafel slope of FeGNT at higher positive potential is different in all the three electrolytes analogous to that of Pt/C. In 0.1 M HClO<sub>4</sub> (Figure 4B.12d), FeGNT shows a Tafel slope of 77.40 mV decade<sup>-1</sup>, which is higher than that of Pt/C (68.94 mV decade<sup>-1</sup>) in the same electrolyte. Similarly, in 0.5 M H<sub>2</sub>SO<sub>4</sub> (Figure 4B.12e), FeGNT shows a Tafel slope of 77.94 mV decade<sup>-1</sup>, which is higher than that of Pt/C (64.23 mV decade<sup>-1</sup>) in the same electrolyte. Similar Tafel slopes of FeGNT in both 0.1 M HClO<sub>4</sub> and 0.5 M H<sub>2</sub>SO<sub>4</sub> are indicating that the reaction mechanism for ORR followed by these systems is same in these acid electrolytes. In 0.1 M KOH (Figure 4B.12f), FeGNT (84.84 mV decade<sup>-1</sup>) shows lower Tafel slope than Pt/C (91.00 mV decade<sup>-1</sup>) which indicates that ORR is more facile on FeGNT. Different Tafel slopes of FeGNT in the different electrolytes further emphasize the effect of the counter ions in the electrolyte towards ORR. Similarly, both FeNCNT and NCNH also show lower Tafel slope respectively at 84.86 mV decades<sup>-1</sup> and 91.14 mV decades<sup>-1</sup> in 0.1 M KOH.

However, in acidic condition, the Tafel slopes of both FeNCNT and NCNH deviate a lot in comparison with FeGNT and Pt/C, which indicates the poor ORR kinetics of these

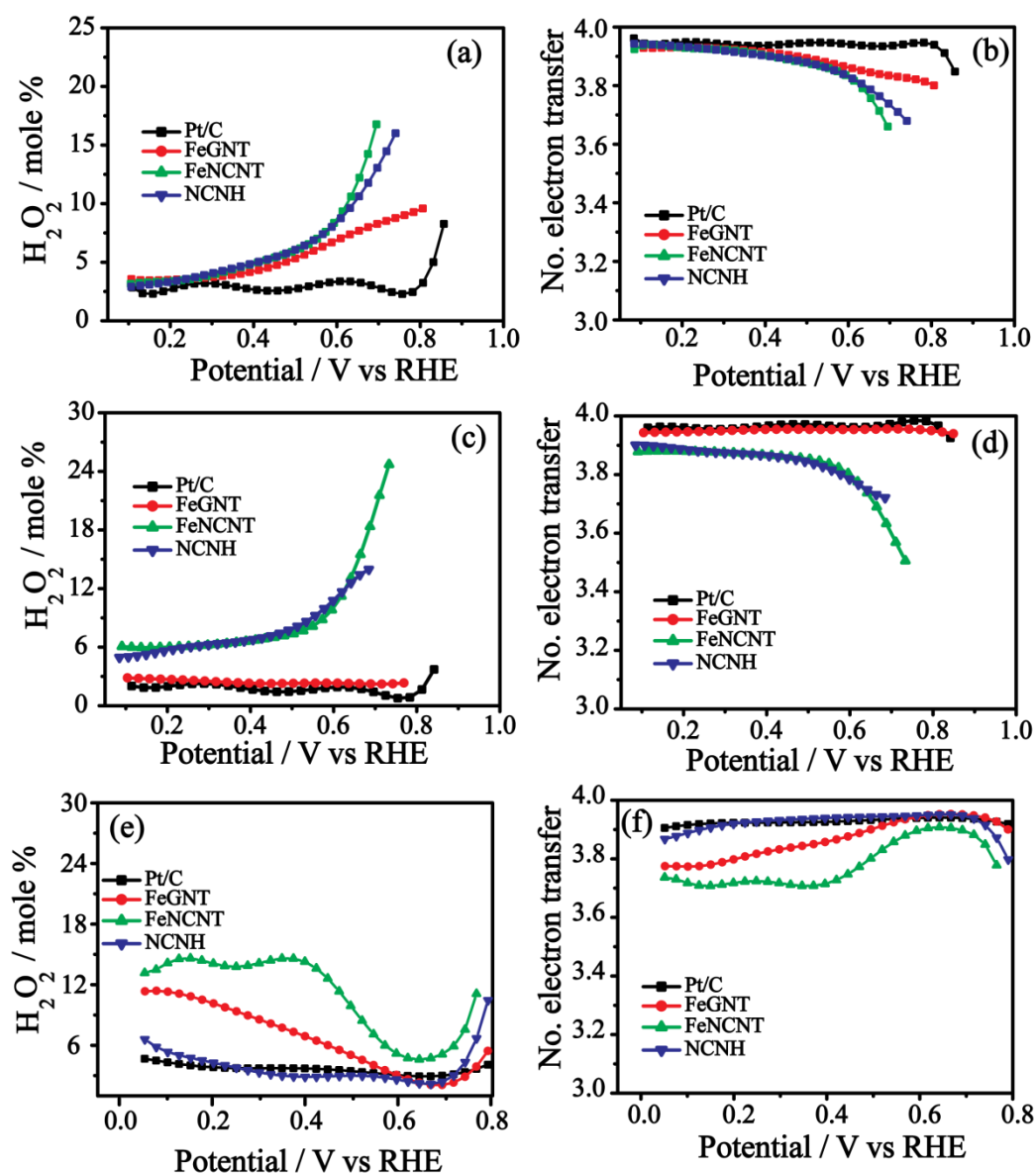


**Figure 4B.13.** (a) Hydrogen peroxide yield and (b) number of electron transfer of the samples at different potentials in 0.1 M  $HClO_4$  calculated from RRDE. (c) Hydrogen peroxide yield and (d) number of electron transfer of the samples at different potentials in 0.5 M  $H_2SO_4$  calculated from RRDE. (e) Hydrogen peroxide yield and (f) number of electron transfer of the samples at different potentials in 0.1 M KOH calculated from RRDE.

materials in acidic environment. To further understand about the amount of peroxide generated during ORR, rotating ring disc electrode (RRDE) analysis was performed. In

alkaline medium (Figure 4B.13 e & f), FeGNT shows an increasing trend of peroxide yield of  $\sim 11$  mole % with increase in the negative potentials. However, this value is lower than that of FeNCNT ( $\sim 15$  mole %) and a little higher than that of NCNH ( $\sim 7$  mole %). The electron transfer number calculated from the peroxide yield shows that all the catalysts follow a direct four-electron pathway to reduce dioxygen molecule to hydroxide in alkaline conditions.

In both 0.1 M HClO<sub>4</sub> (Figure 4B.12 a & b) and 0.5 M H<sub>2</sub>SO<sub>4</sub> (Figure 4B.12 c & d), FeGNT shows a peroxide yield similar to Pt/C (5 mole %) in the entire potential range. However, both FeNCNT and NCNH show higher peroxide yield at higher positive potential, which is found to be decreasing with increasing the negative potential. Similar trend is also observed in the case of the number of electron transfer. This stands out as a valid evidence for the involvement of the 4 e<sup>-</sup> transfer for the reduction of oxygen molecule to water in the case of FeGNT, which is a similar mechanism as followed by Pt/C.

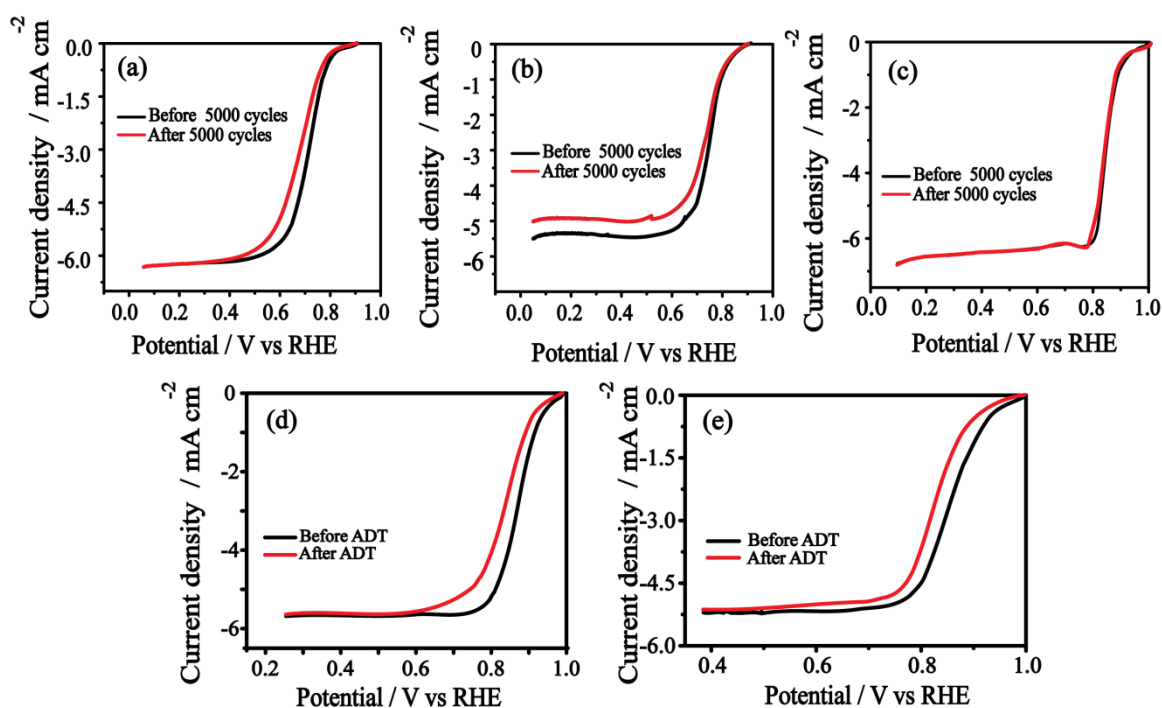


**Figure 4B.14:** LSVs of FeGNT before and after ADT at 1600 rpm with  $5 \text{ mV s}^{-1}$  scan rate in oxygen saturated (g) 0.1 M HClO<sub>4</sub>, (h) 0.5 M H<sub>2</sub>SO<sub>4</sub> and (i) 0.1 M KOH and LSVs of Pt/C before and after ADT in (d) 0.1 M HClO<sub>4</sub> and (e) 0.1 M KOH with an electrode rotation rate of 1600 rpm and a scan rate of  $5 \text{ mV s}^{-1}$ .

Electrochemical stability of the FeGNT catalyst was analyzed using accelerated durability test (ADT) according to the DOE protocol.<sup>[33]</sup> In 0.1 M HClO<sub>4</sub> (Figure 4B.14a), FeGNT shows only 40 mV difference in  $E_{1/2}$  after 5000 potential cycles without any change in  $E_{\text{onset}}$ . However, Pt/C shows a negative shift in both  $E_{\text{onset}}$  (40 mV) and  $E_{1/2}$  (50 mV) after the 5000 cycles (Table 4B.3). In case where 0.5 M H<sub>2</sub>SO<sub>4</sub> was used as the electrolyte (Figure 4B.14 b), FeGNT shows only 20 mV decrease in  $E_{1/2}$  after the 5000 cycles without any change in  $E_{\text{onset}}$ . However, the limiting current density of FeGNT is found to be decreased after the 5000 cycles. This type of reduction in the current density is not observed during the experiments in HClO<sub>4</sub>. This also emphasizes the effect of the electrolyte on the ORR performance of the non-platinum electrocatalysts. This improved electrochemical stability of FeGNT is not only visible in acidic media but also is observed in alkaline conditions (Figure 4B.14c). In alkaline condition, FeGNT shows improved electrochemical stability. Only 10 mV difference in  $E_{1/2}$  is observed for FeGNT even after the 5000 potential cycles, which is less compared to Pt/C (31 mV) (Figure 4B.14e). The improved ORR activity and stability of FeGNT is credited to the peculiar structure and morphology of FeGNT where quaternary nitrogen and Fe-N<sub>x</sub> are uniformly distributed. With this high density of the active reaction sites, the effective oxygen adsorption and its reduction is expected to be improved in FeGNT compared to NCNH and FeNCNT.

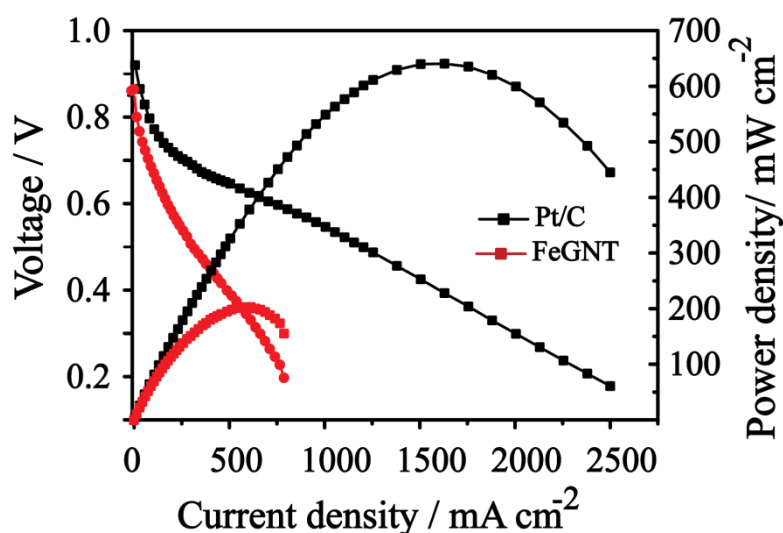


**Figure 4B.15:** Single cell polarization taken (active area is 4 cm<sup>2</sup>) at 65 °C of a PEMFC with FeGNT (2 mg cm<sup>-2</sup>) as the cathode catalyst and Nafion 212 as the proton conducting membrane. H<sub>2</sub> and O<sub>2</sub> were used as the fuel and oxidant with flow rates of 50 sccm and 100 sccm, respectively.



Since FeGNT shows improved ORR activity in acidic conditions, a single cell analysis was performed by using FeGNT as the cathode catalyst ( $2 \text{ mg cm}^{-2}$ ) and Pt/C as the anode catalyst ( $0.5 \text{ mg cm}^{-2}$ ) in a membrane electrode assembly (MEA) having an active area of  $4 \text{ cm}^2$  (Figure 4B.15). Nafion 212 membrane was used as the electrolyte in the MEA. The single cell analysis was performed under 100 % relative humidity at an operating temperature of  $60 \text{ }^\circ\text{C}$ . The testing was done by using a fuel cell test station (Fuel Cell Technologies Inc, USA with data acquisition by a Labview 5.1 software) by purging  $\text{H}_2$  with a flow rate of 50 sccm at the anode and  $\text{O}_2$  with a flow rate of 100 sccm at the cathode. Single cell analysis of the FeGNT based MEA delivers a maximum power density of  $200 \text{ mW cm}^{-2}$  and  $500 \text{ mA cm}^{-2}$  current density at  $0.60 \text{ V}$ . These values are comparable to the recently reported cell performances of various Fe and Co based electrocatalysts. It should be noted that the active area of the current MEA ( $4 \text{ cm}^2$ ) is much larger than the ones reported in the literature (eg  $1$  or  $2 \text{ cm}^2$ ).<sup>[1b, 34]</sup> This significantly good performance on a larger MEA, where the issues due to ohmic overpotential is expected to be high, clearly indicates that the excellent intrinsic activity of FeGNT as revealed from the half-cell electrochemical measurements can be translated effectively as power output in the device level. Even though the obtained fuel cell performance of FeGNT is less compared to Pt/C ( $600 \text{ mW cm}^{-2}$ ), considering the cost, availability and ease of synthesis with respect to Pt/C, FeGNT can be considered as a potential alternative cathode catalyst for PEMFC applications.

## 4.2 Conclusion

This chapter explains about improvement in the active reaction centre density of SWCNH by doping Fe and N for ORR. Apart from the activity modulation of SWCNH, this chapter also provides an insight on the effect of precursor loading on the final morphology of SWCNH.

High temperature annealing of SWCNH, melamine and Fe salt in the ratio of 1:3:0.01 in inert atmosphere results in Fe and N doped SWCNH without any change in the morphology of SWCNH. The synthesised catalyst shows greater activity towards ORR, both in terms of onset potential and half-wave potential, than the commercial 40 wt.% Pt/C in alkaline medium. From the electrochemical and structural analysis, it is inferred that the pyrrolic nitrogen coordinated with Fe at the edge of the micropores was responsible for the creation of the main active reaction centres by promoting the adsorption of dioxygen and

its subsequent reduction. FeNCNH-900 (the 900 °C annealed sample) showed excellent ORR activity with the involvement of the four-electron pathway, with a 30 mV gain in the overpotential compared to its Pt counterpart. Moreover, the electrocatalytic activity of the catalyst was found to increase during the cycling of the potential, as indicated by the positive shift in the onset potential of oxygen reduction. Under similar experimental conditions, Pt, on the other hand, was found to be susceptible to degradation. A single cell test of the membrane electrode assembly with the cathode electrode derived from the Pt-free catalyst gives a maximum power density of 35 mW cm<sup>-2</sup> under AEMFC conditions and at an operating temperature of 50 °C in the cell.

If SWCNH, melamine and Fe salt ratio is 1:10:2.5, high temperature annealing in inert atmosphere results in Fe and N doped graphene nanotube (FeGNT). In this case, the SWCNH morphology is completely transformed into that of graphene nanotube. The as prepared nanotube possesses a tubular morphology of loosely bounded graphene layer with an average diameter of 150 nm and length of several micrometers. The Fe<sub>3</sub>O<sub>4</sub> nanoparticles are found to be located at the tip of the nanotube. The SWCNH precursor plays an important role in the graphene nanotube formation by maintaining its high surface area, good electrical conductivity and higher content of nitrogen moieties. From the XPS analysis, it was found that the quaternary nitrogens as well as Fe-N<sub>x</sub> coordinations, which are known for their ability to facilitate ORR, are present on the FeGNT surface. The uniform distribution of these sites along the surface is confirmed by elemental mapping. FeGNT shows enhanced ORR activity in acidic and alkaline conditions with improved stability. FeGNT reduces dioxygen through a direct four electron pathway with very less percentage of peroxide yields. Single cell polarization of the PEM fuel cell made by using FeGNT as the cathode catalyst delivered a maximum power density of 200 mW cm<sup>-2</sup> by using Nafion 212 as the proton conducting membrane. The single cell performance proves the prospect of FeGNT to serve as a potential non-Pt ORR catalyst for PEMFC applications.

### 4.3 References

- [1] a) L. Wang, A. Ambrosi, M. Pumera, *Angew. Chem. Int. Ed.* **2013**, 52, 13818-13821; b) R. Bashyam, P. Zelenay, *Nature* **2006**, 443, 63-66; c) H. Peng, Z. Mo, S. Liao, H. Liang, L. Yang, F. Luo, H. Song, Y. Zhong, B. Zhang, *Sci. Rep.* **2013**, 3, 1765; d) M. Lefèvre, E. Proietti, F. Jaouen, J.-P. Dodelet, *Science* **2009**, 324, 71-74 ;

- e)G. Wu, K. L. More, C. M. Johnston, P. Zelenay, *Science* **2011**, 332 443-447 ; f) D. Yu, Y. Xue, L. Dai, *The Journal of Physical Chemistry Letters* **2012**, 3, 2863-2870.
- [2] a) J. Liu, X. Sun, P. Song, Y. Zhang, W. Xing, W. Xu, *Adv. Mater.* **2013**, 25, 6879-6883; b)H. T. Chung, J. H. Won, P. Zelenay, *Nat Commun* **2013**, 4, 1922; c)Y. Li, W. Zhou, H. Wang, L. Xie, Y. Liang, F. Wei, J.-C. Idrobo, S. J. Pennycook, H. Dai, *Nat Nanotech.* **2012**, 7, 394-400; d) J. Xu, Y. Zhao, C. Shen, L. Guan, *ACS Appl. Mater. Inter.* **2013**, 5, 12594-12601; e)K. Parvez, S. Yang, Y. Hernandez, A. Winter, A. Turchanin, X. Feng, K. Müllen, *ACS Nano* **2012**, 6, 9541-9550; f)S. Wang, D. Yu, L. Dai, D. W. Chang, J.-B. Baek, *ACS Nano* **2011**, 5, 6202-6209; g)H. Yin, C. Zhang, F. Liu, Y. Hou, *Adv. Function. Mater.* **2014**, 24, 2930-2937; h)J. Liang, R. F. Zhou, X. M. Chen, Y. H. Tang, S. Z. Qiao, *Adv. Mater.* **2014**, n/a-n/a; i)Y. Hu, J. O. Jensen, W. Zhang, L. N. Cleemann, W. Xing, N. J. Bjerrum, Q. Li, *Angew. Chem. Int. Ed.* **2014**, 53, 3675-3679; j)J.-S. Lee, G. S. Park, S. T. Kim, M. Liu, J. Cho, *Angew. Chem. Int. Ed.* **2013**, 52, 1026-1030; k)Z.-S. Wu, S. Yang, Y. Sun, K. Parvez, X. Feng, K. Müllen, *J. Am. Chem. Soc.* **2012**, 134, 9082-9085.
- [3] a)T. Palaniselvam, B. P. Biswal, R. Banerjee, S. Kurungot, *Chemistry – A European Journal* **2013**, 19, 9335-9342; b)P. Zhang, F. Sun, Z. Xiang, Z. Shen, J. Yun, D. Cao, *Energy Environ. Sci.* **2014**, 7, 442-450.
- [4] a)S. Zhu, G. Xu, *Nanoscale* **2010**, 2, 2538-2549; b)C. M. Yang, H. Noguchi, K. Murata, M. Yudasaka, A. Hashimoto, S. Iijima, K. Kaneko, *Adv. Mater.* **2005**, 17, 866-870; c)J. Fan, M. Yudasaka, J. Miyawaki, K. Ajima, K. Murata, S. Iijima, *J. Phys. Chem. B* **2006**, 110, 1587-1591.
- [5] L. Brandão, C. Pässeira, D. Mirabile Gattia, A. Mendes, *J. Mater. Sci.* **2011**, 46, 7198-7205.
- [6] a)C. Cioffi, S. Campidelli, F. G. Brunetti, M. Meneghetti, M. Prato, *Chem. Commun.* **2006**, 2129-2131; b)C. Cioffi, S. Campidelli, C. Sooambar, M. Marcaccio, G. Marcolongo, M. Meneghetti, D. Paolucci, F. Paolucci, C. Ehli, G. M. A. Rahman, V. Sgobba, D. M. Guldi, M. Prato, *J. Am. Chem. Soc.* **2007**, 129, 3938-3945.
- [7] S. M. Unni, S. N. Bhange, R. Illathvalappil, N. Mutneja, K. R. Patil, S. Kurungot, *Small* **2014**, DOI:10.1002/sml.201303892.
- [8] S. M. Unni, S. N. Bhange, R. Illathvalappil, N. Mutneja, K. R. Patil, S. Kurungot, *Small* **2014**, 10.1002/sml.201303892.

- [9] J. Casanovas, J. M. Ricart, J. Rubio, F. Illas, J. M. Jiménez-Mateos, *J. Am. Chem. Soc.* **1996**, *118*, 8071-8076.
- [10] H. Wang, T. Maiyalagan, X. Wang, *ACS Catal.* **2012**, *2*, 781-794.
- [11] L. Lai, J. R. Potts, D. Zhan, L. Wang, C. K. Poh, C. Tang, H. Gong, Z. Shen, J. Lin, R. S. Ruoff, *Energy Environ. Sci.* **2012**, *5*, 7936-7942.
- [12] G. Wu, C. M. Johnston, N. H. Mack, K. Artyushkova, M. Ferrandon, M. Nelson, J. S. Lezama-Pacheco, S. D. Conradson, K. L. More, D. J. Myers, P. Zelenay, *J. Mater. Chem.* **2011**, *21*, 11392.
- [13] C. Venkateswara Rao, Y. Ishikawa, *J. Phys. Chem. C* **2012**, *116*, 4340-4346.
- [14] K. R. S. Chandrakumar, J. D. Readle, C. Rouleau, A. Puretzky, D. B. Geohegan, K. More, V. Krishnan, M. Tian, G. Duscher, B. Sumpter, S. Irle, K. Morokuma, *Nanoscale* **2013**, *5*, 1849-1857.
- [15] S. M. Unni, S. N. Bhange, R. Illathvalappil, N. Mutneja, K. R. Patil, S. Kurungot, *Small* **2015**, *11*, 352-360.
- [16] S. M. Unni, S. Ramadas, R. Illathvalappil, S. N. Bhange, S. Kurungot, *J. Mater. Chem. A* **2015**, *3*, 4361-4367.
- [17] Z. Li, G. Li, L. Jiang, J. Li, G. Sun, C. Xia, F. Li, *Angew. Chem. Int. Ed.* **2014**, DOI : 10.1002/anie.201409579.
- [18] M. Thi Thu Trang, H. Phuong Thu, P. Hong Nam, L. Thi Thu Huong, P. Hoai Linh, P. Thi Bich Hoa, T. Dai Lam, N. Xuan Phuc, *Adv. Nat. Sci: Nanosci. Nanotechnol.* **2012**, *3*, 015006.
- [19] Q. Li, P. Xu, W. Gao, S. Ma, G. Zhang, R. Cao, J. Cho, H.-L. Wang, G. Wu, *Adv. Mater.* **2014**, *26*, 1378-1386.
- [20] T. Palaniselvam, R. Kannan, S. Kurungot, *Chem. Commun.* **2011**, *47*, 2910-2912.
- [21] a) Y. Zhong, M. Jaidann, Y. Zhang, G. Zhang, H. Liu, M. Ioan Ionescu, R. Li, X. Sun, H. Abou-Rachid, L.-S. Lussier, *J. Phys. Chem. Solids* **2010**, *71*, 134-139; b) X. Li, L. Kong, J. Yang, M. Gao, T. Hu, X. Wu, M. Li, *Appl. Phys. A* **2013**, *113*, 735-739.
- [22] Z. Wen, S. Ci, F. Zhang, X. Feng, S. Cui, S. Mao, S. Luo, Z. He, J. Chen, *Adv. Mater.* **2012**, *24*, 1399-1404.
- [23] Y. Fan, Z. Zhao, Q. Zhou, G. Li, X. Wang, J. Qiu, Y. Gogotsi, *Carbon* **2013**, *58*, 128-133.

- [24] a)X. Wu, Y. Tao, Y. Lu, L. Dong, Z. Hu, *Diamond Relat. Mater* **2006**, *15*, 164-170; b)R. Rao, R. Sharma, F. Abild-Pedersen, J. K. Norskov, A. R. Harutyunyan, *Sci. Rep.* **2014**, *4*.
- [25] S. Zhang, H. Zhang, Q. Liu, S. Chen, *J. Mater. Chem. A* **2013**, *1*, 3302-3308.
- [26] X. Zou, X. Huang, A. Goswami, R. Silva, B. R. Sathe, E. Mikmeková, T. Asefa, *Angew. Chem. Int. Ed.* **2014**, *53*, 4372-4376.
- [27] a)G. Tuci, C. Zafferoni, P. D'Ambrosio, S. Caporali, M. Ceppatelli, A. Rossin, T. Tsoufis, M. Innocenti, G. Giambastiani, *ACS Catal.* **2013**, *3*, 2108-2111; b)F. Gao, G.-L. Zhao, S. Yang, *ACS Catal.* **2014**, *4*, 1267-1273; c)S. Ni, Z. Li, J. Yang, *Nanoscale* **2012**, *4*, 1184-1189.
- [28] a)P. M. Hallam, M. Gomez-Mingot, D. K. Kampouris, C. E. Banks, *RSC Adv.* **2012**, *2*, 6672-6679; b)L. Lin, Q. Zhu, A.-W. Xu, *J. Am. Chem. Soc.* **2014**, *136*, 11027-11033.
- [29] U. Wiedwald, L. Han, J. Biskupek, U. Kaiser, P. Ziemann, *Beilstein J. Nanotech.* **2010**, *1*, 24-47.
- [30] a)A. Kong, X. Zhu, Z. Han, Y. Yu, Y. Zhang, B. Dong, Y. Shan, *ACS Catal.* **2014**, *4*, 1793-1800; b)W. Li, J. Wu, D. C. Higgins, J.-Y. Choi, Z. Chen, *ACS Catal.* **2012**, *2*, 2761-2768; c)H. Peng, F. Liu, X. Liu, S. Liao, C. You, X. Tian, H. Nan, F. Luo, H. Song, Z. Fu, P. Huang, *ACS Catal.* **2014**, *4*, 3797-3805; d)D. Singh, K. Mamtani, C. R. Bruening, J. T. Miller, U. S. Ozkan, *ACS Catal.* **2014**, *4*, 3454-3462; e)M.-Q. Wang, W.-H. Yang, H.-H. Wang, C. Chen, Z.-Y. Zhou, S.-G. Sun, *ACS Catal.* **2014**, 3928-3936.
- [31] Y. Zhao, K. Watanabe, K. Hashimoto, *J. Am. Chem. Soc.* **2012**, *134*, 19528-19531.
- [32] a)X. Wang, X. Chen, A. Thomas, X. Fu, M. Antonietti, *Adv. Mater.* **2009**, *21*, 1609-1612; b)H. R. Byon, J. Suntivich, Y. Shao-Horn, *Chem. Mater.* **2011**, *23*, 3421-3428.
- [33] Y. Li, W. Zhou, H. Wang, L. Xie, Y. Liang, F. Wei, J.-C. Idrobo, S. J. Pennycook, H. Dai, *Nat Nano* **2012**, *7*, 394-400.
- [34] a)Q. Wang, Z.-Y. Zhou, Y.-J. Lai, Y. You, J.-G. Liu, X.-L. Wu, E. Terefe, C. Chen, L. Song, M. Rauf, N. Tian, S.-G. Sun, *J. Am. Chem. Soc.* **2014**, *136*, 10882-10885; b)M. Lefèvre, E. Proietti, F. Jaouen, J.-P. Dodelet, *Science* **2009**, *324*, 71-74.



## Chapter 5

### *Summary and Conclusion*

This chapter provides an overall summary and conclusion of the research activities as explained in the previous chapters targeting on the development of efficient non-precious metal based electrocatalysts for ORR. The chapter highlights the approaches adopted and implemented for improving the ORR performance of the non-precious electrocatalysts by modifying the active reaction site density by inducing changes in the physicochemical properties of graphene and carbon nanohorn. The proper selection of the carbon morphologies along with the attainment of high surface area with micro or mesopores, good electrical conductivity and preferred coordination of the heteroatoms etc are found to be strongly influencing the activity of a non-precious electrocatalyst. The different approaches used for modifying these properties are concisely summarized in this chapter. This chapter also highlights the future prospects of the materials described in the thesis for other inevitable energy sectors like batteries, solar cells, water splitting etc. Moreover, this chapter also provides a glimpse about the current global scenario of the non-precious fuel cell catalyst research and the position of India in the world map among other countries involved in the development of the non-precious electrocatalysts.



## 5.1 Summary

Overwhelming energy demands and alarming depletion rate of fossil fuel resources have urged authorities and researchers worldwide to search environmentally benign and cost effective renewable energy resources. Among various available renewable energy resources, electrochemically driven green energy devices fuel cells have attracted huge attention. Fuel cell, mainly Polymer Electrolyte Membrane Fuel Cell (PEMFC) is one of the most desirable energy devices because of its low temperature operability, fast start-up and simplicity. PEMFC is working with the help of hydrogen and small organic molecules (methanol, formic acid etc.) as the fuels, oxygen as the oxidant and producing electrical energy and heat energy along with water as the by-product. Each and every PEMFC components are equally important to deliver high efficiency (more than 60 %); however, the cathode catalyst is supposed to be the “heart” of a PEMFC, where oxygen is reduced to form water.

Platinum is the most widely accepted electrocatalyst for PEMFC to the date. However, the high cost and low availability of platinum impose serious practical implications to the commercialization of these renewable energy based devices to meet the energy crisis of the century. For example, more than 50 % of the total cost of a fuel cell device is derived from the platinum electrocatalyst. Performance degradation of the platinum based catalyst in long term usage due to platinum agglomeration and poisoning is still an unresolved mystery. In this scenario, the most challenging task in front of the fuel cell researchers is to replace platinum with low cost materials without affecting the fuel cell performance. Many electrocatalysts such as transition metal nanoparticles (mainly, 3d metals,  $M = \text{Co, Ni, Cu, Fe, Mn}$ ), metal oxides, metal nitrides, metal chalcogenides, metal carbides etc prove to be good alternates of the Pt like metals. However, less stability and low electrical conductivity of the metal oxides, nitrides, chalcogenides and carbides still prohibit the application of these materials as the cathode materials in PEMFCs.

At present, carbon based electrode materials have attracted great attention due to their high electrical conductivity, low density etc. However, to apply these carbon morphologies as alternatives for Pt in fuel cell cathode, one should modify the electronic structure by a process called “doping”. Doping of hetero atoms (mainly nitrogen) in carbon morphologies could modify their physico-chemical properties and this can enable the carbon atoms to be more efficient towards the adsorption of oxygen molecule and its



reduction through efficient electron transfer in between them. However, overall efficiency of the carbon based electrocatalysts towards ORR strongly depends on the active reaction site density (ARSD). ARSD of a non-precious electrocatalyst can be tuned by proper selection of carbon morphologies, creating preferred coordination of heteroatoms in the carbon matrix, maintaining high electrical conductivity of the substrate and enhancing the surface area of the final catalyst etc.

The main theme of the thesis is to develop appropriate strategies to create well accessible active sites on the carbon morphologies such as graphene and carbon nanohorn to improve ARSD for accomplishing facile reduction of dioxygen molecules. Tuning of the carbon morphologies, mode of nitrogen and iron doping, enhancement in surface area and electrical conductivity etc were carefully taken into account while setting up the preparation protocols to improve the ARSD of the graphene and carbon nanohorn based systems for ensuring better ORR activity in both acidic and alkaline mediums.

Major accomplishments of the present research activities are summarised as below:

## **Nitrogen doped graphene based electrocatalysts for ORR**

Graphene, the two-dimensional carbon allotrope, has been recently identified as a potential candidate to replace platinum from energy devices due to its exceptional physiochemical properties such as high surface area, high electrical conductivity, high mechanical strength and high electro-chemical stability. However, synthesis of good quality graphene sheets is a major hurdle to transform them into good electrode materials. Major reason is the mode of synthesis. Since bulk quantities of graphene sheets are essential for commercial applications, graphene oxide (GO) reduction route is being considered as the more preferred technique. However, during the reduction of GO, the sheet stacking possibility is higher, which in turn reduces the active surface area of the system.

A mutually assisted redox reaction between graphene oxide (GO) and pyrrole, followed by thermal treatment at elevated temperatures bring in an efficient template-free synthetic route for the preparation of mesoporous nitrogen-doped graphene (NGE). The system contains a high weight percentage of pyrrolic nitrogen and it retains good specific surface area, which help the electrocatalyst to display comparable electrochemical oxygen reduction activity as that of the state-of-the-art 40 wt.% Pt/C catalyst. NGE exhibits a high

surface area of  $528 \text{ m}^2 \text{ g}^{-1}$  and a pore diameter of  $\sim 3$  to  $7 \text{ nm}$ . The heat treatment temperature plays a pivotal role in establishing the desired pyrrolic coordination of the nitrogen in graphene for the electrochemical oxygen reduction reaction. The NGE sample obtained after the heat treatment at  $1000 \text{ }^\circ\text{C}$  (NGE-1000) has 53% pyrrolic nitrogen content compared to the similar samples prepared by treating at low temperatures. Most importantly, NGE-1000 has displayed a significantly low overpotential for oxygen reduction with the onset potential very closely matching to that of the commercial 40 wt.% Pt/C in alkaline medium. However, it lacks proper ARSD. The fuel tolerance and durability under the electrochemical environment of the NGE catalyst is found to be superior to the Pt/C catalyst.

By adopting a facile synthesis approach for the preparation of NGE with high surface area, the intrinsic activity of NGE towards ORR could be improved. However, ARSD of NGE is still inferior compared to the Pt based electrocatalysts. In order to further improve ARSD, a facile synthesis approach is adopted by which the morphology of NGE could be arranged in a three dimensional (3D) manner. Layer-separated 3D nitrogen doped graphene (NGE) with an accessible interstitial surface and modulated activity characteristics for oxygen reduction in acidic medium could be prepared by wrapping NGE sheets on *in-situ* generated carbon nitride ( $\text{CN}_x$ ) tetrapods by annealing melamine foam (MF) containing graphene oxide (GO) at  $900 \text{ }^\circ\text{C}$  in inert atmosphere. The NGE content on  $\text{CN}_x$  could be easily controlled by changing the number of dip coating of MF in the GO solution. Moreover, the  $\text{CN}_x$  backbone in the catalyst reduces the restacking of graphene sheets at high temperature and provides high surface area. The material prepared by annealing MF after three times dip-coating in the GO solution (CNG-3) shows ORR activity in acidic condition with lower overpotential compared to 20 wt.% Pt/C and it is found to be reducing oxygen molecule to water through the preferred four electron transfer mechanism. The well interconnected 3D architecture in CNG-3 provides facile routes for mass transport and this enhances the exposure of the active reaction sites. XPS analysis reveals that the pyridinic and pyridone coordinations of the nitrogen are responsible for the improved activity in acidic medium. Compared to Pt/C, CNG-3 shows improved electrochemical stability and fuel tolerance. Even after 5000 potential cycles,  $E_{1/2}$  of CNG-3 is shifting towards more positive, indicating potential induced generation of more active reaction centers or further activation of the existing sites.

## Nitrogen doped carbon nanohorn and its metal chalcogenide composite as an ORR electrocatalyst

Nitrogen-doped carbon morphologies have been proven to be better alternatives to Pt in polymer-electrolyte membrane (PEM) fuel cells. However, efficient modulation of the active sites by the simultaneous escalation of the porosity and nitrogen doping, without affecting the intrinsic electrical conductivity, still remains to be solved. The thesis discloses a simple strategy to solve this issue by treating single-walled carbon nanohorn (SWCNH) with urea at 800 °C. The resulting nitrogen-doped carbon nanohorn shows a high surface area of  $1836 \text{ m}^2 \text{ g}^{-1}$  along with an increased electron conductivity, which are the pre-requisites of an electrocatalyst. The nitrogen-doped nanohorn annealed at 800 °C (N-800) also shows a high oxygen reduction activity (ORR). Because of the high weight percentage of the pyridinic nitrogen coordination in N-800, the present catalyst shows a clear 4-electron reduction pathway at only 50 mV overpotential and 16 mV negative shift in the half-wave potential for ORR compared to Pt/C along with a high fuel selectivity and electrochemical stability in alkaline medium. More importantly, a membrane electrode assembly (MEA) based on N-800 provides a maximum power density of  $30 \text{ mW cm}^{-2}$  under anion-exchange membrane fuel cell (AEMFC) testing conditions. Even though ARSD of NCNH got improved compared to NGE, the intrinsic activity and ARSD are still lagging behind the current *state-of-the-art* Pt/C. To further improve ARSD, CoSe<sub>2</sub> nanoparticles were supported on the nitrogen-doped carbon nanohorn (CoSe<sub>2</sub>/NCNH) and studied the influence of the CoSe<sub>2</sub> metal centre interaction with NCNH for ORR. CoSe<sub>2</sub>/NCNH shows a 50 mV lower overpotential in onset and a 150 mV positive shift in half-wave potential ( $E_{1/2}$ ) as compared to CoSe<sub>2</sub> supported on carbon and carbon nanohorn in alkaline condition. This suggests that the intrinsic activity as well as the active reaction centre density of CoSe<sub>2</sub> is modified by NCNH. More interestingly, CoSe<sub>2</sub>/NCNH shows a better  $E_{1/2}$  compared to Pt/C even though its intrinsic activity is much higher as expected. The onset potential of CoSe<sub>2</sub>/NCNH is shifted to more positive, which indicates that the intrinsic activity of NCNH towards ORR has improved after dispersing CoSe<sub>2</sub> on it. An air breathing direct methanol micro-laminar flow fuel cell ( $\mu$ LFFCs) could be constructed using CoSe<sub>2</sub>/NCNH as a methanol tolerant cathode catalyst. A maximum power density of  $10.05 \text{ mW cm}^{-2}$  and a maximum current density  $124.20 \text{ mA cm}^{-2}$  are achieved with CoSe<sub>2</sub>/NCNH compared to the catalysts like CoSe<sub>2</sub>/CNH, CoSe<sub>2</sub>/C and Pt/C with 5 M

methanol as the fuel. The improved activity of CoSe<sub>2</sub>/NCNH is attributed to the peculiar morphology and nitrogen doping of carbon nanohorn.

## Nitrogen and iron co-doped carbon nanohorn for ORR

Even though the high surface area carbon nanohorn improves ARCD as well as the intrinsic activity as compared to NGE, the overall ORR activity of these materials still lags behind Pt/C. In order to further boost the activity of NCNH, iron moieties were introduced to NCNH. A simple surface modification of single-walled carbon nanohorn was carried out by simultaneous doping with Fe and N at 900 °C (FeNCNH-900). The ratio of the mixture of SWCNH:melamine:iron salt was used as 1:3:0.1 for the annealing purpose. In this particular ratio, the morphology of SWCNH is remaining intact. Interestingly, FeNCNH-900 has an ORR activity superior to that of 40 wt.% Pt on carbon (Pt/C) in alkaline condition. Compared to Pt/C, FeNCNH-900 gives a 30 mV improvement in the onset potential and a 20 mV gain in the half-wave potential for ORR. This indicates that both the intrinsic activity as well as ARSD get improved in the system to meet the activity characteristics of Pt/C. Its high activity is the result of the simultaneous modulation achieved by the high surface area and the microporosity of carbon nanohorn, together with the establishment of the desired nitrogen-iron coordinated pyrrolic active centres. The catalyst shows excellent electrochemical stability and, most notably, its ORR activity is found to be still increasing after the 1000 potential cycles given in alkaline condition. Single-cell fuel cell performance using FeNCNH-900 as the cathode catalyst shows a maximum power density of 35 mW cm<sup>-2</sup> under alkaline conditions. Even though, FeNCNH-900 shows excellent activity towards ORR in alkaline condition, the ORR activity of this material in acidic environment is quite poor. This further demonstrates the importance in attaining more active centres for ORR with less sensitivity to the pH of the medium. As a way to improve the characteristics of the active centres for attaining enhanced activity at lower pH, the melamine as well as iron salt loadings were increased compared to the previous case (SWCNH:melamine:iron salt ratio is maintained as 1:10:2.5 in the present case). After high temperature annealing of the reaction mixture with this particular ratio, interestingly, a graphene nanotube like morphology has been derived from single walled nanohorn, which comprises thin layers of graphene sheets with encapsulated iron oxide nanoparticles (FeGNT). FeGNT shows a surface area of 750 m<sup>2</sup> g<sup>-1</sup>, which is the highest ever reported among the metal encapsulated nanotubes. Moreover, the

graphene protected iron oxide nanoparticles assist the system to attain efficient distribution of Fe-N<sub>x</sub> and quaternary nitrogen based active reaction centres, which provide better activity and electrochemical stability towards ORR in acidic as well as alkaline conditions. Single cell performance of a proton exchange membrane fuel cell by using FeGNT as the cathode catalyst delivered a maximum power density of 200 mW cm<sup>-2</sup> with Nafion as the proton exchange membrane at 60 °C.

Overall, the thesis shows a road map for the development of a non-precious electrocatalyst as a replacement for the current *state-of-the-art* Pt catalysts by simple and scalable approaches. The journey starts from the nitrogen doped graphene based system and ends at the Fe-N<sub>x</sub> doped graphene nanotube. During the course of the journey, a systematic approach has been taken to tune the active reaction centre density by modifying the factors such as the morphology of the substrate, mode of heteroatom doping, coordination of the nitrogen atoms and iron moieties, surface area, electrical conductivity etc. The Fe-N<sub>x</sub> doped graphene nanotube shows superior activity towards ORR in both acidic and alkaline conditions and this advantage of the system to function effectively under the acidic conditions could be validated through single cell analysis using Nafion as the proton exchange membrane. The present research activities and the obtained performance during the single cell analysis based on FeGNT as the cathode, offer a scalable and commercially viable process and a system to eventually fulfil the dream of running PEMFCs which contain noble metal-free electrodes.

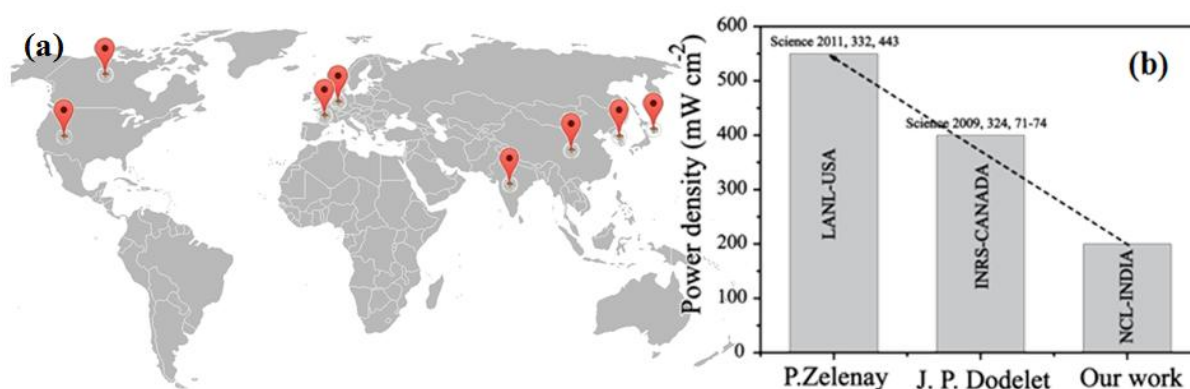


**Figure 5.1:** (a) Position of India in the world map for non-precious catalyst development and (b) current status of CSIR-NCL's research activities towards the development of non-precious electrocatalysts in comparison with the current global standards.

## 5.2 Future prospects

The thesis is devoted to the development of non-precious electrocatalysts for PEMFC. In order to fulfil the dream of “*Pt-free*” fuel cell, it is necessary to work also on the anode materials which can enhance the hydrogen oxidation reaction (HOR) and alcohol oxidation reaction (AOR). Even though handful reports are available for the development of ORR catalysts, the reports on the development of cost-effective HOR/AOR catalysts are very limited. This indicates the challenge involved in the development of such materials. Surface modified graphene and carbon nanohorn supported with RuO<sub>2</sub>, Mo and Ni alloys etc will work as better catalysts for HOR/AOR. Since the surface area of nitrogen doped nanohorn is very high without compromising its electrical conductivity, dispersion of the abovementioned catalytic centres will be relatively high with size less than 5 nm.

Apart from fuel cell, the materials used in the study for ORR can also be applied in energy storage devices such as Li-air batteries and Zn-air batteries, where the cathode reaction is the reduction of oxygen molecule present in air. Also, NCNH and NGE can act as support materials for SnO<sub>2</sub> for storing Li ions, which in turn can act as anode materials for Li-ion batteries. Since most of the materials described in this thesis have high surface area and good conductivity, these materials can also find applications in ultracapacitors.

NCNH and FeGNT also help to produce hydrogen through photocatalytic water splitting. Also, dispersion of metal oxides on these materials can assist water oxidation reactions. Since water oxidation and hydrogen evolution are very important for photosynthesis, utilization of such materials will help to develop a device for accomplishing artificial photosynthesis. CoSe<sub>2</sub>/NCNH will also help for hydrogen evolution as well as oxygen evolution reactions, which in turn can help to construct an electrolyser for water splitting and fuel production.

In a material point of view, the materials described in this thesis can find applications in fuel production, fuel storage, electrolysers and also in energy storage/conversion devices, which include supercapacitors, batteries, dye sensitised solar cells, fuel cells etc.

## *List of Publications*

### **AWARDS AND HONORS**

- 1 Raman-Charpak Fellowship 2013 (Fellowship by Indio-French centre for the promotion of advanced research)

### **PATENTS**

- 1 Simple strategy for the preparation of PBI based membrane electrode assembly (MEA) with improved fuel cell performance and stability. S. Kurungot, R. Illathuvalapil, S. N. Bhangé and **S. M. Unni**, Indian Patent application no. **3569-DEL-2013**
- 2 New strategy to synthesis high surface area nitrogen doped single walled carbon nanohorns for enhanced oxygen reduction electrocatalyst, S. Kurungot, **S. M Unni**, S. Ramadas, Indian patent application No. **3169DEL2013; WO 2015/059718 A1**
- 3 Novel step towards a comprehensive solution to the problem of cost effective energy and food waste management. S. B. Ogale, S. Kurungot, R. Ghokale, **S. M. Unni**, Indian patent application No: **2593/DEL/2013; WO 2015029076 A1**
- 4 Process for the preparation of membrane electrode assemblies (MEAs) K. V. Pillai, S. Kurungot, U. K. Kharul, H. Chawdhari, **S. M. Unni**, B. Unni, H. N. Kagalwala **US 2014/0017595 A1** published on 16-01-2014.
- 5 An improved process for the preparation of membrane electrode assemblies (MEAs) K. V. Pillai, S. Kurungot, U. K. Kharul, H. Chawdhari, **S. M. Unni**, B. Unni, H. N. Kagalwala, **WO 2012/131718/A1**, Indian patent No: **869/DEL/2011 A** published on 22-11-2013.

### **PUBLICATIONS**

- 1 CoSe<sub>2</sub> supported on nitrogen-doped carbon nanohorn as methanol tolerant cathode for air breathing micro laminar flow fuel cells  
**S. M. Unni** , J. M. Mora-Hernandez, S. Kurungot and N. Alonso-Vante, ChemElectroChem, **2015**, DOI:10.1002/celec.201500154
- 2 The Effect of Carbon-Based Substrates onto Non-precious and Precious Electrocatalytic Center.

- S. M. Unni**, C. A. Campos-Roldan, J. M. Mora-Hernandez, Y. Luo, L. A. Estudillo-Wong, and N. Alonso-Vante, **ECS Trans.**, **2015** Accepted
- 3 In vitro and in silico antifungal efficacy of nitrogen doped carbon nanohorn (NCNH) against *Rhizoctonia solani*.  
**S. Dharni**, Sanchita, **S. M. Unni**, S. Kurungot, A.I Samad, A. Sharma, D. D. Patra, **J. Biomol. Struct. Dyn.**, **2015**, DOI: 10.1080/07391102.2015.1018841
- 4 Substrate effects on the catalytic centre of CoSe<sub>2</sub> for oxygen reduction reaction  
**S. M. Unni** , J. M. Mora-Hernández , Y. Luo , and N. Alonso-Vante, **ECS Trans.**, **2015**, 64, 1-9.
- 5 Surface Modified Single Wall Carbon Nanohorn as an Efficient Electrocatalyst for Platinum-Free Fuel Cell Cathode  
**S. M. Unni**, S. Ramdas, R. Illathvalappil, S. N. Bhange and S. Kurungot, **J. Mater. Chem. A**, **2015**, 3, 4361 - 4367
- 6 Layer-separated distribution of nitrogen doped graphene by wrapping on carbon nitride tetrapods for enhanced oxygen reduction reaction in acid medium  
**S. M. Unni**, R. Illathvalapil, P. K. Gangadharan, S. N. Bhange and S. Kurungot **Chem. Commun.**, **2014**, 50, 13769 - 13772
- 7 Nitrogen induced surface area and conductivity modulation of carbon nanohorn and its function as an efficient metal-free oxygen reduction electrocatalyst for anion exchange membrane fuel cells  
**S. M. Unni**, S. N. Bhange, R. Illathvalappil, N. Mutneja, K. R. Patil and S. Kurungot, **Small**, **2014**, 11, 352-360
- 8 An efficient heteroatom-doped carbon electro-catalyst for oxygen reduction reaction by pyrolysis of protein-rich pulse flour cooked with SiO<sub>2</sub> nanoparticles  
R. Ghokale, **S. M. Unni**, D. Puthussery, S. Kurungot and S. B. Ogale **PhysChemChemPhys**, 2014, **16**, 4251-4259
- 9 A unique strategy in the design of a high performance thin all-solid-state supercapacitor mimicking the active interface of its liquid-state counterpart  
B. Anothumakkool, A. T. A. Torris, S. N. Bhange, **S. M. Unni**, M. V. Badiger and S. Kurungot, **Appl. Mater. Interfaces**, **2013**, 5, 13397–13404.
- 10 Two-in-one: Inherent Anhydrous and Water-assisted High Proton Conduction in a 3D Metal-organic Framework  
S. S. Nagarkar, **S. M. Unni**, A. Sharma, S. Kurungot, and S. K. Ghosh, **Angew.**



- Chem. Int. Ed.* **2013**, 53, 2638–2642.
- 11 Functionalized graphene using ethylenedioxythiophene as a 2-D multifunctional electrocatalyst for energy conversion applications.  
**S. M. Unni**, S. N. Bhange, B. Anothumakkool and S. Kurungot, *ChemPlusChem*, **2013**, 78, 1296–1303.
- 12 1-Dimensional Alignment of Porous Polyethylenedioxythiophene Using Carbon Nanofiber as a Solid Template: An Efficient Charge Storage Material with Improved Capacitance Retention and Cycle Stability  
B. Anothumakkool, S. N. Bhange, **S. M. Unni**, S. Kurungot, *RSC Advances* **2013**, 3, 11877-11887.
- 13 3-Dimensionally self assembled single crystalline Platinum nanostructure on few layer graphene as an efficient oxygen reduction electrocatalyst.  
**S. M. Unni**, V. K. Pillai and S. Kurungot, *RSC Advances*, **2013**, 3, 6913-6921.
- 14 Hierarchically nano-perforated graphene as a high performance electrode material for ultra capacitor  
D. Mhamane, A. Suryawanshi, **S. M. Unni**, S. Kurungot, S. B. Ogale, *Small*, **2013**, 9, 2801–2809.
- 15 Graphene enriched with pyrrolic coordination of the doped nitrogen as an efficient metal-free electrocatalyst for oxygen reduction.  
**S. M. Unni**, S. Devulapally, N Karjule and S. Kurungot, *J. Mater. Chem.*, **2012**, 22, 23506-23513.
- 16 Single-layer-graphene-assembled 3D hexaporous carbon for high performance supercapacitor.  
P. Yadav, A. Banerjee, **S. M. Unni**, J. Jog, S. Kurungot and S. B. Ogale, *ChemSusChem*. **2012**, 5, 2159 – 2164.
- 17 Disordered brownmillerite with enhanced oxygen reduction activity  
C. P. Jijil, S. M. Unni, S. Kurungot and R. N. Devi, *Chem. Mater.* **2012**, 24, 2823–2828.
- 18 Trigol based reduction of graphite oxide to graphene with enhanced charge storage activity  
D. Mhamane, **S. M. Unni**, A. Suryawanshi, O. Game, C. Rode, B. Hannoyer, S. Kurungot, and S. B. Ogale, *J. Mater. Chem.*, **2012**, 22, 11140-11145.
- 19 *Ex-situ* dispersion of core-shell nanoparticles of Cu-Pt on an *in situ* modified

- carbon surface and their enhanced electrocatalytic activities  
V.M. Dhavale, **S. M. Unni**, H. N. Kagalwala, V. K. Pillai and S.Kurungot *Chem. Commun.*, **2011**, 47, 3951-3953.
- 20 High Pt Utilization Electrodes for Polymer Electrolyte Membrane Fuel Cells by Dispersing Pt Particles Formed by a Preprecipitation Method on Carbon “Polished” with Polypyrrole  
**S. M. Unni**, V. M. Dhavale, V. K. Pillai and S. Kurungot, *J. Phys. Chem. C*, **2010**, *114*,14654–14661.
- 21 Pt–MoO<sub>x</sub>-carbon nanotube redox couple based electrocatalyst as a potential partner with polybenzimidazole membrane for high temperature Polymer Electrolyte Membrane Fuel Cell application.  
R. Vellacheri, **S. M. Unni**, S. Nahire, U. K. Kharul and S. Kurungot  
*Electrochim. Acta*, **2010**, *55*, 2878-2887.
- 22 Carbon Nanofiber with Selectively Decorated Pt Both on Inner and Outer Walls as an Efficient Electrocatalyst for Fuel Cell Applications  
B. K. Balan, **S. M. Unni** and S. Kurungot *J. Phys. Chem. C*, **2009**, *113*, 17572–17578.
- 23 Domain Size Manipulation of Perfluorinated Polymer Electrolytes by Sulfonic Acid-Functionalized MWCNTs to Enhance Fuel Cell Performance  
R. Kannan, M. Parthasarathy, **S. M. Unni**, S. Kurungot and V. K. Pillai,  
*Langmuir*, **2009**, *25*, 8299–8305.
- 24 Carbon Nanohorn-derived Graphene Nanotubes as a Platinum-free Fuel Cell Cathode  
**S. M. Unni**, R. Illathvalappil, S. N. Bhange, H. Puthenpediakkal and S. Kurungot  
**2015**, ACS Appl. Mater. Interfaces, DOI: 10.1021/acsami.5b07802
- 25 Nitrogen doped nanohorns as an efficient photocatalyst for hydrogen production from water  
**S. M. Unni**, L. George, S. Thayyil, R. Nandinidevi and S. Kurungot, communicated
- 26 Valorization of Coffee Bean Waste: Coffee Bean Waste Derived Multifunctional Catalyst for Photocatalytic Hydrogen Production and Electrocatalytic Oxygen Reduction Reactions

- 
- S. M. Unni**, L. George, S. N. Bhange, R. Nandinidevi and S. Kurungot communicated
- 27 Nitrogen and Sulphur Co-doped Crumbled Graphene for Oxygen Reduction Reaction with Improved Activity and Stability in Acidic Medium  
S. N. Bhange, **S. M. Unni** and S. Kurungot, Communicated
- 28 Layer-separated MoS<sub>2</sub> bearing reduced graphene oxide formed by an in-situ intercalation-cum-anchoring route as a Pt-free electrocatalyst for oxygen reduction  
R. Illathvalappil, **S. M. Unni** and S. Kurungot, *Nanoscale*, **2015**, 7, 16729-16736



*Erratum*











